

1

<sup>2</sup>A SEARCH FOR LONG-LIVED, CHARGED, SUPERSYMMETRIC PARTICLES  
<sup>3</sup>USING IONIZATION WITH THE ATLAS DETECTOR

<sup>4</sup>BRADLEY AXEN

5



6

September 2016 – Version 0.62

<sup>8</sup> Bradley Axen: *A Search for Long-Lived, Charged, Supersymmetric Particles using*  
<sup>9</sup> *Ionization with the ATLAS Detector*, Subtitle, © September 2016

<sup>10</sup> The dissertation of Bradley Axen, titled *A Search for Long-Lived, Charged, Super-*  
<sup>11</sup> *symmetric Particles using Ionization with the ATLAS Detector*, is approved:

<sup>12</sup> \_\_\_\_\_  
<sup>13</sup> Chair \_\_\_\_\_ Date

<sup>14</sup> \_\_\_\_\_  
<sup>15</sup> \_\_\_\_\_ Date

<sup>16</sup> \_\_\_\_\_  
<sup>17</sup> \_\_\_\_\_ Date

<sup>18</sup> University of California, Berkeley

19

Usually a quotation.

20

Dedicated to.

<sub>21</sub> ABSTRACT

---

<sub>22</sub> How to write a good abstract:

<sub>23</sub> <https://plg.uwaterloo.ca/~migod/research/beck00PSLA.html>

<sup>24</sup> PUBLICATIONS

---

<sup>25</sup> Some ideas and figures have appeared previously in the following publications:

<sup>26</sup>

<sup>27</sup> Put your publications from the thesis here. The packages `multibib` or `bibtopic`  
<sup>28</sup> etc. can be used to handle multiple different bibliographies in your document.

30 ACKNOWLEDGEMENTS

---

31 Put your acknowledgements here.

32

33 And potentially a second round.

34

<sup>35</sup> CONTENTS

---

<sup>36</sup> 1	INTRODUCTION	<sup>1</sup>
<sup>37</sup> I	THEORETICAL CONTEXT	<sup>3</sup>
<sup>38</sup> 2	STANDARD MODEL	<sup>4</sup>
<sup>39</sup> 2.1	Action and the Lagrangian . . . . .	<sup>4</sup>
<sup>40</sup> 2.2	Gauge Invariance and Forces . . . . .	<sup>5</sup>
<sup>41</sup> 2.2.1	$SU(2) \times U(1)$ and the Electroweak Force . . . . .	<sup>7</sup>
<sup>42</sup> 2.2.2	$SU(3)$ and the Strong Force . . . . .	<sup>7</sup>
<sup>43</sup> 2.3	Noether's Theorem, Charges, and Matter . . . . .	<sup>8</sup>
<sup>44</sup> 2.3.1	Quarks . . . . .	<sup>8</sup>
<sup>45</sup> 2.3.2	Leptons . . . . .	<sup>9</sup>
<sup>46</sup> 2.3.3	Chirality . . . . .	<sup>10</sup>
<sup>47</sup> 2.4	Higgs Mechanism and Mass . . . . .	<sup>10</sup>
<sup>48</sup> 2.5	Phenomenology . . . . .	<sup>12</sup>
<sup>49</sup> 2.5.1	Electroweak Physics . . . . .	<sup>12</sup>
<sup>50</sup> 2.5.2	Strong Physics . . . . .	<sup>12</sup>
<sup>51</sup> 2.5.3	Proton-Proton Collisions . . . . .	<sup>13</sup>
<sup>52</sup> 2.6	Limitations . . . . .	<sup>13</sup>
<sup>53</sup> 2.6.1	Theoretical Concerns . . . . .	<sup>14</sup>
<sup>54</sup> 2.6.2	Cosmological Observations . . . . .	<sup>15</sup>
<sup>55</sup> 3	SUPERSYMMETRY	<sup>17</sup>
<sup>56</sup> 3.1	Structure . . . . .	<sup>17</sup>
<sup>57</sup> 3.2	Motivation . . . . .	<sup>19</sup>
<sup>58</sup> 3.3	Simplified Models . . . . .	<sup>20</sup>
<sup>59</sup> 3.4	Long-Lived Particles . . . . .	<sup>21</sup>
<sup>60</sup> II	EXPERIMENTAL STRUCTURE AND RECONSTRUCTION	<sup>23</sup>
<sup>61</sup> 4	THE LARGE HADRON COLLIDER	<sup>24</sup>
<sup>62</sup> 4.1	Injection Chain . . . . .	<sup>25</sup>
<sup>63</sup> 4.2	Design . . . . .	<sup>26</sup>
<sup>64</sup> 4.2.1	Layout . . . . .	<sup>26</sup>
<sup>65</sup> 4.2.2	Magnets . . . . .	<sup>27</sup>
<sup>66</sup> 4.2.3	RF Cavities . . . . .	<sup>28</sup>
<sup>67</sup> 4.2.4	Beam . . . . .	<sup>30</sup>
<sup>68</sup> 4.3	Luminosity Parameters . . . . .	<sup>30</sup>
<sup>69</sup> 4.4	Delivered Luminosity . . . . .	<sup>31</sup>
<sup>70</sup> 5	THE ATLAS DETECTOR	<sup>34</sup>
<sup>71</sup> 5.1	Coordinate System . . . . .	<sup>36</sup>
<sup>72</sup> 5.2	Magnetic Field . . . . .	<sup>37</sup>
<sup>73</sup> 5.3	Inner Detector . . . . .	<sup>39</sup>
<sup>74</sup> 5.3.1	Pixel Detector . . . . .	<sup>42</sup>
<sup>75</sup> 5.3.2	Semiconductor Tracker . . . . .	<sup>44</sup>

76	5.3.3	Transition Radiation Tracker . . . . .	47
77	5.4	Calorimetry . . . . .	48
78	5.4.1	Electromagnetic Calorimeter . . . . .	49
79	5.4.2	Hadronic Calorimeters . . . . .	50
80	5.5	Muon Spectrometer . . . . .	52
81	5.5.1	Monitored Drift Tube . . . . .	54
82	5.5.2	Resistive Plate Chamber . . . . .	55
83	5.5.3	Cathode Strip Chamber . . . . .	55
84	5.5.4	Thin Gap Chamber . . . . .	56
85	5.6	Trigger . . . . .	57
86	6	EVENT RECONSTRUCTION . . . . .	61
87	6.1	Charged Particles . . . . .	61
88	6.1.1	Pixel Neural Network . . . . .	63
89	6.1.2	Pixel dE/dx . . . . .	64
90	6.1.3	Vertex Reconstruction . . . . .	65
91	6.2	Electrons and Photons . . . . .	65
92	6.2.1	Photon Identification . . . . .	67
93	6.2.2	Electron Identification . . . . .	67
94	6.3	Muons . . . . .	67
95	6.3.1	Muon Identification . . . . .	68
96	6.4	Jets . . . . .	68
97	6.4.1	Topological Clustering . . . . .	68
98	6.4.2	Jet Algorithms . . . . .	70
99	6.4.3	Jet Energy Scale . . . . .	70
100	6.5	Missing Transverse Energy . . . . .	71
101	III	CALORIMETER RESPONSE . . . . .	74
102	7	RESPONSE MEASUREMENT WITH SINGLE HADRONS . . . . .	75
103	7.1	Dataset and Simulation . . . . .	76
104	7.1.1	Data Samples . . . . .	76
105	7.1.2	Simulated Samples . . . . .	76
106	7.1.3	Event Selection . . . . .	76
107	7.2	Inclusive Hadron Response . . . . .	77
108	7.2.1	E/p Distribution . . . . .	77
109	7.2.2	Zero Fraction . . . . .	78
110	7.2.3	Neutral Background Subtraction . . . . .	80
111	7.2.4	Corrected Response . . . . .	81
112	7.2.5	Additional Studies . . . . .	83
113	7.3	Identified Particle Response . . . . .	86
114	7.3.1	Decay Reconstruction . . . . .	87
115	7.3.2	Identified Response . . . . .	88
116	7.3.3	Additional Species in Simulation . . . . .	90
117	7.4	Summary . . . . .	90
118	8	JET ENERGY RESPONSE AND UNCERTAINTY . . . . .	92
119	8.1	Motivation . . . . .	92
120	8.2	Uncertainty Estimate . . . . .	92

121	8.3	Summary . . . . .	95
122	IV	SEARCH FOR LONG-LIVED PARTICLES	98
123	9	LONG-LIVED PARTICLES IN ATLAS	99
124	9.1	Event Topology . . . . .	99
125	9.1.1	Detector Interactions . . . . .	100
126	9.1.2	Lifetime Dependence . . . . .	102
127	9.2	Simulation . . . . .	105
128	10	EVENT SELECTION	108
129	10.1	Trigger . . . . .	109
130	10.2	Kinematics and Isolation . . . . .	110
131	10.3	Particle Species Rejection . . . . .	114
132	10.4	Ionization . . . . .	118
133	10.4.1	Mass Estimation . . . . .	118
134	10.5	Event Selection . . . . .	120
135	11	BACKGROUND ESTIMATION	122
136	11.1	Background Sources . . . . .	122
137	11.2	Prediction Method . . . . .	123
138	11.3	Validation . . . . .	124
139	11.3.1	Closure in Simulation . . . . .	124
140	11.3.2	Validation Region in Data . . . . .	125
141	11.4	Expected Background . . . . .	126
142	12	SYSTEMATIC UNCERTAINTIES	128
143	12.1	Background Estimate . . . . .	128
144	12.1.1	Analytic Description of $dE/dx$ . . . . .	129
145	12.1.2	Muon Fraction . . . . .	129
146	12.1.3	IBL Corrections . . . . .	129
147	12.1.4	Normalization . . . . .	129
148	12.2	Signal Yield . . . . .	130
149	12.2.1	initial state radiation ( <b>ISR</b> ) Modeling . . . . .	130
150	12.2.2	Pileup Reweighting . . . . .	130
151	12.2.3	Trigger Efficiency Reweighting . . . . .	131
152	12.2.4	Missing Transverse Momentum Scale . . . . .	132
153	12.2.5	Momentum Parametrization . . . . .	132
154	12.2.6	Ionization Requirement . . . . .	133
155	12.2.7	Electron and Jet Rejection . . . . .	133
156	12.2.8	Muon Veto . . . . .	133
157	12.2.9	Luminosity . . . . .	134
158	12.2.10	Signal Cross Section . . . . .	134
159	13	RESULTS	136
160	13.1	Cross Section Limits . . . . .	136
161	13.2	Mass Limits . . . . .	139
162	14	SUMMARY AND OUTLOOK	143
163	V	APPENDIX	145
164	A	EXPANDED R-HADRON YIELDS AND LIMITS	146



166 LIST OF FIGURES

---

167	Figure 1	A Feynman diagram representing the interaction of the $A$ field with a generic fermion, $f$ . . . . .	7
168			
169	Figure 2	The particle content of the <a href="#">SM</a> . . . . .	9
170	Figure 3	The Feynman diagrams representing the decays of the W and Z bosons to fermions. Here $f$ indicates a generic fermion, $\bar{f}$ its antiparticle, and $f'$ the partner of that fermion in the same generation. . . . .	12
171			
172			
173			
174	Figure 4	The parton distribution functions ( <a href="#">PDFs</a> ) for proton-proton collisions at $Q^2 = 10 \text{ GeV}^2$ and $Q^2 = 10^4 \text{ GeV}^2$ . Each shows the fraction of particles which carry a fraction $x$ of the total proton energy at the specified scale [1]. . . . .	14
175			
176			
177			
178			
179	Figure 5	An approximation of the running of the coupling constants in the Standard Model ( <a href="#">SM</a> ) up to the Planck scale [2]. . . . .	15
180			
181			
182	Figure 6	The distribution of velocities of stars as a function of the radius from the center of the galaxy. The contributions to the velocity from the various components of matter in the galaxy are shown [3]. . . . .	16
183			
184			
185			
186	Figure 7	An approximation of the running of the coupling constants in the Minimal Supersymmetric Model ( <a href="#">MSSM</a> ) up to the Planck scale [2]. . . . .	20
187			
188			
189	Figure 8	The decay of a gluino to quarks and an <a href="#">LSP</a> , which precedes through a squark. . . . .	21
190			
191	Figure 9	The four collision points and corresponding experiments of the Large Hadron Collider ( <a href="#">LHC</a> ). The image includes the location of the nearby city of Geneva as well as the border of France and Switzerland. . . . .	25
192			
193			
194			
195	Figure 10	The cumulative luminosity over time delivered to the ATLAS experiment from high energy proton-proton collisions since 2011. The energies of the collisions are listed for each of the data-taking periods. . . . .	26
196			
197			
198			
199	Figure 11	The accelerator complex that builds up to the full design energies at the <a href="#">LHC</a> . The protons are passed in order to Linac 2, the <a href="#">PSB</a> , the <a href="#">PS</a> , the <a href="#">SPS</a> and then the <a href="#">LHC</a> . . . . .	27
200			
201			
202			
203	Figure 12	A schematic of the layout of the <a href="#">LHC</a> , not to scale. The arched and straight sections are illustrated at the bottom of the schematic, and all four crossing sites are indicated with their respective experiments. . . . .	28
204			
205			
206			

207	Figure 13	A cross section of the the cryodipole magnets which bend the flight path of protons around the circumference of the LHC. The diagram includes both the superconducting coils which produce the magnetic field and the structural elements which keep the magnets precisely aligned. . . . .	29
208			
209			
210			
211			
212			
213	Figure 14	The arrangement of four radiofrequency (RF) cavities within a cryomodule. . . . .	29
214			
215	Figure 15	The cumulative luminosity versus time delivered to ATLAS (green), recorded by ATLAS (yellow), and certified to be good quality data (blue) during stable beams for pp collisions at 13 TeV in 2015. . . . .	32
216			
217			
218			
219	Figure 16	The luminosity-weighted distribution of the mean number of interactions per crossing for the 2015 pp collision data at 13 TeV. . . . .	33
220			
221			
222	Figure 17	A cut-away schematic of the layout of the ATLAS detector. Each of the major subsystems is indicated. . . . .	35
223			
224	Figure 18	A cross-sectional slice of the ATLAS experiment which illustrates how the various SM particles interact with the detector systems. . . . .	35
225			
226			
227	Figure 19	The layout of the four superconducting magnets in the ATLAS detector. . . . .	38
228			
229	Figure 20	The arrangement of the subdetectors of the ATLAS inner detector. Each of the subdetectors is labeled in the cut-away view of the system. . . . .	40
230			
231			
232	Figure 21	A quarter section of the ATLAS inner detector which shows the layout of each of the subdetectors in detail. The lower panel shows an enlarged view of the pixel detector. Example trajectories for a particle with $\eta = 1.0, 1.5, 2.0, 2.5$ are shown. The Insertible B-Layer (IBL), which was added after the original detector commissioning, is not shown. . . . .	40
233			
234			
235			
236			
237			
238			
239	Figure 22	A computer generated three-dimensional view of the inner detector along the line of the beam axis. The subdetectors and their positions are labeled. . . . .	41
240			
241			
242	Figure 23	An alternative computer generated three-dimensional view of the inner detector transverse to the beam axis. The subdetectors and their positions are labeled. . . . .	41
243			
244			
245	Figure 24	The integrated radiation lengths traversed by a straight track at the exit of the ID envelope, including the services and thermal enclosures. The distribution is shown as a function of $ \eta $ and averaged over $\phi$ . The breakdown indicates the contributions of individual subdetectors, including services in their active volume. . . . .	42
246			
247			
248			
249			
250			
251	Figure 25	A cut away image of the outer three layers of the pixel detector. . . . .	45
252			

253	Figure 26	An image of the insertion of the <b>IBL</b> into the current pixel detector. . . . .	45
254			
255	Figure 27	A three-dimensional computer-generated image of the geometry of the <b>IBL</b> with a view (a) mostly transverse to the beam pipe (b) mostly parallel to the beam pipe. . . . .	46
256			
257			
258	Figure 28	An expanded view of the geometry of the silicon microstrip ( <b>SCT</b> ) double layers in the barrel region. . . . .	47
259			
260	Figure 29	. . . . .	48
261	Figure 30	The depth of (a) the electromagnetic barrel calorimeter in radiation lengths and (b) all calorimeters in interaction lengths as a function of pseudorapidity. . . . .	49
262			
263			
264	Figure 31	A schematic of the liquid argon ( <b>LAr</b> ) calorimeter in the barrel region, highlighting the accordion structure. . . . .	50
265			
266	Figure 32	A schematic of a hadronic tile module which shows the alternating layers of steel and plastic scintillator. . . . .	51
267			
268	Figure 33	The segmentation in depth and $\eta$ of the tile-calorimeter modules in the central (left) and extended (right) barrels. . . . .	52
269			
270	Figure 34	A cut-away diagram of the muon systems on ATLAS. . . . .	53
271	Figure 35	A quarter view of the muon spectrometer which highlights the layout of each of the detecting elements. The BOL, BML, BIL, EOL, EML, and EIL are all Monitored Drift Tube ( <b>MDT</b> ) elements, where the acronyms encode their positions. . . . .	53
272			
273			
274			
275			
276	Figure 36	A schematic of the cross-section of the muon spectrometer in the barrel region. . . . .	54
277			
278	Figure 37	A schematic of a single <b>MDT</b> chamber, which shows the multilayers of drift tubes as well as the alignment system. . . . .	55
279			
280			
281	Figure 38	A schematic of the Cathode Strip Chamber ( <b>CSC</b> ) end-cap, showing the overlapping arrangement of the eight large and eight small chambers. . . . .	56
282			
283			
284	Figure 39	A schematic of the Thin Gap Chamber ( <b>TGC</b> ) doublet and triplet layers. . . . .	57
285			
286	Figure 40	The L1 Trigger rate broken down into the types of triggers as a function of the luminosity block for the 2015 data collection period. . . . .	59
287			
288			
289	Figure 41	The HLT Trigger rate broken down into the types of triggers as a function of the luminosity block for the 2015 data collection period. . . . .	60
290			
291			
292	Figure 42	An illustration of the perigee representation of track parameters for an example track. The charge is not directly shown, but is indicated by the direction of curvature of the track [21]. . . . .	62
293			
294			
295			

296	Figure 43	The $x$ and $y$ locations of the hits generated in a simulated $t\bar{t}$ event in the inner detector. The hits which belong to tracks formed using the inside-out algorithm are highlighted in red, while the hits which belong to tracks formed using the outside-in algorithm are circled in black. . . . .	63
302	Figure 44	Examples of the clusters formed in a single layer of the pixel detector for (a) a single isolated particle, (b) two nearly-overlapping particles, and (c) a particle which emits a $\delta$ -ray [22]. . . . .	64
306	Figure 45	The total, fractional jet energy scale ( <a href="#">JES</a> ) uncertainties estimated for 2015 data as a function of jet $p_T$ . . . . .	72
308	Figure 46	The $E/p$ distribution and ratio of simulation to data for isolated tracks with (a) $ \eta  < 0.6$ and $1.2 < p/\text{GeV} < 1.8$ and (b) $ \eta  < 0.6$ and $2.2 < p/\text{GeV} < 2.8$ . . . . .	78
311	Figure 47	The fraction of tracks as a function (a, b) of momentum, (c, d) of interaction lengths with $E \leq 0$ for tracks with positive (on the left) and negative (on the right) charge. . . . .	79
315	Figure 48	An illustration (a) of the geometry of energy deposits in the calorimeter. The red energy deposits come from the charged particle targeted for measurement, while the blue energy deposits are from nearby neutral particles and must be subtracted. The same diagram (b) for the neutral-background selection, described in Section 7.2.3. . . . .	80
322	Figure 49	$\langle E/p \rangle_{\text{BG}}$ as a function of the track momentum for tracks with (a) $ \eta  < 0.6$ , (b) $0.6 <  \eta  < 1.1$ , and as a function of the track pseudorapidity for tracks with (c) $1.2 < p/\text{GeV} < 1.8$ , (d) $1.8 < p/\text{GeV} < 2.2$ . . . . .	81
326	Figure 50	$\langle E/p \rangle_{\text{COR}}$ as a function of track momentum, for tracks with (a) $ \eta  < 0.6$ , (b) $0.6 <  \eta  < 1.1$ , (c) $1.8 <  \eta  < 1.9$ , and (d) $1.9 <  \eta  < 2.3$ . . . . .	82
329	Figure 51	$\langle E/p \rangle_{\text{COR}}$ calculated using LCW-calibrated topological clusters as a function of track momentum for tracks with (a) zero or more associated topological clusters or (b) one or more associated topological clusters. . . . .	83
333	Figure 52	Comparison of the $\langle E/p \rangle_{\text{COR}}$ for tracks with (a) less than and (b) greater than 20 hits in the TRT. . . . .	84
335	Figure 53	Comparison of the $\langle E/p \rangle_{\text{COR}}$ for (a) positive and (b) negative tracks as a function of track momentum for tracks with $ \eta  < 0.6$ . . . . .	85
338	Figure 54	Comparison of the $E/p$ distributions for (a) positive and (b) negative tracks with $0.8 < p/\text{GeV} < 1.2$ and $ \eta  < 0.6$ , in simulation with the FTFP_BERT and QGSP_BERT physics lists. . . . .	85

342	Figure 55	Comparison of the response of the hadronic calorimeter as a function of track momentum (a) at the EM-scale and (b) after the LCW calibration. . . . .	86
343			
344			
345	Figure 56	Comparison of the response of the EM calorimeter as a function of track momentum (a) at the EM-scale and (b) with the LCW calibration. . . . .	86
346			
347			
348	Figure 57	The reconstructed mass peaks of (a) $K_S^0$ , (b) $\Lambda$ , and (c) $\bar{\Lambda}$ candidates. . . . .	87
349			
350	Figure 58	The $E/p$ distribution for isolated (a) $\pi^+$ , (b) $\pi^-$ , (c) proton, and (d) anti-proton tracks. . . . .	88
351			
352	Figure 59	The fraction of tracks with $E \leq 0$ for identified (a) $\pi^+$ and $\pi^-$ , and (b) proton and anti-proton tracks . . . . .	89
353			
354	Figure 60	The difference in $\langle E/p \rangle$ between (a) $\pi^+$ and $\pi^-$ (b) $p$ and $\pi^+$ , and (c) $\bar{p}$ and $\pi^-$ . . . . .	90
355			
356	Figure 61	$\langle E/p \rangle_{\text{COR}}$ as a function of track momentum for (a) $\pi^+$ tracks and (b) $\pi^-$ tracks. . . . .	91
357			
358	Figure 62	The ratio of the calorimeter response to single particles of various species to the calorimeter response to $\pi^+$ with the physics list FTFP_BERT. . . . .	91
359			
360			
361	Figure 63	The spectra of true particles inside anti- $k_t$ , $R = 0.4$ jets with (a) $90 < p_T/\text{GeV} < 100$ , (b) $400 < p_T/\text{GeV} < 500$ , and (c) $1800 < p_T/\text{GeV} < 2300$ . . . . .	93
362			
363			
364	Figure 64	The JES response uncertainty contributions, as well as the total JES uncertainty, as a function of jet $p_T$ for (a) $ \eta  < 0.6$ and (b) $0.6 <  \eta  < 1.1$ . . . . .	96
365			
366			
367	Figure 65	The correlations between bins of average reconstructed jet momentum as a function of jet $p_T$ and $ \eta $ for jets in the central region of the detector. . . . .	97
368			
369			
370	Figure 66	The processes which contribute to gluino pair production in the proton proton collisions, where the quarks and gluons are proton constituents. . . . .	100
371			
372			
373	Figure 67	The generated $p_T$ and $\beta$ distributions for R-Hadrons with $M = 1600 \text{ GeV}$ . . . . .	100
374			
375	Figure 68	A schematic diagram of an R-Hadron event with a lifetime around 0.01 ns. The diagram includes one charged R-Hadron (solid blue), one neutral R-Hadron (dashed blue), Lightest Supersymmetric Particles (LSPs) (dashed green) and charged hadrons (solid orange). The pixel detector, calorimeters, and muon system are illustrated but not to scale. . . . .	103
376			
377			
378			
379			
380			
381			

382	Figure 69	Schematic diagram of an R-Hadron event with a life-time around 5 ns, where the masses of the R-Hadron and LSP are nearly degenerate. The diagram includes charged R-Hadrons (solid blue), neutral R-Hadrons (dashed blue), LSPs (dashed green) and charged hadrons (solid orange). The pixel detector, calorimeters, and muon system are illustrated but not to scale. . . . .	104
383			
384			
385			
386			
387			
388			
389	Figure 70	Schematic diagram of an R-Hadron event with a life-time around 5 ns, where the masses of the R-Hadron and LSP are not degenerate. The diagram includes charged R-Hadrons (solid blue), neutral R-Hadrons (dashed blue), LSPs (dashed green) and charged hadrons (solid orange). The pixel detector, calorimeters, and muon system are illustrated but not to scale. . . . .	105
390			
391			
392			
393			
394			
395			
396	Figure 71	A schematic diagram of an R-Hadron event with a life-time around 20 ns. The diagram includes one charged R-Hadron (solid blue), one neutral R-Hadron (dashed blue), LSPs (dashed green) and charged hadrons (solid orange). The pixel detector, calorimeters, and muon system are illustrated but not to scale. . . . .	106
397			
398			
399			
400			
401			
402	Figure 72	A schematic diagram of a very long-lived (VLL) R-Hadron event. The diagram includes one charged R-Hadron (solid blue) and one neutral R-Hadron (dashed blue). The pixel detector, calorimeters, and muon system are illustrated but not to scale. . . . .	107
403			
404			
405			
406			
407	Figure 73	The distribution of (a) $E_T^{\text{miss}}$ and (b) Calorimeter $E_T^{\text{miss}}$ for simulated signal events before the trigger requirement. The final bin includes all events above the axis range. . . . .	110
408			
409			
410			
411	Figure 74	The distribution of $E_T^{\text{miss}}$ for data and simulated signal events, after the trigger requirement. The final bin includes all events above the axis range. . . . .	111
412			
413			
414	Figure 75	The trigger efficiency for the HLT_xe70 trigger requirement as a function of (a) $E_T^{\text{miss}}$ and (b) Calorimeter $E_T^{\text{miss}}$ for simulated signal events. . . . .	112
415			
416			
417	Figure 76	The dependence of $dE/dx$ on $N_{\text{split}}$ in data after basic track hit requirements have been applied. . . . .	113
418			
419	Figure 77	The distribution of $dE/dx$ with various selections applied in data and simulated signal events. The final bin includes all tracks above the axis range. . . . .	113
420			
421			
422	Figure 78	The distribution of track momentum for data and simulated signal events, after previous selection requirements have been applied. The final bin includes all tracks above the axis range. . . . .	114
423			
424			
425			

426	Figure 79	The distribution of $M_T$ for data and simulated signal events, after previous selection requirements have been applied. The final bin includes all tracks above the axis range. . . . .	115
427			
428			
429			
430	Figure 80	The distribution of summed tracked momentum within a cone of $\Delta R < 0.25$ around the candidate track for data and simulated signal events, after previous selection requirements have been applied. The final bin includes all tracks above the axis range. . . . .	116
431			
432			
433			
434			
435	Figure 81	The normalized, two-dimensional distribution of $E/p$ and $f_{EM}$ for simulated (a) 1200 GeV <b>VLL</b> R-Hadron, and (b) 1200 GeV, 10 ns R-Hadron, (c) $Z \rightarrow ee$ , and (d) $Z \rightarrow \tau\tau$ events. . . . .	117
436			
437			
438			
439	Figure 82	Two-dimensional distribution of $dE/dx$ versus charge signed momentum ( $qp$ ) for minimum-bias tracks. The fitted distributions of the most probable values for pions, kaons and protons are superimposed. . . . .	119
440			
441			
442			
443	Figure 83	The distribution of mass estimated using $dE/dx$ for simulated <b>VLL</b> R-Hadrons with masses between 1000 and 1600 GeV. . . . .	119
444			
445			
446	Figure 84	The acceptance $\times$ efficiency as a function of R-Hadron (a) mass and (b) lifetime. (a) shows all of the combinations of mass and lifetime considered in this search, and (b) highlights the lifetime dependence for 1000 GeV and 1600 GeV R-Hadrons. . . . .	121
447			
448			
449			
450			
451	Figure 85	The distribution of (a) $dE/dx$ and (b) momentum for tracks in data and simulated signal after requiring the event level selection and the track selection on $p_T$ , hits, and $N_{\text{split}}$ . Each sub-figure shows the normalized distributions for tracks classified as hadrons, electrons, and muons in data and R-Hadrons in the simulated signal. . . . .	123
452			
453			
454			
455			
456			
457			
458	Figure 86	The distribution of $M_{dE/dx}$ (a) before and (b) after the ionization requirement for tracks in simulated W boson decays and for the randomly generated background estimate. . . . .	125
459			
460			
461			
462	Figure 87	The distribution of $M_{dE/dx}$ (a) before and (b) after the ionization requirement for tracks in the validation region and for the randomly generated background estimate. . . . .	126
463			
464			
465			
466	Figure 88	The trigger efficiency for the HLT_xe70 trigger requirement as a function of Calorimeter $E_T^{\text{miss}}$ for simulated data events with a W boson selection. Simulated signal events and simulated W boson events are also included. . . . .	131
467			
468			
469			
470			

471	Figure 89	The efficiency of the muon veto for $R$ -hadrons of two different masses, as a function of $\frac{1}{\beta}$ for simulated R-Hadron tracks. . . . .	134
472			
473			
474	Figure 90	The average reconstructed MDT $\beta$ distribution for $Z \rightarrow \mu\mu$ events in which one of the muons has a late arrival time in the MDT, for both data and simulation. A gaussian fit is superimposed. . . . .	135
475			
476			
477			
478	Figure 91	The observed mass distribution of events in data and the generated background distribution in (a) the VLL and (b) the long-lived (LL) signal region. A few example simulated signal distributions are superimposed. . .	137
479			
480			
481			
482	Figure 92	The observed and expected cross section limits as a function of mass for the VLL simulated signal. The predicted cross section values for the corresponding signals are also shown. . . . .	139
483			
484			
485			
486	Figure 93	The observed and expected cross section limits as a function of mass for each generated lifetime. The predicted cross section values for the corresponding signals are also shown. An example of Run 1 cross section limits and predicted cross sections are shown in (d) for comparison. . . . .	140
487			
488			
489			
490			
491			
492	Figure 94	The excluded range of masses as a function of gluino lifetime. The expected lower limit (LL), with its experimental $\pm 1\sigma$ band, is given with respect to the nominal theoretical cross section. The observed 95% LL obtained at $\sqrt{s} = 8$ TeV [83] is also shown for comparison.	142
493			
494			
495			
496			
497	Figure 95	The constraints on the gluino mass as a function of lifetime for a split-supersymmetry model with the gluino R-Hadrons decaying into a gluon or light quarks and a neutralino with mass of 100 GeV. The solid lines indicate the observed limits, while the dashed lines indicate the expected limits. The area below the curves is excluded. The dots represent results for which the particle is assumed to be prompt or VLL. This curve representing this analysis is shown in orange. . . . .	144
498			
499			
500			
501			
502			
503			
504			
505			

506 LIST OF TABLES

---

507	Table 1	The particles in the <b>SM</b> and their corresponding superpartners in the <b>MSSM</b> . . . . .	18
508			
509	Table 2	The design parameters of the <b>LHC</b> beam that determines the energy of collisions and the luminosity, for both the injection of protons and at the nominal circulation. . . . .	31
510			
511			
512			
513	Table 3	The performance goals for each of the subsystems of the ATLAS detector. The $ \eta $ coverage specifies the range where the subsystem needs to be able to provide measurements with the specified resolution. The resolutions include a $p_T$ or E dependence that is added in quadrature with a $p_T/E$ independent piece. . . . .	36
514			
515			
516			
517			
518			
519	Table 4	A summary of the parameters of each of the three magnet systems on ATLAS. . . . .	38
520			
521	Table 5	A summary of the parameters of the inner detector and each of the subdetectors [13]. . . . .	43
522			
523	Table 6	A summary of the expected performance of the combined inner detector [17]. Included are the reconstruction efficiencies for multiple particle types as well as the momentum and impact parameter ( <b>IP</b> ) resolution for various momenta. . . . .	44
524			
525			
526			
527			
528	Table 7	The trigger menu for the 2015 data collection with $L = 5 \times 10^{33} \text{ cm}^{-2} \text{ s}^{-1}$ . Both the L1 and high level trigger ( <b>HLT</b> ) selection requirements and their trigger rates are shown measured at the specified luminosity are shown. The typical offline selections represent a typical set of offline requirements imposed after the trigger in an analysis. . . . .	58
529			
530			
531			
532			
533			
534			
535	Table 8	The dominant sources of corrections and systematic uncertainties in the <b>JES</b> estimation technique, including typical values for the correcting shift ( $\Delta$ ) and the associated uncertainty ( $\sigma$ ). . . . .	94
536			
537			
538			
539	Table 9	The radial distances of each of the subdetectors and example arrival times for an R-Hadron with $\eta = 0$ and the specified $\beta$ . . . . .	101
540			
541			

542	Table 10	The expected number of events at each level of the selection for <b>LL</b> 1600 GeV, 10 ns R-Hadrons, along with the number of events observed in data, for $3.2 \text{ fb}^{-1}$ . The simulated yields are shown with statistical uncertainties only. The total efficiency $\times$ acceptance is also shown for the signal and the rejection factor relative to initial track requirement is shown for data. . . . .	120
543			
544			
545			
546			
547			
548			
549	Table 11	The expected number of background events within each of the mass windows for the stable and metastable signal regions. . . . .	127
550			
551			
552	Table 12	A summary of the sources of systematic uncertainty for the data-driven background in the signal region. If the uncertainty depends on the mass, the maximum values are reported. . . . .	128
553			
554			
555			
556	Table 13	A summary of the sources of systematic uncertainty for the simulated signal yield. The uncertainty depends on the mass and lifetime, and the maximum negative and positive values are reported in the table. . . . .	130
557			
558			
559			
560	Table 14	Example of the contributing systematic variations to the total systematic for the $E_T^{\text{miss}}$ Scale, as measured in a 1200 GeV, <b>VLL</b> R-Hadron signal sample. . . . .	132
561			
562			
563	Table 15	The estimated number of background events and the number of observed events in data for the specified selection regions prior to the requirement on mass. The background estimates show statistical and systematic uncertainties. . . . .	136
564			
565			
566			
567			
568	Table 16	The left and right extremum of the mass window for each generated mass point with a 10 ns lifetime. . . . .	137
569			
570	Table 17	The left and right extremum of the mass window used for each generated <b>VLL</b> mass point. . . . .	137
571			
572	Table 18	The expected number of signal events, the expected number of background events, and the observed number of events in data with their respective statistical errors within the respective mass window for each generated <b>VLL</b> mass point . . . . .	138
573			
574			
575			
576			
577	Table 19	The expected number of signal events, the expected number of background events, and the observed number of events in data with their respective statistical errors within the respective mass window for each generated mass point with a lifetime of 10 ns. . . . .	138
578			
579			
580			
581			
582	Table 20	The observed and expected 95% CL lower limit on mass for gluino R-Hadrons for each considered lifetime. . . . .	141
583			
584	Table 21	The left and right extremum of the mass window for each generated mass point with a 50 ns lifetime. . . . .	146
585			
586	Table 22	The left and right extremum of the mass window for each generated mass point with a 30 ns lifetime. . . . .	146
587			

588	Table 23	The left and right extremum of the mass window for each generated mass point with a 10 ns lifetime. . . . .	147
589			
590	Table 24	The left and right extremum of the mass window used for each generated mass point with a lifetime of 3 ns. . . . .	147
591			
592	Table 25	The left and right extremum of the mass window used for each mass point with a lifetime of 1 ns. . . . . . . . .	147
593			
594	Table 26	The left and right extremum of the mass window for each generated mass point with a lifetime of 0.4 ns. . . . .	148
595			
596	Table 27	The left and right extremum of the mass window used for each generated stable mass point. . . . . . . . .	148
597			
598	Table 28	The expected number of signal events, the expected number of background events, and the observed number of events in data with their respective statistical errors within the respective mass window for each generated mass point with a lifetime of 50 ns. . . . . . . . .	148
599			
600			
601			
602			
603	Table 29	The expected number of signal events, the expected number of background events, and the observed number of events in data with their respective statistical errors within the respective mass window for each generated mass point with a lifetime of 30 ns. . . . . . . . .	149
604			
605			
606			
607			
608	Table 30	The expected number of signal events, the expected number of background events, and the observed number of events in data with their respective statistical errors within the respective mass window for each generated mass point with a lifetime of 10 ns. . . . . . . . .	149
609			
610			
611			
612			
613	Table 31	The expected number of signal events, the expected number of background events, and the observed number of events in data with their respective statistical errors within the respective mass window for each generated mass point with a lifetime of 3 ns. . . . . . . . .	150
614			
615			
616			
617			
618	Table 32	The expected number of signal events, the expected number of background events, and the observed number of events in data with their respective statistical errors within the respective mass window for each generated mass point with a lifetime of 1 ns. . . . . . . . .	150
619			
620			
621			
622			
623	Table 33	The expected number of signal events, the expected number of background events, and the observed number of events in data with their respective statistical errors within the respective mass window for each generated mass point with a lifetime of p4 ns. . . . . . . . .	151
624			
625			
626			
627			
628	Table 34	The expected number of signal events, the expected number of background events, and the observed number of events in data with their respective statistical errors within the respective mass window for each generated stable mass point . . . . . . . . . .	151
629			
630			
631			
632			

633 LISTINGS

---

634 ACRONYMS

---

- 635 SM Standard Model  
636 CERN European Organization for Nuclear Research  
637 SUSY Supersymmetry  
638 MSSM Minimal Supersymmetric Model  
639 cMSSM Constrained MSSM  
640 pMSSM Phenomenological MSSM  
641 LSP Lightest Supersymmetric Particle  
642 LHC Large Hadron Collider  
643 ATLAS A Toroidal LHC ApparatuS  
644 CMS Compact Muon Solenoid  
645 ALICE A Large Ion Collider Experiment  
646 LHCb Large Hadron Collider beauty experiment  
647 LEP the Large Electron Positron collider  
648 PS Proton Synchrotron  
649 PSB Proton Synchrotron Booster  
650 SPS Super Proton Synchrotron  
651 SCT silicon microstrip  
652 TRT Transition Radiation Tracker  
653 LAr liquid argon  
654 EM electromagnetic  
655 RPC Resistive Plate Chamber  
656 TGC Thin Gap Chamber  
657 MDT Monitored Drift Tube  
658 CSC Cathode Strip Chamber  
659 ToT time over threshold  
660 RoI Region of Interest

- 661 LCW local cluster weighted  
662 MIP minimally ionizing particle  
663 IP impact parameter  
664 EPJC European Physical Journal C  
665 JES jet energy scale  
666 LLP Long-Lived Particle  
667 LL long-lived  
668 VLL very long-lived  
669 CR Control Region  
670 NLO next-to-leading order  
671 NLL next-to-leading logarithmic  
672 PDF parton distribution function  
673 ISR initial state radiation  
674 RMS root mean square  
675 IBL Insertible B-Layer  
676 CP Combined Performance  
677 MDT Monitored Drift Tube  
678 RF radiofrequency  
679 HLT high level trigger  
680 QCD quantum chromodynamics  
681 BSM beyond the Standard Model

682

683 INTRODUCTION

---

684 As of 2012, with the discovery of the Higgs boson, the **SM** provides a complete  
685 and validated description of the interactions of fundamental particles. It de-  
686 scribes a remarkable range of phenomena given its simple foundation, and has  
687 been successful in explaining high energy physics in all experiments yet per-  
688 formed. However, it is clear that the picture is incomplete: without a description  
689 of gravity or an explanation for dark matter, an extension is necessary to de-  
690 scribe new physics at higher energies. These deficiencies motivate a wide range  
691 of experiments that search for new physics. The **LHC** provides the highest en-  
692 ergy approach, seeking to discover unobserved particles or interactions in high  
693 energy proton collisions.

694 The experiments at the **LHC** have searched for a variety of new phenomena  
695 in the years since collisions began in 2010. A major focus of these searches has  
696 been on Supersymmetry (**SUSY**), an extension to the **SM** which has the potential  
697 to ameliorate many of its shortfalls. None of the searches have found evidence of  
698 new physics, and between them they have begun to rule out a number of models  
699 that would predict new particles at the TeV scale. This motivates searches for  
700 more exotic signals that may have been missed, using analysis techniques tuned  
701 specifically for those signals.

702 This dissertation presents a search for Long-Lived Particles (**LLPs**) using the  
703 13 TeV collisions collected during 2015 at the **LHC**. Charged **LLPs** are predicted  
704 to exist in a subset of **SUSY** models, and have dramatically different detector sig-  
705 natures than both **SM** processes and other **SUSY** models. This search focuses on  
706 isolating that unique signature using ionization in the ATLAS detector.

707 Part I provides the theoretical context and motivation for a search for new  
708 physics in high energy collisions. Chapter 2 outlines the basic framework of the  
709 **SM** and describes its particles and interactions. It also discusses the limitations of  
710 the **SM** that motivate the existence of new physics. Chapter 3 discusses a possible  
711 solution to the shortcomings of the **SM**, the theory of Supersymmetry, and the  
712 ways that it can generate **LLP**.

713 Part II discusses the structure of the accelerator complex that provides col-  
714 lisions as well as the experiment that measures them. Chapter 4 summarizes  
715 the design and performance of the **LHC** and the features of the proton-proton  
716 collisions it produces. Chapter 5 then discusses the components of the ATLAS  
717 detector and how they can be used to measure the particles produced in **LHC** col-  
718 lisions. Chapter 6 describes the algorithms used to reconstruct physics particles  
719 and processes from the electronic signals in the detector.

720 Part III presents a measurement of calorimeter response, an important compo-  
721 nent of event reconstruction used in many physics analyses. Chapter 7 describes  
722 a direct, in situ measurement of calorimeter response using isolated hadrons, and  
723 investigates the modeling of that response in simulation. Chapter 8 uses those

724 measurements to construct a correction for the energy of jets in simulation, the  
725 **JES**, and to estimate an uncertainty for that correction.

726 Part **IV** details the search for **LLPs**. It begins with a discussion of the simulation  
727 of **LLPs** in ATLAS, focusing on the detector signatures and how they vary with  
728 the properties of those particles in Chapter **9**. Then Chapter **10** discusses the  
729 strategy of the search and the requirements used to select **LLPs** and to reject **SM**  
730 backgrounds. Chapter **11** explains a method for predicting the background from  
731 **SM** processes, and shows a validation of the technique. Chapter **12** describes the  
732 systematic uncertainties on both the selection efficiency for signal events and  
733 the background method. The results of the search are presented in Chapter **13**.

734

## PART I

735

### THEORETICAL CONTEXT

736

You can put some informational part preamble text here.

737

## 738 STANDARD MODEL

739 The SM of particle physics seeks to explain the symmetries and interactions of  
 740 fundamental particles. The SM provides predictions in particle physics for inter-  
 741 actions up to the Planck scale ( $10^{19}$  GeV). It has been tested by several genera-  
 742 tions of experiments and has been remarkably successful; no significant devia-  
 743 tions from its predictions have been found.

744 The theory itself is a quantum field theory grown from an underlying sym-  
 745 metry,  $SU(3) \times SU(2) \times U(1)$ , that generates all of the interactions consis-  
 746 tent with experimental observations<sup>1</sup>. These interactions are referred to as the  
 747 Strong, Weak, and Electromagnetic forces. Each postulated symmetry necessi-  
 748 tates the existence of an associated conserved charge, which appear as properties  
 749 of the observed particles in nature.

750 Although this model has been very predictive, the theory is incomplete; for  
 751 example, it is not able to describe gravity or astronomically observed dark mat-  
 752 ter. These limitations suggest a need for an extension or new theory to describe  
 753 physics at higher energies.

## 754 2.1 ACTION AND THE LAGRANGIAN

Originally, both action and the Lagrangian were constructed for an integral reformulation of the laws of classical mechanics, which is a purely mathematical step: any differential equation can be re-expressed in terms of an integral equation. The Lagrangian,  $\mathcal{L}$ , is classically given by the difference of kinetic energy and potential energy. The Lagrangian is defined this way so that the action,  $\mathcal{S}$ , given by

$$\mathcal{S}[\mathbf{q}(t)] = \int_{t_1}^{t_2} \mathcal{L}(\mathbf{q}, \dot{\mathbf{q}}, t) dt \quad (1)$$

755 returns the classical equations of motion when one requires it to be stationary  
 756 in the path,  $\mathbf{q}(t)$ . This formulation of classical mechanics is extremely useful in  
 757 calculations, and generalizes beautifully to cover all types of physics.

758 In particular, with the development of quantum mechanics in the twentieth  
 759 century, the concepts of action and the Lagrangian were found to generalize to  
 760 more complicated physics for which the classical laws do not hold. Quantum  
 761 mechanics and quantum field theory can be constructed from the action, using  
 762 the path integral formulation, by assuming that a particle undergoes all possible  
 763 paths  $\mathbf{q}(t)$  with an imaginary phase given by  $e^{i\mathcal{S}[\mathbf{q}(t)]/\hbar}$ . This reduces to classical  
 764 mechanics in the limit as  $\hbar$  goes to zero, as all paths for which the action is not  
 765 stationary interfere with each other so as to cancel their contributions. Because

<sup>1</sup> excluding gravity

766 the wavefunction of a particle can be completely determined through the action  
 767 and the action depends only on the Lagrangian, the Lagrangian itself is sufficient  
 768 to describe the physics governing the particle.

769 So, in both classical and quantum mechanics, the Lagrangian of a system con-  
 770 tains everything there is to know about the system, apart from initial conditions.  
 771 Thus, the most natural way to express that a system has a certain symmetry is to  
 772 require that the Lagrangian is invariant under a corresponding symmetry trans-  
 773 formation. This makes the Lagrangian the central piece of the discussion of  
 774 gauge invariance; the mathematical representation of gauge invariance is that a  
 775 gauge transformation on the appropriate components of the Lagrangian returns  
 776 an identical Lagrangian. That is,

$$\mathcal{L}(\psi, D^\mu) = \mathcal{L}(U\psi, D'^\mu) \quad (2)$$

777 where  $\psi$  is the wavefunction and  $D^\mu$  is the derivative operator, both of which  
 778 may transform under a symmetry operation. There are a number of immedi-  
 779 ate and surprisingly powerful consequences of requiring that the Lagrangian is  
 780 invariant under a symmetry operation.

## 781 2.2 GAUGE INVARIANCE AND FORCES

782 The simplest possible relativistic, quantum Lagrangian for matter particles is the  
 783 free Dirac Lagrangian, which describes a relativistic fermion in a vacuum.

$$\mathcal{L} = i\bar{\psi}\not{d}\psi - m\bar{\psi}\psi \quad (3)$$

784 A fermion denotes a particle with spin-1/2, and the kinematic term ( $i\bar{\psi}\not{d}\psi$ ) is  
 785 chosen to correctly describe the free propagation of a fermionic particle with  
 786 mass  $m$ . This equation is clearly invariant under a global  $U(1)$  transformation,  
 787 that is changing  $\psi$  by a complex phase has no effect. The derivative operator  
 788 commutes with a constant phase factor, and wherever  $\psi$  appears its complex  
 789 conjugate also appears so as to cancel out the change of phase. However, the  
 790 Lagrangian as written is not invariant under the local  $U(1)$  symmetry postulated  
 791 for the **SM**, which can be written as  $U = e^{i\alpha(x)}$ . The piece of the Lagrangian  
 792 involving a derivative will return an extra term that will break the invariance of  
 793 the Lagrangian under this transformation:

$$\begin{aligned} \mathcal{L}' &= i(\bar{\psi}U^\dagger)\not{d}(U\psi) - m(\bar{\psi}U^\dagger)(U\psi) \\ &= i(\bar{\psi}U^\dagger)U(\not{d} - \gamma^\mu\partial_\mu\alpha(x))\psi - m(\bar{\psi}U^\dagger)(U\psi) \\ &= i\bar{\psi}\not{d}\psi - m\bar{\psi}\psi - i\gamma^\mu\partial_\mu\alpha(x)\bar{\psi}\psi \\ &= \mathcal{L} - i\gamma^\mu\partial_\mu\alpha(x)\bar{\psi}\psi \\ &\neq \mathcal{L} \end{aligned}$$

794 So, in order to enforce the required symmetry, the typical approach is to con-  
 795 struct a covariant derivative, that is to add a term to the derivative operator

796 so that the unwanted term in  $\mathcal{L}'$  is exactly canceled. A generic form for such  
 797 a derivative is given by

$$D^\mu = \partial^\mu - iqA^\mu$$

798 where at this point  $A^\mu$  is an arbitrary field that transforms under the  $U(1)$  op-  
 799 erator and  $q$  is a scaling factor. Adding this component to the above Lagrangian  
 800 gives

$$\mathcal{L}' = i(\bar{\psi}U^\dagger)U(\not{d} - \gamma^\mu\partial_\mu\alpha(x) - iq\gamma^\mu A'_\mu)\psi - m(\bar{\psi}U^\dagger)(U\psi) \quad (4)$$

$$\mathcal{L}' = \mathcal{L} + \gamma^\mu(-i\partial_\mu\alpha(x) - iqA'_\mu + iqA_\mu)\bar{\psi}\psi \quad (5)$$

801 and because the transformation of  $A^\mu$  is unspecified,  $\mathcal{L} = \mathcal{L}'$  whenever

$$A'_\mu = A_\mu - \frac{1}{q}\partial_\mu\alpha(x)$$

802 The above procedure demonstrated that beginning with the Lagrangian for a  
 803 free fermion and imposing a local  $U(1)$  symmetry required the existence of a  
 804 vector field  $A^\mu$ , and specified its transformation under the  $U(1)$  gauge group.  
 805 The additional term in the derivative can be expanded to form a completely sep-  
 806 arate term in the Lagrangian,

$$\mathcal{L} = i\bar{\psi}\not{d}\psi - m\bar{\psi}\psi - (q\bar{\psi}\gamma^\mu\psi)A^\mu \quad (6)$$

807 and in this form it is clear that the  $A^\mu$  term has the exact form of the electromag-  
 808 netic interaction. That is, this is the Lagrangian which reproduces the relativistic  
 809 form of Maxwell's equations for a particle interacting with an electromagnetic  
 810 field. It is natural to also introduce a term to the Lagrangian at this point to  
 811 describe the free propagation of the vector  $A$  field, where the propagation of a  
 812 vector field has the form of

$$-\frac{1}{16\pi}F^{\mu\nu}F_{\mu\nu} \quad \text{with} \quad F_{\mu\nu} = \partial_\mu A_\nu - \partial_\nu A_\mu \quad (7)$$

813 This then also describes the electromagnetic interactions in a vacuum and the  
 814 propagation of a photon. This component of the Lagrangian should also poten-  
 815 tially include a mass term, but such a term would not be gauge invariant and so  
 816 must be excluded. The photon is an example of a gauge boson, a spin-1 particle  
 817 required to exist by a gauge symmetry of the Lagrangian and one that corre-  
 818 sponds to a force. In summary, requiring the  $U(1)$  symmetry was enough to  
 819 recover all of electromagnetism and to predict the existence of a photon in the  
 820 [SM](#).

821 The interaction term that was placed into the Lagrangian by this procedure  
 822 can be conveniently summarized with Feynman diagrams, which diagrammati-  
 823 cally represent a transition from an initial state to a final state. The contribution

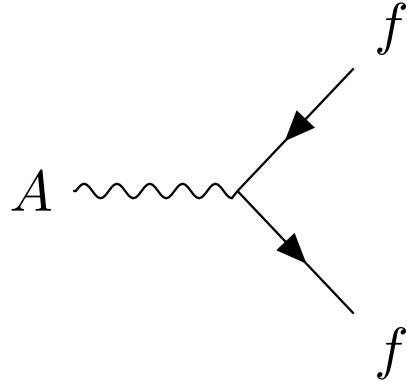


Figure 1: A Feynman diagram representing the interaction of the  $A$  field with a generic fermion,  $f$ .

of all diagrams that start with the same initial state and end with the same final state must be summed, but more complicated diagrams can be built by linking together the simplest versions. A diagram that corresponds to the above term,  $(q\bar{\psi}\gamma^\mu\psi)A^\mu$ , is shown in Figure 1, for an interaction with a generic fermion.

### 2.2.1 $SU(2) \times U(1)$ AND THE ELECTROWEAK FORCE

The full picture of the electroweak section of the SM is more complicated than the simplified explanation of the electromagnetic piece described above. In practice, it is necessary to consider the entire  $SU(2) \times U(1)$  symmetry together, but the procedure is the same. Enforcing the symmetry on the Lagrangian requires the introduction of a covariant derivative, this time with four total distinct terms, one for each of the generators of  $SU(2) \times U(1)$ . The result is a series of terms in the Lagrangian which describe the interaction of a fermion with four vector (spin-1) fields, the  $W_1$ ,  $W_2$ ,  $W_3$ , and  $B$  fields. These fields can mix in the quantum sense, and linear combinations form the  $W^+$ ,  $W^-$ ,  $Z$ , and  $A$  fields that are considered actual particles in the SM<sup>2</sup>.

### 2.2.2 $SU(3)$ AND THE STRONG FORCE

The same procedure can be applied starting with the  $SU(3)$  symmetry requirement, where eight additional fields must be introduced, one for each of the generators of  $SU(3)$ . The resulting Lagrangian describes quantum chromodynamics (QCD) and predicts the existence of eight gauge bosons known collectively as gluons. The complexity of the interactions of those eight gluons leads to surprising phenomena, discussed in Section 2.5.2.

---

<sup>2</sup> These states are the actual particles because they are mass eigenstates, but the full explanation of this will have to wait for the discussion of the Higgs mechanism.

## 846 2.3 NOETHER'S THEOREM, CHARGES, AND MATTER

847 Another direct consequence of the symmetries stipulated in the SM are a series  
848 of conserved quantities, Noether charges, named after the mathematician and  
849 physicist Emmy Noether. The charges arise as a direct consequence of Noether's  
850 theorem, which can be informally stated as

851 *For every symmetry of the Lagrangian, there exists a corresponding phys-  
852 ical quantity whose value is conserved in time.*

853 Or, stated another way, symmetries of the Lagrangian mathematically require  
854 the conservation of specific quantities taken from the Lagrangian. This rela-  
855 tionship can also be thought of as operating in the other direction, the exis-  
856 tence of a conserved charge can be shown to generate the symmetry in the La-  
857 grangian. This theorem is actually quite striking in a somewhat unexpected re-  
858 lation between simple geometric symmetries and physically observable conser-  
859 vation laws. For example, the theorem connects the translation invariance of  
860 the Lagrangian in space to the conservation of momentum and the translation  
861 invariance in time to the conservation of energy.

862 In the context of the SM, the required symmetries of  $U(1) \times SU(2) \times SU(3)$   
863 correspond to the charges that are considered properties of all elementary par-  
864 ticles. The most familiar of these properties is the electric charge, Q, which is  
865 one of the conserved quantities of  $SU(2) \times U(1)$ . The remaining pieces of  
866  $SU(2) \times U(1)$  correspond to weak isospin, T and  $T_3$ , where T has only non-  
867 negative values and  $T_3$  can be positive and negative. The  $SU(3)$  symmetry is  
868 generated by the three colors of QCD, red, green, and blue, each with a corre-  
869 sponding opposite color, anti-red, anti-green, and anti-blue.

870 The matter in the observable universe consists of a collection of particles which  
871 carry these charges, in addition to spin and mass. The particles typically thought  
872 of as matter are all fermions: particles with spin-1/2. All of the fermions belong  
873 to one of two groups, quarks and leptons, and one of three generations. Each  
874 of the generations have similar properties but significantly different masses; the  
875 particles in consecutive generations have increasing mass. Quarks are distin-  
876 guished from leptons in that they carry color charge, in addition to electric charge  
877 and weak isospin. The particles in the SM are summarized in Figure 2, and the  
878 matter particles are the twelve types of fermions displayed on the left side of the  
879 graphic.

## 880 2.3.1 QUARKS

881 The three generations of quarks each consist of a quark with electric charge +2/3  
882 and one with charge -1/3. They are called up and down, charm and strange,  
883 and top and bottom respectively, and these are referred to as the quark flavors.  
884 Although Figure 2 only shows these six flavors, there is a unique particle for each  
885 combination of the three colors and flavor. And each quark has an anti-particle  
886 with the opposite electric and color charge values.

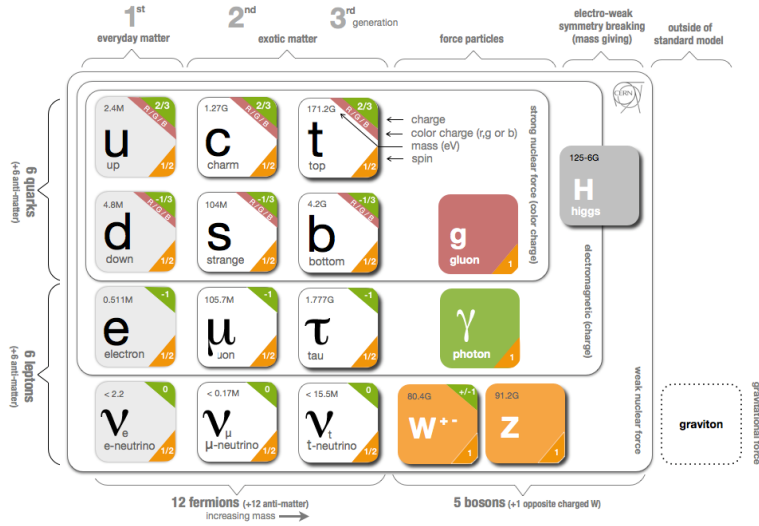


Figure 2: The particle content of the SM.

887 However, individual quarks are never observed in nature, but instead form  
 888 color-neutral bound states. This is a consequence of interaction of gluons with  
 889 color charge called confinement, discussed in Section 2.5.2. One way to form a  
 890 color neutral combination is a bound state of three quarks with three different  
 891 color charges, called a baryon. Baryons are the most common type of quark con-  
 892 figuration in conventional matter, and include protons and neutrons. The other  
 893 common configuration is a bound state of a quark and an anti-quark, called a  
 894 meson, where the two quarks have opposite colors. Although there is no direct  
 895 conservation law resulting from the symmetries of the SM Lagrangian, an acci-  
 896 dental symmetry results in the approximate conservation of baryon number,  $B$ ,  
 897 where baryons have  $B = 1$  and mesons have  $B = 0$ . That is, no interactions are  
 898 present which directly<sup>3</sup> alter baryon number

### 899 2.3.2 LEPTONS

900 The remaining fermions, the leptons, do not carry color charge. Each generation  
 901 contains an electrically charged lepton, the electron, muon, and tau, and an elec-  
 902 trically neutral lepton called a neutrino. For the charged leptons, the flavors are  
 903 mass eigenstates, with the masses listed in Figure 2. The flavors of the neutrinos,  
 904 on the other hand, are not mass eigenstates: their propagation in quantum super-  
 905 positions of flavor states leads to oscillations between different flavors. The ab-  
 906 solute masses of the neutrinos are not currently known, but the phenomenon of  
 907 oscillations shows that they have three different mass values. Another accidental  
 908 symmetry leads to an approximate<sup>4</sup> conservation of lepton number  $L$ , the differ-

<sup>3</sup> There are combinations of interactions which can modify either  $B$  or  $L$  individually, but the combination  $B - L$  appears to be conserved in the SM.

<sup>4</sup> See footnote 3.

ence in the number of leptons and anti-leptons; again there are no interactions present in the SM which directly alter lepton number.

### 2.3.3 CHIRALITY

All of the fermions described above have two possible values of the magnitude of weak isospin,  $T$ , either 0 or 1/2. The fermions with  $T = 0$  are called right-handed, while those with  $T = 1/2$  are called left-handed. Because  $T$  is the charge corresponding to the weak force, right-handed particles do not interact with the weak gauge bosons in the same way that neutral particles do not interact with photons. For left-handed fermions, each of the quark and lepton generations have one particle with  $T_3 = -1/2$  and one with  $T_3 = +1/2$ . The neutrinos have  $T_3 = +1/2$ , while the charged leptons have  $T_3 = -1/2$ . Similarly, the positively charged quarks have  $T_3 = +1/2$  and the negatively charged quarks have  $T_3 = -1/2$ . Because the right-handed neutrinos would have no charge of any type, it is not clear if they exist at all.

## 2.4 HIGGS MECHANISM AND MASS

The description of the electroweak forces above left out an important part of the observed nature of the electroweak force. Many physical experiments observed phenomena corresponding to the interaction of the weak bosons that were best explained if they had significant masses. But as mentioned before, massive bosons would break the gauge invariance of the Lagrangian. A large mass for the W and Z bosons would explain the relative weakness of their interactions compared to the electromagnetic field. The Lagrangian's discussed above did not include a mass term for the gauge bosons, and in fact such a term would not be allowed by the requirement of gauge invariance. This was a significant problem for the SM, and the symmetry of the electroweak sector would have to be broken in order to allow for non zero masses for some of the gauge bosons.

One mechanism to allow for this spontaneous symmetry breaking is the Higgs mechanism, which posits the existence of an additional scalar field. It begins with a  $SU(2) \times U(1)$  invariant Lagrangian of the form

$$\mathcal{L} = |D_\mu \phi|^2 - \frac{1}{2}\mu^2\phi^+\phi - \frac{1}{4}\lambda(\phi^+\phi)^2 \quad (8)$$

where  $\phi$  is the new scalar field with two components and, importantly,  $\mu^2$  is negative. This leads to a minimum value of the field at a non-zero value of  $\phi$ , specifically where

$$\langle\phi\rangle = \frac{1}{\sqrt{2}} \begin{pmatrix} 0 \\ v \end{pmatrix} \quad \text{with} \quad v = \frac{2\mu^2}{\lambda} \quad (9)$$

941 Expanding the original Lagrangian about its expectation value in terms of the  
 942 perturbation  $H$ ,

$$\langle \phi \rangle = \frac{1}{\sqrt{2}} \begin{pmatrix} 0 \\ v + H \end{pmatrix} \quad (10)$$

943 gives potential terms in the Lagrangian like

$$\mathcal{L}_H = -\frac{1}{2} m_H^2 H^2 - \sqrt{\frac{\lambda}{2}} m_H H^3 - \frac{1}{4} \lambda H^4 \quad (11)$$

944 where  $m_H = \sqrt{2}\mu$ . The form of this Lagrangian shows that the non-zero ex-  
 945 pectation value of the  $\phi$  field has introduced a massive scalar field  $H$  with self  
 946 interaction terms. It has an additional important consequence on the description  
 947 of the gauge bosons, through the expansion of the term involving the covariant  
 948 derivative:

$$|D_\mu \phi|^2 \supset \frac{1}{8} (g^2 (W_{1\mu} W_1^\mu + W_{2\mu} W_2^\mu) + (g' B_\mu - g W_3 \mu)^2) \quad (12)$$

949 where the  $W_i$  and  $B$  fields are the original  $SU(2) \times U(1)$  gauge fields men-  
 950 tioned previously. The above equation can be rearranged using linear combi-  
 951 nations of the fields to from mass terms for the gauge bosons, and the mass eigen-  
 952 states are exactly the  $W^\pm$ ,  $Z$ , and  $A$  fields. Only the  $A$  field, corresponding to  
 953 the photon, results in a zero mass, and the remaining three fields acquire masses.  
 954 Because the previously introduced Lagrangian, written in terms of  $\phi$ , was clearly  
 955 gauge invariant, this resulting configuration must also be gauge invariant.

956 This is the Higgs mechanism, where the introduction of a gauge invariant  
 957 scalar field with a non-zero expectation value can generate masses for the gauge  
 958 bosons without violating the underlying symmetries. The particle that is associ-  
 959 ated with the perturbations of this field,  $H$ , is called the Higgs boson, and is said  
 960 to generate the masses of the remaining bosons because the vacuum expectation  
 961 value introduces mass-like terms for each of the bosons. The resulting masses  
 962 are listed in Figure 2. Because this mechanism was so successful in describing  
 963 the observed properties of the  $W$  and  $Z$  bosons, it has been considered part of  
 964 the SM for decades, although the actual Higgs boson was only recently observed  
 965 in 2012, confirming the theory.

966 The Higgs mechanism is also responsible for generating the masses of the  
 967 fermions. The original mass terms that were listed in the Lagrangian for fermions  
 968 are replaced with Yukawa coupling terms, which introduce interactions between  
 969 the  $\phi$  field and the fermions. Like with the gauge bosons, the non-zero expec-  
 970 tation value of the field yields mass terms, and the expansion about that value  
 971 introduces interaction terms between the fermions and the Higgs boson. The  
 972 masses are different between each fermion because each has a different Yukawa  
 973 coupling, which results in the masses listed in Figure 2.

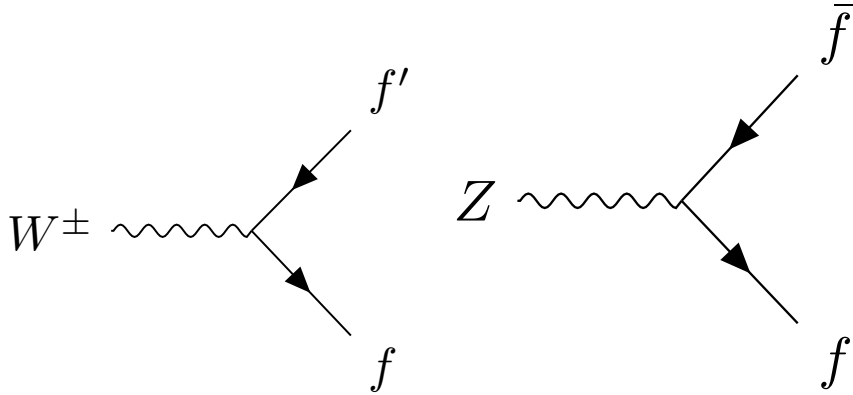


Figure 3: The Feynman diagrams representing the decays of the  $W$  and  $Z$  bosons to fermions. Here  $f$  indicates a generic fermion,  $\bar{f}$  its antiparticle, and  $f'$  the partner of that fermion in the same generation.

## 974 2.5 PHENOMENOLOGY

975 The SM Lagrangian described above contains all of the information necessary  
 976 to describe particle physics through the path integral formulation. However, a  
 977 tremendous amount of complexity emerges from that description because of the  
 978 diverse allowed interactions between the ensemble of particles in the SM. A qual-  
 979 itative understanding of the phenomenology produced by those interactions is  
 980 immensely helpful in understanding the analysis of particle physics.

### 981 2.5.1 ELECTROWEAK PHYSICS

982 The masses of the  $W$  and  $Z$  bosons result in significantly different processes  
 983 for the weak fields than the electromagnetic field, despite their interactions be-  
 984 ing similar before symmetry breaking. The massless photon is stable, and can  
 985 propagate in a vacuum, resulting in the familiar long range interactions of elec-  
 986 tromagnetism. The  $W$  and  $Z$  bosons, however, are unstable, as they have large  
 987 enough masses to decay to fermions, such as the decays shown in Figure 3. For  
 988 this reason, photons can be observed directly, while the other bosons are suffi-  
 989 ciently short-lived that they can only be measured from their decay products.

990 Because the electroweak bosons interact with both quarks and leptons, they  
 991 are responsible for the production of leptons in proton-proton collisions.  $Z$   
 992 bosons and photons produce pairs of opposite sign, same flavor leptons.  $W$   
 993 bosons, on the other hand, produce a single lepton and the corresponding neu-  
 994 trino.

### 995 2.5.2 STRONG PHYSICS

996 The phenomenology of the strong sector differs significantly from the weak sec-  
 997 tor because the gluons are massless but color charged. Because of this, gluons

998 can interact with each other, and contributions from multiple gluon interactions  
 999 lead to a significant growth in the strength of the field at low energies. The depen-  
 1000 dence of the field strength on the energy scale is described by renormalization,  
 1001 and in QCD the coupling is only small at high energies. Below approximately 1  
 1002 GeV, the strength of those interactions results in confinement: the interactions  
 1003 are so strong that when quark-antiquark pairs separate, the fields between them  
 1004 generate additional quarks to form color neutral bound states. Above around  
 1005 the GeV scale, the interactions of quarks become perturbative, similar to the  
 1006 electroweak fields; this phenomenon is known as asymptotic freedom.

1007 At lower energies, however, the strength of the strong interaction is so signif-  
 1008 icant that the interactions of color-charged particles create additional particles  
 1009 until they form neutral bound-states. This process is known as hadronization,  
 1010 and explains why no quarks are observed isolated in nature: they all form bound  
 1011 states of hadrons like protons, neutrons, and pions. The hadronization process  
 1012 can produce a significant number of particles, so that a single energetic quark  
 1013 recoiling against another quark can generate a cascade of dozens of hadrons.  
 1014 Because of the initial boost of such an energetic configuration, the resulting  
 1015 hadrons are collimated, and conical spray of particles often referred to as a jet.

### 1016 2.5.3 PROTON-PROTON COLLISIONS

1017 Proton-proton collisions are a convenient way to generate high energy interac-  
 1018 tions to probe the SM and to search for new physics. At the energies that will be  
 1019 discussed in this analysis, the substructure of the protons is very important to the  
 1020 description of the resulting interactions. At lowest order, protons are composed  
 1021 of two up quarks and one down quark, but this description is incomplete. The  
 1022 actual bound state includes a chaotic sea of additional quarks and gluons, each of  
 1023 which carries a variable fraction of the proton's energy. When a proton-proton  
 1024 collision takes place, it is these constituents that interact with each other, result-  
 1025 ing in a highly variable collision energy even when the proton-proton energy is  
 1026 consistent.

1027 The fraction of the energy carried by each constituent varies moment to mo-  
 1028 ment, but can be modelled probabilistically by PDFs. These are difficult to pre-  
 1029 dict theoretically, as the QCD calculations are extremely complex, and instead  
 1030 are measured in hard-scattering experiments. They are usually represented by  
 1031 how often a given type of particle carries a fraction  $x$  of the total proton energy.  
 1032 Those fraction change significantly with the scale of the interaction,  $Q$ ; the PDFs  
 1033 of proton-proton collisions at both  $Q^2 = 10 \text{ GeV}^2$  and  $Q^2 = 10^4 \text{ GeV}^2$  are  
 1034 shown in Figure 4.

## 1035 2.6 LIMITATIONS

1036 Despite the great success of the relatively simple SM in describing such a broad  
 1037 range of emergent phenomena, it is clear that the picture it presents of the in-  
 1038 teractions of fundamental particles is incomplete. The SM contains concerning  
 1039 coincidences that suggest a more ordered underlying substructure that is not ex-

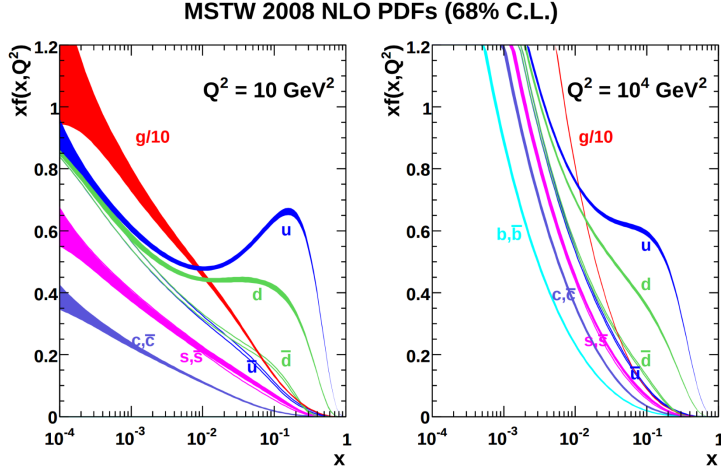


Figure 4: The PDFs for proton-proton collisions at  $Q^2 = 10 \text{ GeV}^2$  and  $Q^2 = 10^4 \text{ GeV}^2$ . Each shows the fraction of particles which carry a fraction  $x$  of the total proton energy at the specified scale [1].

1040 pressed in the current form. It also fails to explain a number of cosmological  
 1041 measurements of the nature of matter in the universe. These limitations suggest  
 1042 the need for new, beyond the Standard Model (BSM) physics that would provide  
 1043 a more complete description at higher energies.

#### 1044 2.6.1 THEORETICAL CONCERNS

1045 There have been no successful integrations of the SM's description of the elec-  
 1046 troweak and strong forces with the description of gravity, and it is still unclear  
 1047 how to account for the effects of gravity at the Planck scale of approximately  $10^{19}$   
 1048 GeV, where its interactions are as strong as the remaining forces. The Planck  
 1049 scale is an important cutoff for the SM, as it is clear that the SM must break down  
 1050 somewhere between the current highest energy tests of the SM, around 1 TeV,  
 1051 and the Planck scale.

1052 One example of this is the Higgs mass, which is determined in the SM by a  
 1053 sum of its bare mass and the interactions in the vacuum with all massive parti-  
 1054 cles. As there must be new physics at the Planck scale to describe gravity, some  
 1055 of those corrections would include contributions at a scale seventeen orders of  
 1056 magnitude above the mass of the Higgs. Either the bare mass of the Higgs boson  
 1057 precisely cancels those contributions to leave a remainder seventeen orders of  
 1058 magnitudes smaller, or a new theory exists at a lower scale the shields the Higgs  
 1059 mass from those terms. A theory where such a unlikely cancellation of free pa-  
 1060 rameters occurs is called fine-tuned, and one that is free from such cancellations  
 1061 is called natural. Theories where the mass of the Higgs is natural are usually pre-  
 1062 ferred, as the suggest an underlying, coherent structure. The enormous differ-  
 1063 ence in scales between the weak scale (including the Higgs mass), and the Planck  
 1064 scale, is often referred to as the hierarchy problem.

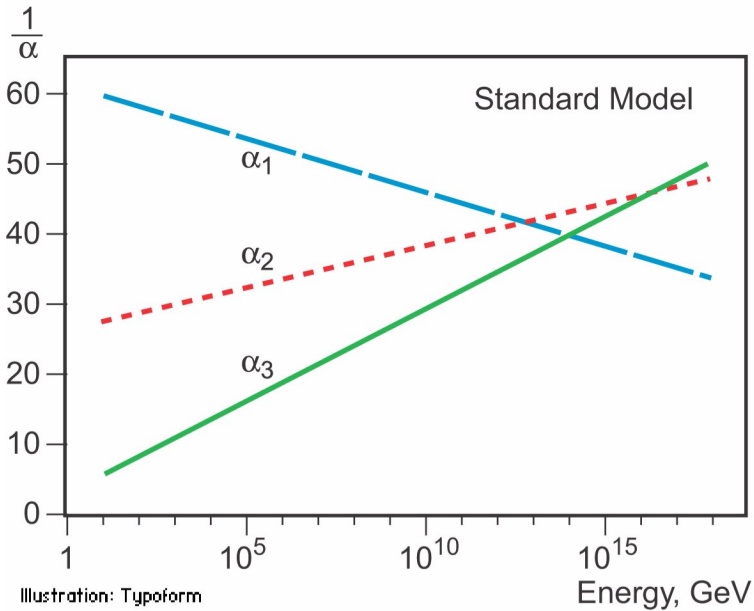


Figure 5: An approximation of the running of the coupling constants in the SM up to the Planck scale [2].

1065 There is also a compelling argument that the  $SU(3) \times SU(2) \times U(1)$  gauge  
 1066 structure of the SM might originate from a single, unified gauge theory. For ex-  
 1067 ample, it is possible to represent that gauge structure as a  $SU(5)$  gauge group  
 1068 with only a few inconsistencies with the current implementation. This unifica-  
 1069 tion is suggested by the scaling of the coupling constants for each of the forces  
 1070 under renormalization; they come close to converging to a single value at higher  
 1071 energies, as seen in Figure 5. An additional correction to the scaling of the cou-  
 1072 pling constants from new physics above the TeV scale could cause them to merge  
 1073 into a single value at high energies.

## 1074 2.6.2 COSMOLOGICAL OBSERVATIONS

1075 The SM contains a symmetry in the description of matter and antimatter that is  
 1076 not reflected in cosmological observations. The processes of the standard model  
 1077 create or remove matter and antimatter in equal amounts, so a universe that be-  
 1078 gins with an equal quantity of each should result in a universe with an approxi-  
 1079 mate<sup>5</sup> balance of matter and antimatter. However, cosmological observations of  
 1080 the relative amount of each type clearly show that the directly observable mass  
 1081 of the universe is overwhelmingly made of matter. As this difference is largely  
 1082 a difference in the generation of baryons and anti-baryons, this discrepancy is  
 1083 often referred to as the baryogenesis problem.

1084 A number of astrophysical observations of large scale gravitational interac-  
 1085 tions suggest the presence of a significant amount of non-luminous matter that  
 1086 interacts with the normal matter only gravitationally. The first evidence of this

---

5 There are some processes in the standard model which can result in a small imbalance of matter and antimatter, but not at the scale observed cosmologically.

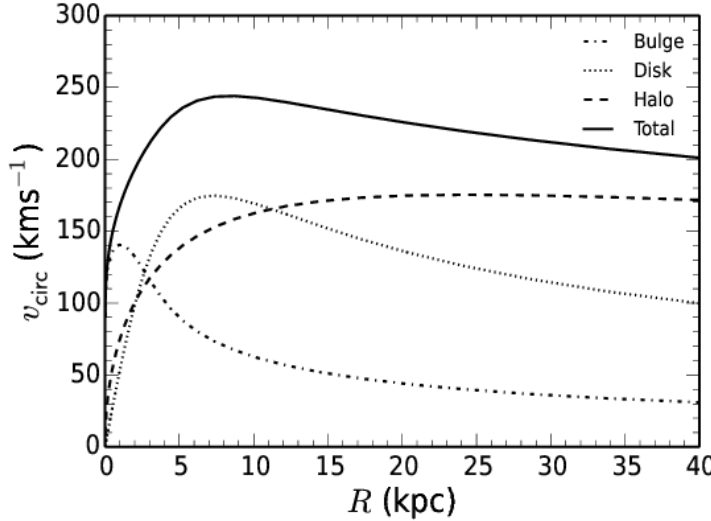


Figure 6: The distribution of velocities of stars as a function of the radius from the center of the galaxy. The contributions to the velocity from the various components of matter in the galaxy are shown [3].

1087 came from the observation of galactic rotation curves, the velocities of stars as  
 1088 a function of the radius from the center of a galaxy. These can be directly pre-  
 1089 dicted from the amount of matter contained within the sphere up to the radius of  
 1090 the star. An estimate of velocity based only on the luminous matter in the galax-  
 1091 ies would predict a dependence that falls off with the radius, but the observed  
 1092 curves show a mostly constant distribution of velocities [3], as seen in Figure 6.  
 1093 The higher velocities than predicted by the luminous matter can be explained by  
 1094 a halo of dark matter that extends significantly outside the galactic disk.

1095 This dark matter accounts for a majority of the matter in the universe, and is  
 1096 incompatible with the matter particles predicted by the SM. Many observations  
 1097 support its existence, but there have been no direct detections of a particle which  
 1098 could account for the large quantity of gravitationally interacting dark matter.  
 1099 The SM would have to require a significant extension to include the particles  
 1100 needed to explain dark matter and the processes needed to explain the observed  
 1101 matter-antimatter asymmetry.

1102

1103 SUPERSYMMETRY

---

1104 The theory of [SUSY](#) presents an extension to the [SM](#) that solves a number of the  
1105 outstanding issues. It is based on another proposed symmetry, one which intro-  
1106 duces an equality between the fermionic particles and proposed bosonic partners  
1107 and also between bosonic particles and their proposed fermionic partners. The  
1108 symmetry is defined by extending spacetime into a superspace, which includes  
1109 one dimension that describes a particle's spin: a transformation in this space  
1110 moves a fermion with spin-1/2 to a boson with spin-0 or vice-versa. Requiring  
1111 the [SM](#) to be symmetrical under these transformations requires the existence of a  
1112 bosonic partner for every current matter fermion in the [SM](#) and a fermionic part-  
1113 ner for every boson. The partners are called superparticles (sparticles), where  
1114 quarks partner with squarks and leptons partner with sleptons, and each boson  
1115 has a fermionic partner called a gaugino. The superpartners, in the original form  
1116 of the theory, should be identical to the original particle in every way except for  
1117 spin; that is they would have the same quantum charges and the same mass.

1118 However, the simplest version of the theory, where the symmetry is unbro-  
1119 ken, is incompatible with current observations of physics in a number of sys-  
1120 tems. The most striking example comes from the electron, as the superpartner  
1121 of an electron would introduce a stable, negatively charged, and bosonic parti-  
1122 cle. Such a particle would drastically alter atomic properties by providing a way  
1123 to create atoms without the valence structure of electrons that results from the  
1124 Pauli exclusion principle for fermions. Various high energy physics measure-  
1125 ments have also confirmed the spin of the W and Z bosons, for example, and  
1126 a fermionic gaugino has never been produced at those masses. The solution to  
1127 this incompatibility with observation is to conjecture that the symmetry exists  
1128 but is spontaneously broken, where the masses of the supersymmetric particles  
1129 are significantly larger than those of the current [SM](#) particles. Like the sponta-  
1130 neous symmetry breaking of the electroweak system, this symmetry breaking  
1131 can be accomplished by introducing an additional Higgs mechanism.

## 1132 3.1 STRUCTURE

1133 There are a number of ways to model the particulars of [SUSY](#), but many of the  
1134 resulting phenomena are similar, and a discussion of an example is sufficient  
1135 to describe the structure and results of the theory. The [MSSM](#) is one example of  
1136 a complete description that includes the necessary symmetry breaking to result  
1137 in the different masses between particles and sparticles [4]. It is called minimal  
1138 because it is designed to use the simplest possible extension to the [SM](#) that incor-  
1139 porates [SUSY](#). However even a minimal version includes a remarkable number of  
1140 free parameters, over 100, and the [MSSM](#) is often further constrained to include

Sector	Particles	Sparticles
Baryonic Matter	$(u, d)$	$(\tilde{u}, \tilde{d})$
	$(c, s)$	$(\tilde{c}, \tilde{s})$
	$(t, b)$	$(\tilde{t}, \tilde{b})$
Leptonic Matter	$(\nu_e, e)$	$(\tilde{\nu}_e, \tilde{e})$
	$(\nu_\mu, \mu)$	$(\tilde{\nu}_m u, \tilde{\mu})$
	$(\nu_\tau, \tau)$	$(\tilde{\nu}_\tau, \tilde{\tau})$
Higgs	$(H_u^+, H_u^0)$	$(\tilde{H}_u^+, \tilde{H}_u^0)$
	$(H_d^0, H_d^-)$	$(\tilde{H}_d^0, \tilde{H}_d^-)$
Strong	$g$	$\tilde{g}$
Electroweak	$(W^\pm, W^0)$	$(\tilde{W}^\pm, \tilde{W}^0)$
	$B^0$	$\tilde{B}^0$

Table 1: The particles in the SM and their corresponding superpartners in the MSSM.

1141 fewer parameters in models such as the Phenomenological MSSM ([pMSSM](#)) and  
 1142 the Constrained MSSM ([cMSSM](#)) [5].

1143 The theory includes a sparticle partner for every SM particle, which are listed  
 1144 in Table 1. To then provide the different masses for those sparticles, the MSSM  
 1145 introduces a second Higgs interaction. The resulting scalar field, along with the  
 1146 original Higgs field, generates five total particles,  $h^0$ , the original Higgs boson,  
 1147  $A^0$ ,  $H^0$ , and  $H^\pm$ , where the last two are electrically charged. These Higgs bosons  
 1148 can mix with the supersymmetric gauginos to form a series of mass eigenstates.  
 1149 These are usually referred to by the order of their masses, where the neutral  
 1150 gauginos (neutralinos) are labeled  $\tilde{\chi}_1^0, \tilde{\chi}_2^0, \tilde{\chi}_3^0$ , and  $\tilde{\chi}_4^0$ . The charged gauginos  
 1151 (charginos) are similarly labeled  $\tilde{\chi}_1^\pm$  and  $\tilde{\chi}_2^\pm$ . Table 1, lists the gauginos which are  
 1152 direct partners of the original gauge bosons in the SM rather than these resulting  
 1153 mass eigenstates.

In addition to the new particle content, the MSSM introduces new interactions  
 for the gauge bosons and gauginos. All interaction terms are added to the La-  
 grangian which describe the interaction of a gauge boson or gaugino with a par-  
 ticle or sparticle with the appropriate charge. Such terms include a few interac-  
 tions which would violate the observed  $B - L$  symmetry that prevents proton  
 decay. Either the couplings on these terms must be extremely small to match  
 the experimental limits on those decays, or an additional symmetry must be im-  
 posed to exclude the terms. The MSSM and several other SUSY models choose  
 to introduce a new symmetry known as R-parity, where the conserved quantity,  
 $P_R$  is defined as

$$P_R = (-1)^{2s+3(B-L)}$$

1154 with  $s$  as the spin of the particle. Sparticles are R-parity odd while SM particles  
 1155 are R-parity even. And by requiring that each term in the supersymmetric La-  
 1156 grangian conserves R-parity, it is enforced that sparticles are produced in pairs.

1157     The conservation of R-parity removes the  $B - L$  violating terms from the La-  
 1158 grangian. The remaining terms include all of the interactions of the **SM** where  
 1159 two of the particles are replaced with their **SUSY** partners, so that R-parity is con-  
 1160 served in the interactions. This also has an important significance in making the  
 1161 Lightest Supersymmetric Particle (**LSP**), the  $\tilde{\chi}_1^0$ , stable, as it cannot decay to only  
 1162 **SM** particles without violating the conservation of R-parity. The heavier sparti-  
 1163 cles then decay in chains, emitting an **SM** particle in each step, and leave behind  
 1164 the **LSP** at the end of the chain.

## 1165 3.2 MOTIVATION

1166 **SUSY** models, including the **MSSM**, ameliorate many of the issues in the **SM** dis-  
 1167 cussed in Section 2.6. **SUSY** is particularly well motivated as a natural extension  
 1168 to the **SM** because the simple underlying assumption solves three major, seem-  
 1169 ingly unrelated concerns. And these benefits all require that at least some of the  
 1170 sparticles exist at the TeV scale, within the reach of modern collider experiments.

1171     The first, a solution to the hierarchy problem, comes as a direct consequence  
 1172 of the introduction of massive superpartners for each **SM** particle. The contribu-  
 1173 tions to the Higgs mass from the much higher energy Planck scale come from a  
 1174 series of loop diagrams in the **SM**, where each massive **SM** particle has a loop con-  
 1175 tribution. The introduction of superpartners generates a series of corresponding  
 1176 diagrams for correction to the Higgs mass, with opposite sign contributions be-  
 1177 cause the superpartners have different spins. Those opposite sign contributions  
 1178 cancel the divergences from the original loop diagrams at high energies, leaving  
 1179 behind a correction to the Higgs mass that is at the same scale as the masses of the  
 1180 superpartners. If the superpartners exist at the TeV scale, then the Higgs mass  
 1181 of 125 GeV can be explained without significant fine-tuning, and the theory be-  
 1182 comes natural.

1183     **SUSY** also has the potential to precisely enable the unification of the coupling  
 1184 constants at high energy. Without supersymmetric contributions, the coupling  
 1185 constants come close to a single value near the Planck scale suggesting an un-  
 1186 derlying trend, as shown in Figure 5, but they do not exactly merge. With the  
 1187 addition of the **MSSM**, they can join almost exactly at a single point, enabling a  
 1188 unification into a single gauge theory at high energy, as shown in Figure 7. This  
 1189 precise unification, like the naturalness argument, also requires that the masses  
 1190 of the superpartners be near the TeV scale.

1191     The presence of R-parity in a **SUSY** model also provides an explanation for  
 1192 dark matter. The **LSP**, as discussed in Section 3.1, is a massive, neutral, and stable  
 1193 particle as long as R-parity is conserved. In the early universe, when the energy  
 1194 density was extremely high, **LSPs** could be spontaneously produced just as often  
 1195 as other particles like photons, and would result in a thermal equilibrium. Then,  
 1196 as the universe cooled, the average energy would be too low to create additional  
 1197 **LSPs**, and they would be left behind and only interact with the remaining matter  
 1198 gravitationally, a process called freeze out. Since those particles are stable, they  
 1199 would remain indefinitely. With the existence of an **LSP** at around the TeV scale,  
 1200 this process can explain the observed amount of dark matter in the universe. A

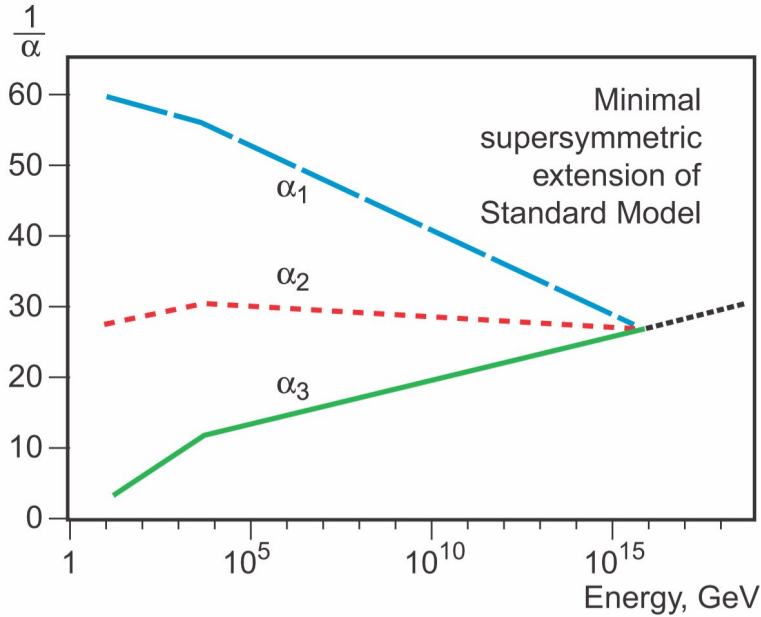


Figure 7: An approximation of the running of the coupling constants in the [MSSM](#) up to the Planck scale [2].

1201     **WIMP!** (**WIMP!**), exactly what is proposed in the [LSP](#), provides the correct interaction  
 1202     rate to predict the currently observed ratio of dark matter to baryonic matter.  
 1203

1204     Together, this variety of solutions to existing problems provides strong theoretical  
 1205     support for the existence of [SUSY](#) near the TeV scale. The [LHC](#) is the first  
 1206     collider experiment to be able to probe into TeV scale interactions, providing a  
 1207     new opportunity to search for this extension to the [SM](#). A range of models have  
 1208     begun to be excluded with masses above 1 TeV [6], leading to a motivation to  
 1209     explore a wider variety of models with phenomena that may have been missed  
 1210     by the most direct search strategies.

### 1211     3.3 SIMPLIFIED MODELS

1212     The [MSSM](#) is just one example of a large suite of [SUSY](#) models with similar results.  
 1213     Each of those models can have hundreds of individual parameters that ultimately  
 1214     determine the masses and interactions of the supersymmetric particles. To avoid  
 1215     this complexity in making experimental measurements, the analyses of high en-  
 1216     ergy collisions often rely on simplified models. These models focus on a single  
 1217     process predicted by a theory, and the observable parameters such as the mass  
 1218     of the particles and their lifetimes are controlled directly, rather than tuning the  
 1219     hundreds of underlying parameters. This allows straightforward simulation of  
 1220     a specific event topology with control over the parameters that most directly  
 1221     influence the experimental signatures.

1222     Experimental analyses use these models to search for new physics and to set  
 1223     limits on the production rates for a given type of process with working points  
 1224     of a few observable parameters. As one example, a simplified model may specify

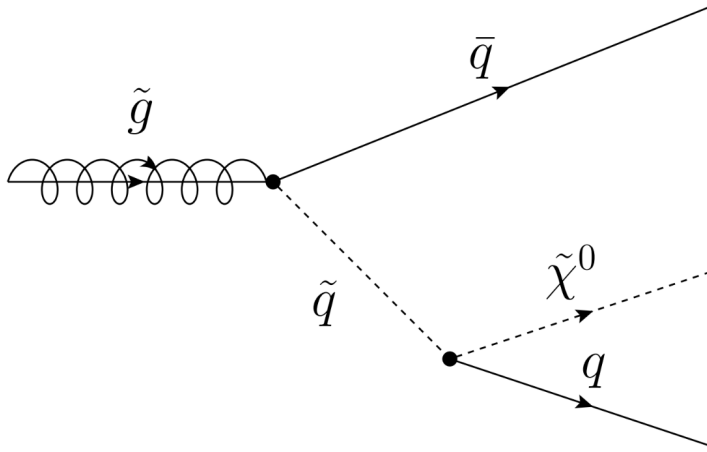


Figure 8: The decay of a gluino to quarks and an LSP, which precedes through a squark.

pair production of gluinos where the free parameters are the mass of the gluino and the types and masses of the particles it can decay into. The small number of parameters allows the phase space to be searched in a grid by simulating events with a few examples for the parameters and interpolating between them. The resulting analysis can set cross sectional limits as a function of the simplified parameters, and this allows for an easy interpretation of the result in a number of SUSY models.

### 3.4 LONG-LIVED PARTICLES

Some proposed SUSY models can produce LLPs other than just the LSP. The most direct search strategies for SUSY often assume that the various non-stable sparticles decay promptly, rather than propagating through some fraction of the detector. Although the processes involved are very similar, the long-lifetime of the produced particles can lead to very different experimental signatures, and often require separate dedicated searches. It is important to design and execute search strategies for LLPs in order to completely cover possible production of new physics.

There are several ways to generate long lifetimes for the massive SUSY particles, depending on the specific model. In examples like Spread Supersymmetry [7] and Split Supersymmetry [8, 9], the introduction of a split between two mass scales suppresses the decay of gluinos. In these and similar models, the squarks are much heavier than the gluino, where the mass scale of the squarks is roughly  $10^6$  GeV while the mass scale of the gluinos is roughly  $10^3$  GeV. The gluino must decay through the production of a virtual squark, as shown in the diagram of Figure 8. The large mass of the squarks in the split models suppresses the decay rate, and can result in lifetimes of the order of 1 ns [7].

Nearly degenerate particles can also result in long lifetimes, again by suppressing decay rates. When a particle must decay to another particle with nearly the same mass, the phase space factor in the decay results in a low decay rate. For

1253 example, a neutron has a lifetime of roughly fifteen minutes because its mass is  
1254 so close to the proton. Models which result in a nearly degenerate chargino and  
1255 LSP provide a long-lived chargino as well.

1256 Again, because of the wide variety of models which can produce LLPs and the  
1257 large number of parameters which determine their masses and lifetimes, the anal-  
1258 ysis presented here focuses on simplified models rather than assuming any par-  
1259 ticular underlying theory. The models directly specify the decay mode of the  
1260 LLPs as well as their masses and lifetimes, using a grid of values. The results of  
1261 searches using these simplified models can be interpreted over a very wide range  
1262 of models that predict LLPs, even including non-supersymmetric extensions to  
1263 the SM.

1264

## PART II

1265

### EXPERIMENTAL STRUCTURE AND RECONSTRUCTION

1266

You can put some informational part preamble text here.

1267

1268 THE LARGE HADRON COLLIDER

---

1269 The LHC, a two-ring superconducting hadron accelerator, provides high energy  
1270 proton-proton collisions for several large experiments at European Organiza-  
1271 tion for Nuclear Research (CERN) in Geneva, Switzerland [10, 11]. It is the largest,  
1272 highest-luminosity, and highest-energy proton collider ever built, and was con-  
1273 structed by a collaboration of more than 10,000 scientists from the more than  
1274 100 countries that contribute to CERN. The original design of the LHC focused on  
1275 providing collision energies of up to 14 TeV and generating enough collisions to  
1276 reveal physics beyond the SM which is predicted to exist at higher energy scales.

1277 The LHC was installed in an existing 27 km tunnel at CERN which was orig-  
1278 inally designed to house the Large Electron Positron collider (LEP) [12]. This  
1279 allows the collider to use existing accelerators at the same complex to provide  
1280 the initial acceleration of protons up to 450 GeV before injecting into LHC. The  
1281 injected hadrons are accelerated up to as much as 14 TeV while being focused  
1282 into two beams traveling in opposite directions. During this process the protons  
1283 circulate around the tunnel millions of times, while the beams are intermittently  
1284 crossed at the four locations of the experiments to provide collisions. These col-  
1285 lision points correspond to the four major LHC experiments: ATLAS, Compact  
1286 Muon Solenoid (CMS), Large Hadron Collider beauty experiment (LHCb), and  
1287 A Large Ion Collider Experiment (ALICE), and Figure 9 shows the layout of the  
1288 experiments both on the surface and below. ATLAS and CMS are both general  
1289 purpose, high-luminosity detectors which search for a wide range of new types  
1290 of physics [13, 14]. LHCb studies the interactions of b-hadrons to explore the  
1291 asymmetry between matter and antimatter [15]. ALICE focuses on the collisions  
1292 of lead ions, which the LHC also provides, in order to study the properties of  
1293 quark-gluon plasma [16].

1294 During the first five years of continued operation, after the LHC turned on in  
1295 2010, the LHC has provided four major data collecting periods. In 2010 the LHC  
1296 generated collisions at several energies, starting at 900 GeV. It increased the  
1297 energy from 900 GeV to 2.76 TeV and then subsequently to 7 TeV, with a peak  
1298 luminosity of  $2 \times 10^{32} \text{ cm}^{-2}\text{s}^{-1}$ , and a total delivered luminosity of  $50 \text{ pb}^{-1}$ .  
1299 The next run, during 2011, continued the operation at 7 TeV and provided an  
1300 additional  $5 \text{ fb}^{-1}$  with a peak luminosity of  $4 \times 10^{33} \text{ cm}^{-2}\text{s}^{-1}$ . The energy was  
1301 then increased to 8 TeV for the data collection during 2012, which provided  $23 \text{ fb}^{-1}$   
1302 with a peak luminosity of  $7.7 \times 10^{33} \text{ cm}^{-2}\text{s}^{-1}$ . After the first long shutdown  
1303 for 2013 and 2014, the LHC resumed operation and increased the energy to 13  
1304 TeV in 2015, where it delivered  $4.2 \text{ fb}^{-1}$  with a peak luminosity of  $5.5 \times 10^{33} \text{ cm}^{-2}\text{s}^{-1}$ .  
1305 The LHC is currently providing additional 13 TeV collisions in 2016 with higher  
1306 luminosities than during any previous data collection periods. These  
1307 running periods are summarized in Figure 10, which shows the total delivered

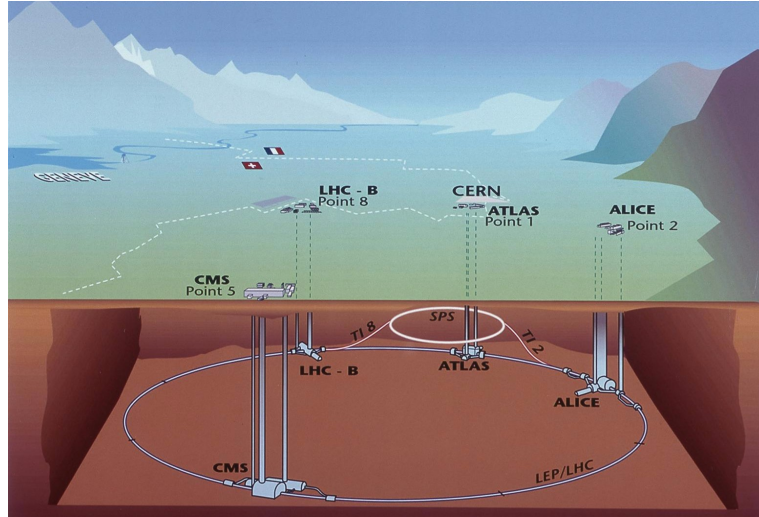


Figure 9: The four collision points and corresponding experiments of the [LHC](#). The image includes the location of the nearby city of Geneva as well as the border of France and Switzerland.

luminosity over time for the ATLAS experiment during each of the four years of data collection since 2011.

## 4.1 INJECTION CHAIN

The [LHC](#) takes advantage of the presence of previously built accelerators at [CERN](#) to work up to the target energy in consecutive stages. The series of accelerators that feed into the [LHC](#) are known collectively as the injection chain, and together with the [LHC](#) form the accelerator complex. The full complex is illustrated in Figure 11, which details the complex series required to reach collisions of 13 or 14 TeV.

Protons at the [LHC](#) begin as hydrogen atoms in the Linac 2, a linear accelerator which replaced Linac 1 as the primary proton accelerator at CERN in 1978. In Linac 2, the hydrogen atoms are stripped of their electrons by a strong magnetic field, and the resulting protons are accelerated up to 50 MeV by cylindrical conductors charged by radio frequency cavities. The protons are then transferred to the Proton Synchrotron Booster ([PSB](#)), which uses a stack of four synchrotron rings to accelerate the protons up to 1.4 GeV. Then the protons are injected into the Proton Synchrotron ([PS](#)) which again uses synchrotron rings to bring the energy up to 25 GeV. The intermediate step between Linac 2 and the [PS](#) is not directly necessary, as the [PS](#) can accelerate protons starting from as low as 50 MeV. The inclusion of the [PSB](#) allows the [PS](#) to accept a higher intensity of injection and so increases the deliverable luminosity in the [LHC](#). The penultimate stage of acceleration is provided by the Super Proton Synchrotron ([SPS](#)), a large synchrotron with a 7 km circumference that was commissioned at CERN in 1976. During this step the protons increase in energy to 450 GeV, after which they can be directly injected into the [LHC](#).

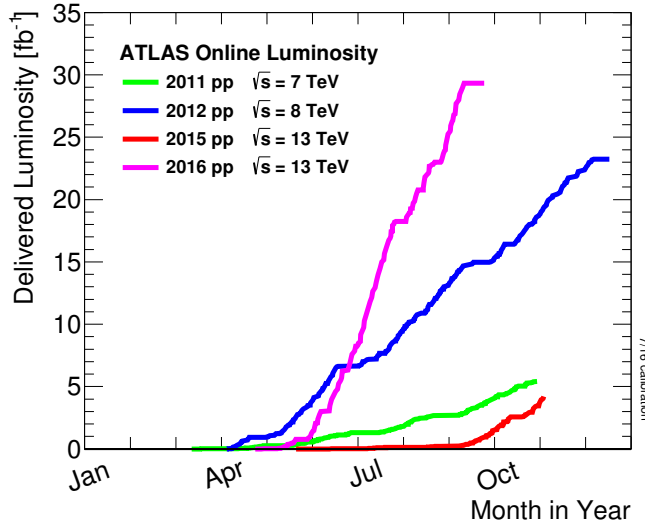


Figure 10: The cumulative luminosity over time delivered to the ATLAS experiment from high energy proton-proton collisions since 2011. The energies of the collisions are listed for each of the data-taking periods.

1333      The final step is the **LHC** itself, which receives protons from the **SPS** into two  
 1334      separate beam pipes which circulate in opposite directions. The filling process  
 1335      at this steps takes approximately 4 minutes, and the subsequent acceleration to  
 1336      the final energy (6.5 TeV during 2015 and up to 7 TeV by design) takes approxi-  
 1337      mately half an hour. At this point the protons circulate around the circumference  
 1338      tens of thousands of times a second and continue for up to two hours.

## 1339      4.2 DESIGN

### 1340      4.2.1 LAYOUT

1341      Many of the aspects of the **LHC** design are driven by the use of the existing **LEP**  
 1342      tunnel. This tunnel slopes gradually, with a 1.4% decline, with 90% of its length  
 1343      built into molasse rock which is particularly well suited to the application. The  
 1344      circumference is composed of eight 2987 meter arcs and eight 528 meter straight  
 1345      sections which connect them; this configuration is illustrated in Figure 12. The  
 1346      tunnel diameter is 3.7 m throughout its length.

The design energy is directly limited by the size of this tunnel, with its radius of curvature of 2804 m. A significant magnetic field is required to curve the protons around that radius of curvature; the relationship is given by

$$p \simeq 0.3BR \quad (13)$$

1347      where  $p$  is the momentum of the particle in GeV,  $B$  is the magnetic field in Tesla,  
 1348      and  $R$  is the radius of curvature in meters. From the target design energy of  
 1349      14 TeV, or 7 TeV of momentum for protons in each beam, the required mag-  
 1350      netic field is 8.33 Tesla. This is too large a field strength to be practical with  
 1351      iron electromagnets, because of the enormous power required and the resulting

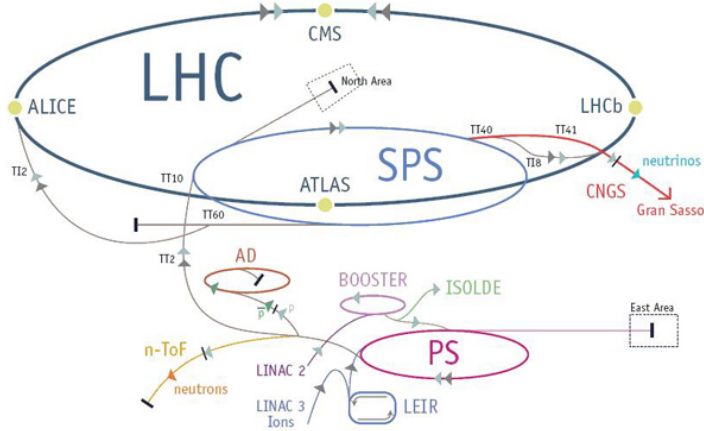


Figure 11: The accelerator complex that builds up to the full design energies at the LHC. The protons are passed in order to Linac 2, the PSB, the PS, the SPS and then the LHC.

1352 requirements for cooling. Because of these constraints, the LHC uses superconducting  
 1353 magnets which can maintain that field strength with significantly less power consumption.  
 1354

#### 1355 4.2.2 MAGNETS

1356 The magnets chosen were Niobium and Titanium (NbTi) which allow for field  
 1357 strengths as high as 10 Tesla when cooled down to 1.9 K. Reaching the target  
 1358 temperature of 1.9 K for all of the magnets requires superfluid helium and a large  
 1359 cryogenic system along the entire length of the tunnel. During normal operation,  
 1360 the LHC uses 120 tonnes of helium within the magnets, and the entire system is  
 1361 cooled by eight cryogenic helium refrigerators. The temperature increase that  
 1362 occurs during transit from the refrigerator along the beam necessitates that the  
 1363 refrigerators cool the helium down to 1.8 K. Any significant increase above this  
 1364 temperature range can remove the superconductive properties of the magnets,  
 1365 which in turn generates drastically larger heat losses from the current within the  
 1366 magnets and causes a rapid rise in temperature called a quench.  
 1367

1368 There are approximately 8000 superconducting magnets distributed around  
 1369 the LHC. The 1232 bending magnets, which keep the protons curving along the  
 1370 length of the beam, are twin bore cryodipoles, which allow both proton beams  
 1371 to be accommodated by one magnet and all of the associated cooling structure.  
 1372 Figure 13 shows the cross section of the design for these dipoles. The magnets  
 1373 are very large, 16.5 m long with a diameter of 0.57 meters and a total weight of 28  
 1374 tonnes. They are slightly curved, with an angle of 5.1 mrad, in order to carefully  
 1375 match the beam path. The twin bore accommodates both magnets inside the  
 1376 two 5 cm diameter holes which are surrounded by the superconducting coils.  
 1377 The coils require 12 kA of current in order to produce the required magnetic  
 field. These coils are comprised of NbTi cable wound in two layers; the wire in

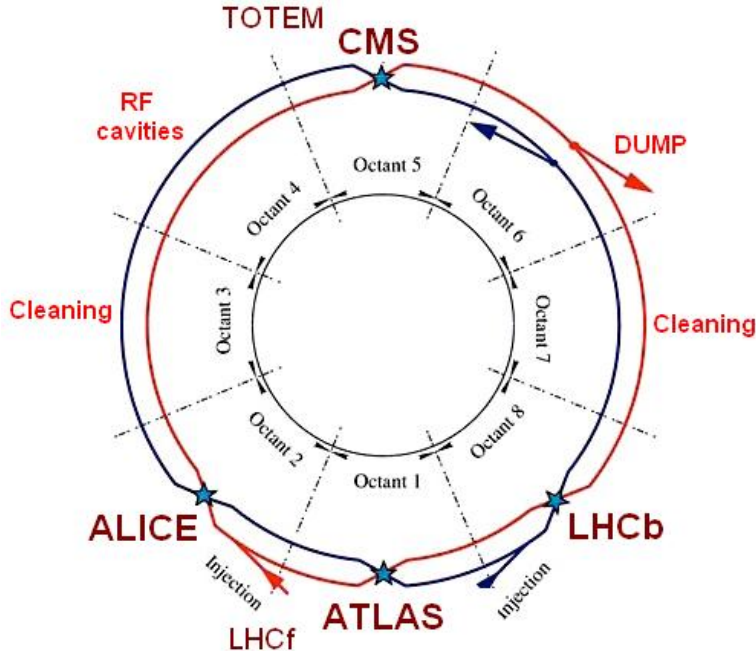


Figure 12: A schematic of the layout of the LHC, not to scale. The arched and straight sections are illustrated at the bottom of the schematic, and all four crossing sites are indicated with their respective experiments.

1378 the inner layer has a diameter of 1.065 mm while the wire in the outer layer has  
 1379 a diameter of 0.825 mm.

1380 The large currents in the wires, along with the magnetic field produced, result  
 1381 in forces on the magnets which would tend to push them apart with over 10,000  
 1382 Newtons per meter. Constraining the magnets requires a significant amount of  
 1383 structure including non-magnetic stainless steel collars. Both the presence of  
 1384 these electromagnetic forces and the varying thermal contraction coefficient of  
 1385 the pieces of the magnet produce significant forces on the cold mass structure.  
 1386 The cold mass is carefully engineered to so that these stresses do not significantly  
 1387 alter the magnetic field shape, which must be maintained between magnets to a  
 1388 precision of approximately  $10^{-4}$  for successful operation.

1389 The remaining 6800 magnets are a variety of quadrupole, sextapole, octopole,  
 1390 and single bore dipole magnets. These are used to damp oscillations, correct  
 1391 beam trajectories, focus the beams during circulation, and to squeeze the beams  
 1392 before collisions.

### 1393 4.2.3 RF CAVITIES

1394 Sixteen RF cavities produce the actual acceleration of the proton beam up to the  
 1395 design energy. These RF cavities are tuned to operate at 400 MHz, and are pow-  
 1396 ered by high-powered electron beams modulated at the same frequency, called  
 1397 klystrons. The resonance within the cavity with the oscillating electric field  
 1398 establishes a voltage differential of 2 MV per cavity. The sixteen cavities are  
 1399 split between the two beams, so combined the cavities provide 16 MV per beam,

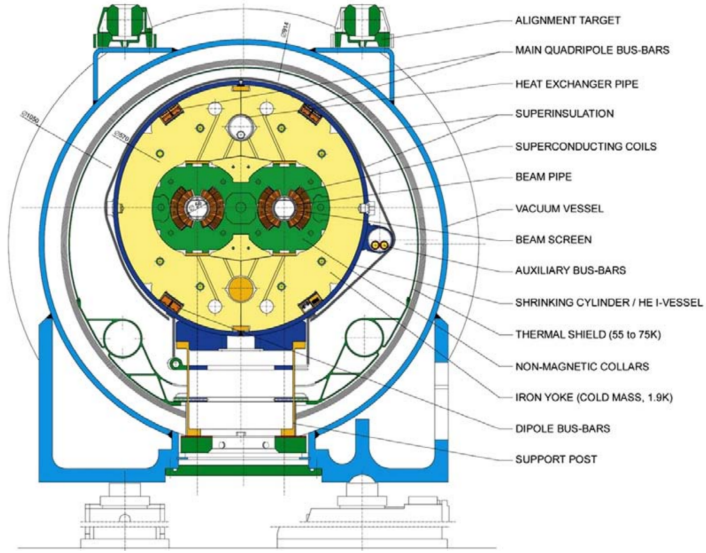


Figure 13: A cross section of the the cryodipole magnets which bend the flight path of protons around the circumference of the LHC. The diagram includes both the superconducting coils which produce the magnetic field and the structural elements which keep the magnets precisely aligned.

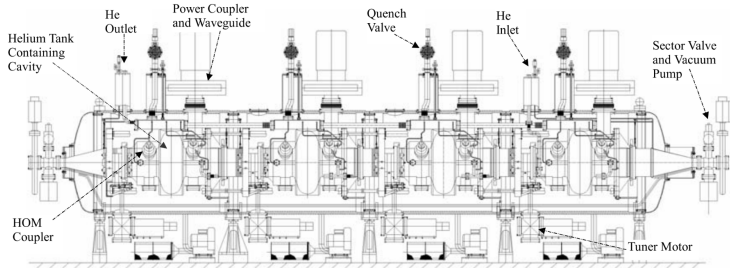


Figure 14: The arrangement of four RF cavities within a cryomodule.

1400 which accelerate the protons on each consecutive pass through the cavity. This  
 1401 acceleration is also necessary during circulation even after the target energy has  
 1402 been reach in order to compensate for losses from synchrotron radiation.

1403 The cavities are arranged in cryomodules which contain four cavities, with  
 1404 two cryomodules per beam; this arrangement is illustrated in Figure 14. These  
 1405 cryomodules are necessary to maintain the superconducting state of the cavities,  
 1406 which are also constructed from niobium. The RF cavities use niobium along  
 1407 with copper to allow for low power losses in the superconductors. The copper  
 1408 provides a reduced susceptibility to quenching, as it rapidly conducts away heat  
 1409 generated by imperfections in the niobium, as well as natural shielding from the  
 1410 earth's magnetic field which can interfere with the RF system.

1411 The nature of the radio frequency oscillations tends to group protons together  
 1412 into buckets. A proton traveling exactly in phase with the RF oscillations will not  
 1413 be displaced at all during a single circulation, and those slightly ahead or behind  
 1414 of that phase will slightly decelerate or accelerate, respectively. This produces

1415 separate clusters of protons which arrive in phase to the cavities every 2.5 ns,  
 1416 corresponding to the 400 MHz frequency.

1417 4.2.4 BEAM

1418 The beams of protons circulate within 54 km of 5 cm diameter beam pipe. This  
 1419 entire structure is kept under vacuum at 1.9 K to prevent interactions between  
 1420 the beam pipe and the magnets as well as to prevent any interactions between the  
 1421 circulating protons and gas in the pipe. The vacuum within the pipe establishes  
 1422 a pressure as low as  $10^{-9}$  mbar before the protons are introduced.

1423 Because of the very high energies of the circulating protons, synchrotron ra-  
 1424 diation is not negligible in the bending regions. The protons are expected to  
 1425 radiate 3.9 kW per beam at 14 TeV, with 0.22 W/m, which is enough power to  
 1426 heat the liquid helium and cause a quench were it absorbed by the magnets. To  
 1427 prevent this, a copper screen is placed within the vacuum tube that absorb the  
 1428 emitted photons. This screen is kept between 5 and 20 K by the liquid helium  
 1429 cooling system.

1430 4.3 LUMINOSITY PARAMETERS

In addition to the high energy of the collisions, the rate of collisions is extremely important to enabling the discovery of new physics. Many measurements and searches require a large number of events in order to be able to make statistically significant conclusions. The rate of collisions is measured using luminosity, the number of collisions per unit time and unit cross section for the proton-proton collisions. From the beam parameters, luminosity is given by

$$\mathcal{L} = \frac{N_b^2 n_b f_{rev} \gamma}{4\pi \epsilon_n \beta^*} F \quad (14)$$

1431 where  $N_b$  is the number of protons per bunch,  $n_b$  is the number of bunches per  
 1432 beam,  $f_{rev}$  is the frequency of revolution,  $\gamma$  is the Lorentz factor for the protons  
 1433 at the circulating energy,  $\epsilon_n$  is the emittance,  $\beta^*$  is the amplitude function at the  
 1434 collision point, and  $F$  is a geometric factor that accounts for the crossing angle of  
 1435 the beams at the collision point. The emittance measures the average spread of  
 1436 particles in both position and momentum space, while the amplitude function  
 1437 is a beam parameter which measures how much the beam has been squeezed.  
 1438 Together  $\epsilon_n$  and  $\beta^*$  give the size of the beam in the transverse direction,  $\sigma =$   
 1439  $\sqrt{\epsilon \beta^*}$ .  $\beta$  changes over the length of the beam as the accessory magnets shape the  
 1440 distribution of protons, but only the value at the point of collisions,  $\beta^*$ , affects  
 1441 the luminosity.

1442 The luminosity is maximized to the extent possible by tuning the parameters  
 1443 in Equation 14. A number of these are constrained by the design decisions. The  
 1444 revolution frequency is determined entirely by the length of the tunnel, as the  
 1445 protons travel at very close to the speed of light. The geometric factor  $F$  is de-  
 1446 termined by the crossing angle of the beams at the collision points, again a com-

Parameter	Unit	Injection	Nominal
Beam Energy	TeV	0.450	7
Peak Instantaneous Luminosity	$\text{cm}^{-2}\text{s}^{-1}$	-	$10^{34}$
Bunch Spacing	ns	25	25
Number of Filled Bunches	-	2808	2808
Normalized Transverse Emittance	$\mu\text{m}$	3.75	3.75
Frequency	MHz	400.789	400.790
RF Voltage/Beam	MV	8	16
Stored Energy	MJ	-	362
Magnetic Field	T	0.54	8.33
Operating Temperature	K	1.9	1.9

Table 2: The design parameters of the [LHC](#) beam that determines the energy of collisions and the luminosity, for both the injection of protons and at the nominal circulation.

1447 ponent of the tunnel design; this angle is already very small at  $285 \mu\text{rad}$ , which  
1448 helps to maximize the geometric factor.

1449 The major pieces that can be adjusted are the number of protons per bunch,  
1450  $N_b$ , the number of bunches in the beam,  $n_b$ , and the amplitude function  $\beta$ . In-  
1451 creasing either  $N_b$  or  $n_b$  increases the amount of energy stored in the beam,  
1452 which presents a danger if control of the beam is lost. At design specifications,  
1453 the beam stores 362 MJ, which is enough energy to damage the detectors or ac-  
1454 celerator if the beam were to wander out of the beam pipe. So, the luminosity  
1455 is primarily controlled at the [LHC](#) by adjusting  $\beta^*$ , where lowering  $\beta^*$  increases  
1456 the luminosity.  $\beta^*$  is tuned to provide the various values of luminosity used at  
1457 the [LHC](#) which can be raised to as much as  $10^{34}$ .

1458 The nominal bunch structure consists of 3654 bunches, each holding  $10^{11}$  pro-  
1459 tons, which cross a collision point in 25 ns. These are further subdivided into the  
1460 buckets mentioned in Section 4.2.3 by the clustering properties of the RF cavities.  
1461 The bunches are further grouped into trains of 72 bunches which are separated  
1462 by a gap which would otherwise hold 12 bunches. At nominal operation 2808  
1463 of the bunches will actually be filled with protons, while the remainder are left  
1464 empty to form an abort gap that can be used in case the beam needs to be dumped.

1465 The various beam parameters are summarized in Table 2 for the designed op-  
1466 eration. In practice, the beam has operated at lower energies and lower luminosi-  
1467 ties than the design values for the majority of its lifetime, but the [LHC](#) has begun  
1468 to operate at full design values during Run 2.

#### 1469 4.4 DELIVERED LUMINOSITY

During the data collection of 2015, the [LHC](#) operated at luminosities as large as  
 $5 \times 10^{33} \text{ cm}^{-2}\text{s}^{-1}$ . It is convenient to refer to the integrated luminosity, the inte-

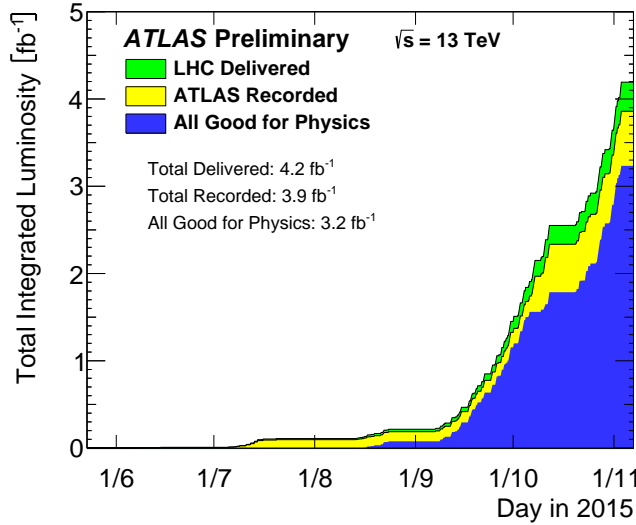


Figure 15: The cumulative luminosity versus time delivered to ATLAS (green), recorded by ATLAS (yellow), and certified to be good quality data (blue) during stable beams for pp collisions at 13 TeV in 2015.

gral of the instantaneous luminosity, which corresponds directly to the number of delivered events for a given process.

$$N = \sigma \times \int \mathcal{L}(t) dt$$

where  $\sigma$  is the cross section for the process of interest. The integrated luminosity over time is shown in Figure 15. This includes the luminosity delivered by the LHC as well as the luminosity that was recorded by ATLAS. ATLAS only records collisions when the LHC reports that the beam conditions are stable, so some of the delivered luminosity is not recorded. The figure also includes the amount of luminosity marked as good for physics, which includes additional requirements on the operation of the detector during data collection that are necessary for precise measurements.

Because the beam circulates and collides bunches of protons, it is possible for a single crossing to produce multiple proton-proton collisions. As the instantaneous luminosity is increased, the average number of collisions generated per bunch crossing increases. An event refers to the entire collection of interactions during a single bunch crossing, while interactions refer to the individual proton-proton collisions. The additional interactions produced during each bunch crossing are referred to as pileup, which can be more precisely defined quantified using the average number of additional proton-proton interactions per crossing, often denoted  $\mu$ . Figure 16 shows the luminosity-weighted distribution of the mean number of interactions for events collected in 2015. The presence of as many as twenty interactions in a single collision provides a significant challenge in reconstructing events and isolating the targeted physical processes.

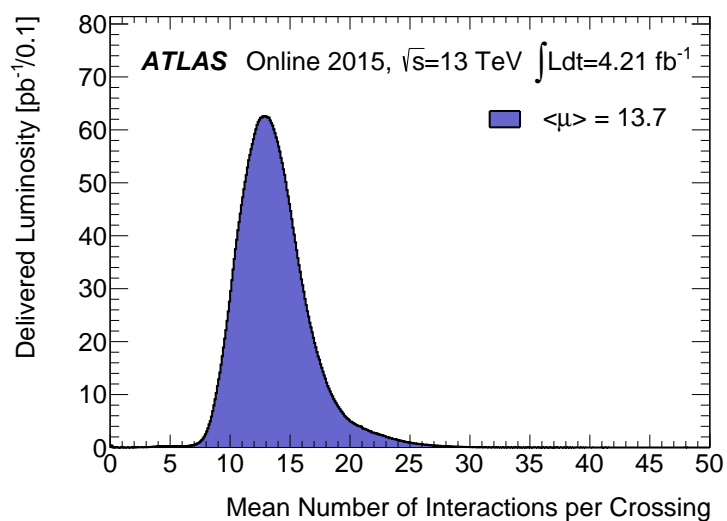


Figure 16: The luminosity-weighted distribution of the mean number of interactions per crossing for the 2015 pp collision data at 13 TeV.

1491

1492 THE ATLAS DETECTOR

---

1493 The four major LHC experiments at CERN seek to use the never before matched  
 1494 energies and luminosities of the new collider to explore the boundaries of par-  
 1495 ticle physics and to gain insight into the fundamental forces of nature. Two of  
 1496 these experiments, ATLAS and CMS, are general purpose detectors that seek to  
 1497 measure a variety of processes in the up to 13 TeV proton-proton collisions that  
 1498 occur as much as 800 million times per second at the LHC at the design lumi-  
 1499 nosity of  $10^{34} \text{ cm}^{-2}\text{s}^{-1}$ . ATLAS employs a hermetic detector design, one which  
 1500 encloses the particle collisions as completely as possible with detecting elements,  
 1501 that allows it to study a wide range of physics from SM and Higgs measurements  
 1502 to searches for new physics in models like SUSY [13].

1503 Accommodating this wide variety of goals is a challenge for the design of the  
 1504 detector. The wide range of energies involved requires high measurement pre-  
 1505 cision over several orders of magnitude, and the numerous physics processes  
 1506 require an ability to measure a variety of particle types. At the time of the con-  
 1507 struction of ATLAS, the Higgs boson had yet to be discovered, but the diphoton  
 1508 decay mode was (correctly) expected to be important and necessitated a high  
 1509 resolution photon measurement. The potential for decays of new heavy gauge  
 1510 bosons,  $W'$  and  $Z'$ , required a similarly high momentum resolution for leptons  
 1511 with momentum up to several TeV. Hadronic decay modes of several possible  
 1512 new high energy particles could result in very energetic jets, again up to several  
 1513 TeV, and reconstructing the decay resonances would again require good energy  
 1514 resolution. Several models, such as SUSY or Extra Dimensions, predict the exis-  
 1515 tence of particles which would not interact with traditional detecting elements.  
 1516 However these particles can still be observed in a hermetic detector by accurately  
 1517 measuring the remaining event constituents to observe an imbalance in energy  
 1518 called missing energy or  $E_T^{\text{miss}}$ . Measuring  $E_T^{\text{miss}}$  implicitly requires a good res-  
 1519 olution on all SM particles that can be produced. And at the lower end of the  
 1520 energy spectrum, precision SM measurements would require good resolution of  
 1521 a variety of particle types at energies as low as a few GeV, so the design needs to  
 1522 accommodate roughly three orders of magnitude.

1523 This broad spectrum of measurements requires a variety of detector systems  
 1524 working together to form a cohesive picture of each collision. Two large mag-  
 1525 net systems produce magnetic fields that provide a curvature to the propaga-  
 1526 tion of charged particles and allows for precision momentum measurements by  
 1527 other systems. The inner detector uses a combination of tracking technologies  
 1528 to reconstruct particle trajectories and vertices for charged particles. A variety  
 1529 of calorimeters measure the energies of hadrons, electrons, and photons over a  
 1530 large solid angle. A large muon spectrometer identifies muons and uses the sec-  
 1531 ond magnet system to provide an independent measurement of their momentum

1532 from the inner detector and improve the resolution. The layout of all of these  
 1533 systems is shown in Figure 17.

1534 The performance goals needed to achieve the various targeted measurements  
 1535 and searches discussed above can be summarized as resolution and coverage re-  
 1536 quirements on each of these systems. Those requirements are listed in Table 3.

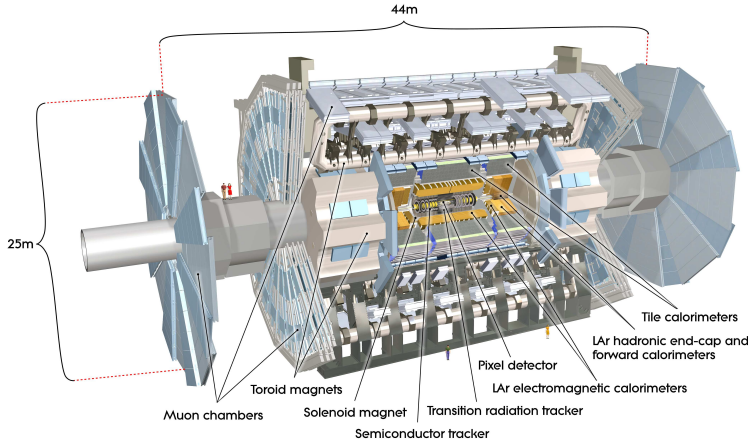


Figure 17: A cut-away schematic of the layout of the ATLAS detector. Each of the major subsystems is indicated.

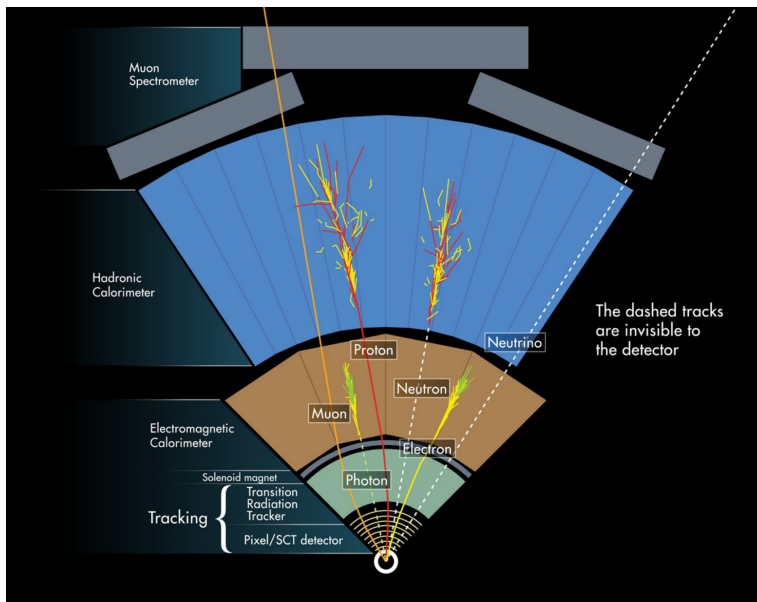


Figure 18: A cross-sectional slice of the ATLAS experiment which illustrates how the various SM particles interact with the detector systems.

1537 Incorporating these various pieces into a single detector is a significant tech-  
 1538 nical challenge. The resulting detector has a diameter of 22 m, is 46 m long,  
 1539 and weighs 7,000 tons; it is the largest volume particle detector ever constructed.  
 1540 The various detector elements need to be constructed and assembled with pre-  
 1541 cision as low as micrometers. These systems all need to function well even after  
 1542 exposure to the significant radiation dose from the collisions. Designing, con-

Detector Component	Required Resolution	$ \eta $ Coverage	
		Measurement	Trigger
Tracking	$\sigma_{p_T}/p_T = 0.05\% p_T + 1\%$	2.5	-
EM Calorimetry	$\sigma_E/E = 10\%/\sqrt{E} + 0.7\%$	3.2	2.5
Hadronic Calorimetry			
Barrel and Endcap	$\sigma_E/E = 50\%/\sqrt{E} + 3\%$	3.2	3.2
Forward	$\sigma_E/E = 100\%/\sqrt{E} + 10\%$	3.1 – 4.9	3.1 – 4.9
Muon Spectrometer	$\sigma_{p_T}/p_T = 10\% \text{ at } p_T = 1 \text{ TeV}$	2.7	2.4

Table 3: The performance goals for each of the subsystems of the ATLAS detector. The  $|\eta|$  coverage specifies the range where the subsystem needs to be able to provide measurements with the specified resolution. The resolutions include a  $p_T$  or  $E$  dependence that is added in quadrature with a  $p_T/E$  independent piece.

1543 structing, and installing the detector took the combined effort of more than 3000  
 1544 scientists from 38 countries over almost two decades.

## 1545 5.1 COORDINATE SYSTEM

1546 The coordinate system defined for the ATLAS detector is used throughout all of  
 1547 the sections of this thesis. The system begins with the choice of a  $z$  axis along  
 1548 the beamline. The positive  $z$  side of the detector is commonly referred to  
 1549 as the *A*-side, and the negative  $z$  side is referred to as the *C*-side. The  $x - y$   
 1550 plane is then the plane transverse to the beam direction, with the  $x$  direction  
 1551 defined as pointing from the interaction point to the center of the LHC ring and  
 1552 the  $y$  direction defined as pointing upwards. The nominal interaction point is  
 1553 the origin of this system.

1554 It is more convenient in practice to use a cylindrical coordinate system; this  
 1555 choice of coordinate system reflects the cylindrical symmetry of the ATLAS de-  
 1556 tector. The distance from the beamline is the radius,  $r'$ , and the angle from the  
 1557  $z$ -axis is  $\theta$ . The azimuthal angle uses the usual definition, with  $\phi$  running around  
 1558 the  $z$ -axis and  $\phi = 0$  corresponding to the  $x$ -axis. Many aspects of the detector  
 1559 are independent of the this coordinate to first order. The  $\theta$  direction is typically  
 1560 specified using rapidity or pseudorapidity, where rapidity is defined as

$$y = \frac{1}{2} \ln \frac{E + p_z}{E - p_z} \quad (15)$$

1561 Rapidity is particularly useful to indicate the component along the  $z$  direction  
 1562 because differences in rapidity are invariant to boosts along the  $z$ -direction. A  
 1563 similar quantity which depends only the  $\theta$  is pseudorapidity,

$$\eta = -\ln \tan \frac{\theta}{2} \quad (16)$$

1564 which is the same as rapidity when the particle is massless and in the limit where  
 1565 the energy is much larger than the particle's mass. It is often useful to refer to  
 1566 differences in solid angle using the pseudorapidity and the azimuthal angle:

$$\Delta R = \sqrt{\Delta\phi^2 + \Delta\eta^2} \quad (17)$$

1567 The pseudorapidity is also invariant to boosts along the  $z$ -axis for high mo-  
 1568 mentum particles, and is preferable to rapidity because it does not depend on  
 1569 the specific choice of particle. Pseudorapidity is also preferable to  $\theta$  because par-  
 1570 ticle production is roughly uniform in equal-width intervals of  $\eta$  up to about  
 1571  $\eta = 5.0$ . A particle traveling along the beampipe has  $\eta = \text{inf}$  and a particle  
 1572 traveling perpendicular to the beampipe has  $\eta = 0$ . The extent of the tracker,  
 1573  $|\eta| < 2.5$ , corresponds to approximately  $0.05\pi < \theta[\text{rad}] < 0.95\pi$  and the  
 1574 extent of the calorimeters,  $|\eta| < 4.9$  corresponds to approximately  $0.005\pi <$   
 1575  $\theta[\text{rad}] < 0.995\pi$ . Many detector components are broken into multiple subsys-  
 1576 tems to provide coverage at greater  $|\eta|$ . The lower  $|\eta|$  region is referred to as the  
 1577 barrel, typically with  $|\eta| \lesssim 2$ , and the greater  $|\eta|$  region is often referred to as the  
 1578 endcap.

1579 The initial energy and momentum of a proton-proton collision along the  $z$  di-  
 1580 rection is unknown in hadron colliders because different energies and momenta  
 1581 can be carried by the partons. Along the transverse plane, however, the vector  
 1582 sum of momentum will be zero. For this reason, many physical quantities are  
 1583 quantified in terms of their projection onto the transverse plan, such as  $p_T$  or  
 1584  $E_T$ . In addition,  $p_T$  alone determines the amount of curvature in the magnetic  
 1585 field, and can be measured independently by measuring the curvature of a parti-  
 1586 cle's propagation.

## 1587 5.2 MAGNETIC FIELD

1588 The magnet system used in ATLAS is designed to provide a substantial magnetic  
 1589 field in the two regions where the trajectory of particles is measured, the inner  
 1590 detector and the muon spectrometer. The magnetic field provides a curvature to  
 1591 the trajectory of charged particles and allows the precision tracking elements to  
 1592 make high resolutions measurements of  $p_T$ . To provide a magnetic field in these  
 1593 regions, ATLAS uses a hybrid system with four separate, superconducting mag-  
 1594 nets. A single solenoid provides a 2 T axial, uniform magnetic field for the inner  
 1595 detector, while a barrel toroid and two endcap toroids produce a non-uniform  
 1596 magnetic field of 0.5 and 1 T, respectively, for the muon detectors. This geom-  
 1597 etry is illustrated in Figure 19, and the parameters of the three magnet systems  
 1598 are summarized in Table 4.

1599 The central solenoid uses a single-layer coil with a current of 7.730 kA to gen-  
 1600 erate the 2 T axial field at the center of the magnet. The single-layer coil design  
 1601 enables a minimal amount of material to be used in the solenoid's construction,  
 1602 which is important because the solenoid is placed between the inner detector  
 1603 and the calorimeters. At normal incidence the magnet has only 0.66 radiation  
 1604 lengths worth of material, where one radiation length is the mean distance over

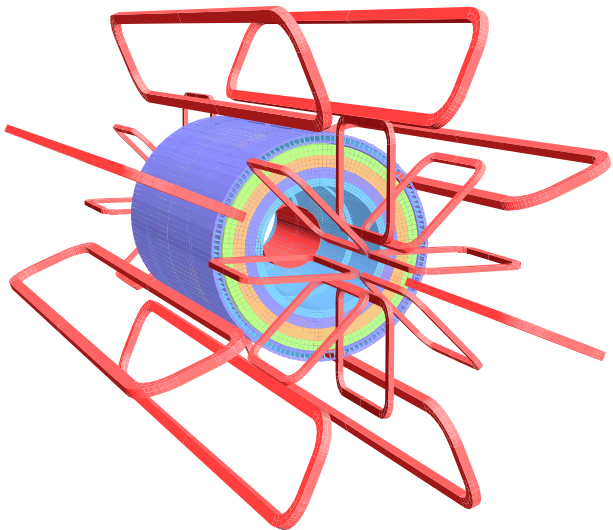


Figure 19: The layout of the four superconducting magnets in the ATLAS detector.

Parameter	Unit	Solenoid	Barrel Toroid	Endcap Toroids
Inner Diameter	m	2.4	9.4	1.7
Outer Diameter	m	2.6	20.1	10.7
Axial Length	m	5.3	25.3	5.0
Weight	tons	5.7	830	239
Conductor Size	mm <sup>2</sup>	30×4.25	57×12	41×4.25
Peak Field	T	2.6	3.9	4.1
Heat Load	W	130	990	330
Current	kA	7.7	20.5	20.0
Stored Energy	MJ	38	1080	206

Table 4: A summary of the parameters of each of the three magnet systems on ATLAS.

which a high-energy electron loses all but  $1/e$  of its energy through material interactions [6]. The coil is made of a high-strength aluminum stabilized NbTi superconductor which was optimized to achieve a high field with minimal thickness. The axial magnetic field produced by the solenoid bends charged particles in the  $\phi$  direction, following a circular path with a radius specified by Maxwell's equations (see Equation 13).

The barrel toroid consists of eight coils which generate a 0.5 T magnetic field, on average, in the cylindrical region around the calorimeters with an approximately 20 kA current. The coils are separated only by air to reduce the scattering of muons as they propagate through the region. The coils are made of an aluminum stabilized NbTiCu superconductor and each is separately housed in a vacuum and cold chamber. This magnetic configuration produces a field in the  $\phi$  and so curves muons traversing the volume primarily in the  $\eta$  direction.

The endcap toroids follow a similar design to the barrel toroid and produce a 1.0 T magnetic field, on average. Each has eight separate NbTiCu coils, and in this case all eight are housed within a single cold mass. This extra structure is necessary to withstand the Lorentz forces exerted by the magnets. These magnets are rotated 22.5% relative to the barrel toroid to provide a uniform field in the transition between the two systems. The endcap toroids also produce a field in the  $\phi$  direction and curve muons primarily in the  $\eta$  direction.

### 5.3 INNER DETECTOR

The ATLAS inner detector provides excellent momentum resolution as well as accurate primary and secondary vertex measurements through robust pattern recognition that identifies tracks left by charged particles. These tracks fulfill a number of important roles in the ATLAS measurement system: they measure the momentum of charged particles including electrons and muons, they can identify electrons or photon conversions, they assign various particles and jets to different vertices, and they provide a correction to  $E_T^{\text{miss}}$  measurements from low energy particles. The system has to be accurate enough to separate tracks from dozens of vertices, to resolve each vertex individually, and to measure the  $p_T$  of very high momentum tracks which curve very little even in the large magnetic field. This is accomplished by several independent layers of tracking systems. Closest to the interaction point is the very high granularity Pixel detector, including the newly added Insertible B-Layer, which is followed by the SCT layers. These silicon subdetectors both use discrete space-points to reconstruct track patterns. The final layer, the Transition Radiation Tracker (TRT), uses many layers of straw tube elements interleaved with transition radiation material to provide continuous tracking. The arrangement of these subdetectors is shown in Figure 20. To provide the desired hermetic coverage, the subdetectors are divided into barrel and endcap geometries. Figure 21 shows the layout of the subdetectors in more detail, and illustrates how tracks at various pseudorapidities can traverse the subdetectors; tracks with  $\eta > 1.1$  begin to traverse the endcap subdetectors rather than those in the barrel, and tracks with  $\eta > 1.7$  use primar-

ily endcap elements. The IBL was not present during the original commissioning of the inner detector and is not shown in this figure.

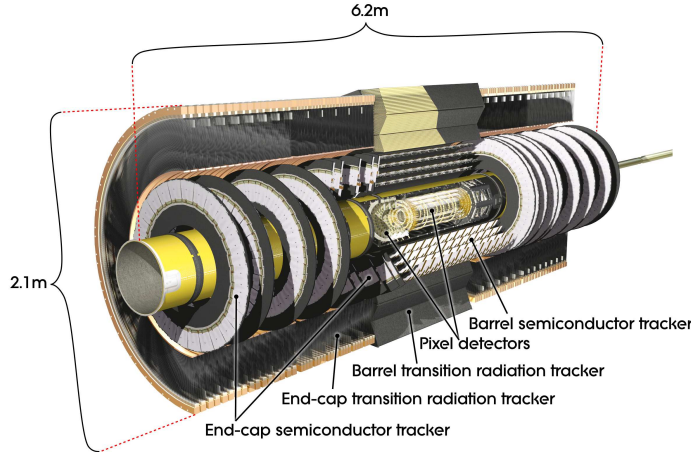


Figure 20: The arrangement of the subdetectors of the ATLAS inner detector. Each of the subdetectors is labeled in the cut-away view of the system.

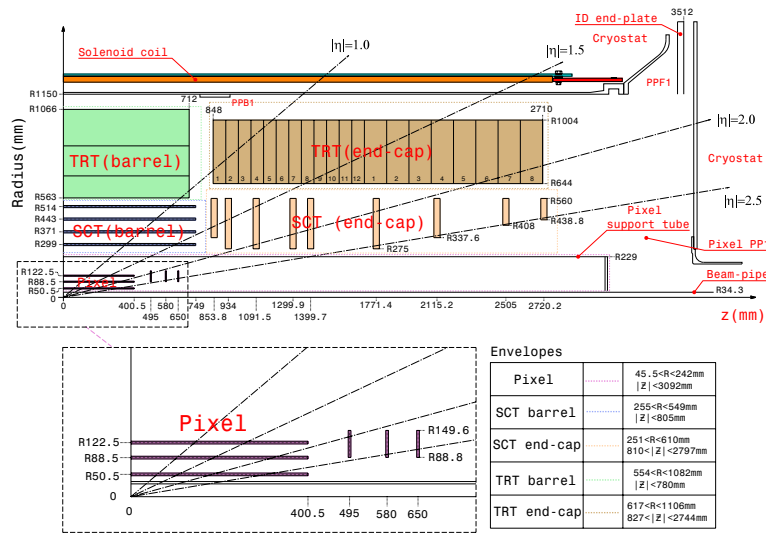


Figure 21: A quarter section of the ATLAS inner detector which shows the layout of each of the subdetectors in detail. The lower panel shows an enlarged view of the pixel detector. Example trajectories for a particle with  $\eta = 1.0, 1.5, 2.0, 2.5$  are shown. The IBL, which was added after the original detector commissioning, is not shown.

Figure 22 shows a computer generated three-dimensional view of the inner detector along the beam axis, which emphasizes the straw tube structure of the TRT as well as the overlapping geometry of the SCT. This figure also includes the IBL, which was added during the long shutdown and provides an additional measurement layer in the Pixel detector as of the beginning of Run 2. Figure 23 shows an alternative computer generated three-dimensional view transverse to the beam axis which emphasizes the endcap structures of the SCT and TRT.

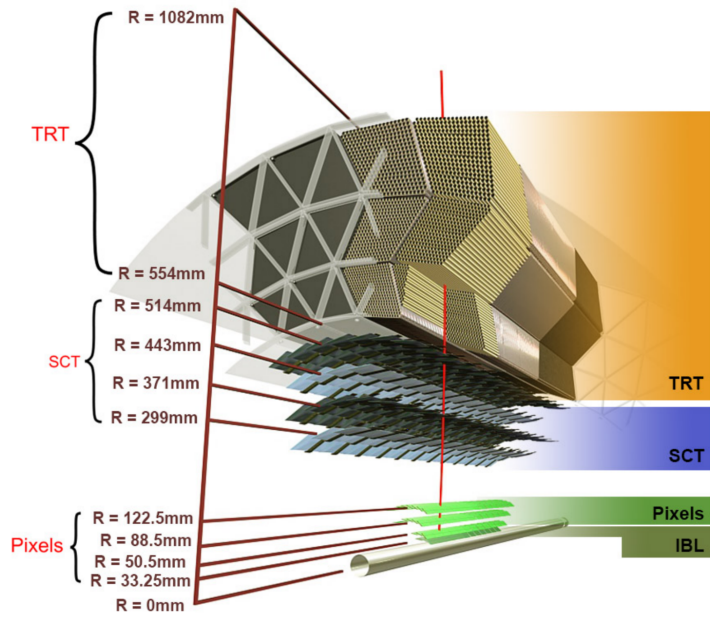


Figure 22: A computer generated three-dimensional view of the inner detector along the line of the beam axis. The subdetectors and their positions are labeled.

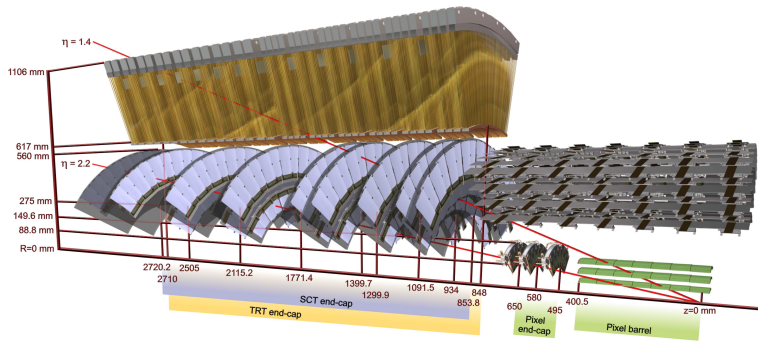


Figure 23: An alternative computer generated three-dimensional view of the inner detector transverse to the beam axis. The subdetectors and their positions are labeled.

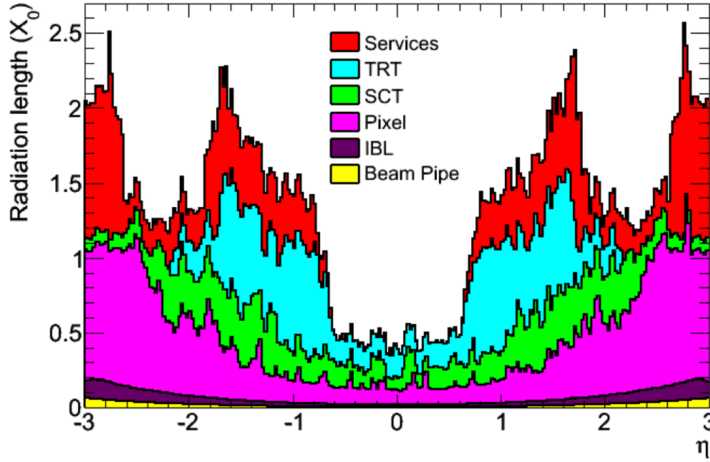


Figure 24: The integrated radiation lengths traversed by a straight track at the exit of the ID envelope, including the services and thermal enclosures. The distribution is shown as a function of  $|\eta|$  and averaged over  $\phi$ . The breakdown indicates the contributions of individual sub-detectors, including services in their active volume.

As the closest system to the interaction point, it is crucial for the inner detector to use as little material as possible to avoid scattering of charged particles or photon conversions before they reach the remaining subdetectors. The various components, including the readout electronics, cooling infrastructure, gas volumes, and support structures, were designed to accommodate this need for minimal components. Even with these optimizations, the combination of stringent performance requirements and the harsh radiation environment in the inner detector requires a significant amount of material. This material causes many electrons to lose most of their energy before reaching the electromagnetic calorimeter and approximately 40% of photons convert into an electron-positron pair while traversing the inner detector. Figure 24 shows the integrated radiation lengths traversed by a straight track in the inner detector as a function of  $\eta$ , grouped by subdetector. There is a large increase in the amount of material for support structures around  $|\eta| = 1.7$ , where the inner detector transitions from barrel to endcap.

The inner detector is designed to work as a cohesive unit to provide complete tracking information for charged particulars, and the subdetectors are complementary. Table 5 summarizes the parameters of each of the subdetectors as well as the parameters of the combined inner detector. Table 6 summarizes the expected performance that can be achieved by the inner detector as a whole.

### 5.3.1 PIXEL DETECTOR

The Pixel detector is the closest detector to the interaction point and therefore is designed to provide extremely high granularity while simultaneously handling a very large dose of radiation from collisions. It consists of four layers of silicon pixel modules, each of which provides a precision measurement on the trajectory

Parameter	Inner Detector	Pixel	SCT	TRT
Inner Radius	3.1 cm	3.1 cm	30 cm	56 cm
$ \eta $ Coverage	-	2.5	2.5	2.0
Cell Width	-	50 $\mu\text{m}$	80 $\mu\text{m}$	4 mm
Cell Length	-	400 $\mu\text{m}$	12 cm	70 cm
Material at $ \eta  = 0.0$	0.3 $X/X_0$			
Material at $ \eta  = 1.7$	1.2 $X/X_0$			
Material at $ \eta  = 2.5$	0.5 $X/X_0$			
Number of Hits	48	4	8	36
Channels	99 M	92 M	6.3 M	350 k

Table 5: A summary of the parameters of the inner detector and each of the subdetectors [13].

of any charged particle. In the barrel region, the four layers are located at radial distances of 31 mm, 51 mm, 89 mm, and 123 mm. The three outer layers also include endcap elements, illustrated in Figure 21, which are located at 495 mm, 580 mm, and 650 mm away from the interaction point.

The pixel sensor technology uses a p-n junction of n-type bulk that contains both p<sup>+</sup> and n<sup>+</sup> impurities. This combination is crucial in maintaining performance after a significant radiation dose, as the n<sup>+</sup> implants allow the sensor to continue function after the n-type bulk has been converted to a p-type bulk by the accumulation of radiation. In either configuration, when a charged particle passes through the bulk, it ionizes thousands of electron-hole pairs. The electrons and holes are pulled in opposite directions by the electric field established between the anode and cathode of the junction, which then produces a current that can be measured and recorded by readout electronics.

The size of the pixels in the original three layers are 50  $\mu\text{m}$  x 400  $\mu\text{m}$  in the  $r - \phi$  and  $z$  directions, respectively. Those pixels are bump-bonded to front-end readout chips, the FE-I3, which contains a total of 2880 pixels per chip. In the three original pixel layers, the chips are grouped into modules composed of 16 chips each with 46,080 pixels per module and a total size of 20 mm x 60 mm x 250  $\mu\text{m}$ . The modules are further arranged into long rectangular structures that run parallel to the beamline called staves. By tiling several staves with an offset of 20°, the stave geometry provides full azimuthal coverage in the barrel region while accommodating the readout and cable systems. The endcap regions are instead arranged into petals and then into wheels. This arrangement can be seen in Figure 25 which shows a computer-generated, cut-away image of the outer three layers of the pixel detector. Together these three layers contain 1744 modules between the barrel and two endcap sections.

The innermost layer, the IBL, was added during the long shutdown before Run 2, and provides the fourth track measurement. It was inserted directly into the existing pixel detector by removing the existing beam pipe and replacing it with a significantly smaller version. This insertion can be seen in action in Figure 26,

Parameter	Particle	Value
Reconstruction Efficiency	Muon, $p_T = 1 \text{ GeV}$	96.8%
	Pion, $p_T = 1 \text{ GeV}$	84.0%
	Electron, $p_T = 5 \text{ GeV}$	90.0%
Momentum Resolution	$p_T = 1 \text{ GeV},  \eta  \approx 0$	1.3%
	$p_T = 1 \text{ GeV},  \eta  \approx 2.5$	2.0%
	$p_T = 100 \text{ GeV},  \eta  \approx 0$	3.8%
	$p_T = 100 \text{ GeV},  \eta  \approx 2.5$	11%
Transverse IP Resolution	$p_T = 1 \text{ GeV},  \eta  \approx 0$	$75 \mu\text{m}$
	$p_T = 1 \text{ GeV},  \eta  \approx 2.5$	$200 \mu\text{m}$
	$p_T = 1000 \text{ GeV},  \eta  \approx 0$	$11 \mu\text{m}$
	$p_T = 1000 \text{ GeV},  \eta  \approx 2.5$	$11 \mu\text{m}$
Longitudinal IP Resolution	$p_T = 1 \text{ GeV},  \eta  \approx 0$	$150 \mu\text{m}$
	$p_T = 1 \text{ GeV},  \eta  \approx 2.5$	$900 \mu\text{m}$
	$p_T = 1000 \text{ GeV},  \eta  \approx 0$	$90 \mu\text{m}$
	$p_T = 1000 \text{ GeV},  \eta  \approx 2.5$	$190 \mu\text{m}$

Table 6: A summary of the expected performance of the combined inner detector [17]. Included are the reconstruction efficiencies for multiple particle types as well as the momentum and IP resolution for various momenta.

which emphasizes the extreme precision required to place the the 70 cm long layer with only 2 mm of clearance. The IBL was commissioned to provide continued tracking robustness and high precision in the higher luminosity environment of Run 2 [18]. The proximity of this layer to the collisions necessitated an even higher granularity and better radiation hardness than the other pixel layers. And the strict space requirements to add an active sensing layer so close to the interaction point required a sensor chip with a much higher active area and a larger overall area per chip. These requirements led to the development of a new chip type, the FE-I4 (compared to the FE-I3 chips used in the original pixel detector) with improved radiation hardness and a larger active footprint of 90%. The IBL is comprised of 448 of these individual chips arranged in 14 staves, with 26,880 pixels per chip and a chip size of 18.5 mm x 41.3 mm x 200  $\mu\text{m}$ . The staves, like in the other layers of the pixel detector, are offset by 14°to provide full azimuthal coverage. This arrangement can be seen in Figure 27, which shows two computer-generated images of the IBL geometry and includes the some of the remaining pixel layers.

### 5.3.2 SEMICONDUCTOR TRACKER

The SCT, the subdetector which immediately surrounds the Pixel detector, provides additional discrete measurements of the trajectory of a charged particle. Because the SCT is further away from the interaction point, the spatial resolution

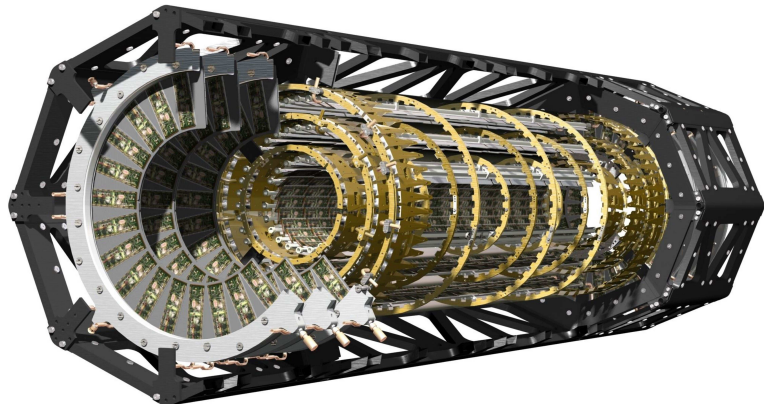


Figure 25: A cut away image of the outer three layers of the pixel detector.

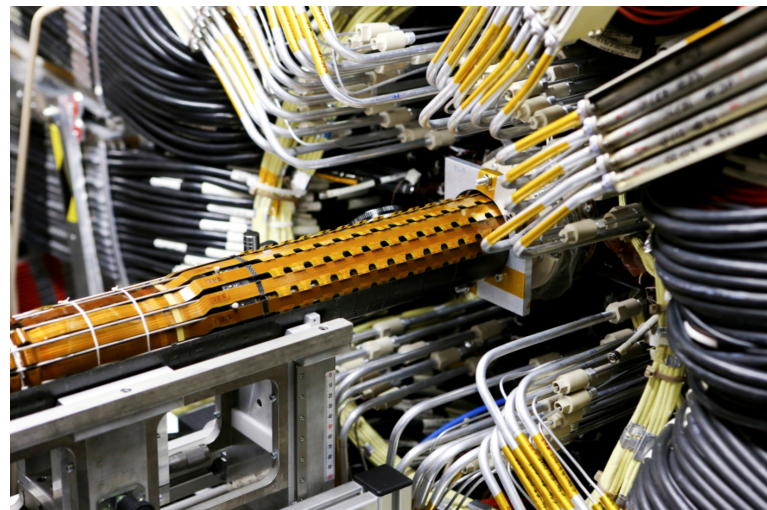


Figure 26: An image of the insertion of the IBL into the current pixel detector.

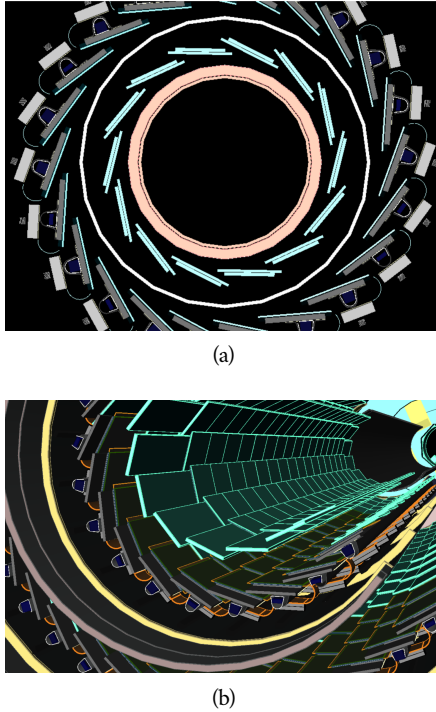


Figure 27: A three-dimensional computer-generated image of the geometry of the **IBL** with a view (a) mostly transverse to the beam pipe (b) mostly parallel to the beam pipe.

1732 does not need to be as high as in the pixel detector, and so the **SCT** uses micro-  
 1733 strips instead of pixels. Although pixels provide a more accurate measurement,  
 1734 the number of pixels and readout channels required to cover the cylindrical area  
 1735 at the radius of the **SCT** layers would be prohibitively complicated and expensive.

1736 Each individual silicon strip sensor contains 768 individual readout strips  
 1737 with a total area of  $6.36 \text{ cm} \times 6.40 \text{ cm}$  and a pitch of  $80 \mu\text{m}$ . Pairs of these sen-  
 1738 sors are then bonded together to form a combined strip with a length of 12.8 cm.  
 1739 Two of these combined strips are then placed back to back with a relative tilt of  
 1740 40 mrad. This geometry is illustrated in an expanded view in Figure 28. The pur-  
 1741 pose of angular offset of the consecutive layers is to allow the strip sensor areas  
 1742 to more accurately measure the position of a particle by comparing the overlap  
 1743 of the two strips which were traversed by a track.

1744 Four of these double layers are placed in the barrel region, with radii of 284  
 1745 mm, 355 mm, 427 mm, and 498 mm. Together these layers provide eight addi-  
 1746 tional measurements for each track that traverses the central  $|\eta|$  region. In the  
 1747 endcap region, the layers are arranged in wheels, with the double layers simi-  
 1748 larly offset to provide improved resolution. With these configurations, the **SCT**  
 1749 achieves a spatial resolution of  $17 \mu\text{m}$  in the  $r - \phi$  direction and  $580 \mu\text{m}$  in the  
 1750  $z$  direction.

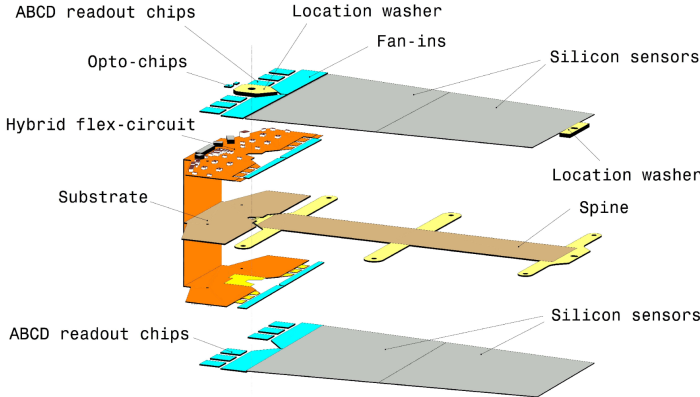


Figure 28: An expanded view of the geometry of the **SCT** double layers in the barrel region.

### 1751 5.3.3 TRANSITION RADIATION TRACKER

1752 The final component of the inner detector, the **TRT**, provides continuous track-  
 1753 ing using straw drift tubes. The tubes are made of Kapton and aluminum with  
 1754 a diameter of 4 mm and are filled with a gas mixture of 70% Xe, 27% CO<sub>2</sub>, and  
 1755 3% O<sub>2</sub>. At the center of each tube is a gold-plated anode tungsten wire 30  $\mu\text{m}$  in  
 1756 diameter. When a charged particle passes through these tubes, it ionizes the gas  
 1757 within. The ions produced drift in the electric field established between the wire  
 1758 and the tube wall, and the large electric field near the wire produces avalanche  
 1759 multiplication and results in an electric current on the wire that is read out by  
 1760 the electronics and provides a track measurement. The time it takes the ioniza-  
 1761 tion to drift to the wire can be used to estimate the distance from the wire that  
 1762 the particle passed through the tube; this gives a resolution on the distance of ap-  
 1763 proximately 130  $\mu\text{m}$ . Combining several such measurements between consecu-  
 1764 tive hits in the **TRT** tubes allows the trajectory of the particle to be reconstructed  
 1765 with much better resolution than is available in each individual tube.

1766 In addition to the continuous tracking, the detector can use transition radi-  
 1767 tion produced when a particle passes between the layers to distinguish between  
 1768 electrons and heavier charged particles. The space between the tubes is filled  
 1769 with CO<sub>2</sub>, and so has a different dielectric constant than the gas within the tubes  
 1770 which contains Xe. At the transition between those media, a relativistic par-  
 1771 ticle emits radiation proportional to  $\gamma$ , so inversely proportional to mass at a  
 1772 fixed momentum. The photons produced in this transition then produce an  
 1773 ionization cascade which is significantly larger than the signal for the minimally-  
 1774 ionizing charged particles. To distinguish between these two cases, the **TRT** de-  
 1775 fines two signal thresholds, a low threshold for the typical signal produced by a  
 1776 minimally ionizing particle (**MIP**) and a high threshold for the the signal produced  
 1777 by transition radiation. A high momentum electron is expected to produce ap-  
 1778 proximately 7 to 10 high threshold hits as it traverses the **TRT**, and thus these hits  
 1779 provide a way to distinguish electrons from other charged particles.

1780     The TRT contains 351,000 tubes in total, divided between the barrel and end-  
 1781     cap regions. In the barrel region, the tubes are 144 cm long and arranged in 73  
 1782     layers parallel to the beampipe. In the endcap region, the tubes are 37 cm long  
 1783     and arranged in 160 layers transverse to the beampipe. These configurations  
 1784     can be seen in Figure 22 and Figure 23. With this geometry the TRT achieves a  
 1785     resolution of 130  $\mu\text{m}$  in the  $r - \phi$  direction.

## 1786     5.4 CALORIMETRY

1787     The combination of calorimeter systems used in ATLAS can measure the energy  
 1788     of electrons, photons, hadrons, and hadronic jets with complete coverage up to  
 1789      $|\eta| < 4.9$  and across  $\phi$ . Unlike the inner detector, the calorimeters are capable  
 1790     of measuring neutral particles. To accomplish precision measurements of these  
 1791     particle types, the ATLAS calorimeter system uses four individual calorimeters,  
 1792     a LAr electromagnetic calorimeter in the barrel region, a tile hadronic calorime-  
 1793     ter in the barrel region, a LAr hadronic endcap calorimeter, and a LAr forward  
 1794     calorimeter. Together these provide hermetic coverage for the ATLAS detec-  
 1795     tor. The configuration of these calorimeters is illustrated in Figure 29. **Note: I**  
 1796     **could make this section much longer. It might be nice to include a more**  
 1797     **complete description of showers for example. I will extend this section if**  
 1798     **there is space at the end.**

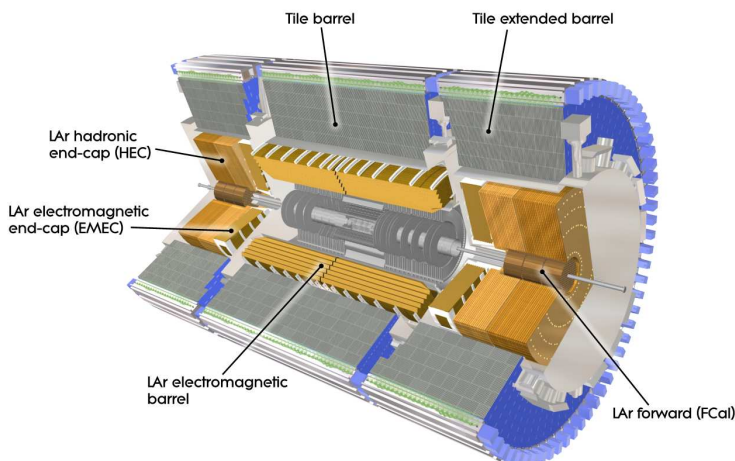


Figure 29

1799     The calorimeters are designed to absorb and measure the energy carried by  
 1800     a particle, and completely stop the particle's propagation in the process. This  
 1801     requires a significant amount of material to provide interactions. These interac-  
 1802     tions then produce secondary particles, which can produce secondary particles  
 1803     in turn, and thus form a cascade of particles called an electromagnetic (EM) or  
 1804     hadronic shower, depending on the governing mechanism. Electromagnetic and  
 1805     hadronic showers have very different properties and require different technolo-  
 1806     gies to measure them accurately. All of the calorimeters in the ATLAS calorime-  
 1807     ter system are sampling calorimeters: they use alternating layers of absorbing

and active material. The dense absorbing layers initiate the showers while the active layers measure the energy of the produced particles. A fraction of the energy is lost in the inactive layers, so the energy measurement from the active layers has to be corrected to estimate the actual energy of the particle.

The EM calorimeter provides around 20 radiation lengths ( $X_0$ ) while the hadronic calorimeter provides around 10 interaction lengths ( $\lambda_0$ ). As mentioned previously, radiation lengths measure the distance over which an electromagnetically interacting particle loses a characteristic fraction of its energy. Interaction lengths, on the other hand, measure the mean distance traveled by a hadronic particle before undergoing a nuclear interaction [6]. Figure 30 show the radiation lengths in the layers of the EM calorimeter in the barrel region as well as the interaction lengths for all calorimeters.

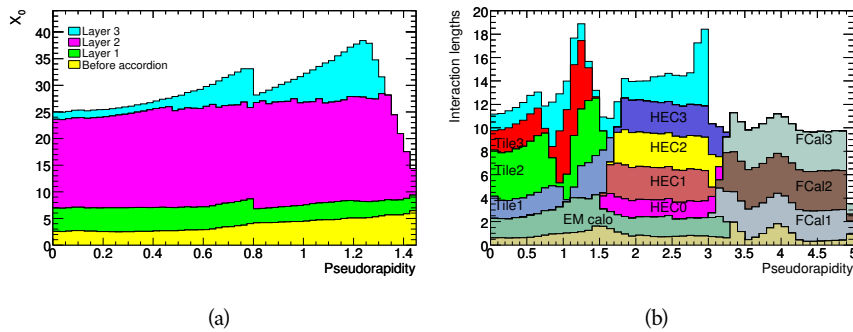


Figure 30: The depth of (a) the electromagnetic barrel calorimeter in radiation lengths and (b) all calorimeters in interaction lengths as a function of pseudorapidity.

#### 5.4.1 ELECTROMAGNETIC CALORIMETER

The electromagnetic calorimeters use alternating layers of liquid argon and lead in an accordion shape. The accordion shape provides complete coverage in the  $\phi$  direction while also providing many alternating layers for the a particle to pass through. The configuration is detailed in Figure 31. When an electron or photon passes through the lead, it produces an electromagnetic shower. The particles produced in those showers then pass into and ionize the liquid argon; the ions produced can then be collected by an electrode in the liquid argon layer to provide the actual energy measurement.

The barrel region is covered by a presampler and three separate sampling layers with decreasing segmentation. The presampler is a thin layer of liquid argon which measures the energy of any electromagnetic showers which are initiated before the particle reaches the calorimeter due to interactions with the detector material. The first layer is the strip layer, which has fine segmentation in  $\eta$  to enhance the identification of shower shapes and to provide a precise  $\eta$  measurement for reconstructing photons and electrons. The strip layer has only 4 radiation lengths worth of material, and has a segmentation of  $\Delta\eta = 0.003$  and  $\Delta\phi = 0.1$ . The second layer is also finely segmented, with a segmentation of  $\Delta\eta = 0.025$  and  $\Delta\phi = 0.025$ , and a thickness of 16  $X_0$ . This layer is designed

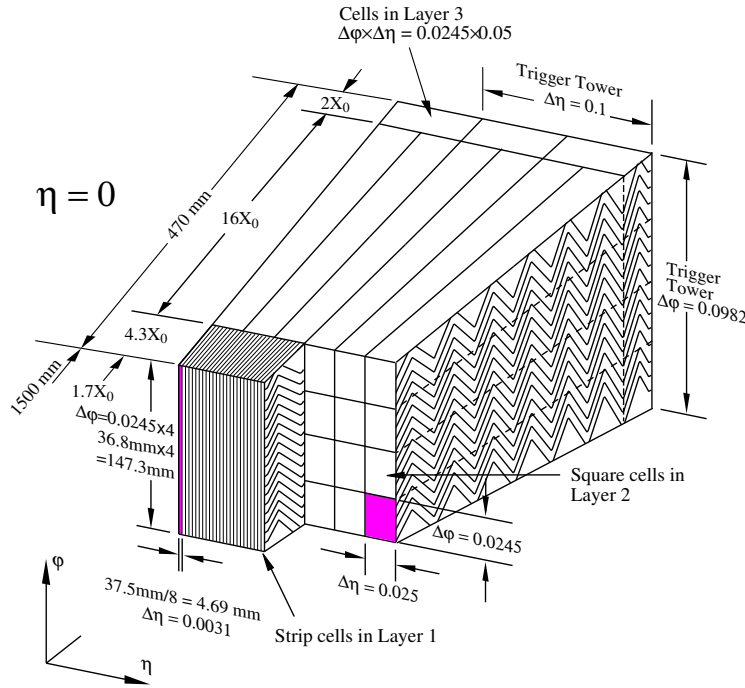


Figure 31: A schematic of the LAr calorimeter in the barrel region, highlighting the accordion structure.

1839 to contain an electromagnetic shower and to measure the majority of the energy  
 1840 for photons and electrons. The third layer is only  $2 X_0$  thick and measures the  
 1841 energy of electromagnetic showers which leak out of the second layer, and helps  
 1842 to separate electromagnetic showers from hadronic showers. The structure of  
 1843 the LAr endcap calorimeter is similar except that the layers are arranged parallel  
 1844 to the beampipe to measure energy deposits from high  $\eta$  particles.

#### 1845 5.4.2 HADRONIC CALORIMETERS

1846 The hadronic calorimeters use a few different technologies to satisfy the resolu-  
 1847 tion demands in the different areas of the detector, and together they cover the  
 1848 region  $|\eta| < 2.7$ . In the barrel region, for  $|\eta| < 1.7$ , the hadronic calorimeters  
 1849 are constructed of alternating tiles of steel and plastic scintillator. Like in the  
 1850 electromagnetic calorimeter, the dense layer initiates a shower (in this case the  
 1851 dense layer is the steel and the shower is hadronic) of particles which pass into  
 1852 and ionize the following layer. The ionization in the plastic scintillator instead  
 1853 produces a light signal proportional to the amount of ionization produced by the  
 1854 shower, and this signal is measured using photomultipliers and provides the ac-  
 1855 tual energy measurement. The construction of a tile in the calorimeter is shown  
 1856 Figure 32, which highlights the alternating layers of steel and scintillator.

1857 This tile calorimeter, as well as the remaining hadronic calorimeters, have a  
 1858 much coarser granularity than the electromagnetic calorimeters. The high gran-  
 1859 ularity is not needed for an accurate energy measurement, and the hadronic  
 1860 calorimeters are not designed to distinguish particle types like the electromag-

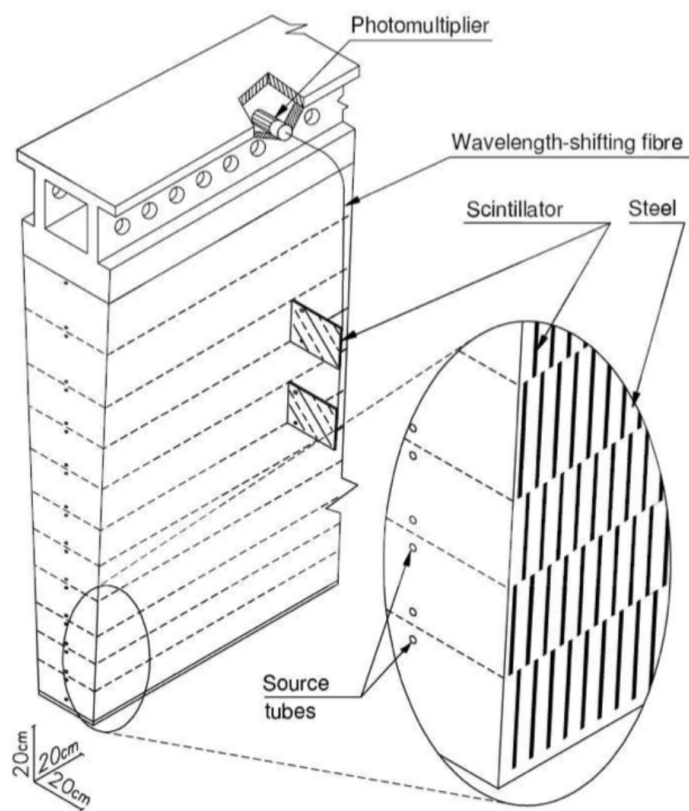


Figure 32: A schematic of a hadronic tile module which shows the alternating layers of steel and plastic scintillator.

netic calorimeters. The tile granularity is approximately  $\Delta\eta = 0.1$  and  $\Delta\phi = 0.1$ , and the segmentation in depth and  $\eta$  is shown in Figure 33.

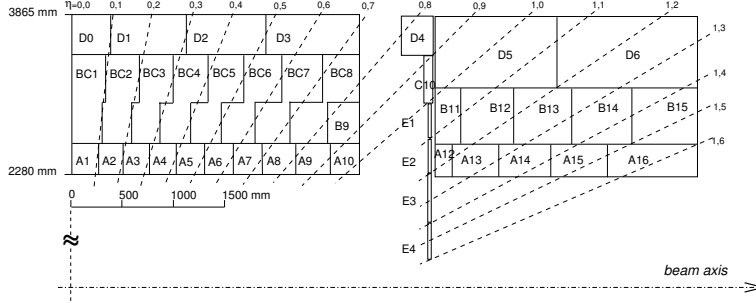


Figure 33: The segmentation in depth and  $\eta$  of the tile-calorimeter modules in the central (left) and extended (right) barrels.

The remaining hadronic calorimeters all use the same alternating sampling structure but with different active and inactive materials. The hadronic endcap calorimeter covers the range of  $1.5 < |\eta| < 3.2$  and uses an inactive layer of copper and an active layer of liquid argon. The forward calorimeter covers the range of  $3.1 < |\eta| < 4.9$  and uses a dense matrix of copper and tungsten filled with liquid argon.

## 5.5 MUON SPECTROMETER

Among SM particles, only muons and neutrinos consistently pass through the calorimeters. Because the neutrinos are also electrically neutral, there is no feasible option to measure them directly in ATLAS. The muons, on the other hand, are charged and are thus already measured as a track in the inner detector. The muon spectrometer provides a way to consistently identify muon tracks and also a way to provide an additional measurement of their momentum.

The muon spectrometer contains four subdetectors that cover the barrel and endcap regions. In the barrel region, the muon spectrometer uses a combination of Resistive Plate Chambers (RPCs) and MDTs to provide both a coarse, fast measurement for triggering and a precise momentum measurement for offline event reconstruction. Similarly, in the endcap region, the TGCs, MDTs, and CSCs allow for both triggering and precise measurements. The CSCs are used only in the innermost layer of the endcap region between  $2.0 < |\eta| < 2.7$  where the particle flux is too large for the MDTs to provide accurate measurements. The overall layout of the muon systems are shown in the cut-away diagram in Figure 34, and Figure 35 shows a precise schematic of the layout of each of the detecting elements. The geometric arrangement shown provides consistent coverage for muons produced up to  $|\eta| < 2.7$ , and takes full advantage of the bending of the muons in the toroidal magnetic field, described in Section 5.2, to measure their momentum. Figure 36 shows a cross-section of the arrangement of the muon spectrometer in the barrel; the layers are divided into eight small and eight large chambers that are overlapped to provide complete coverage in  $\phi$ .

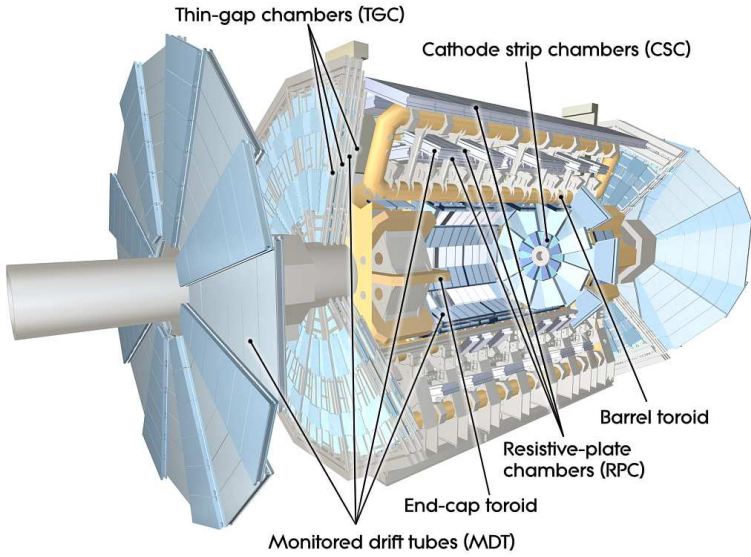


Figure 34: A cut-away diagram of the muon systems on ATLAS.

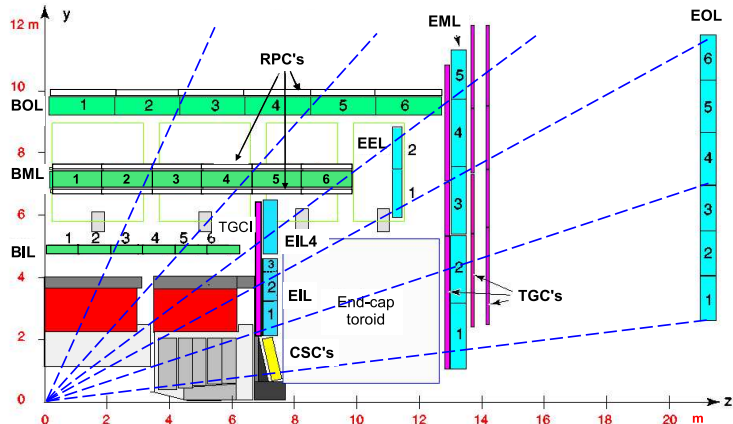


Figure 35: A quarter view of the muon spectrometer which highlights the layout of each of the detecting elements. The BOL, BML, BIL, EOL, EML, and EIL are all MDT elements, where the acronyms encode their positions.

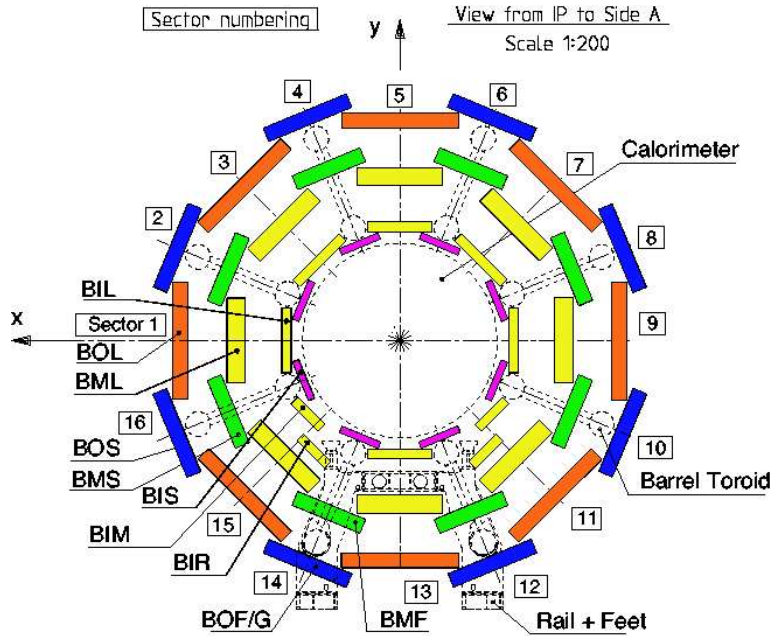


Figure 36: A schematic of the cross-section of the muon spectrometer in the barrel region.

#### 1892 5.5.1 MONITORED DRIFT TUBE

1893 The momentum measurements in the barrel region are provided by three consecutive layers of MDT elements, located at approximately 5 m, 7 m, and 9 m from  
 1894 the interaction point. Each of these layers is a composite of two multilayers of  
 1895 drift tubes: two layers of three to four layers of tubes, as shown in Figure 37.  
 1896 These aluminum tubes are 3 cm in diameter, with lengths between 0.9 and 6.2 m,  
 1897 and are filled with a mixture of ArCO<sub>2</sub> kept at 3 bar absolute pressure. A central  
 1898 tungsten-rhenium wire with a diameter of 50  $\mu\text{m}$  runs along the length of the  
 1899 tube, and is kept at a potential of 3080 V.  
 1900

1901 A muon traversing these tubes ionizes the gas, and the ionization electrons  
 1902 then drift in the electric field toward the central wire. Close to the wire, the  
 1903 electric field is strong enough to cause the original ionization electrons to ionize  
 1904 additional electrons, producing an avalanche that can be measured as a current  
 1905 along the wire. The time of arrival of that current depends on how far the muon  
 1906 entered from the wire, and can be used to achieve a position resolution of 80  $\mu\text{m}$   
 1907 in an individual tube. The combination of the measurements in the consecutive  
 1908 layers of tubes improves this position resolution to 35  $\mu\text{m}$  transverse to the tubes,  
 1909 with a resolution of 1 m along the tube direction.

1910 To achieve a good resolution over the entire length of a muon track, the rel-  
 1911 ative positions of the tubes of the muon spectrometer must be known to an ac-  
 1912 curacy of 30  $\mu\text{m}$ . This is achieved by an optical laser alignment system placed in  
 1913 each of the individual chambers and throughout the cavern. These monitor any  
 1914 changes in position or alignment due to effects like gravitational sag, tempera-  
 1915 ture shifts, and the magnetic field. The configuration of the alignment system  
 1916 within an individual chamber is also shown in Figure 36.

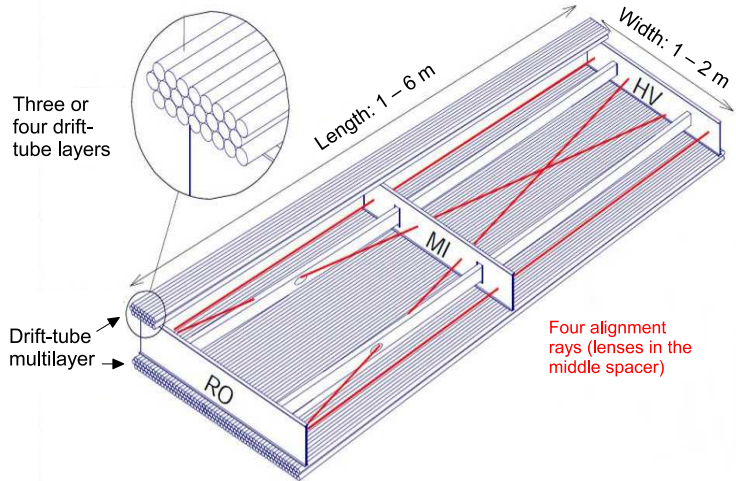


Figure 37: A schematic of a single **MDT** chamber, which shows the multilayers of drift tubes as well as the alignment system.

### 1917 5.5.2 RESISTIVE PLATE CHAMBER

1918 The **RPC** is the outermost detecting layer in the muon spectrometer in the barrel  
 1919 region, and provides a fast measurement of the  $\phi$  position of muons for triggering.  
 1920 The speed of the measurement, with a time resolution of just a few tens of  
 1921 nanoseconds, requires a poor spatial resolution of approximately 1 cm. There  
 1922 are three **RPCs** layers in the muon spectrometer, two located on either side of  
 1923 the central **MDT** layer and one located outside the final **MDT** layer, as shown in  
 1924 Figure 35. The **RPCs** consist of two layers of parallel plates filled with a gas mix-  
 1925 ture of  $C_2H_2F_4$ . A muon passing through these systems ionizes the gas, like in  
 1926 the **MDT**, which causes an avalanche of ionization electrons in the electric field  
 1927 maintained between the plates. Metal strips on the outside of the chamber ca-  
 1928 pacitively couple to the accumulated charge, and are read out to measure the  $\eta$   
 1929 and  $\phi$  positions of the muon track.

### 1930 5.5.3 CATHODE STRIP CHAMBER

1931 The majority of the momentum measurements in the endcap region are provided  
 1932 by the **MDTs**. In the most forward region of the muon spectrometer, between  
 1933  $2.0 < \eta < 2.7$ , the particle flux is very high due to contributions from low energy  
 1934 photons and neutrons. The **MDT** can only sustain a hit rate of approximately 150  
 1935 Hz/cm<sup>2</sup> because of limitations in the drift times of the gas and the capacity of  
 1936 the readout electronics. The **CSCs** were designed to handle higher hit rates, up to  
 1937 1000 Hz/cm<sup>2</sup>, and provide the necessary coverage in that high flux region.

1938 The **CSC** consists of several multiwire proportional chambers, where the wires  
 1939 are oriented in the radial direction out from the beampipe. There are eight large  
 1940 and eight small chambers, arranged to partially overlap in the  $\phi$  direction, as  
 1941 shown in Figure 38. Like in the **MDT**, a muon traversing the system produces  
 1942 ionization in the gas; here, however, the ionization is collected on a number of

wires. These wires couple to cathodes on the chambers which are segmented into strips in two directions. The relative amount of charge on each of the neighboring strips can be used to interpolate to the position of the muon in both  $\eta$  and  $\phi$ .

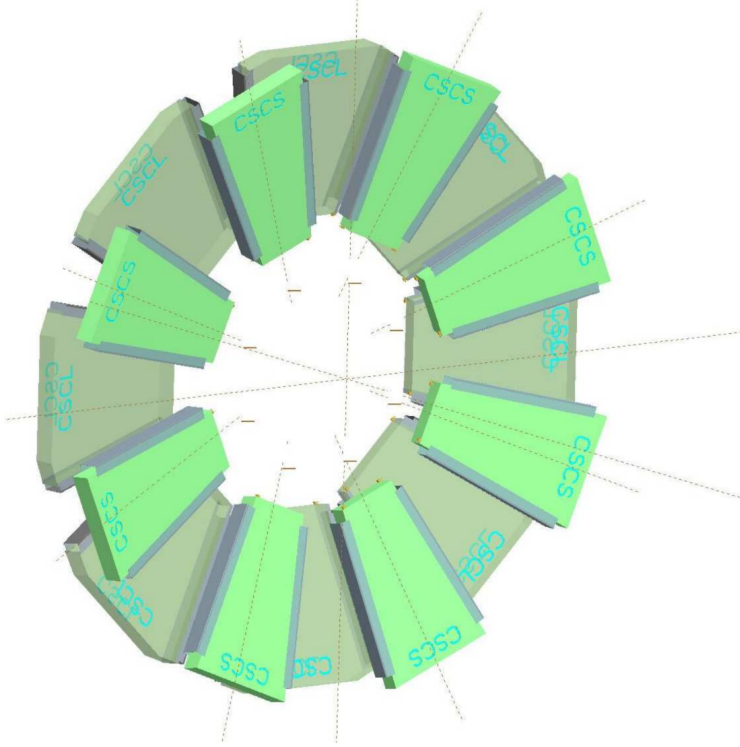


Figure 38: A schematic of the [CSC](#) endcap, showing the overlapping arrangement of the eight large and eight small chambers.

#### 5.5.4 THIN GAP CHAMBER

Like in the barrel region, a separate, fast detector is required to provide position measurements of muons for trigger in the endcap region. This is provided by the [TGC](#) which consists of seven layers in the middle station of the endcap, two doublet layers and one triplet layer, and a single doublet layer in the inner endcap station. Figure 39 shows the arrangement of the triple and doublet layers of the [TGCs](#).

Like the [CSCss](#), the [TGCs](#) are multiwire proportional chambers with a wire-to-cathode distance of 1.4 mm and a wire-to-wire distance of 1.8 mm. Readout strips on the outside of the chambers run perpendicular to the wires, and couple to the charge collected on the wires to provide a position measurement in the  $\eta$  direction. The current induced on the wires is also readout to provide a position measurement in the  $\phi$  direction. The high electric field and small wire-to-wire distance give it the required good time resolution to be used for triggering events.

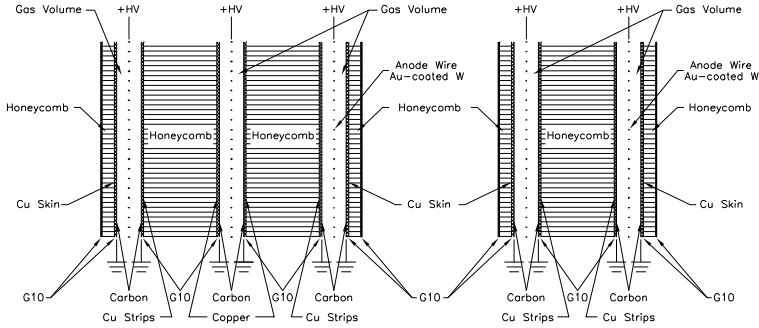


Figure 39: A schematic of the [TGC](#) doublet and triplet layers.

## 1961 5.6 TRIGGER

1962 It is not possible for the detector and the associated computing systems to record  
 1963 the terabytes of data that the 40 MHz event rate produces every second. Instead,  
 1964 a small fraction of these events are selected by the trigger system to be recorded  
 1965 and later analyzed. Selecting interesting events at such a high rate poses a sig-  
 1966 nificant challenge for the both the detector design and the implementation of a  
 1967 trigger decision and data acquisition system. The trigger must balance the time  
 1968 needed to decide to keep an event, to avoid losing information, with the filtering  
 1969 accuracy to consistently select a full menu of physics events that can be used for  
 1970 the wide array of searches and measurements targeted by ATLAS.

1971 The ATLAS trigger system, as of Run 2, consists of two levels of decision mak-  
 1972 ing. The first level, referred to as L1, is hardware based and uses inputs from  
 1973 a subset of the detector elements to narrow the considered event rate from the  
 1974 original 40 MHz down to 100 kHz. The 100 kHz rate is the maximal rate that the  
 1975 event information can be transferred from the detector. The second, software-  
 1976 based level, referred to as the [HLT](#), makes the final decisions on which events to  
 1977 keep for analysis and selects a rate of around 1 kHz. The collection of selection  
 1978 criteria used to make the L1 decisions feed into subsequent selection criteria in  
 1979 the [HLT](#), and the set of these combinations of L1 and [HLT](#) criteria from the trig-  
 1980 ger menu which defines exactly what events are recorded on ATLAS. The trigger  
 1981 menu used for 2015 data collection is shown in Table 7, which summarizes the  
 1982 selection requirements at both levels and additionally shows the peak measured  
 1983 rates contributed by each.

1984 At L1, the trigger system uses information primarily from the calorimeters  
 1985 and muon spectrometer to select high  $p_T$  jets, electrons, photons, and muons.  
 1986 The electromagnetic calorimeter uses reduced granularity energy measurements  
 1987 as well as isolation requirements to select electrons and photons. The hadronic  
 1988 calorimeter also uses a combination of reduced granularity energy measurements  
 1989 and isolation to select high momentum jets and hadronically decaying tau lep-  
 1990 tons.

1991 The calorimeters are also used to provide triggers based on missing energy:  
 1992 the coarse granularity energy measurements are used to calculate a directional  
 1993 sum of energies and to trigger on a significant imbalance. Only the [RPCs](#) and

Trigger	Typical offline selection	Trigger Selection		Level-1 Peak Rate (kHz)	HLT Peak Rate (Hz) $L = 5 \times 10^{33} \text{ cm}^{-2}\text{s}^{-1}$
		Level-1 (GeV)	HLT (GeV)		
Single leptons	Single iso $\mu$ , $p_T > 21$ GeV	15	20	7	130
	Single $e$ , $p_T > 25$ GeV	20	24	18	139
	Single $\mu$ , $p_T > 42$ GeV	20	40	5	33
	Single $\tau$ , $p_T > 90$ GeV	60	80	2	41
Two leptons	Two $\mu$ 's, each $p_T > 11$ GeV	$2 \times 10$	$2 \times 10$	0.8	19
	Two $\mu$ 's, $p_T > 19, 10$ GeV	15	18, 8	7	18
	Two loose $e$ 's, each $p_T > 15$ GeV	$2 \times 10$	$2 \times 12$	10	5
	One $e$ & one $\mu$ , $p_T > 10, 26$ GeV	$20 (\mu)$	7, 24	5	1
	One loose $e$ & one $\mu$ , $p_T > 19, 15$ GeV	15, 10	17, 14	0.4	2
	Two $\tau$ 's, $p_T > 40, 30$ GeV	20, 12	35, 25	2	22
	One $\tau$ , one $\mu$ , $p_T > 30, 15$ GeV	12, 10 (+jets)	25, 14	0.5	10
Three leptons	One $\tau$ , one $e$ , $p_T > 30, 19$ GeV	12, 15 (+jets)	25, 17	1	3.9
	Three loose $e$ 's, $p_T > 19, 11, 11$ GeV	15, $2 \times 7$	17, $2 \times 9$	3	< 0.1
	Three $\mu$ 's, each $p_T > 8$ GeV	$3 \times 6$	$3 \times 6$	< 0.1	4
	Three $\mu$ 's, $p_T > 19, 2 \times 6$ GeV	15	18, $2 \times 4$	7	2
	Two $\mu$ 's & one $e$ , $p_T > 2 \times 11, 14$ GeV	$2 \times 10 (\mu\text{'s})$	$2 \times 10, 12$	0.8	0.2
	Two loose $e$ 's & one $\mu$ , $p_T > 2 \times 11, 11$ GeV	$2 \times 8, 10$	$2 \times 12, 10$	0.3	< 0.1
	One photon	one $\gamma$ , $p_T > 125$ GeV	22	120	8
Two photons	Two loose $\gamma$ 's, $p_T > 40, 30$ GeV	$2 \times 15$	35, 25	1.5	12
	Two tight $\gamma$ 's, $p_T > 25, 25$ GeV	$2 \times 15$	$2 \times 20$	1.5	7
Single jet	Jet ( $R = 0.4$ ), $p_T > 400$ GeV	100	360	0.9	18
	Jet ( $R = 1.0$ ), $p_T > 400$ GeV	100	360	0.9	23
$E_T^{\text{miss}}$	$E_T^{\text{miss}} > 180$ GeV	50	70	0.7	55
Multi-jets	Four jets, each $p_T > 95$ GeV	$3 \times 40$	$4 \times 85$	0.3	20
	Five jets, each $p_T > 70$ GeV	$4 \times 20$	$5 \times 60$	0.4	15
	Six jets, each $p_T > 55$ GeV	$4 \times 15$	$6 \times 45$	1.0	12
$b$ -jets	One loose $b$ , $p_T > 235$ GeV	100	225	0.9	35
	Two medium $b$ 's, $p_T > 160, 60$ GeV	100	150, 50	0.9	9
	One $b$ & three jets, each $p_T > 75$ GeV	$3 \times 25$	$4 \times 65$	0.9	11
	Two $b$ & two jets, each $p_T > 45$ GeV	$3 \times 25$	$4 \times 35$	0.9	9
$b$ -physics	Two $\mu$ 's, $p_T > 6, 4$ GeV plus dedicated $b$ -physics selections	6, 4	6, 4	8	52
Total				70	1400

Table 7: The trigger menu for the 2015 data collection with  $L = 5 \times 10^{33} \text{ cm}^{-2}\text{s}^{-1}$ . Both the L1 and HLT selection requirements and their trigger rates are shown measured at the specified luminosity are shown. The typical offline selections represent a typical set of offline requirements imposed after the trigger in an analysis.

1994    **TGCs** muon subdetectors contribute to the decision at L1, and are used to identify  
 1995    high momentum muons. The contributions to the triggering rate of the various  
 1996    types of L1 triggers are shown in Figure 40. The total rate is indicated in black  
 1997    and is lower than the sum of individual rates because their is significant overlap  
 1998    between different trigger channels. The majority of the rate comes from lepton  
 1999    and photon triggers.

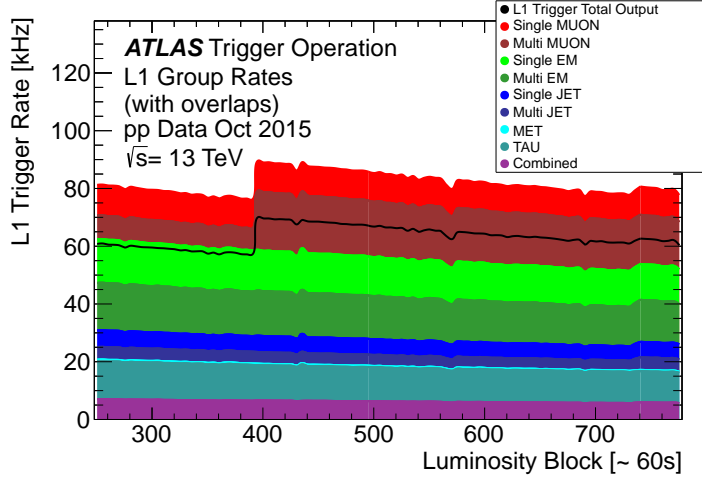


Figure 40: The L1 Trigger rate broken down into the types of triggers as a function of the luminosity block for the 2015 data collection period.

2000    After an event is chosen by the L1 trigger, the detector measurements from the  
 2001    bunch crossing which fired the trigger is read out from the front-end electronics  
 2002    and stored on read-out boards. This inclusive information is necessary to make  
 2003    more the more precise event selections than is possible with the reduced infor-  
 2004    mation at L1. The **HLT** then uses this information with software algorithms to  
 2005    decide whether or not to permanently record the event. The L1 trigger also for-  
 2006    wards which decision was made and Region of Interests (**Rois**) to the **HLT**, which  
 2007    allows the **HLT** to focus on particular algorithms and particular sections of the  
 2008    detector to greatly improve the algorithmic selection speed. The additional in-  
 2009    formation available to the **HLT** allows it to implement additional trigger targets,  
 2010    such as identified jets from the decays of b-hadrons. The contributions to the  
 2011    triggering rate of the various types of **HLT** triggers are shown in Figure 41.

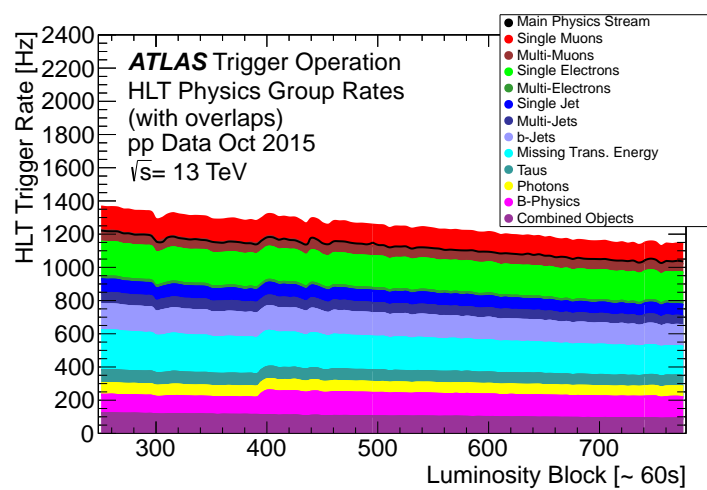


Figure 41: The HLT Trigger rate broken down into the types of triggers as a function of the luminosity block for the 2015 data collection period.

2012

2013 EVENT RECONSTRUCTION

---

2014 The ATLAS experiment combines measurements in the subdetectors to form a  
 2015 cohesive picture of each physics event. The majority of particles that traverse  
 2016 the detector leave behind some combination of ionization hits in the tracking  
 2017 detectors or energy deposits in the calorimeters, and these measurements can  
 2018 be used to reconstruct physical quantities like the particle's energy, momentum,  
 2019 or trajectory. Even the type of the particle can be distinguished by comparing  
 2020 the various ways that different species of stable particles interact with the sub-  
 2021 detectors. Reconstruction is the series of algorithms which take the electronic  
 2022 outputs of the detector and assigns them into individual physics objects. The  
 2023 physics objects summarize the properties of particles produced by the collision  
 2024 or subsequent decays, either for individual isolated particles like leptons, or for  
 2025 a collection of the cascade of products produced in the decay of an energetic  
 2026 hadron, called a jet. These are the objects and quantities most often used in anal-  
 2027 ysis to make measurements of [SM](#) processes or to search for new physics.

## 2028 6.1 CHARGED PARTICLES

2029 As described in Section 5.3, charged particles that traverse the inner detector  
 2030 leave behind hits in the subdetectors. Each of these hits translates into a position  
 2031 measurement along the trajectory of that particle, with position resolutions de-  
 2032 pending on the subdetector that provided the measurement. Track reconstruc-  
 2033 tion uses these position measurements to collect hits in consecutive layers of  
 2034 the detector into a trajectory consistent with a particle curving in a magnetic  
 2035 field [19, 20]. This reconstructed trajectory is called a track. The number of hits  
 2036 in the inner detector for each event makes a combinatorial method completely  
 2037 infeasible: the algorithms that form tracks must be significantly more intelligent  
 2038 so that event reconstruction does not exhaust computing resources.

2039 The first and primary algorithm employed in track reconstruction is called  
 2040 the inside-out method, which begins with the assumption that the track orig-  
 2041 inated from the interaction point. Its purpose is to identify primary particles,  
 2042 those which originate in the proton-proton collisions and with a lifetime long  
 2043 enough to reach the inner detector. Combinations of three hits are considered  
 2044 from measurements in the Pixel detector and the [SCT](#), and form the seed for a  
 2045 track. Specifically, the seeding algorithm looks for a seed using three pixel hits,  
 2046 two pixel hits and one [SCT](#) hit, or three [SCT](#) hits. The seed is then extrapolated  
 2047 forwards and backwards into the Pixel and [SCT](#) detectors depending on the seed  
 2048 location, and hits in each layer are considered to be added to the track using a  
 2049 combinatorial Kalman filter [20]. After all of the silicon layers have been consid-  
 2050 ered, tracks are filtered to reduce ambiguities from other nearby tracks or from  
 2051 combinatorial coincidences. Then the tracks are extended outwards into the [TRT](#)

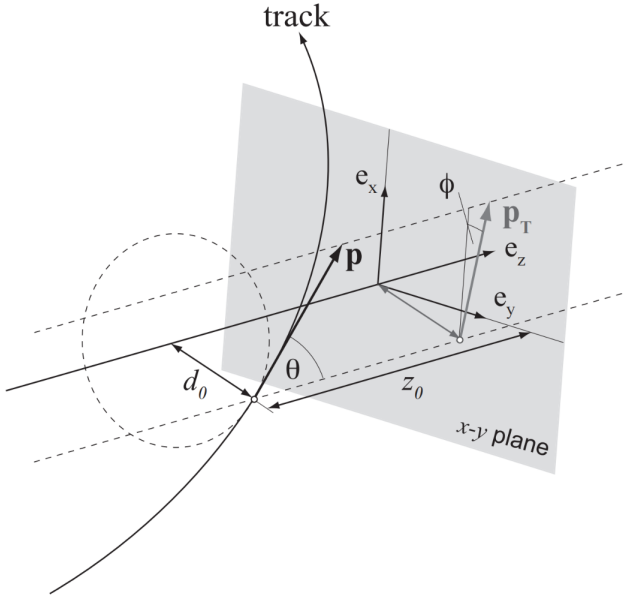


Figure 42: An illustration of the perigee representation of track parameters for an example track. The charge is not directly shown, but is indicated by the direction of curvature of the track [21].

in the same way. This algorithm is how the hits are chosen to be incorporated into a single track. Once the hits are collected, a fitting algorithm calculates the track parameters which best model the locations of the hits and their resolutions. The fitting uses five parameters,  $(d_0, z_0, \phi, \theta, q/p)$ , to specify a track in a perigee representation:  $d_0$  and  $z_0$  are the transverse and longitudinal impact parameters at the closest approach to the nominal beam axis,  $\phi$  and  $\theta$  are the usual angular coordinates, and  $q/p$  is the charge divided by the momentum. These parameters are illustrated in Figure 42. Those parameters directly determine the direction and momentum of the particle which produced the track.

This inside-out algorithm is complemented by an outside-in algorithm, which is used to find tracks from secondary particles, those produced in the decays or interactions of the primary particles inside the detector. As the name indicates, the outside-in algorithm begins by seeding tracks in the outermost layers of the inner detector, in the TRT. The seed in this case is formed by a segment in the TRT, and the track is propagated backwards into the SCT before being refitted to use all the included points. Some tracks are found with TRT segments only, which can result from interactions with the detector following the SCT. Figure 43 shows an example of the geometry of tracks formed by both algorithms, where the hits belonging to tracks found using the inside-out algorithm are highlighted in red, and the hits belonging to the tracks found using the outside-in algorithm are circled in black. The figure highlights the presence of a large number of both primary and secondary tracks in a single event, as well as the overall large number of hits present in the inner detector.

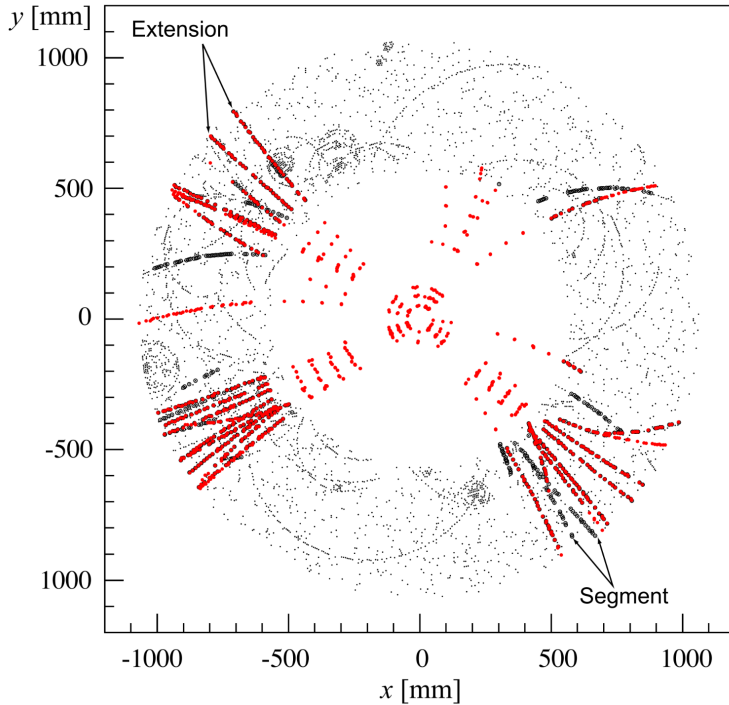


Figure 43: The  $x$  and  $y$  locations of the hits generated in a simulated  $t\bar{t}$  event in the inner detector. The hits which belong to tracks formed using the inside-out algorithm are highlighted in red, while the hits which belong to tracks formed using the outside-in algorithm are circled in black.

2075 The tracks resulting from these algorithms can be contaminated by nearby  
 2076 particles confusing the tracking algorithm in a high luminosity environment.  
 2077 For example, enough hits present in the inner detector can lead to fake tracks  
 2078 from combinations of hits from multiple individual tracks. Therefore, after the  
 2079 tracks are formed and fitted, additional quality requirements are imposed in  
 2080 order to reduce such backgrounds. Most tracking applications require at least  
 2081 seven silicon hits, that is, seven hits between the Pixel detector and **SCT**. Then the  
 2082 tracks are required to have at most two holes in the Pixel detector, where holes  
 2083 are non-existing but expected measurements in a layer of the subdetector. If the  
 2084 missing hit corresponds to an inactive module, however, it is not counted as a  
 2085 hole but instead as a hit for tracking as the lack of a measurement is expected in  
 2086 that case.

2087 6.1.1 PIXEL NEURAL NETWORK

2088 The hits in the Pixel detector are not typically confined to a single pixel, but  
 2089 rather the charge is spread over several pixels per layer which are grouped to-  
 2090 gether into clusters. The clustering of these pixels for isolated tracks is relatively  
 2091 straightforward, but complications can arise in the high occupancy environment  
 2092 where hits from multiple particles can overlap in a single cluster. Figure 44  
 2093 shows examples of clusters generated by a single isolated particle, two nearly  
 2094 overlapping particles, and a particle which emits a  $\delta$ -ray. A  $\delta$ -ray is a secondary

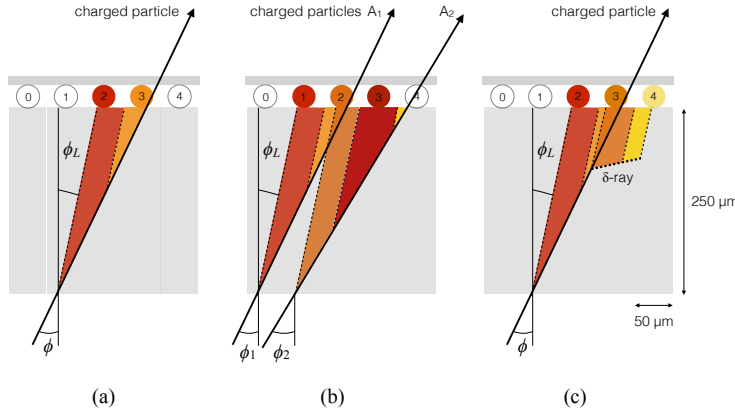


Figure 44: Examples of the clusters formed in a single layer of the pixel detector for (a) a single isolated particle, (b) two nearly-overlapping particles, and (c) a particle which emits a  $\delta$ -ray [22].

2095 electron which is generated with enough energy to escape a significant distance  
2096 away from the original particle and to generate additional ionization.

2097 A series of neural-networks analyzes the shape of the clusters to determine  
2098 how many particles produced the cluster and to estimate the positions of each  
2099 of the particles within the cluster. These allow for an identification of clusters  
2100 caused by more than one particle or by a particle that emits a  $\delta$ -ray. In a high-  
2101 density tracking environment, the multiple position outputs can be used as the  
2102 locations of individual hits to allow reconstruction of tracks which almost over-  
2103 lap and with a much better separation than is possible without the splitting of  
2104 individual clusters.

### 2105 6.1.2 PIXEL DE/DX

2106 A hit in the Pixel detector corresponds to the voltage generated from ionization  
2107 current rising above a threshold value that is tuned to consistently record the  
2108 passing of MIPs. A larger amount of charge deposited results in a larger voltage,  
2109 and a larger signal remains above the threshold for a longer period of time. The  
2110 time over threshold (ToT) is read out of the Pixel detector, and can be used to  
2111 provide a measurement of the charge deposited in each pixel. The charge mea-  
2112 surements from each of the pixels included in a pixel cluster are summed to form  
2113 one charge measurement per layer of the pixel detector. That charge measure-  
2114 ment, combined with the angle of incidence of the track and the known sizes of  
2115 each detector element, can be converted into a measurement of  $dE/dx$ , the ion-  
2116 ization energy deposited per unit distance, measured in  $\text{MeVg}^{-1}\text{cm}^2$ . The IBL  
2117 only has sixteen available values (4 bits) of ToT to readout, compared to the 256  
2118 available values (8 bits) in the remaining pixel layers. To help alleviate this lack  
2119 of range, the IBL also records if it is in overflow: when the ionization is sufficient  
2120 to generate a ToT above the largest value that can be recorded in the 4 bits.

2121 The measurements across multiple layers are combined to form an average  
 2122 value of  $dE/dx$  for the track as a whole. Depending on where a charge particle  
 2123 is produced, it will traverse four Pixel layers and create four clusters on average.  
 2124 It can produce as few as two clusters in the Pixel detector if it passes through in-  
 2125 active modules, and as many as five if it is in a region of the detector where multiple  
 2126 modules overlap. To reduce the influence of the typical long Landau tails of the  
 2127 distribution of  $dE/dx$  deposits [6], the average is calculated as a truncated mean  
 2128 of these clusters. The value measured in the IBL is removed if it is in overflow, as  
 2129 the measured value is not reliable in that case. If a track has five measurements  
 2130 in the pixel detector, the two highest cluster values are removed. If a track has  
 2131 two, three, or four measurements in the pixel detector, only the single highest  
 2132 cluster value is removed. The remaining values are averaged to form the pixel  
 2133  $dE/dx$ .

### 2134 6.1.3 VERTEX RECONSTRUCTION

2135 A vertex represents the intersection of multiple tracks and corresponds to the  
 2136 location of an interaction. If at least two charged particles result from the in-  
 2137 teraction, the intersection of their resulting tracks reveals its position with high  
 2138 precision. Vertices are divided into two groups, primary vertices which corre-  
 2139 spond to the actual proton-proton collisions, and secondary vertices which cor-  
 2140 respond to decays of short-lived particles or interactions with the detector. Pri-  
 2141 mary vertices are particularly important, as they can provide a precise location  
 2142 for the interaction which generated the observed particles. Understanding that  
 2143 location is crucial in understanding the geometry of the event.

2144 Primary vertices are reconstructed by iteratively identifying seeds from recon-  
 2145 structed tracks [23]. Each track's extrapolated  $z$  position at the beamline forms a  
 2146 seed, and nearby tracks are fitted using that position as a point along their trajec-  
 2147 tory. The goodness of fit with that vertex is considered for each track, measured  
 2148 in  $\chi^2$ . The final position of the vertex is determined by a fit to all of the con-  
 2149 sidered tracks, where the contribution from each track is weighted according to  
 2150 the  $\chi^2$  compatibility with that vertex. Any tracks from this procedure that are  
 2151 displaced by more than  $7\sigma$  from that vertex are removed from the fit and used  
 2152 to seed a new vertex. This procedure is iterated until no additional vertices can  
 2153 be found.

2154 This procedure is typically performed twice. The first set of vertices is used  
 2155 to fit a profile for the beamspot, which indicates the position of the intersec-  
 2156 tion of beams in that particular bunch crossing. The fitted beamspot then provides  
 2157 a constraint for the second attempt to locate primary vertices, where both the  
 2158 track fitting and seeding of vertices are required to be consistent with interac-  
 2159 tions occurring within the beamspot.

## 2160 6.2 ELECTRONS AND PHOTONS

2161 Electrons are measured as both a charged particle track and energy deposits in  
 2162 the electromagnetic calorimeter. Photons, on the other hand, leave energy de-

2163 posits in the electromagnetic calorimeter but do not produce a corresponding  
 2164 track. Because the electromagnetic interactions with the calorimeter of both  
 2165 photons and electrons produces more photons and electrons, the behavior in the  
 2166 calorimeter is very similar and there is significant overlap in the reconstruction  
 2167 techniques for each.

2168 The reconstruction of a photon or an electron in the calorimeter is based on  
 2169 clustering algorithms which identify groups of energy deposits [24–26]. For this  
 2170 purpose, the entire electromagnetic calorimeter is subdivided into a grid of 200  
 2171 by 256 towers in the  $\eta$  and  $\phi$  directions, respectively, where the individual grid  
 2172 units have a size of  $\Delta\eta = 0.025$  and  $\Delta\phi = 0.025$ . These towers correspond to  
 2173 individual cells in the middle, coarsest layer of the EM calorimeter, and in the re-  
 2174 maining layers the cells are grouped together cover the same area in  $\eta - \phi$  space.  
 2175 The clustering begins by finding seeds with a sliding-window algorithm based  
 2176 on the towers: a window of 3 by 5 towers is formed and translated until the sum  
 2177 of the energy within the window is maximized. If that energy is above 2.5 GeV,  
 2178 then that region becomes a seed. The choice of 2.5 GeV was chosen to com-  
 2179 promise between maximizing reconstruction efficiency while minimizing fake  
 2180 electron seeds from electronic noise or soft hadrons from additional interactions.  
 2181 The seeds are rejected if the energy measured in the hadronic calorimeter behind  
 2182 the seed is large, as this typically indicates a hadron rather than an electron or  
 2183 photon.

2184 Next, the inner detector tracks within a cone of  $\Delta R = 0.3$  are compared to  
 2185 the location and energy of the seed. Tracks are matched to the cluster if the ex-  
 2186 trapolation of the track to the energy-weighted center in the middle layer of the  
 2187 EM calorimeter falls within  $\Delta\phi < 0.2$  in the direction of the curvature of the  
 2188 track or  $\Delta\phi < 0.05$  in the direction opposite of the curvature of the track. If the  
 2189 seed matches with a track that originated from a primary vertex, the combina-  
 2190 tion of track and electromagnetic cluster is reconstructed as an electron. If the  
 2191 seed matches with a track that did not originate from a primary vertex, then the  
 2192 electromagnetic cluster is reconstructed as a converted photon. And if there is  
 2193 no corresponding track in the inner detector, then the cluster is reconstructed  
 2194 as a photon.

2195 After classification, the final clustering of the energy in the EM calorimeter  
 2196 calorimeter is performed. The classification must be done first, as the expected  
 2197 size of the energy deposits in the calorimeter are different for electrons and pho-  
 2198 tons. In the barrel region, the final clusters for electrons are formed in rectangles  
 2199 of 3 towers in the  $\eta$ -direction and 7 towers in the  $\phi$ -direction. This asymmetric  
 2200 window accounts for the curving of the produced charged particles only in the  
 2201  $\phi$  direction. For photons, the size of the rectangle is 3 towers by 5 towers. In the  
 2202 endcap region, all object types are clustered in rectangles of 5 towers by 5 tow-  
 2203 ers, as the effect of the magnetic field curvature is less pronounced in this region.  
 2204 The sum of the energies in these clusters provide the final energy measurement  
 2205 for the electron or photon.

## 2206 6.2.1 PHOTON IDENTIFICATION

2207 The original requirement for constructing a photon cluster, a significant energy  
 2208 deposit in the electromagnetic calorimeter without a corresponding track or en-  
 2209 ergy deposits in the hadronic calorimeter, is already effective in identifying pho-  
 2210 tons. However, there is a significant background for prompt photon production  
 2211 from the decays of pions,  $\pi^0 \rightarrow \gamma\gamma$ . These can be identified using the shape of  
 2212 the cluster in the narrow  $\eta$  granularity in the first layer of the EM calorimeter.

## 2213 6.2.2 ELECTRON IDENTIFICATION

2214 Prompt electrons have a number of backgrounds, such as secondary electrons  
 2215 from hadron decays or misidentified hadronic jets, that can be rejected using ad-  
 2216 dditional information from the EM calorimeter and the inner detector. The most  
 2217 basic level of electron identification, referred to as Loose, makes requirements  
 2218 on the shower shapes in the high granularity first layer of the EM calorimeter  
 2219 as well as the quality of the inner detector track. It also requires a good match  
 2220 between the track and the calorimeter energy deposits and a small fraction of  
 2221 energy in the hadronic calorimeter behind the electromagnetic cluster. ATLAS  
 2222 defines several additional working points, including Medium and Tight, which  
 2223 provide progressively lower background rates for electrons by imposing addi-  
 2224 tionally strict requirements on the above variables as well as new requirements  
 2225 like the impact parameter of the inner detector track or the comparison of the  
 2226 cluster energy to the momentum in the inner detector.

## 2227 6.3 MUONS

2228 Muons produced in ATLAS first traverse the inner detector and leave behind a  
 2229 track as described in Section 6.1. The muon then passes through the calorimeter,  
 2230 leaving behind a small, characteristic amount of energy, and then passes through  
 2231 the muon spectrometer where it produces hits in the MDTs or CSCs. Muon tracks  
 2232 are formed from local segments of hits in each layer of the MDTs or CSCs, and  
 2233 then the final muon spectrometer track is formed by combining the two local  
 2234 segments [27]. When a track is reconstructed in both the inner detector and  
 2235 the muon spectrometer, the track is refitted to include the hits in both the inner  
 2236 detector and the muon spectrometer, and forms a combined muon.

2237 In a few regions of the detector, a muon may fail to leave behind both a com-  
 2238 plete inner detector and muon system track. For a very small fraction of the  
 2239 acceptance of the muon system, there is only one layer of muon chambers and a  
 2240 global muon system track is not formed. In this case, as long as the track in the  
 2241 inner detector exists and geometrically matches to a segment, a segment-tagged  
 2242 muon is formed using momentum measurements from the inner detector. In  
 2243 the region where the muon system has coverage but the inner detector does not,  
 2244  $2.5 < |\eta| < 2.7$ , a stand-alone muon is formed which uses only information  
 2245 from the muon system. And for muons produced within one of the few holes in  
 2246 the muon system, including  $|\eta| < 0.1$ , the characteristic energy deposits in the

2247 calorimeter can be used to tag an inner detector track as a calo-tag muon. These  
 2248 additional categories are used to achieve high efficiency over a larger range of  
 2249 acceptance, but the combined muons are the most reliable.

### 2250 6.3.1 MUON IDENTIFICATION

2251 The various types of muons are incorporated into three working points: Loose,  
 2252 Medium, and Tight, which reflect the increasing muon purity for each of the  
 2253 selections definitions. Tight muons include only combined muons with a good  
 2254 track fit quality and momentum resolution and at least two hits in a precision  
 2255 muon system layer. Medium muons include those in tight as well as combined  
 2256 muons with one precision hit and one precision hole, where hole is defined in  
 2257 the same way as in Section 6.1. The medium working point also includes stand-  
 2258 alone muons with  $|\eta| > 2.5$  and at least two hits in precision layers. And finally  
 2259 the loose working point includes both medium and tight muons, but additional  
 2260 includes segment-tagged and calo-tagged muons in the region  $|\eta| < 0.1$ .

## 2261 6.4 JETS

2262 A jet does not directly correspond to a physical particle, unlike all of the recon-  
 2263 structed objects described above, but instead tries to capture the conical cascade  
 2264 of particles produced in the hadronization of a quark or gluon from the proton-  
 2265 proton collision. The hadronization process creates a very large number of col-  
 2266 limated particles, with a high enough density that individually reconstructing all  
 2267 of the produced particles in the calorimeter is not possible within ATLAS. How-  
 2268 ever most analyses are interested only in the kinematics of the particle which  
 2269 produced the cascade, rather than the individual products. Therefore, jets are  
 2270 a useful tool to measure the combined energy and direction of the ensemble of  
 2271 products and thus represents the kinematics of the original. Jet algorithms are  
 2272 very generic and can be used to group together a number of types of objects to  
 2273 form aggregate representations. For example, truth particles in simulation can  
 2274 be grouped in truth jets, or tracks from the inner detector can be grouped to-  
 2275 gether to form track jets. This section, however, will focus on calorimeter jets  
 2276 which take topoclusters of energy deposits in the calorimeter as inputs and pro-  
 2277 duce a combined object which represents the energy measured by the calorime-  
 2278 ter and the location where it was deposited.

### 2279 6.4.1 TOPOLOGICAL CLUSTERING

2280 Hadrons often deposit their energy into multiple individual cells in both the elec-  
 2281 tromagnetic and hadronic calorimeters. The purpose of topological clustering is  
 2282 to group cells in all three dimensions into clusters that represent a single energy  
 2283 deposit. The procedure must be robust enough to reject noise fluctuations in  
 2284 the cell energy measurements that can come from both electronic noise and ad-  
 2285 dditional low energy particles produced in pileup activity. The background level

2286 of calorimeter noise is called  $\sigma_{\text{noise}}$ , and is an important component of the topo-  
 2287 logical clustering.

2288 The topological clusters are formed in a three step process called the 4-2-0  
 2289 threshold scheme, which uses three energy thresholds to build up a cluster from  
 2290 cells [28]. First, any cells with a measured energy above  $4\sigma_{\text{noise}}$  are identified  
 2291 as seed cells. The cells adjacent to the seed cells with a measured energy above  
 2292  $2\sigma_{\text{noise}}$  are called secondary cells. All of the cells which are adjacent to a sec-  
 2293 ondary cell with  $E_{\text{cell}} > 2\sigma_{\text{noise}}$  are also labeled secondary cells. Tertiary cells  
 2294 are those immediately adjacent to a seed or secondary cell with a measured en-  
 2295 ergy above zero. Adjacency in this sense is defined in three dimensions, cells are  
 2296 adjacent if they are neighbors within a layer but also if they have the same  $\eta - \phi$   
 2297 coordinates but are in adjacent layers or even in an adjacent layer in another  
 2298 calorimeter.

2299 From these definitions, clusters are built by resolving the seeds in order of  
 2300 significance, the ratio  $E_{\text{cell}}/\sigma_{\text{noise}}$ . All adjacent secondary cells to the highest  
 2301 significance seed are added to that seed's topocluster, and any of those cells which  
 2302 would also have qualified as seeds are removed from the list of seeds. Once all  
 2303 of the secondary cells have been added, the tertiary cells are then added to that  
 2304 cluster as well. This procedure is then iterated until no seeds remain, forming  
 2305 the first round of topoclusters.

2306 It is also useful to split topoclusters into multiples if local maxima are present  
 2307 within the topocluster, as clusters produced by multiple nearby particles can  
 2308 merge. The splitting process begins by finding local maxima cells in the middle  
 2309 layer of the calorimeters with a minimum energy of 500 MeV and at least four  
 2310 neighboring secondary cells. These requirements reduce the likelihood to split  
 2311 a cluster due to random fluctuations, as the middle layers provide the most reli-  
 2312 able energy measurements. Cells between two local maxima can then be shared  
 2313 between two clusters to account for overlapping contributions from two parti-  
 2314 cles. The energy sharing is weighted by the energy of each cluster as well as the  
 2315 distance of the cell to the centroid of that cluster.

2316 The energies of all the cells in the cluster are then summed together to form  
 2317 the energy of that cluster. The energy needs to be corrected for the various losses  
 2318 expected in the calorimeter, as described in Section 5.4. The simplest correction,  
 2319 scaling the measured energy by the sampling fraction, brings the cluster energies  
 2320 to the EM scale. It is called the EM scale because it accurately describes the energy  
 2321 of electromagnetic showers.

2322 Another scale is defined to improve accuracy for hadronic processes, the local  
 2323 cluster weighted (LCW) scale, that helps to correct for the expected variations in  
 2324 hadronic energy deposits. The LCW correction first determines if the shower is  
 2325 hadronic or electromagnetic, based on the depth of the shower and the cluster  
 2326 energy density. For hadronic showers, the energy is corrected for calorimeter  
 2327 non-compensation, an effect which reduces the measured energy of hadronic  
 2328 showers because some of the energy goes into invisible processes like the break  
 2329 up of nuclei. All clusters are then corrected for energy that may be deposited in  
 2330 uninstrumented regions in that cluster's location in the calorimeter, and they are

2331 also corrected with an estimate of how much energy falls outside the extent of  
 2332 the cluster based on its shape and the deposit type.

2333 6.4.2 JET ALGORITHMS

2334 Using the topological clusters as inputs, a jet algorithm groups them together  
 2335 into a collection of adjacent energy deposits that is intended to correspond to  
 2336 a single process [29]. Jet algorithms need a few key characteristics to be usable  
 2337 for physics analysis. First, the jets produced by the algorithm should have little  
 2338 dependence on the addition of soft particles to the event (infrared safety), as a  
 2339 negligible addition of energy should not significantly modify the event topology.  
 2340 Similarly, the jets produced by the algorithm should also not significantly depend  
 2341 on mostly collinear splitting of an input particle (collinear safety); that is, a single  
 2342 quark replaced by two, parallel quarks with half the original's momentum should  
 2343 not change the resulting jets, which are intended to capture only the properties  
 2344 of the aggregate and not those of individual particles. And finally the algorithm  
 2345 needs to be sufficiently simple and fast to be used for the large rate of collected  
 2346 proton-proton collisions on ATLAS.

2347 The most commonly used algorithm on ATLAS that satisfies these require-  
 2348 ments is called the anti- $k_t$  algorithm, and is discussed in further detail in Refer-  
 2349 ence [30]. The anti- $k_t$ , in brief, relies on iteratively combining the input objects  
 2350 that are closest together, where closest is defined by a particular distance metric,  
 2351  $d_{i,j}$ , where the index  $i$  represents the combination constructed so far and  $j$  is an  
 2352 additional object being considered. The combinations stop when the closest re-  
 2353 maining object is the beam itself, where the distance to the beam is called  $d_{i,B}$ .  
 2354 An entire class of algorithms follows this procedure with the following distance  
 2355 metrics

$$d_{i,j} = \min(k_{ti}^{2p}, k_{tj}^{2p}) \frac{\Delta_{ij}^2}{R^2} \quad (18)$$

$$d_{i,B} = k_{ti}^{2p} \quad (19)$$

2356 where  $\Delta_{ij} = (y_i - y_j)^2 + (\phi_i - \phi_j)^2$ ,  $k_{ti}$  is the transverse momentum of the  
 2357 object,  $y$  is the rapidity, and  $p$  is a parameter of the algorithm. Anti- $k_t$  is the  
 2358 particular case where  $p = -1$ , and is a choice that results in an algorithm that is  
 2359 both infrared and collinear safe.

2360 The algorithm is repeated until there are no input objects remaining, which  
 2361 results in a series of jets. Each jet has a complete four momentum from the com-  
 2362 bination of its input clusters, where the combinations assume a mass of zero.  
 2363 The jet energies then need to be calibrated to attempt to match the energy of the  
 2364 object which produced the jet.

2365 6.4.3 JET ENERGY SCALE

2366 Though the LCW scheme attempts to correct the topoclusters to reflect the true  
 2367 deposited energy, the correction does not fully account for energy lost within

2368 the calorimeters. Because of these effects, the original reconstructed jet energy  
 2369 does not reflect the true energy of the particle which initiated the jet. Therefore  
 2370 it is necessary to additionally correct the reconstructed jet itself, in addition to  
 2371 the corrections on the inputs. This correction is referred to as the **JES**, which  
 2372 combines several individual steps of calibration [31].

2373 The first calibration step corrections the direction of the jet to ensure that it  
 2374 points back to the primary vertex. Next, the energy of the jet is corrected for  
 2375 pileup by subtracting the expected contribution from pileup based on the mo-  
 2376 mentum,  $\eta$ , and area of the jet as well as the number of reconstructed vertices  
 2377 and expected number of interactions per crossing. The largest single correction  
 2378 is the absolute  $\eta$  and scale correction, where the jet energy and pseudorapidity  
 2379 is corrected to attempt to match the energy and pseudorapidity of the parton  
 2380 which produced it. This correction is measured in simulation by comparing the  
 2381 reconstructed jet energies to the energy of the truth particle which produced it.  
 2382 However the simulation is not relied on alone to estimate this correction, and an  
 2383 additional step applies an additional energy correction based on in-situ measure-  
 2384 ments in data. These corrections come from various techniques which measure  
 2385 jet energies indirectly by balancing them with other, well-measured objects. In  
 2386 the central region ( $|\eta| < 1.2$ ), jets are balanced against photons and the leptonic  
 2387 decays of Z bosons and high momentum jets ( $p_T > 210$  GeV) are also balanced  
 2388 against multiple smaller jets in multijet events. Jets at larger pseudorapidities,  
 2389 above  $|\eta| = 1.2$ , are calibrated by balancing with lower pseudorapidity jets.

2390 These steps introduce a number of systematic uncertainties, referred to as  
 2391 the **JES** uncertainty. The largest of these comes from the in-situ measurements,  
 2392 which are statistically limited in measuring high momentum and high pseudora-  
 2393 pidity jets. The total, fractional **JES** uncertainty is shown as a function of  $p_T$  in  
 2394 Figure 45. The uncertainty falls to a minimum value of just over 1.0% around a  
 2395 few hundred GeV, and rises again at high momentum because of the difficulty of  
 2396 measuring jet balance in data above 2-3 TeV. The uncertainty is also minimized  
 2397 at low  $|\eta|$ , and grows at large  $|\eta|$  again where making in-situ measurements is  
 2398 difficult. This technique does not actually provide a measurement of the uncer-  
 2399 tainty for the highest energy jets, above 3 TeV, because there are not enough  
 2400 measured data events to provide them. An alternative method for deriving the  
 2401 **JES** and **JES** uncertainty that can be used even for very high  $p_T$  jets will be dis-  
 2402 cussed in Chapter 8.

## 2403 6.5 MISSING TRANSVERSE ENERGY

2404 Among stable **SM** particles, only the neutrino cannot be directly measured in the  
 2405 ATLAS detector. Because the neutrino carries neither electric nor color charge,  
 2406 it is very unlikely to interact with the tracking detectors or the calorimeters,  
 2407 and instead passes through the detector completely unobserved. Some particles  
 2408 which have been conjectured to exist, like the **LSP** in many **SUSY** models, would  
 2409 also have the same behavior. Therefore, it is important for ATLAS to provide  
 2410 some way to assess the momentum carried away by a neutral, colorless parti-  
 2411 cle. This can be accomplished through a measurement of missing energy in the

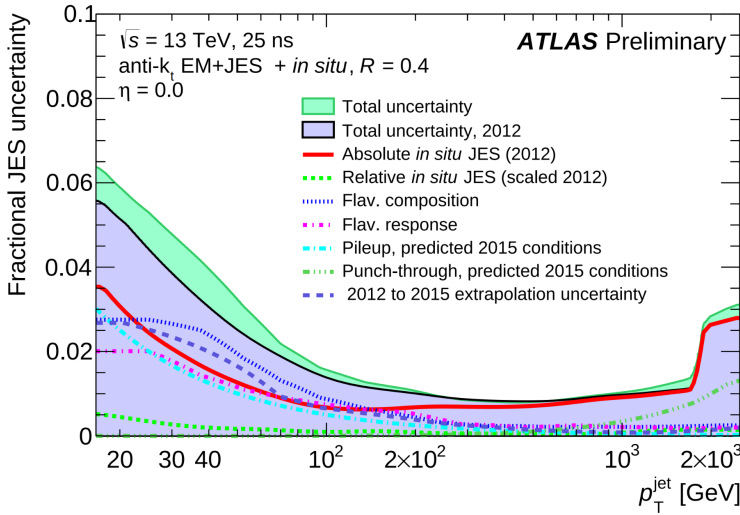


Figure 45: The total, fractional JES uncertainties estimated for 2015 data as a function of jet  $p_T$ .

transverse direction, or  $E_T^{\text{miss}}$ , which quantifies the momentum imbalance of the observed particles. From the conservation of momentum and the lack of the initial momentum in the transverse plane in the proton-proton collisions, any imbalance of momentum can be inferred to be carried away by an unmeasured particle.

$E_T^{\text{miss}}$  is more precisely defined as the magnitude of the vector sum of the  $(p_x, p_y)$  components of each observed object's momentum. The definition is simple, but there can be significant complexity in defining the inputs. As of Run 2, ATLAS uses a common algorithmic approach to carefully calculate missing energy, but each analysis is free to define its own inputs. For the analysis discussed throughout this thesis, the missing energy inputs consist of the electrons, photons, muons, and jets discussed in the previous sections, in addition to a track-based soft term.

To produce the most precise measurement of  $E_T^{\text{miss}}$ , it is important to use the best representation of the momentum of each of the input objects, which can often be reconstructed as multiple different types in a single event. For example, an electron can be reconstructed separately as an electron (Section 6.2) and a jet (Section 6.4), but the electron representation has the highest precision for reconstructing the true electron momentum. To ensure no duplications in the  $E_T^{\text{miss}}$  definition, the inputs are collectively considered for overlap removal. Only the most precise object type is kept for objects that fall within a cone of  $\Delta R < 0.2$  for pairs of electrons and jets and a cone of  $\Delta R < 0.4$  for other pair types.

The fully reconstructed objects do not include all of the energy within the events, as some clusters do not enter into a jet and some tracks are not classified as electrons or muons. These momentum carried by these objects is accounted for in a soft-term, which tallies all of the energy carried by the particles too soft to form separate objects. The track soft term uses only tracking information to estimate the contribution of soft objects, and does so by vectorially summing the momentum of all well-reconstructed tracks with momentum above 400 MeV.

2441 All of these contributions together give a single  $E_T^{\text{miss}}$  value for a given event.  
2442 The direction of that missing energy is taken as opposite the vector sum of all the  
2443 constituents, to correspond to the momentum an invisible particle would have to  
2444 have to make the event balanced. Depending on the context, this missing energy  
2445 can be considered the energy of a neutrino or an LSP, with a large missing energy  
2446 being a common signal criteria for searches for new physics.

2447

### PART III

2448

## CALORIMETER RESPONSE

2449

You can put some informational part preamble text here.

2450

2451 RESPONSE MEASUREMENT WITH SINGLE HADRONS

---

2452 As discussed in Section 6.4, colored particles produced in collisions hadronize  
2453 into jets of multiple hadrons. One approach to understanding jet energy mea-  
2454 surements in the ATLAS calorimeters is to evaluate the calorimeter response to  
2455 those individual hadrons; measurements of individual hadrons can be used to  
2456 build up an understanding of the jets that they form. The redundancy of the  
2457 momentum provided by the tracking system and the energy provided by the  
2458 calorimeter provides an opportunity to study calorimeter response using real  
2459 collisions, as described further in Section 7.2.

2460 Calorimeter response includes a number of physical effects that can be ex-  
2461 tracted to provide insight into many aspects of jet modeling. First, many charged  
2462 hadrons interact with the material of the detector prior to reaching the calorime-  
2463 ters and thus do not deposit any energy. Comparing this effect in data and simu-  
2464 lation is a powerful tool in validating the interactions of particles with the mate-  
2465 rial of the detector and the model of the detector geometry in simulation, see Sec-  
2466 tion 7.2.2. The particles which do reach the calorimeter deposit their energy into  
2467 several adjacent cells, which are then clustered together. The energy of the clus-  
2468 ter is then the total energy deposited by that particle. Comparing the response of  
2469 hadrons in data to that of simulated hadrons provides a direct evaluation of the  
2470 showering of hadronic particles and the energy deposited by particles in matter  
(Section 7.2.4).

2472 The above studies all use an inclusive selection of charged particles, which are  
2473 comprised predominantly of pions, kaons, and (anti)protons. It is also possible to  
2474 measure the response to various identified particle types separately to evaluate  
2475 the simulated interactions of each particle, particularly at low energies where  
2476 differences between species are very relevant. Pions and (anti)protons can be  
2477 identified through decays of long-lived particles, in particular  $\Lambda$ ,  $\bar{\Lambda}$ , and  $K_S^0$ , and  
2478 then used to measure response as described above. This is discussed in detail in  
2479 Section 7.3.

2480 The results in this chapter use data collected at 7 and 8 TeV collected in 2010  
2481 and 2012, respectively. Both are included as the calorimeter was repaired and  
2482 recalibrated between those two data-taking periods. Both sets of data are com-  
2483 pared to an updated simulation that includes new physics models provided by  
2484 Geant4 [32] and improvements in the detector description [33, 34]. The present  
2485 results are published in European Physical Journal C (EPJC) [35] and can be com-  
2486 compared to a similar measurement performed in 2009 and 2010 [36], which used  
2487 the previous version of the simulation framework [37].

## 2488 7.1 DATASET AND SIMULATION

## 2489 7.1.1 DATA SAMPLES

2490 The two datasets used in this chapter are taken from dedicated low-pileup runs  
 2491 where the fraction of events with multiple interactions was negligible. These  
 2492 datasets are used rather than those containing full-pileup events to facilitate mea-  
 2493 surement of isolated hadrons. The 2012 dataset at  $\sqrt{s} = 8$  TeV contains 8 mil-  
 2494 lion events and corresponds to an integrated luminosity of  $0.1 \text{ nb}^{-1}$ . The 2010  
 2495 dataset at  $\sqrt{s} = 7$  TeV contains 3 million events and corresponds to an inte-  
 2496 grated luminosity of  $3.2 \text{ nb}^{-1}$ . The latter dataset was also used for the 2010 re-  
 2497 sults [36], but it has since been reanalyzed with an updated reconstruction in-  
 2498 cluding the final, best understanding of the detector description for the material  
 2499 and alignment from Run 1.

## 2500 7.1.2 SIMULATED SAMPLES

2501 The two datasets above are compared to simulated single-, double-, and non-  
 2502 diffractive events generated with Pythia8 [38] using the A2 configuration of  
 2503 hadronization [39] and the MSTW 2008 parton-distribution function set [40,  
 2504 41]. The admixture of the single-, double-, and non-diffractive events uses the  
 2505 default relative contributions from Pythia8. The conditions and energies for  
 2506 the two simulations are chosen so that they match those of the corresponding  
 2507 dataset.

2508 To evaluate the interaction of hadrons with detector material, the simulation  
 2509 uses two different collections of hadronic physics models, called physics lists, in  
 2510 Geant4 9.4 [42]. The first, QGSP\_BERT, combines the Bertini intra-nuclear  
 2511 cascade [43–45] below 9.9 GeV, a parametrized proton inelastic model from 9.5  
 2512 to 25 GeV [46], and a quark-gluon string model above 12 GeV [47–51]. The  
 2513 second, FTFP\_BERT, combines the Bertini intra-nuclear cascade [43–45] below  
 2514 5 GeV and the Fritiof model [52–55] above 4 GeV. In either list, Geant4 en-  
 2515 forces a smooth transition between models where multiple models overlap.

## 2516 7.1.3 EVENT SELECTION

2517 The event selection for this study is minimal, as the only requirement is selecting  
 2518 good-quality events with an isolated track. Such events are triggered by requir-  
 2519 ing at least two hits in the minimum-bias trigger scintillators. After trigger, each  
 2520 event is required to have exactly one reconstructed vertex, and that vertex is re-  
 2521 quired to have four or more associated tracks.

2522 The particles which are selected for the response measurements are first iden-  
 2523 tified as tracks in the inner detector. The tracks are required to have at least 500  
 2524 MeV of transverse momentum. To ensure a reliable momentum measurement,  
 2525 these tracks are required to have at least one hit in the pixel detector, six hits in  
 2526 the SCT, and small longitudinal and transverse impact parameters with respect  
 2527 to the primary vertex [36]. For the majority of the measurements in this chapter,

2528 the track is additionally required to have 20 hits in the TRT, which significantly  
 2529 reduces the contribution from tracks which undergo nuclear interactions. This  
 2530 requirement and its effect is discussed in more detail in Section 7.2.5. In addition,  
 2531 tracks are rejected if there is any other reconstructed track which extrapolates  
 2532 to the calorimeter within a cone of  $\Delta R = \sqrt{(\Delta\phi)^2 + (\Delta\eta)^2} < 0.4$ . This require-  
 2533 ment guarantees that the contamination of energy from nearby charged particles  
 2534 is negligible [36].

## 2535 7.2 INCLUSIVE HADRON RESPONSE

2536 The calorimeter response is more precisely defined as the ratio of the measured  
 2537 calorimeter energy to the true energy carried by the particle, although this true  
 2538 energy is unknown. For charged particles, however, the inner detector provides  
 2539 a very precise measurement of momentum (with uncertainty less than 1%) that  
 2540 can be used as a proxy for true energy. The ratio of the energy deposited by  
 2541 the charged particle in the calorimeter,  $E$ , to its momentum measured in the  
 2542 inner detector  $p$ , forms the calorimeter response measure called  $E/p$ . Though  
 2543 the distribution of  $E/p$  contains a number of physical features, this study focuses  
 2544 on the trends in two aggregated quantities:  $\langle E/p \rangle$ , the average of  $E/p$  for the  
 2545 selected tracks, and the zero fraction, the fraction of tracks with no associated  
 2546 energy in the calorimeter for those tracks.

2547 The calorimeter energy assigned to a track is defined using clusters. The clus-  
 2548 ters are formed using a 4–2–0 algorithm [56] that begins with seeds requiring  
 2549 at least 4 times the average calorimeter cell noise. The neighboring cells with  
 2550 at least twice that noise threshold are then added to the cluster, and all bound-  
 2551 ing cells are then added with no requirement. This algorithm minimizes noise  
 2552 contributions through its seeding process, and including the bounding cells im-  
 2553 proves the energy resolution [57]. The clusters are associated to a given track  
 2554 if they fall within a cone of  $\Delta R = 0.2$  of the extrapolated position of the track,  
 2555 which includes about 90% of the energy on average [36].

### 2556 7.2.1 E/P DISTRIBUTION

2557 The  $E/p$  distributions measured in both data and simulation are shown in Fig-  
 2558 ure 46 for two example bins of track momentum and for tracks in the central  
 2559 region of the detector. These distributions show several important features of  
 2560 the  $E/p$  observable. The large content in the bin at  $E = 0$  comes from tracks that  
 2561 have no associated cluster, which occurs due to interactions with detector mate-  
 2562 rial prior to reaching the calorimeter or the energy deposit being insuffi-  
 2563 ciently large to generate a seed, and are discussed in Section 7.2.2. The small negative  
 2564 tail also comes from tracks that do not deposit any energy in the calorimeter but  
 2565 are randomly associated to a cluster with an energy below the noise threshold.  
 2566 The long positive tail above 1.0 comes from the contribution of neutral parti-  
 2567 cles. Nearby neutral particles deposit (sometimes large) additional energy in the  
 2568 calorimeter but do not produce tracks in the inner detector, so they cannot be  
 2569 rejected by the track isolation requirement. Additionally the peak and mean of

2570 the distribution falls below 1.0 because of the loss of energy not found within  
 2571 the cone as well as the non-compensation of the calorimeter.

2572 The data and simulation share the same features, but the high and low tails  
 2573 are significantly different. The simulated events tend to overestimate the con-  
 2574 tribution of neutral particles to the long tail, an effect which can be isolated and  
 2575 removed as discussed in Section 7.2.3. Additionally, the simulated clusters have  
 2576 less noise on average, although this is a small effect on the overall response.

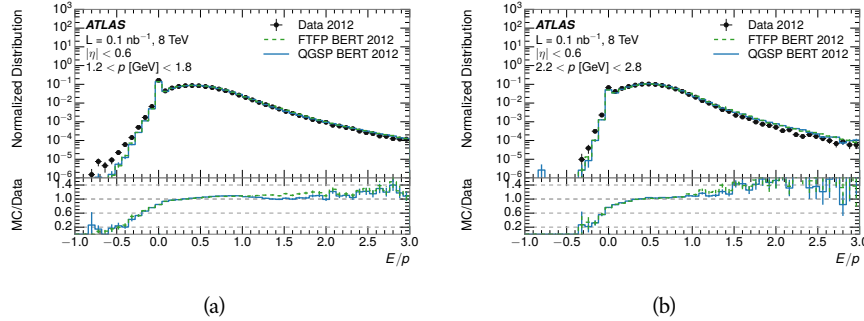


Figure 46: The  $E/p$  distribution and ratio of simulation to data for isolated tracks with  
 (a)  $|\eta| < 0.6$  and  $1.2 < p/\text{GeV} < 1.8$  and (b)  $|\eta| < 0.6$  and  $2.2 < p/\text{GeV} < 2.8$ .

## 2577 7.2.2 ZERO FRACTION

2578 The fraction of particles with no associated clusters, or similarly those with  $E \leq$   
 2579 0, reflects the modeling of both the detector geometry and hadronic interactions.  
 2580 The zero fraction is expected to rise as the amount of material a particle traverses  
 2581 increases, while it is expected to decrease as the particle energy increases. This  
 2582 dependence can be seen in Figure 47, where the zero fraction in data and simula-  
 2583 tion is shown as a function of momentum and the amount of material measured  
 2584 in interaction lengths. The trends are similar between 2010 and 2012 and for  
 2585 positively and negatively charged particles. The zero fraction decreases with  
 2586 energy as expected. The absolute discrepancy in zero fraction between data and  
 2587 simulation decreases with momentum from 5% to less than 1%, but this becomes  
 2588 more pronounced in the ratio as the zero fraction shrinks quickly with increas-  
 2589 ing momentum. The amount of material in the detector increases with  $\eta$ , which  
 2590 is used to obtain results for interaction lengths ranging between 0.1 and 0.65  $\lambda$ .  
 2591 As the data and simulation have significant disagreement in the zero fraction  
 2592 over a number of interaction lengths, the difference must be primarily from the  
 2593 modeling of hadronic interactions with detector material and not just the detec-  
 2594 tor geometry. Although two different hadronic interaction models are shown  
 2595 in the figure, they have very similar discrepancies to data because both use the  
 2596 same description (the BERT model) at low momentum.

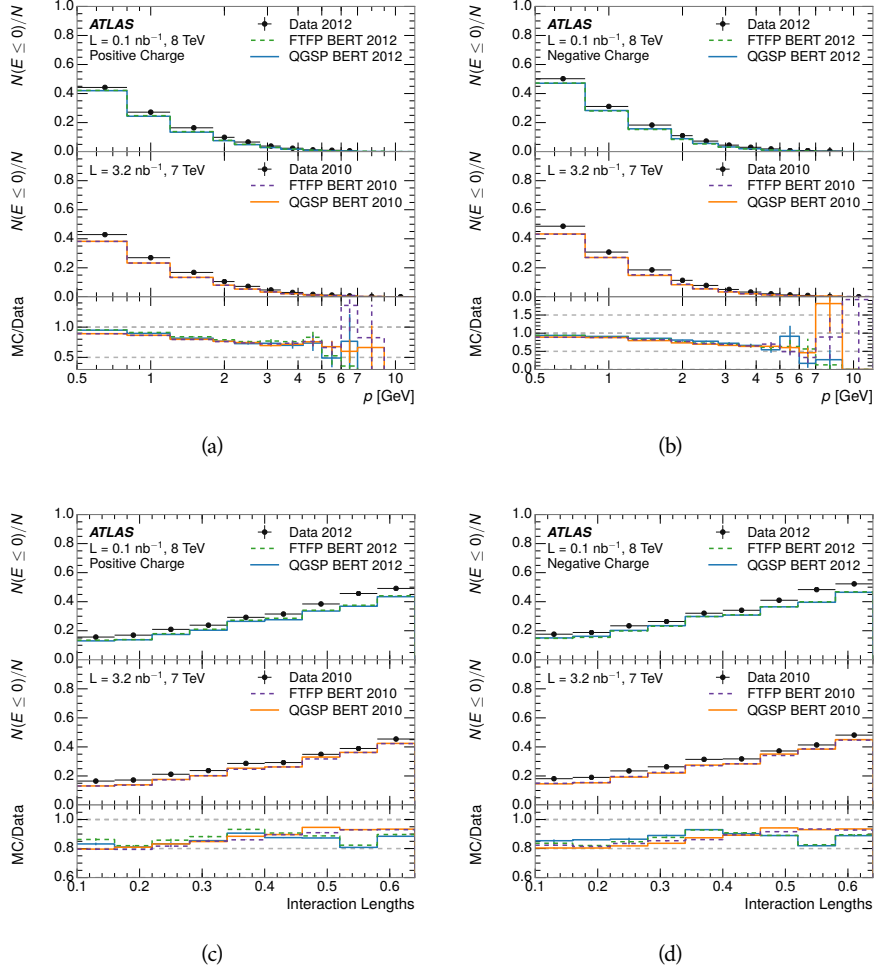
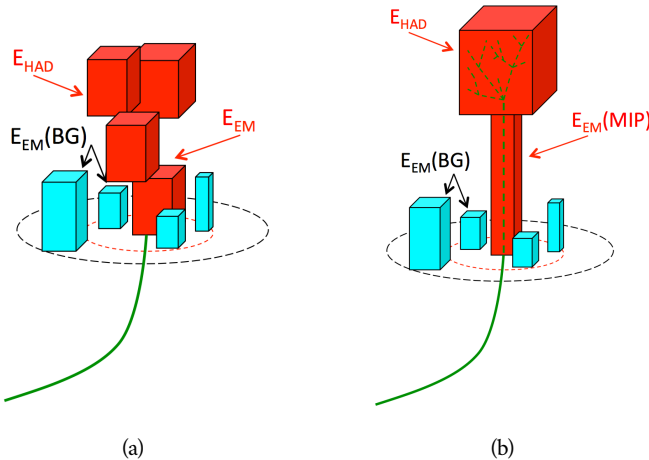


Figure 47: The fraction of tracks as a function (a, b) of momentum, (c, d) of interaction lengths with  $E \leq 0$  for tracks with positive (on the left) and negative (on the right) charge.

## 2597 7.2.3 NEUTRAL BACKGROUND SUBTRACTION

2598 The isolation requirement on hadrons is only effective in removing an energy  
 2599 contribution from nearby charged particles. Nearby neutral particles, predomi-  
 2600 nantly photons from  $\pi^0$  decays, also add their energy to the calorimeter clusters,  
 2601 but mostly in the electromagnetic calorimeter. The arrangement of energy de-  
 2602 posits is shown in Figure 48, which illustrates both energy deposits from the  
 2603 hadronic particle and additional deposits from neutral particles. It is possible to  
 2604 measure this contribution, on average, using late-showering hadrons that min-  
 2605 imally ionize in the electromagnetic calorimeter. Such particles are selected by  
 2606 requiring that they deposit less than 1.1 GeV in the EM calorimeter within a  
 2607 cone of  $\Delta R < 0.1$  around the track. To ensure that these particles are well mea-  
 2608 sured, they are additionally required to deposit between 40% and 90% of their  
 2609 energy in the hadronic calorimeter within the same cone.



2610 Figure 48: An illustration (a) of the geometry of energy deposits in the calorimeter. The  
 2611 red energy deposits come from the charged particle targeted for measure-  
 2612 ment, while the blue energy deposits are from nearby neutral particles and  
 2613 must be subtracted. The same diagram (b) for the neutral-background selec-  
 2614 tion, described in Section 7.2.3.

2615 These particles provide a clean sample to measure the nearby neutral back-  
 2616 ground because they do not deposit energy in the area immediately surround-  
 2617 ing them in the EM calorimeter, as shown in Figure 48. So, the energy deposits in the  
 2618 region  $0.1 < \Delta R < 0.2$  can be attributed to neutral particles alone. To estimate  
 2619 the contribution to the whole cone considered for the response measurement,  
 2620 that energy is scaled by a geometric factor of  $4/3$ . This quantity,  $\langle E/p \rangle_{BG}$ , mea-  
 2621 sured in aggregate over a number of particles, gives the contribution to  $\langle E/p \rangle$   
 2622 from neutral particles in the EM calorimeter. Similar techniques were used in  
 2623 the individual layers of the hadronic calorimeters to show that the background  
 2624 from neutrals is negligible in those layers [36].

2625 The distribution of this background estimate is shown in Figure 49 for data  
 2626 and simulation with the two different physics lists. The contribution from neu-

tral particles falls from 0.1 at low momentum to around 0.03 for particles above 7 GeV. Although the simulation captures the overall trend, it significantly overestimates the neutral contribution for tracks with momentum between 2 and 8 GeV. This effect was also seen in the tails of the  $E/p$  distributions in Figure 46. This difference is likely due to modeling of coherent neutral particle radiation in Pythia8 that overestimates the production of  $\pi^0$  near the production of the charged particles. The discrepancy does not depend on  $\eta$  and thus is unlikely to be a mismodeling of the detector. This difference can be subtracted to form a corrected average of  $E/p$ .

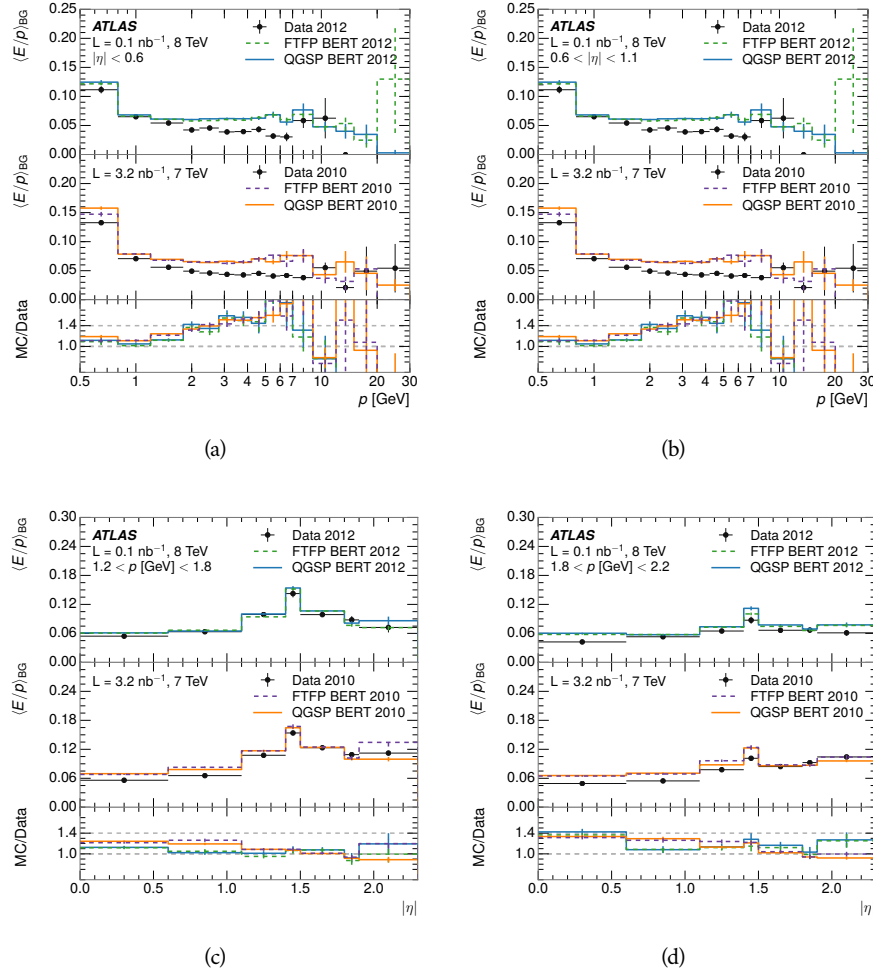


Figure 49:  $\langle E/p \rangle_{BG}$  as a function of the track momentum for tracks with (a)  $|\eta| < 0.6$ , (b)  $0.6 < |\eta| < 1.1$ , and as a function of the track pseudorapidity for tracks with (c)  $1.2 < p/\text{GeV} < 1.8$ , (d)  $1.8 < p/\text{GeV} < 2.2$ .

#### 7.2.4 CORRECTED RESPONSE

Figure 50 shows  $\langle E/p \rangle_{COR}$  as a function of momentum for several bins of pseudorapidity. This corrected  $\langle E/p \rangle_{COR} \equiv \langle E/p \rangle - \langle E/p \rangle_{BG}$  measures the average calorimeter response without the contamination of neutral particles. It is the

most direct measurement of calorimeter response in that it is the energy measured for fully isolated hadrons. The correction is performed separately in data and simulation, so that the mismodeling of the neutral background in simulation is removed from the comparison of response. The simulation overestimates the response at low momentum by about 5%, an effect that can be mostly attributed to the underestimation of the zero fraction mentioned previously. For  $|\eta| < 0.6$ , the data-simulation agreement has a larger discrepancy by about 5% for 2010 than 2012, although this is not reproduced in at higher pseudorapidity.

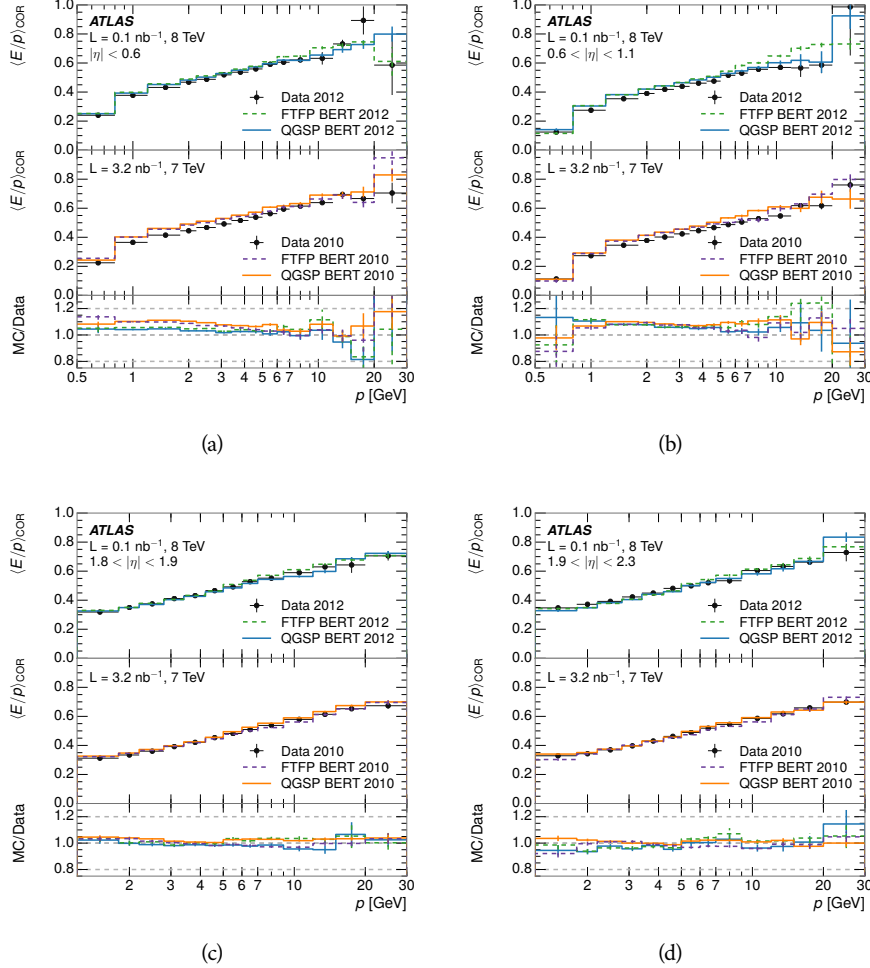


Figure 50:  $\langle E/p \rangle_{\text{COR}}$  as a function of track momentum, for tracks with (a)  $|\eta| < 0.6$ , (b)  $0.6 < |\eta| < 1.1$ , (c)  $1.8 < |\eta| < 1.9$ , and (d)  $1.9 < |\eta| < 2.3$ .

The response measurement above used topological clustering at the EM scale, that is clusters were formed to measure energy but no corrections were applied to correct for expected effects like energy lost outside of the cluster or in uninstrumented material. It is also interesting to measure  $\langle E/p \rangle_{\text{COR}}$  using LCW energies, which accounts for those effects by calibrating the energy based on the properties of the cluster such as energy density and depth in the calorimeter. Figure 51 shows these distributions for tracks with zero or more clusters and separately for tracks with one or more clusters. The calibration moves the mean

value of  $\langle E/p \rangle_{\text{COR}}$  significantly closer to 1.0 as desired, but the discrepancy between data and simulation remains in the comparison that includes tracks with zero associated clusters. The agreement between data and simulation improves noticeably when at least one cluster is required, as this removes the contribution from the mismodeling of the zero fraction.

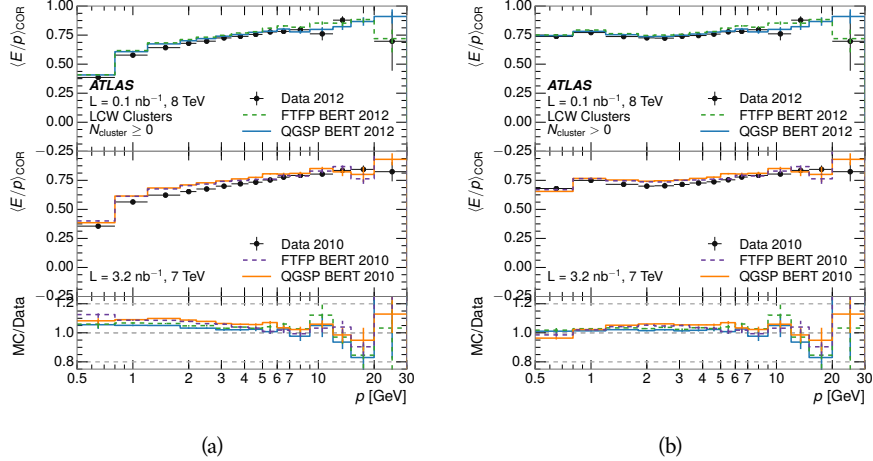


Figure 51:  $\langle E/p \rangle_{\text{COR}}$  calculated using LCW-calibrated topological clusters as a function of track momentum for tracks with (a) zero or more associated topological clusters or (b) one or more associated topological clusters.

### 7.2.5 ADDITIONAL STUDIES

As has been seen in several measurements in previous sections, the simulation does not correctly model the chance of a low momentum hadron to reach the calorimeter. Because of the consistent discrepancy across pseudorapidity and interaction lengths, this can be best explained by incomplete understanding of hadronic interactions with the detector [35]. For example, a hadron that scatters off of a nucleus in the inner detector can be deflected through a significant angle and not reach the expected location in the calorimeter. In addition, these interactions can produce secondary particles that are difficult to model.

The requirement used throughout the previous sections on the number of hits in the TRT reduces these effects by preferentially selecting tracks that do not undergo nuclear interactions. It is interesting to check how well the simulation models tracks with low numbers of TRT hits, which selects tracks that are more likely to have undergone a hadronic interaction. Figure 52 compares the distributions with  $N_{\text{TRT}} < 20$  to  $N_{\text{TRT}} > 20$  for real and simulated particles<sup>1</sup>. As expected, the tracks with fewer hits are poorly modeled in the simulation as  $\langle E/p \rangle_{\text{COR}}$  differs by as much as 25% at low momentum. They also have significantly lower  $\langle E/p \rangle_{\text{COR}}$  on average, because they are much less likely to have an associated cluster.

<sup>1</sup> The distribution with  $N_{\text{TRT}} > 20$  is the same as shown in Figure 50 (a) and is included again here for the comparison.

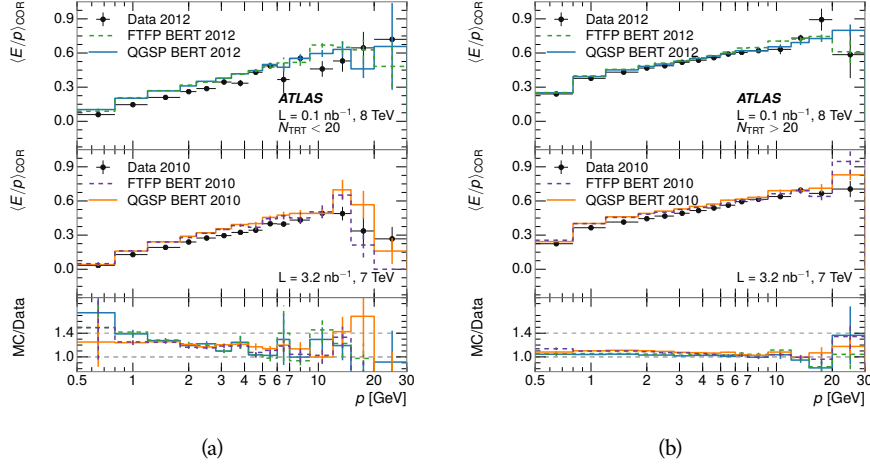


Figure 52: Comparison of the  $\langle E/p \rangle_{\text{COR}}$  for tracks with (a) less than and (b) greater than 20 hits in the TRT.

Another interesting aspect of the simulation is the description of antiprotons at low momentum, where QGSP\_BERT and FTFP\_BERT have significant differences. This can be seen to have an effect in the inclusive response measurement when separated into positive and negative charge. The  $\langle E/p \rangle_{\text{COR}}$  distributions for positive and negative particles are shown in Figure 53, where a small difference between QGSP\_BERT and FTFP\_BERT can be seen in the distribution for negative tracks. The figure also includes data, and the simulation overestimates  $\langle E/p \rangle_{\text{COR}}$  mostly due to an underestimation in zero fraction. There is an approximately 5% difference between the 2010 and 2012 simulated events. The difference between positive and negative particles is demonstrated more clearly in Figure 54, which shows the  $E/p$  distribution in the two simulations separated by charge. There is a small difference around  $E/p > 1.0$ , which can be explained by the additional energy deposited by the annihilation of the antiproton in the calorimeter that is modeled well only in FTFP\_BERT. This is also explored with data using identified antiprotons in Section 7.3.

The  $\langle E/p \rangle$  results in previous sections have considered the electromagnetic and hadronic calorimeters together as a single energy measurement, to emphasize the total energy deposited for a given particle. However, the deposits in each calorimeter are measured separately and  $\langle E/p \rangle$  can be constructed for each layer separately. As the layers are composed of different materials and are modeled separately in the detector geometry, confirmation that the simulation matches the data well in each layer adds confidence in both the description of hadronic interactions with the two different materials and also the geometric description of each.

The technique discussed in Section 7.2.3 for selecting MIPs in the electromagnetic calorimeter is also useful in studying deposits in the hadronic calorimeter. The tracks selected with the MIP requirements deposit almost all of their energy exclusively in the hadronic calorimeter. Figure 55 shows  $\langle E/p \rangle_{\text{RAW}}^{\text{Had}}$ , where RAW indicates that no correction has been applied for neutral backgrounds and

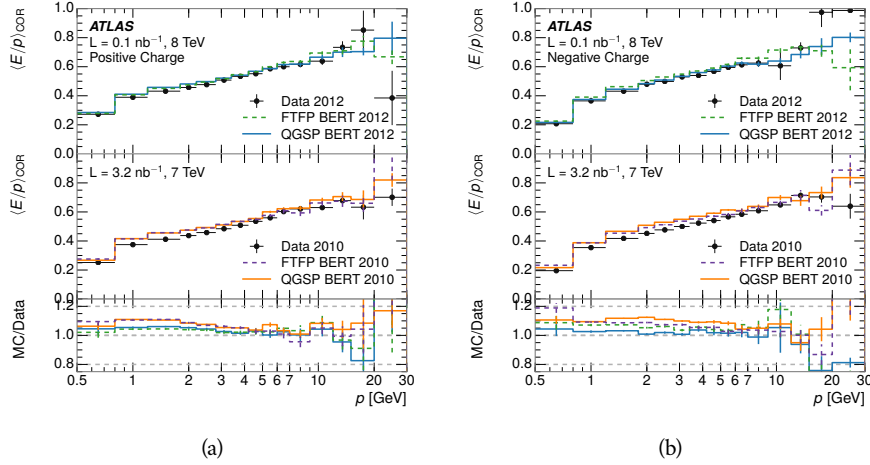


Figure 53: Comparison of the  $\langle E/p \rangle_{\text{COR}}$  for (a) positive and (b) negative tracks as a function of track momentum for tracks with  $|\eta| < 0.6$ .

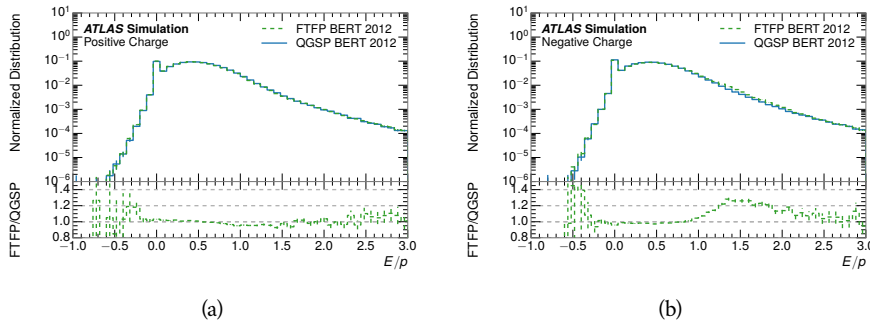


Figure 54: Comparison of the  $E/p$  distributions for (a) positive and (b) negative tracks with  $0.8 < p/\text{GeV} < 1.2$  and  $|\eta| < 0.6$ , in simulation with the FTFP\_BERT and QGSP\_BERT physics lists.

Had indicates that only clusters for the hadronic calorimeter are included<sup>2</sup>. The distributions are shown both for the original EM scale calibration and after LCW calibration. The data and simulation agree very well in this comparison, except in the lowest momentum bin where there is a 5% discrepancy that has already been seen in the measurements in Section 7.2.4.

A similar comparison can be made in the electromagnetic calorimeter by selecting particles which have no associated energy in the hadronic calorimeter. These results are measured in terms of  $\langle E/p \rangle_{\text{COR}}^{\text{EM}}$ , where EM designates that only clusters in the electromagnetic calorimeter are included and COR designates that the neutral background is subtracted as the neutral background is present in this case. Figure 56 shows the analogous comparisons to Figure 55 in the electromagnetic calorimeter. The  $\langle E/p \rangle_{\text{COR}}$  values are lower on average in the EM calorimeter than in the hadronic calorimeter, which is an expected conse-

<sup>2</sup> The RAW and COR versions of  $\langle E/p \rangle$  in this case are the same, as the neutral background is negligible in that calorimeter layer.

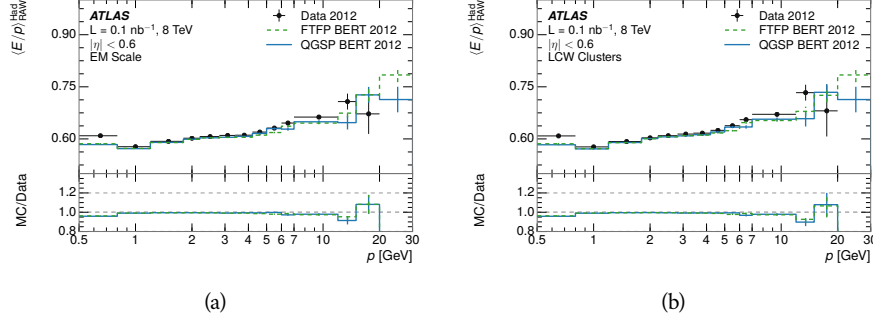


Figure 55: Comparison of the response of the hadronic calorimeter as a function of track momentum (a) at the EM-scale and (b) after the LCW calibration.

quence of their different material types (discussed in Section 5.4). In this case the disagreement between data and simulation is more pronounced, with discrepancies as high as 5% over a larger range of momenta. This level of discrepancy indicates that the description of the electromagnetic calorimeter is actually the dominant source of discrepancy in the combined distributions in Section 7.2.4.

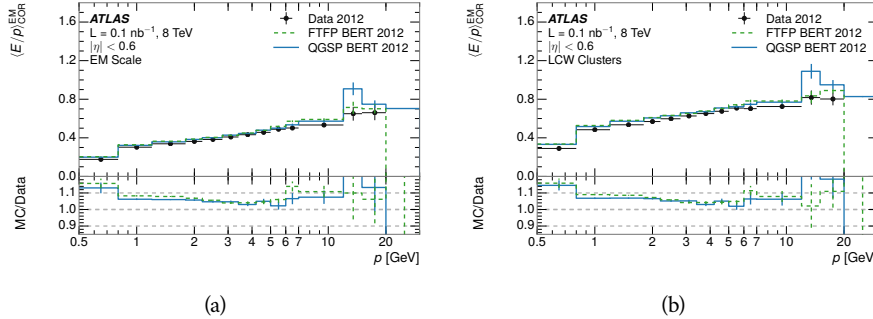


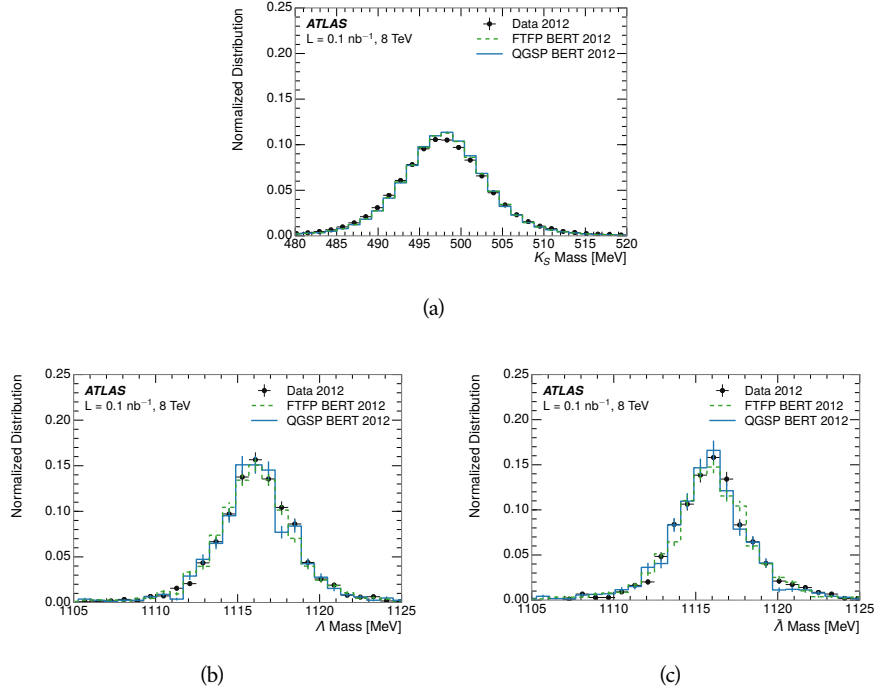
Figure 56: Comparison of the response of the EM calorimeter as a function of track momentum (a) at the EM-scale and (b) with the LCW calibration.

## 7.3 IDENTIFIED PARTICLE RESPONSE

The inclusive response measurement for hadrons can be augmented by measuring the response for specific particle species. The simulation models each particle type separately, and understanding the properties of each is important in constraining the uncertainty on jets. In order to select and measure specific hadrons, this section relies on the displaced decays of long-lived particles. Such decays can be identified by reconstructing secondary vertices with a requirement on mass. In particular,  $\Lambda$ ,  $\bar{\Lambda}$ , and  $K_S^0$  can be used to select a pure sample of protons, antiprotons, and pions, respectively.

## 2731 7.3.1 DECAY RECONSTRUCTION

2732 The measurement of the response for identified particles uses the same selection  
 2733 as for inclusive particles (Section 7.1.3) with a few additions. Each event used is  
 2734 required to have at least one secondary vertex, as described in Section 6.1.3, and  
 2735 the tracks are required to match to that vertex rather than the primary vertex.  
 2736 Pions are selected from decays of  $K_S^0 \rightarrow \pi^+ \pi^-$ , which is the dominant decay for  
 2737  $K_S^0$  to charged particles. Protons are selected from decays of  $\Lambda \rightarrow \pi^- p$  and an-  
 2738 tiprotons from  $\bar{\Lambda} \rightarrow \pi^+ \bar{p}$ , which are similarly the dominant decays of  $\Lambda$  and  $\bar{\Lambda}$   
 2739 to charged particles. The species of parent hadron in these decays is determined  
 2740 by reconstructing the mass of the tracks associated to the secondary vertex. The  
 2741 sign of the higher momentum decay particle can distinguish between  $\Lambda$  and  $\bar{\Lambda}$ ,  
 2742 which of course have the same mass, as the proton or antiproton is kinemati-  
 2743 cally favored to have higher momentum. The proton or antiproton will carry  
 2744 the higher momentum above 95% of the time. Examples of the reconstructed  
 2745 masses used to select these decays are shown in Figure 57. The mass peaks in  
 2746 data and both simulation models are very similar.



2747 Figure 57: The reconstructed mass peaks of (a)  $K_S^0$ , (b)  $\Lambda$ , and (c)  $\bar{\Lambda}$  candidates.

2748 The dominant backgrounds for the identified particle decays are nuclear in-  
 2749 teractions and combinatoric sources. These are suppressed by the kinematic re-  
 2750 quirements on the tracks as well as an additional veto which removes candidates  
 2751 that are consistent with both a  $\Lambda$  or  $\bar{\Lambda}$  and a  $K_S^0$  hypothesis, which is possible  
 2752 because of the different assumptions on particle mass in each case [36]. After  
 2753 these requirements, the backgrounds are found to be negligible compared to the  
 2754 statistical errors on these measurements.

## 2754 7.3.2 IDENTIFIED RESPONSE

With these techniques the  $E/p$  distributions are extracted in data and simulation for each particle species and shown in Figure 58. These distributions are shown for a particular bin of  $E_a$  ( $2.2 < E_a/\text{GeV} < 2.8$ ), rather than  $p$ .  $E_a$  is the energy available to be deposited in the calorimeter: for pions  $E_a = \sqrt{p^2 + m_\pi^2}$ , for protons  $E_a = \sqrt{p^2 + m_p^2} - m_p$ , and for antiprotons  $E_a = \sqrt{p^2 + m_p^2} + m_p$ . In the pion case, the entire energy of the pion is deposited in the calorimeter, so  $E_a$  is just the usual energy. For protons, the proton remains after depositing its energy in the calorimeter, so its mass is not available and must be subtracted from  $E_a$ . And for antiprotons, the antiproton constituents annihilate with the quarks in the protons and neutrons of the calorimeter material, so it deposits its entire energy as well as an the additional energy from the annihilation; this extra energy is equal to the mass of the antiproton and is added to the available energy. The features of the  $E/p$  distributions are similar to the inclusive case, with a peak around 0.5 at low momentum. The zero fraction is not as pronounced as in the inclusive case. There is a small negative tail from noise and a large fraction of tracks with zero energy from particles which do not reach the calorimeter. The long positive tail is noticeably more pronounced for antiprotons because of the additional energy generated by the annihilation of the antiproton with the material of the detector, and the peak of the distribution is also increased for the same reason. The simulation correctly captures these features, and the agreement between data and simulation is good to within the available statistical limitations.

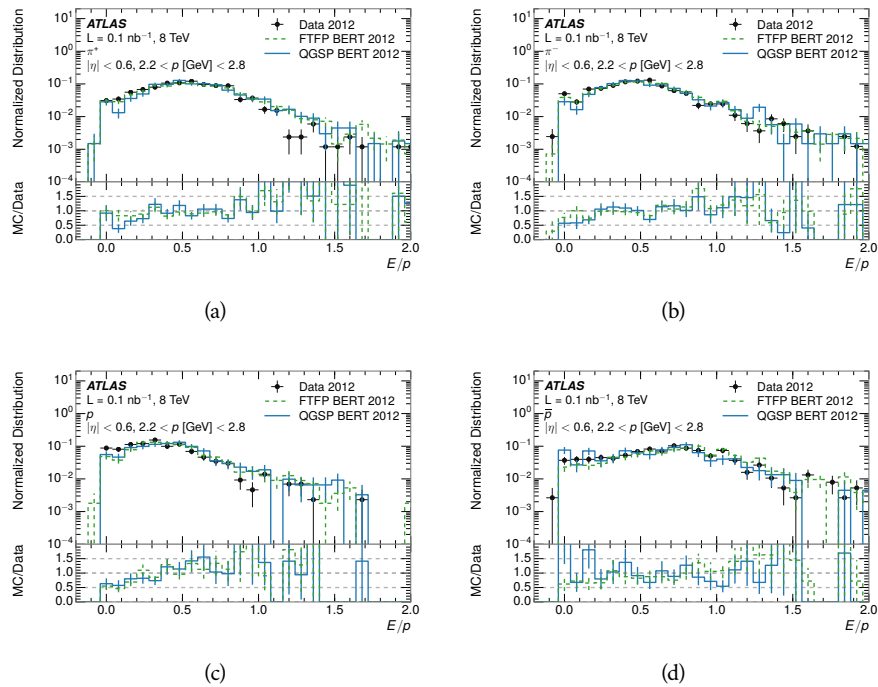


Figure 58: The  $E/p$  distribution for isolated (a)  $\pi^+$ , (b)  $\pi^-$ , (c) proton, and (d) anti-proton tracks.

The zero fraction is further explored in Figure 59 for pions and protons in data and simulation. The simulation consistently underestimates the zero fraction independent of particle species, which implies that this discrepancy is not caused by the model of a particular species but rather a feature common to all. The zero fraction is larger for  $\pi^-$  than  $\pi^+$ , which is evident in both data and simulation. However there is some suggestion that this increase in zero fraction leads to an even larger discrepancy in the modeling of  $\pi^-$  in simulation.

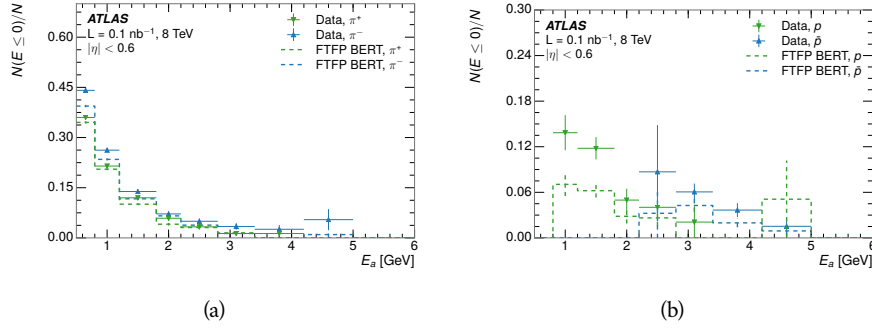


Figure 59: The fraction of tracks with  $E \leq 0$  for identified (a)  $\pi^+$  and  $\pi^-$ , and (b) proton and anti-proton tracks

It is also interesting to compare the response between the different particle species. One approach to do this is to measure the difference in  $\langle E/p \rangle$  between two types, which has the advantage of removing the neutral background. These differences are shown in various combinations in Figure 60. The response for  $\pi^+$  is greater on average than the response to  $\pi^-$  because of a charge-exchange effect which causes the production of additional neutral pions in the showers of  $\pi^+$  [58]. This effect becomes less significant as the  $\langle E/p \rangle$  increases, and the difference approaches zero. Both version of the simulation correctly model this trend. The response for  $\pi^+$  is also greater on average than the response to  $p$ , because a large fraction of the energy of  $\pi^+$  hadrons is converted to an electromagnetic shower [59, 60]. This effect is again reproduced by both simulations. The  $\bar{p}$  response, however, is significantly higher than the response to  $\pi^-$  because of the annihilation of the antiproton, but the difference decreases at higher energies where the additional energy has less relative importance. FTFP\_BERT models this effect more accurately than QGSP\_BERT because of their different descriptions of  $\bar{p}$  interactions with material.

It is also possible to remove the neutral background from these response distributions using the same technique as in Section 7.2.3. The technique is largely independent of the particle species and so can be directly applied to  $\langle E/p \rangle$  for pions. The  $\langle E/p \rangle_{\text{COR}}$  distributions for pions are shown in Figure 61, which are very similar to the inclusive results. The inclusive hadrons are comprised mostly of pions, so this similarity is not surprising. It is also possible to see the small differences between  $\pi^+$  and  $\pi^-$  response here, where  $\langle E/p \rangle_{\text{COR}}$  is higher on average for  $\pi^+$ . The agreement between data and simulation is significantly worse for the  $\pi^-$  distributions than for the  $\pi^+$ , with a discrepancy greater than 10% below 2-3 GeV.

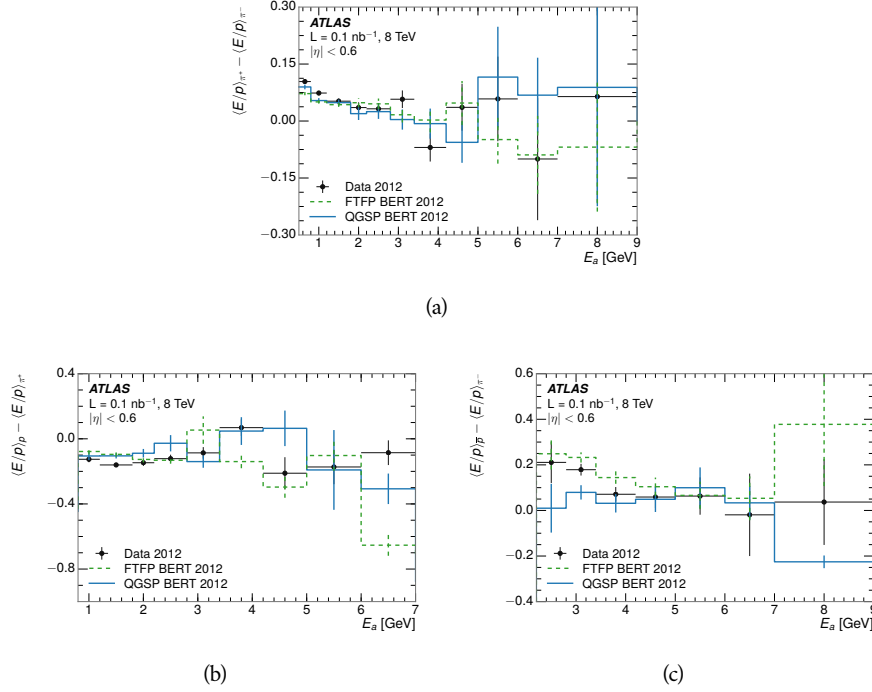


Figure 60: The difference in  $\langle E/p \rangle$  between (a)  $\pi^+$  and  $\pi^-$  (b)  $p$  and  $\pi^+$ , and (c)  $\bar{p}$  and  $\pi^-$ .

2809 7.3.3 ADDITIONAL SPECIES IN SIMULATION

2810 The techniques above provide a method to measure the response separately for  
 2811 only pions and protons. However the hadrons which forms jets include a number  
 2812 of additional species such as kaons and neutrons. The charged kaons are an im-  
 2813 portant component of the inclusive charged hadron distribution, which is com-  
 2814 prised of roughly 60-70% pions, 15-20% kaons, and 5-15% protons [35]. These  
 2815 fractions vary depending on the production mechanism, and the ranges are in-  
 2816 dicative of the variations between different events. These are difficult to measure  
 2817 in data at the ATLAS detector, as the particles which decay to kaons such as  $\phi$  and  
 2818  $D$  mesons have shorter lifetimes and are comparatively rare. These properties  
 2819 make it impractical to identify a sufficient number of decays to make statistically  
 2820 meaningful measurements. The simulation of these particles includes noticeable  
 2821 differences in response between species at low energies, which are shown in Fig-  
 2822 ure 62 for FTFP\_BERT. The significant differences in response between protons  
 2823 and antiprotons below 1 GeV are accounted for above in the definitions of  $E_a$ .

2824 7.4 SUMMARY

2825 These various measurements of calorimeter response shown above for data and  
 2826 simulation illuminate the accuracy of the simulation of hadronic interactions at  
 2827 the ATLAS detector. The results were obtained using 2010 and 2012 data at 7  
 2828 and 8 TeV, but reflect the most current understanding of the detector alignment

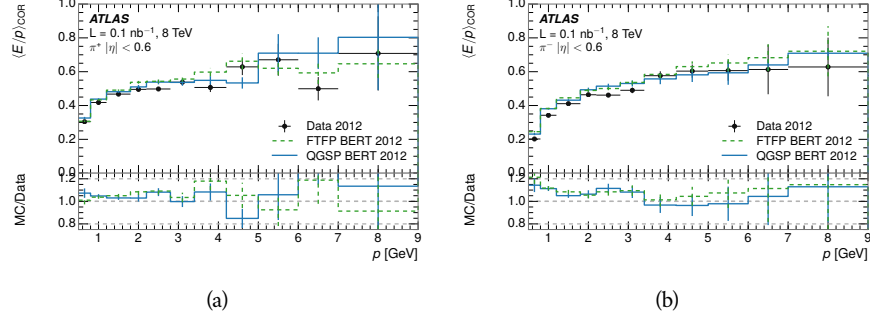


Figure 61:  $\langle E/p \rangle_{\text{COR}}$  as a function of track momentum for (a)  $\pi^+$  tracks and (b)  $\pi^-$  tracks.

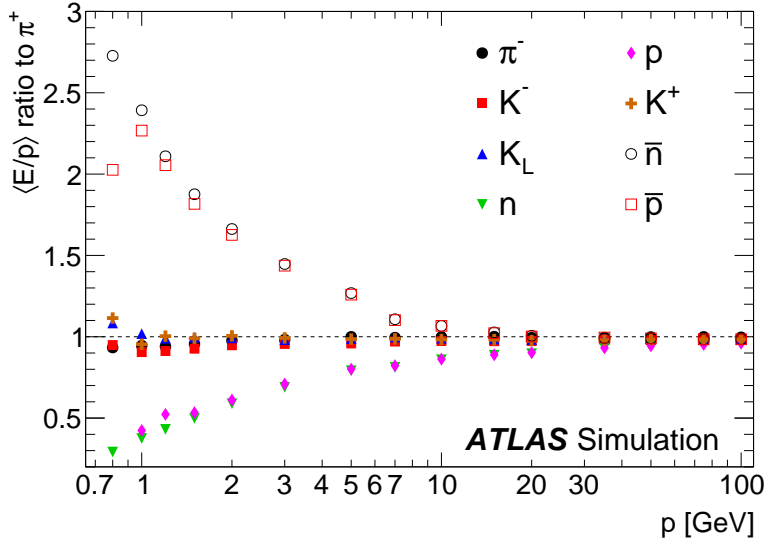


Figure 62: The ratio of the calorimeter response to single particles of various species to the calorimeter response to  $\pi^+$  with the physics list FTFP\_BERT.

and geometry. A number of measurements focusing on a comparison between protons and antiprotons suggest that FTFP\_BERT models those interaction more accurately than QGSP\_BERT. These measurements, among others, were the motivation to switch the default Geant4 simulation from QGSP\_BERT to FTFP\_BERT for all ATLAS samples.

Even with these updates, there are a number of approximately 5% discrepancies in response between the data and simulation. The differences result mostly from a difference in the modeling of the zero fraction, which is most significant at low energies. The difference in response without the zero fraction are primarily in the electromagnetic calorimeter, while the modeling of the hadronic calorimeter is accurate. At higher momenta the simulation of hadronic interactions is very consistent with data. Chapter 8 discusses how to use these observed differences to constrain the jet energy scale and its associated uncertainties.

2842

## 2843 JET ENERGY RESPONSE AND UNCERTAINTY

## 2844 8.1 MOTIVATION

2845 As jets form a major component of many physics analyses at ATLAS, it is crucial  
 2846 to carefully calibrate the measurement of jet energies and to derive an uncer-  
 2847 tainty on that measurement. These uncertainties are often the dominant sys-  
 2848 tematic uncertainty in high-energy analyses at the LHC. Jet balance techniques,  
 2849 as discussed in Section 6.4.3, provide a method to constrain the JES and its uncer-  
 2850 tainty in data, and provide the default values used for ATLAS jet measurements at  
 2851 most energies [61]. These techniques are limited by their reliance on measuring  
 2852 jets in data, so they are statistically limited in estimating the jet energy scale at the  
 2853 highest jet energies. This chapter presents another method for estimating the jet  
 2854 energy scale and its uncertainty which builds up a jet from its constituents and  
 2855 thus can be naturally extended to high jet momentum. Throughout this chapter  
 2856 the jets studied are simulated using Pythia8 with the CT10 parton distribution  
 2857 set [62] and the AU2 tune [39], and corrections are taken from the studies includ-  
 2858 ing data and simulation in Chapter 7.

2859 As described in Section 6.4, jets are formed from topological clusters of energy  
 2860 in the calorimeters using the anti- $k_t$  algorithm. These clusters originate from a  
 2861 diverse spectrum of particles, in terms of both species and momentum, leading to  
 2862 significantly varied jet properties and response between jets of similar produced  
 2863 momentum. Figure 63 shows the momentum and particle distributions of sim-  
 2864 ulated particles within jets at a few examples energies. Each bin for each distri-  
 2865 bution shows the fraction of jet constituents of that particle type and that truth  
 2866 energy for a jet of the specified energy. These show that majority of particles in  
 2867 jets are charged pions and photons, and the charged pions constituent carry the  
 2868 highest energies on average. The figure also demonstrates that the majority of  
 2869 the particles in a jet have much lower momentum than the jet itself; for example  
 2870 in 90-100 GeV jets less than 1% of particles have energies above 20 GeV. The  
 2871  $E/p$  measurements provide a thorough understanding of the dominant particle  
 2872 content of jets, the charged hadrons.

## 2873 8.2 UNCERTAINTY ESTIMATE

2874 A correct modeling of jets in the data by simulation requires that both the parti-  
 2875 cle production inside jets as well as the response of the calorimeter to particles  
 2876 are correctly modeled. Chapter 7 showed that the simulation does not perfectly  
 2877 model the calorimeter response, and provided measurements that can be used  
 2878 to correct for discrepancies. To determine the corrections appropriate for jets,  
 2879 that is to evaluate a jet energy response, the simulated jet energies are compared

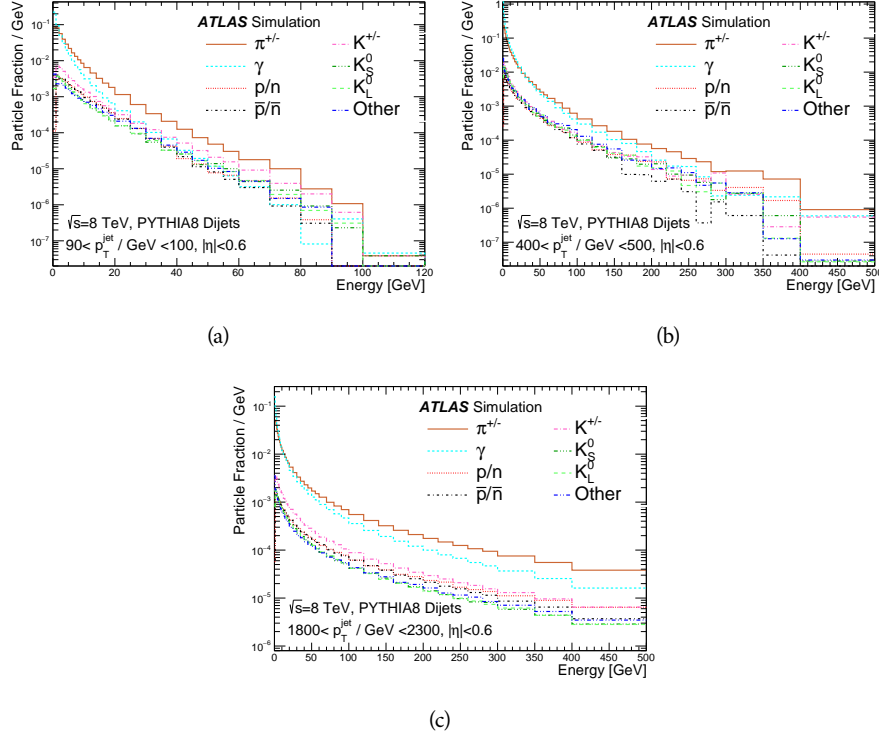


Figure 63: The spectra of true particles inside anti- $k_t$ ,  $R = 0.4$  jets with (a)  $90 < p_T/\text{GeV} < 100$ , (b)  $400 < p_T/\text{GeV} < 500$ , and (c)  $1800 < p_T/\text{GeV} < 2300$ .

2880 to a corrected jet built up at the particle level. Each cluster in a jet is associated  
2881 to the truth particle which deposited it, and the energy in that cluster is then  
2882 corrected for a number of effects based on measurements in data. The primary  
2883 corrections come from the single hadron response measurements in addition to  
2884 response measured using the combined test beam which covers higher momen-  
2885 tum particles [63]. These corrections include both a shift ( $\Delta$ ), in order to make  
2886 the simulation match the average response in data, and an uncertainty ( $\sigma$ ) asso-  
2887 ciated with the ability to constrain the difference between data and simulation.  
2888 Some of the dominant sources of uncertainty are itemized in Table 8 with typi-  
2889 cal values, and the full list considered is described in detail in the associated pa-  
2890 per [35]. These uncertainties cover differences between the data and simulation  
2891 in the modeling of calorimeter response to a given particle. The typical values  
2892 are listed as ranges to show the variation over momentum and pseudorapidity.  
2893 For the in situ  $E/p$  term, for example,  $\Delta$  corresponds to the difference between  
2894 data and simulation for  $\langle E/p \rangle_{\text{COR}}$  at the LCW scale (shown in Figure 51 (b)) and  
2895  $\sigma$  is the uncertainty on that difference including the statistical uncertainties of  
2896 both the data and simulated events. No uncertainties are added for the differ-  
2897 ence between particle composition of jets in data and simulation, as this method  
2898 focuses on providing a response correction for discrepancies of particle interac-  
2899 tions rather than differences in particle composition.

2900 From these terms, the jet energy scale and uncertainty is built up from in-  
 2901 dividual energy deposits in simulation. Each uncertainty term is treated inde-

Abbrev.	Description	$\Delta$ (%)	$\sigma$ (%)
In situ $E/p$	The comparison of $\langle E/p \rangle_{\text{COR}}$ , at the <a href="#">LCW</a> scale, as described in Chapter 7 with statistical uncertainties from 500 MeV to 20 GeV.	0-3	1-5
CTB	The main $\langle E/p \rangle$ comparison uncertainties, binned in $p$ and $ \eta $ , as derived from the combined test beam results, from 20 to 350 GeV [63].	0-3	1-5
$E/p$ Zero Fraction	The difference in the zero-fraction between data and MC simulation from 500 MeV to 20 GeV.	5-25	1-5
$E/p$ Threshold	The uncertainty in the EM calorimeter response from the potential mismodeling of threshold effects in topological clustering.	0	0-10
Neutral	The uncertainty in the calorimeter response to neutral hadrons based on studies of physics model variations.	0	5-10
$K_L$	An additional uncertainty in the response to neutral $K_L$ in the calorimeter based on studies of physics model variations.	0	20
$E/p$ Misalignment	The uncertainty in the $p$ measurement from misalignment of the ID.	0	1
Hadrons, $p > 350$ GeV	An energy independent uncertainty for all particles above the energy range or outside the longitudinal range probed with the combined test beam.	0	10

Table 8: The dominant sources of corrections and systematic uncertainties in the [JES](#) estimation technique, including typical values for the correcting shift ( $\Delta$ ) and the associated uncertainty ( $\sigma$ ).

pendently, and is taken to be gaussian distributed. The resulting scale and uncertainty is shown in Figure 64, where the mean response is measured relative to the calibrated energy reported by simulation. The mean response is slightly below one, indicating that the simulation slightly overestimates the calorimeter response on average, and this response is relatively constant as a function of the jet  $p_T$ . The dominant uncertainties come from the statistical uncertainties on the  $E/p$  measurements at lower energies and the additional uncertainty for out of range measurements at higher energies. Combined the resulting uncertainty ranges from between 1.5% at low momentum and pseudorapidity to as much as 4% at higher momentum and pseudorapidity. The total uncertainty from this method at intermediate jet energies is comparable to other simulation-based methods [64] and is about twice as large as in-situ methods using data [61]. This method is the only one which provides an estimation above 1.8 TeV, however, and so is still a crucial technique in analyses that search for very energetic jets.

These techniques can also be used to measure the correlation between bins of average reconstructed jet momentum across a range of  $p_T$  and  $|\eta|$ , where correlations are expected because of a similarity in particle composition at similar energies. Figure 65 shows these correlations, where the uncertainties on jets in neighboring bins are typically between 30% and 60% correlated. The uncertainty on all jets becomes significantly correlated at high energies and larger pseudorapidities, when the uncertainty becomes dominated by the single term reflecting out of range particles.

### 8.3 SUMMARY

The technique described above provides a jet energy scale and uncertainty by building up jet corrections from the energy deposits of constituent particles. The  $E/p$  measurements are crucial in providing corrections for the majority of particles in the jets. The uncertainty derived this way is between 2 and 5% and is about twice as large at corresponding momentum than jet balance methods. However this is the only uncertainty available for very energetic jets using 2012 data and simulation, and repeating this method with Run 2 data and simulation will be important in providing an uncertainty for the most energetic jets in 13 TeV collisions.

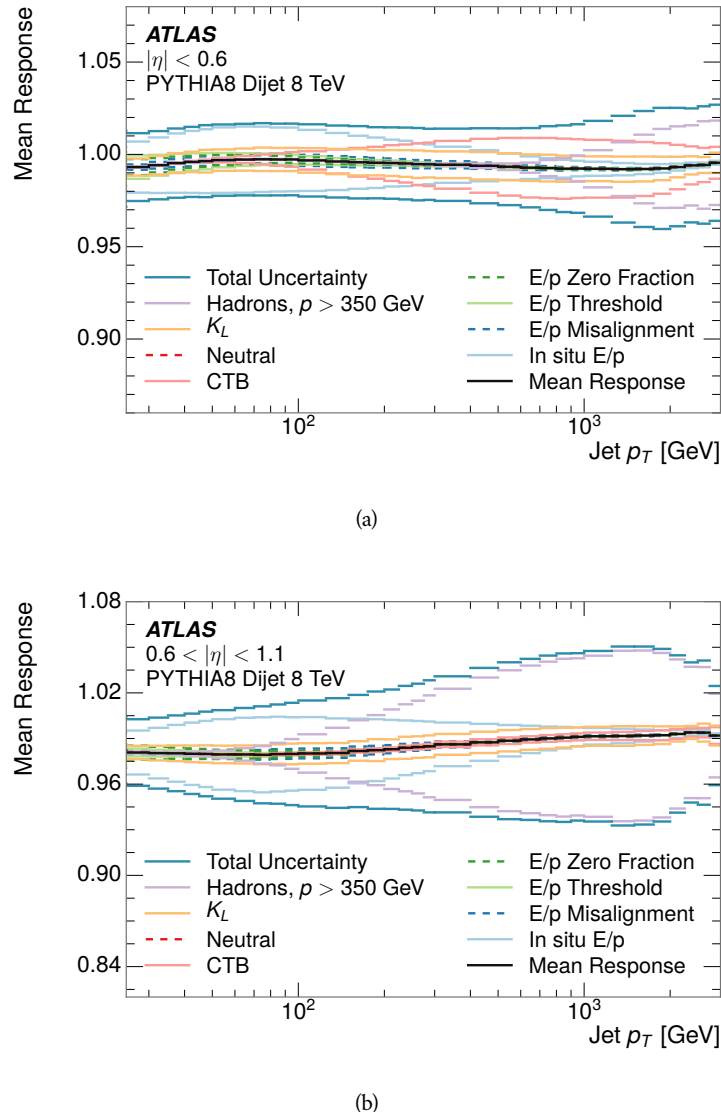


Figure 64: The JES response uncertainty contributions, as well as the total JES uncertainty, as a function of jet  $p_T$  for (a)  $|\eta| < 0.6$  and (b)  $0.6 < |\eta| < 1.1$ .

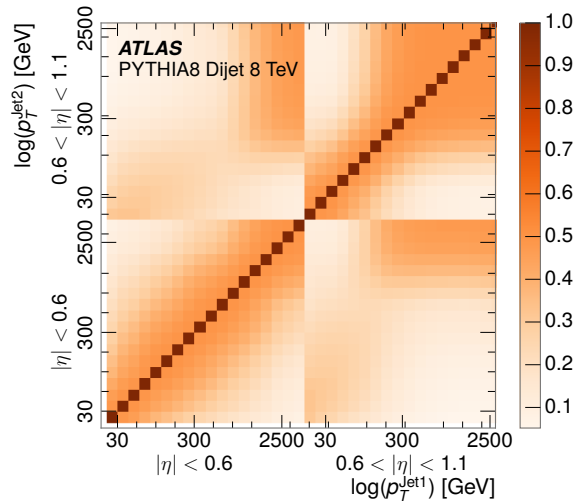


Figure 65: The correlations between bins of average reconstructed jet momentum as a function of jet  $p_T$  and  $|\eta|$  for jets in the central region of the detector.

2935

## PART IV

2936

### SEARCH FOR LONG-LIVED PARTICLES

2937

You can put some informational part preamble text here.

2938

2939 LONG-LIVED PARTICLES IN ATLAS

---

2940 As discussed in Section 2.6, various limitations in the SM suggest a need for new  
 2941 particles at the TeV scale. A wide range of extensions to the Standard Model  
 2942 predict that these new particles can have lifetimes greater than approximately  
 2943 one-hundredth of a nanosecond. These include theories with universal extra-  
 2944 dimensions [65, 66], with new fermions [67], and with leptoquarks [68]. As dis-  
 2945 cussed in Section 3.4, many SUSY theories also produce these LLPs, in both R-  
 2946 Parity violating [69–71] and R-Parity conserving [72–75] formulations. Split su-  
 2947 persymmetry [8, 9], for example, predicts long-lived gluinos with O(TeV) masses.  
 2948 This search focuses specifically on the SUSY case, but many of the results are  
 2949 generic to any model with LLPs.

2950 Long-lived gluinos or squarks carry color-charge and will thus hadronize into  
 2951 color neutral bound states called R-Hadrons. These are composit particles like  
 2952 the known hadrons but with one supersymmetric constituent, for example  $\tilde{g}q\bar{q}$   
 2953 and  $\tilde{q}\bar{q}$ . In this hadronization process, the gluino can acquire an electric charge.  
 2954 Gluino pair production,  $pp \rightarrow \tilde{g}\tilde{g} + X$ , where X denotes the proton remnants,  
 2955 has the largest cross sectional increase with the increase in energy to 13 TeV,  
 2956 and so this search uses gluino R-Hadrons as its benchmark model. The features,  
 2957 techniques, and cross section limits discussed here are all largely independent  
 2958 of the model. Planned future updates will extend the case to include additional  
 2959 refinements for squark and chargino models, but the current method covers any  
 2960 long-lived, charged, massive particle.

## 2961 9.1 EVENT TOPOLOGY

2962 R-parity conserving SUSY models predict that gluinos will be produced in pairs  
 2963 at the LHC, through the processes shown in Figure 66, where the quarks and  
 2964 gluons are proton constituents. The gluon-initiated mode dominates for the col-  
 2965 lision energy and gluino masses considered for this search. During their produc-  
 2966 tion, the long-lived gluinos hadronize into color singlet bound states including  
 2967  $\tilde{g}q\bar{q}$  and even  $\tilde{g}g$  [76]. The probability to form the gluon-only bound states is  
 2968 a free parameter usually taken to be 0.1, and 90% of the remaining R-Hadrons  
 2969 form meson states [77]. The charged and neutral states are approximately equally  
 2970 likely for mesons, so the R-Hadrons will be charged roughly 50% of the time.

2971 These channels produce R-Hadrons with large  $p_T$ , but lower on average than  
 2972 their mass, so that they typically propagate with  $0.2 < \beta < 0.9$  [77]. Figure 67  
 2973 shows the generated  $p_T$  and  $\beta$  distributions for a simulated example of R-Hadrons  
 2974 with a mass of 1600 GeV. The mean  $p_T$  is roughly half of the mass at 800 GeV,  
 2975 and so  $\beta$  peaks around 0.5. The fragmentation that produces that hadrons is  
 2976 very hard, so the jet structure around the R-Hadron is minimal, with less than 5  
 2977 GeV of summed particle momentum expected in a cone of  $\Delta R < 0.25$  around

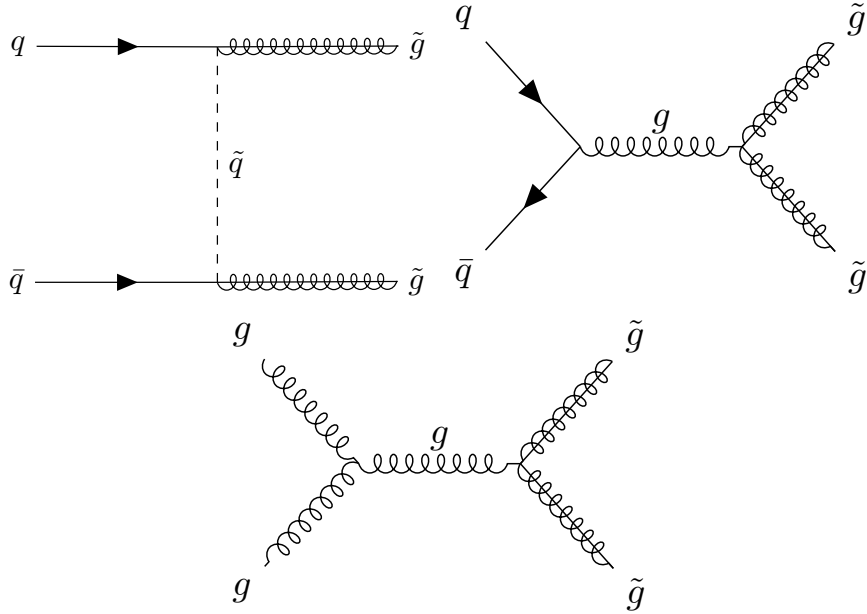


Figure 66: The processes which contribute to gluino pair production in the proton-proton collisions, where the quarks and gluons are proton constituents.

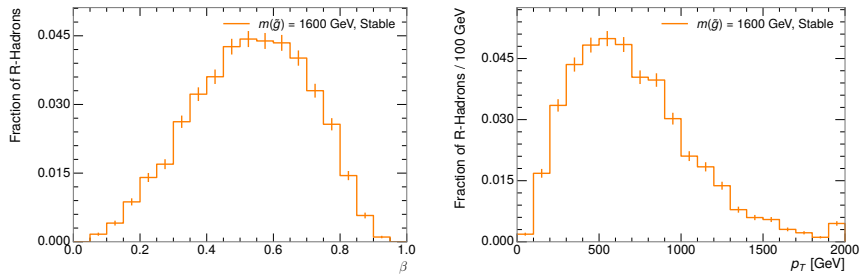


Figure 67: The generated  $p_T$  and  $\beta$  distributions for R-Hadrons with  $M = 1600$  GeV.

2978 the R-Hadron [77]. After hadronization, depending on the gluino lifetime, the  
2979 R-Hadrons then decay into hadrons and a LSP [76].

2980 In summary, the expected event for pair-produced long-lived gluinos is very  
2981 simple: two isolated, high-momentum R-Hadrons that propagate through the  
2982 detector before decaying to jets. The observable features of such events depend  
2983 strongly on the interaction of the R-Hadron with the material of the detector  
2984 and also its lifetime. Section 9.1.1 describes the interactions of R-Hadrons which  
2985 reach the various detector elements in ATLAS and Section 9.1.2 provides a sum-  
2986 mary of the observable event descriptions for R-Hadrons of various lifetimes.

2987 9.1.1 DETECTOR INTERACTIONS

2988 Although the distribution of decay times can be parametrized with a single pa-  
2989 rameter,  $\tau$ , the time before individual R-Hadrons decay follows an exponential  
2990 distribution, leading to a range of decay times for any individual lifetime. This is

further confounded by the distribution of  $\beta$  as well as  $\eta$ , so that each R-Hadron propagates at a different velocity and travels a different distance before reaching each detector element. Therefore, the lifetime-dependent event topologies must be discussed as an average, and all times referred to within this section will assume  $\beta = 0.5$ , an  $\eta = 0$ , and that the particle decays after a time equal to its lifetime. Table 9 lists the distances of various subdetectors and the time after which a LLP will arrive at that subdetector for a few values of  $\beta$  and with  $\eta = 0$ .

Subdetector	Distance	$\tau$ at $\beta = 0.3$	$\tau$ at $\beta = 0.5$	$\tau$ at $\beta = 0.7$
Pixel	3.1 cm	0.35 ns	0.20 ns	0.15 ns
Calorimeter	1.5 m	17 ns	10 ns	7.2 ns
Muon System	5 m	56 ns	33 ns	24 ns

Table 9: The radial distances of each of the subdetectors and example arrival times for an R-Hadron with  $\eta = 0$  and the specified  $\beta$ .

After approximately 0.2 ns, the R-Hadron reaches the first layer of the pixel detector. If charged, it deposits energy into the material through repeated single collisions that result in ionization of the silicon substrate [6]. Because of its comparatively low  $\beta$ , the ionization energy can be significantly greater than expected for SM particles because the most-probable energy loss grows significantly as  $\beta$  decreases [6]. This large ionization can be measured through the ToT read out from the pixel detector as described in Section 6.1.2. Large ionization in the inner detector is one of the major characteristic features of LLPs. The particle propagates through all four layers of the pixel detector, where each provides a measurement of ionization, and then exits the pixel detector at 0.8 ns.

Throughout the next few nanoseconds, the R-Hadron propagates through the remainder of the inner detector. A charged R-Hadron will provide hits in each of these systems as would any other charged particle, and can be reconstructed as a track. The track reconstruction provides a measurement of its trajectory and thus its  $p$  as described in Section 6.1. The large  $p_T$ , shown in Figure 67, is another characteristic feature of massive particles produced at the LHC.

As of roughly 10 ns, the R-Hadron enters the calorimeter where it interacts hadronically with the material. Because of its large mass and  $p$ , the R-Hadron does not typically stop in the calorimeter, but rather deposits a small fraction of its energy through repeated interactions with nucleons. The probability of interaction between the gluino itself and a nucleon is low because the cross section drops off with the inverse square of its mass, so the interactions are primarily governed by the light constituents [78]. Each of these interactions can potentially change that quark content and thus change the sign of the R-Hadron, so that the charge at exit is typically uncorrelated with the charge at entry [77]. The total energy deposited in the calorimeters during the propagation is small compared to the kinetic energy of the R-Hadron, around 20-40 GeV, so that  $E/p$  is typically less than 0.1 [77].

Then, 30 ns after the collision, it reaches the muon system, where it again ionizes in the material if charged and can be reconstructed as a muon track. Because of the charge-flipping interactions in the calorimeter, this track may have

3029 the opposite sign of the track reconstructed in the inner detector, or there may  
 3030 be a track present when there was none in the inner detector and vice-versa  
 3031 for those which are detected. The propagation time at the typically lower  $\beta$  re-  
 3032 sults in a significant delay compared to muons, and a delay over 25 ns causes  
 3033 the muon signal to be lost outside the readout window. Between the probabili-  
 3034 ty of charge-flip and late arrival, there is a significant chance that an R-Hadron  
 3035 which was produced with a charge will not be identified as a muon. When it is  
 3036 reconstructed as a muon, that delay can be assessed in terms of a time-of-flight  
 3037 measurement, which is another characteristic feature of R-Hadrons.

3038 9.1.2 LIFETIME DEPENDENCE

3039 The above description assumed a lifetime long enough for the R-Hadron to exit  
 3040 the detector, which through this search is referred to as **VLL**, as the particle may  
 3041 decay after exiting the detector. There are several unique signatures at shorter  
 3042 lifetimes where the R-Hadron decays in various parts of the inner detector; these  
 3043 lifetimes are referred to as **LL**.

3044 The shortest case where the R-Hadron is considered **LL** is for lifetimes around  
 3045 0.01 ns, where the particle decays before reaching any of the detector elements.  
 3046 Although the R-Hadrons are produced opposite each other in the transverse  
 3047 plane, each R-Hadron decays to a jet and an **LSP**. The two decays are uncorrelated,  
 3048 so the two **LSPs** carry different momenta and in different directions. And, since  
 3049 the **LSPs** are not measured, the produced jets can be significantly imbalanced in  
 3050 the transverse plane which results in large missing energy. That missing energy  
 3051 can be used to trigger candidate events, and provides the most efficient trigger  
 3052 option for shorter lifetimes. Additionally, the precision of the tracking system  
 3053 allows the displaced vertex of the R-Hadron decay to be reconstructed from the  
 3054 charged particles in the jet. The distance of that vertex from the interaction point  
 3055 can be used to distinguish R-Hadron decays from other processes. Figure 68  
 3056 shows a schematic diagram of an example R-Hadron event with such a lifetime.  
 3057 The diagram is not to scale, but instead illustrates the detector interactions in the  
 3058 pixel detector, calorimeters, and muon system. It includes a representation of a  
 3059 charged R-Hadron and a neutral R-Hadron, as well as the **LSPs** and jets (shown as  
 3060 charged hadrons) produced in the decay. Neutral hadrons may also be produced  
 3061 in the decay but are not depicted. Previous searches on ATLAS have used the  
 3062 displaced vertex to target **LLP** decays [79].

3063 The next distinguishable case occurs at lifetimes greater than 0.1 ns but less  
 3064 than 10 ns, where the R-Hadron forms a partial track in the inner detector. This  
 3065 forms a unique signature of a disappearing track. Two examples of such an event  
 3066 are illustrated in Figure 69 and Figure 70, which show the short track in the inner  
 3067 detector. The decay distance must be sufficiently long that it reaches the **SCT**, or  
 3068 else to track will not be reconstructed at all. Depending on the mass difference  
 3069 between the R-Hadron and the **LSP**, the decay products will either be a single, soft  
 3070 charged hadron and a **LSP** (Figure 69), or a jet and a **LSP** (Figure 70). A dedicated  
 3071 search on ATLAS used the disappearing track signature in the former case to  
 3072 search for **LLP** in Run 1 [80].

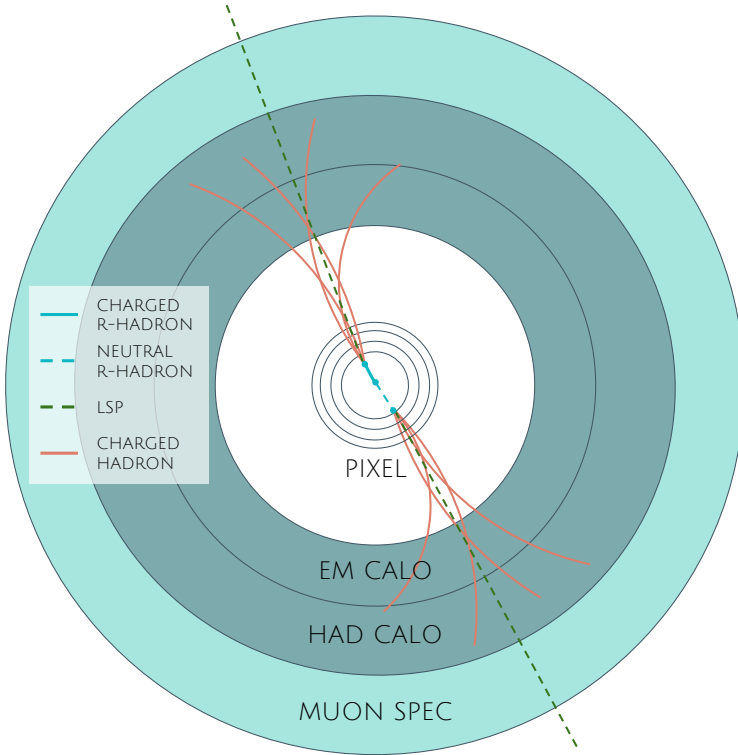


Figure 68: A schematic diagram of an R-Hadron event with a lifetime around 0.01 ns. The diagram includes one charged R-Hadron (solid blue), one neutral R-Hadron (dashed blue), LSPs (dashed green) and charged hadrons (solid orange). The pixel detector, calorimeters, and muon system are illustrated but not to scale.

3073 In the latter case, the decays result in an event-level signature of up to two high-  
 3074  $p$  tracks, jets, and significant missing energy. The missing energy has the same  
 3075 origin as in the case of 0.01 ns lifetimes, from the decay to unmeasured particles,  
 3076 and again can be large. The high- $p$  tracks will also have the characteristically high-  
 3077 ionization of massive, long-lived particles in the Pixel detector. Figure 70 shows  
 3078 how the jets from the decay can still be reconstructed in the calorimeter. Several  
 3079 previous searches on ATLAS from Run 1 have used this signature to search for  
 3080 R-Hadrons [81, 82], including a dedicated search for LL particles [83].

3081 If the lifetime is longer than several nanoseconds, in the range of 10–30 ns,  
 3082 the R-Hadron decay can occur in or after the calorimeters, but prior to reaching  
 3083 the muon system. In the case that the decays occur early enough within the  
 3084 calorimeters that the decay can be measured, the event topology is very similar  
 3085 to the above with jets originating in the inner detector. If the decay occurs after  
 3086 the calorimeter, jets may not be reconstructed at all. The events still often have  
 3087 large missing energy, although it is generated through different mechanisms, and  
 3088 so the same search strategy can be used. The R-Hadrons do not deposit much  
 3089 energy in the calorimeters, so a neutral R-Hadron will not enter into the miss-  
 3090 ing energy calculation. A charged R-Hadron opposite a neutral R-Hadron will  
 3091 thus generate significant missing energy, and close to 50% of pair-produced R-  
 3092 Hadron events fall into this category. If both R-Hadrons are neutral then the

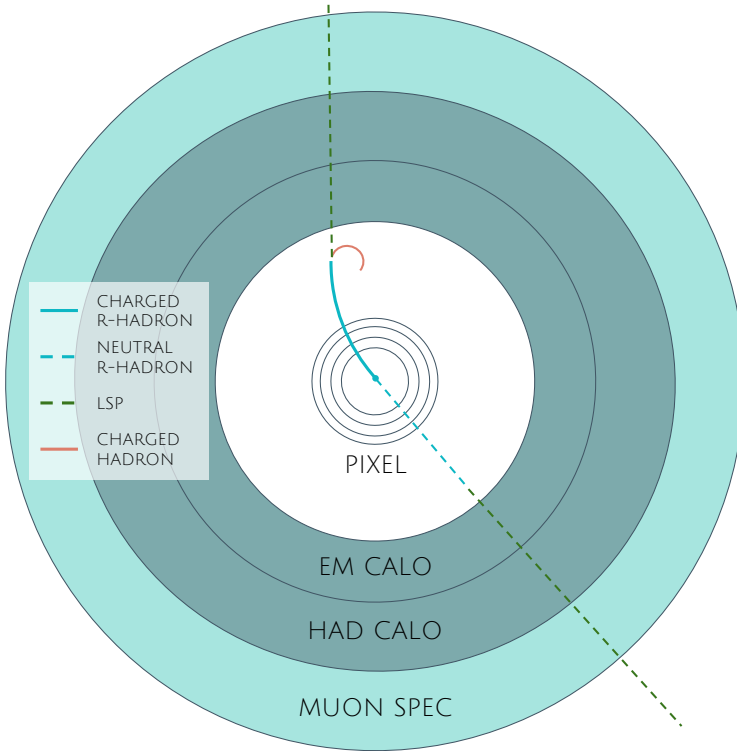


Figure 69: Schematic diagram of an R-Hadron event with a lifetime around 5 ns, where the masses of the R-Hadron and LSP are nearly degenerate. The diagram includes charged R-Hadrons (solid blue), neutral R-Hadrons (dashed blue), LSPs (dashed green) and charged hadrons (solid orange). The pixel detector, calorimeters, and muon system are illustrated but not to scale.

missing energy will be low because neither is detected. Two charged R-Hadrons will also result in low missing energy because both are reconstructed as tracks and will balance each other in the transverse plane. A small fraction of the time, one of the charged R-Hadron tracks may fail quality requirements and thus be excluded from the missing energy calculation and again result in significant missing energy. Figure 71 illustrates another example event with one charged R-Hadron which decays after approximately 20 ns, and shows how the jets from the decay might not be reconstructed.

The longest lifetimes, the VLL case, has all of the features of the 30-50 ns case but with the addition of muon tracks for any R-Hadrons that exit the calorimeter with a charge. That muon track can provide additional information from time-of-flight measurements to help identify LLPs. An example of the event topology for one charged and one neutral VLL R-Hadron is shown in Figure 72. Some searches on ATLAS have included this information to improve the search reach for VLL particles [82, 84].

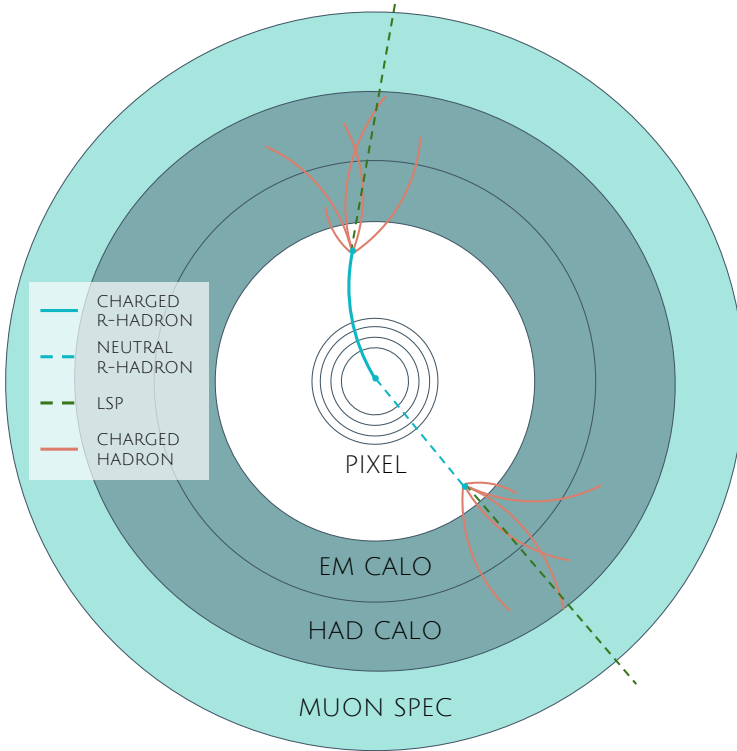


Figure 70: Schematic diagram of an R-Hadron event with a lifetime around 5 ns, where the masses of the R-Hadron and LSP are not degenerate. The diagram includes charged R-Hadrons (solid blue), neutral R-Hadrons (dashed blue), LSPs (dashed green) and charged hadrons (solid orange). The pixel detector, calorimeters, and muon system are illustrated but not to scale.

## 3108 9.2 SIMULATION

3109 All of the event topologies discussed above are modeled by simulations of R-  
 3110 Hadron events in the ATLAS detector. A large number of such samples are  
 3111 generated to determine efficiencies, to measure expected yields, and to estimate  
 3112 uncertainties. The primary interaction, pair production of gluinos with masses  
 3113 between 400 and 3000 GeV, is simulated using `Pythia 6.4.27` [85] with the  
 3114 `AUET2B` [86] set of tuned parameters for the underlying event and the `CTEQ6L1` [62]  
 3115 `PDF` set. The simulated interactions include a modeling of pileup by adding sec-  
 3116 ondary, minimum bias interactions from both the same (in-time pileup) and  
 3117 nearby (out-of-time pileup) bunch crossings. This event generation is then aug-  
 3118 mented with a dedicated hadronization routine to hadronize the long-lived gluinos  
 3119 into final states with R-Hadrons [87], with the probability to form a gluon-gluino  
 3120 bound set at 10% [88].

3121 The cross sections used for these processes are calculated at next-to-leading  
 3122 order (`NLO`) in the strong coupling constant with a resummation of soft-gluon  
 3123 emmision at next-to-leading logarithmic (`NLL`) [89–93]. The nominal predic-  
 3124 tions and the uncertainties for each mass point are taken from an envelope of  
 3125 cross-section predictions using different `PDF` sets and factorization and renor-  
 3126 malization scales [94]. As discussed in Section 2.5.3, the `PDFs` and scales deter-

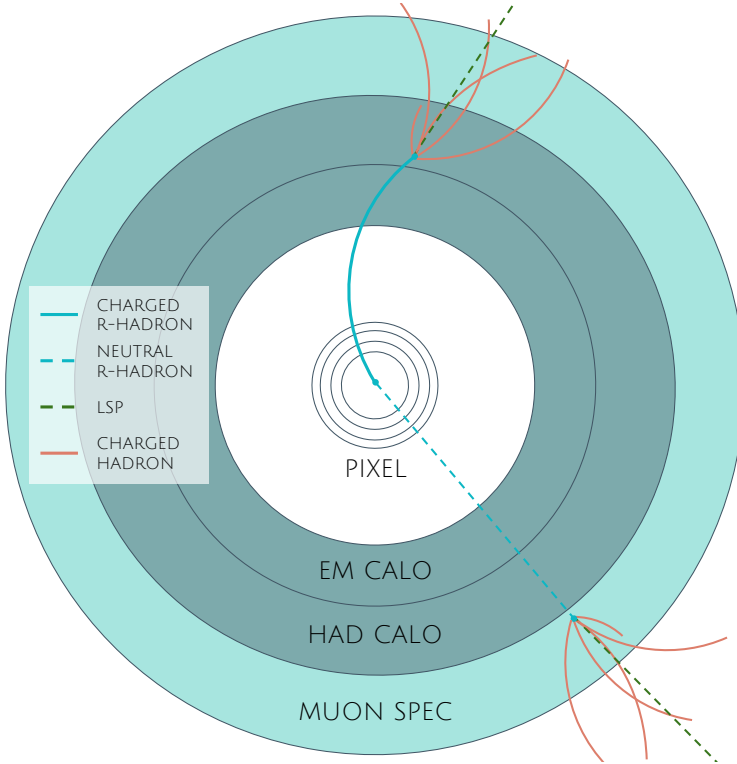


Figure 71: A schematic diagram of an R-Hadron event with a lifetime around 20 ns. The diagram includes one charged R-Hadron (solid blue), one neutral R-Hadron (dashed blue), LSPs (dashed green) and charged hadrons (solid orange). The pixel detector, calorimeters, and muon system are illustrated but not to scale.

3127 mine the cross section by providing the probabilities of the proton constituents  
 3128 to interact. Multiple estimates for the PDF and scales at 13 TeV can be used to  
 3129 provide an average cross section calculation and its uncertainty.

3130 The R-Hadrons then undergo a full detector simulation [37], where the inter-  
 3131 actions of the R-Hadrons with the material of the detector are described by ded-  
 3132 icated Geant4 [32] routines. These routines model the interactions described in  
 3133 Section 9.1.1, including the ionizing interactions in the silicon modules of the in-  
 3134 inner detector and the R-Hadron-nucleon interactions in the calorimeters [95, 96].  
 3135 The specific routine chosen to describe the interactions of the R-Hadrons with  
 3136 nucleons, the “generic model”, uses a pragmatic approach where the scattering  
 3137 cross section is taken to be a constant 12 mb per light quark. In this model the  
 3138 gluino itself does not interact at all, although it carries most of the kinetic energy  
 3139 of the bound state.

3140 The lifetimes of these R-Hadrons are then simulated at several working points,  
 3141  $\tau = 0.1, 1.0, 3.0, 10, 30, 50$  and  $> 50\text{ns}$ . The actual decay times follow an expo-  
 3142 nential distribution, where  $\tau$  is the characteristic time. Only one decay mode is  
 3143 simulated for these benchmark samples,  $\tilde{g} \rightarrow q\bar{q}\tilde{\chi}_1^0$  with the neutralino mass set  
 3144 to 100 GeV. The search discussed here is also efficient for heavier neutralinos,  
 3145 which have very similar topologies but which generate less missing energy.

3146 All of the simulated events are then reconstructed using the same software  
 3147 used for collision data. The fully reconstructed events are then reweighted to

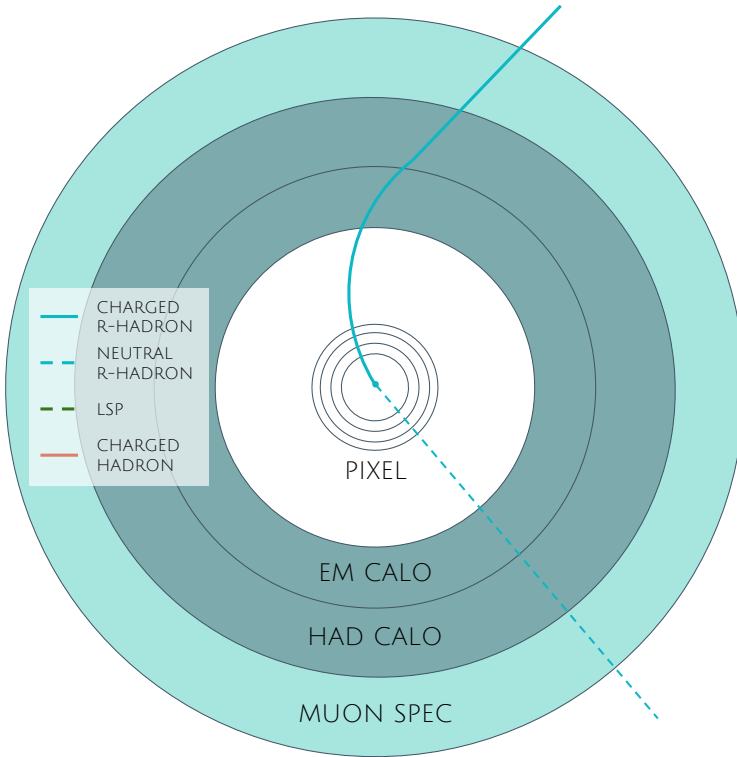


Figure 72: A schematic diagram of a [VLL](#) R-Hadron event. The diagram includes one charged R-Hadron (solid blue) and one neutral R-Hadron (dashed blue). The pixel detector, calorimeters, and muon system are illustrated but not to scale.

3148 match the distribution of initial state radiation in an alternative sample of events,  
 3149 generated with MG5\_aMC@NLO [97], which has had a more accurate description  
 3150 of radiate effects than Pythia6 in previous iterations [83]. MG5\_aMC@NLO pre-  
 3151 dictes a harder distribution of initial state radiation, where 28% more simulated  
 3152 events generate sufficient missing energy to trigger for [VLL](#) R-Hadrons. This  
 3153 reweighting provides a more accurate description of the  $p$  of the gluino-gluino  
 3154 system and is important in modeling the efficiency of triggering and offline event  
 3155 selection.

3156

3157 EVENT SELECTION

---

3158 The **LLPs** targeted by this search differ in their interactions with the detector from  
 3159 **SM** particles primarily because of their large mass. When produced at the ener-  
 3160 gies available at the **LHC**, that large mass results in a low  $\beta$  (typically  $0.2 < \beta < 0.9$   
 3161 as shown in Figure 67). Such slow-moving particles heavily ionize in detector  
 3162 material. Each layer of the pixel detector provides a measurement of that ion-  
 3163 ization, through **ToT**, as discussed in Section 6.1.2. The ionization in the pixel  
 3164 detector, quantified in terms of  $dE/dx$ , provides the major focus for this search  
 3165 technique, along with the momentum measured in the entire inner detector. It is  
 3166 effective both for its discriminating power and its use in reconstructing a parti-  
 3167 cle's mass, and it can be used for a wide range of masses and lifetimes as discussed  
 3168 in Section 9.1.2. However  $dE/dx$  needs to be augmented with a few additional  
 3169 selection requirements to provide a mechanism for triggering and to further re-  
 3170 duce backgrounds.

3171 Ionization itself is not currently accessible for triggering, so this search in-  
 3172 stead relies on  $E_T^{\text{miss}}$  to trigger signal events. Although triggering on  $E_T^{\text{miss}}$  can  
 3173 be inefficient,  $E_T^{\text{miss}}$  is often large for many production mechanisms of **LLPs**, as  
 3174 discussed in Section 9.1.

3175 The use of ionization to reject **SM** backgrounds relies on well-measured, high-  
 3176 momentum tracks, so some basic requirements on quality and kinematics are  
 3177 placed on the tracks considered in this search. A few additional requirements  
 3178 are placed on the tracks considered for **LLP** candidates that increase background  
 3179 rejection by targeting specific types of **SM** particles.

3179 The ionization measurement with the Pixel detector can be calibrated to pro-  
 3180 vide an estimator of  $\beta\gamma$ . That estimate, together with the momentum measure-  
 3181 ment provided by tracking, can be used to reconstruct a mass for each track  
 3182 which traverses the pixel detector,

$$m = \frac{p}{\beta\gamma} \quad (20)$$

3180 That mass variable will be peaked at the **LLP** mass for any signal, and provides an  
 3181 additional tool to search for an excess. In addition to an explicit requirement on  
 3182 ionization, this search constructs a mass-window for each targeted signal mass  
 3183 in order to search for an excess of events.

3184 The strategy discussed here is optimized for lifetimes of  $O(1) - O(10)$  ns.  
 3185 The specific values for each requirement in signal region were optimized con-  
 3186 sidering the increase in discovery reach for tightening the requirement on each  
 3187 discriminating variable. Pixel ionization is especially useful in this regime as  
 3188 particles only need to propagate through the first seven layers of the inner de-  
 3189 tector, about 37 cm from the beam axis. The search is still competitive with  
 3190 other searches for **LLPs** at longer lifetimes, because the primary discriminating

variables are still applicable even for particles that do not decay within the detector [84]. Although the majority of the requirements will be the same for all lifetimes, two signal regions are defined to optimize separately for intermediate and long lifetime particles.

## 10.1 TRIGGER

Triggering remains a significant difficulty in defining an event selection with high signal efficiency in a search for LLPs. There are no triggers available in the current ATLAS system that can fire directly from a high momentum track with large ionization, as tracking is not available at L1 (Section 5.6). Although in some configurations a charged LLP can fire muon triggers, this requirement introduces significant model dependence on both the allowed lifetimes and the interactions in the calorimeter [77], as discussed in Section 9.1.1.

For a search targeting particles which may decay prior to reaching the muon system, the most efficient available trigger is based on missing energy [77]. As discussed in Section 9.1, signal events can produce significant  $E_T^{\text{miss}}$  by a few mechanisms. At the trigger level however, the missing energy is only calculated using the calorimeters (Section 5.6) where the R-Hadrons deposit little energy. So, at short lifetimes,  $E_T^{\text{miss}}$  measured in the calorimeter is generated by an imbalance between the jets and undetected LSPs produced in R-Hadron decays. At longer lifetimes, without the decay products, missing energy is only produced in the calorimeters when the R-Hadrons recoil against an ISR jet.

These features are highlighted in Figure 73, which shows the  $E_T^{\text{miss}}$  distributions for simulated short lifetime (3 ns) and VLL R-Hadron events. The figure includes both the offline  $E_T^{\text{miss}}$ , the missing energy calculated with all available information, and Calorimeter  $E_T^{\text{miss}}$ , the missing energy calculated using only information available at the calorimeter which approximates the missing energy available at the trigger. The short lifetime sample has significantly greater  $E_T^{\text{miss}}$  and Calorimeter  $E_T^{\text{miss}}$  than the VLL sample as expected. For the VLL sample, a small fraction of events with very large  $E_T^{\text{miss}}$  (about 5%) migrate into the bin with very small Calorimeter  $E_T^{\text{miss}}$  because the  $E_T^{\text{miss}}$  produced by a charged R-Hadron track opposite a neutral R-Hadron track does not contribute any missing energy in the calorimeters.

So, either case to some extent relies on kinematic degrees of freedom to produce missing energy, as the pair-produced LLPs tend to balance each other in the transverse plain. For long lifetimes in particular, the presence of ISR is important in providing an imbalance in the transverse plane, and is an important aspect of modeling the selection efficiency for R-Hadron events. The missing energy trigger with the lowest threshold available is chosen for this selection in order to maximize the trigger efficiency. The formation of the trigger decision for missing energy was discussed in more detail in Section 5.6. During 2015 data collection this was the HLT\_xe70 trigger, which used a 50 GeV threshold on missing energy at L1 and a 70 GeV threshold on missing energy at the HLT which is nearly 100% efficient after the L1 requirement. With these thresholds, the incomplete balance of the LSPs results in a relatively low efficiency for long-

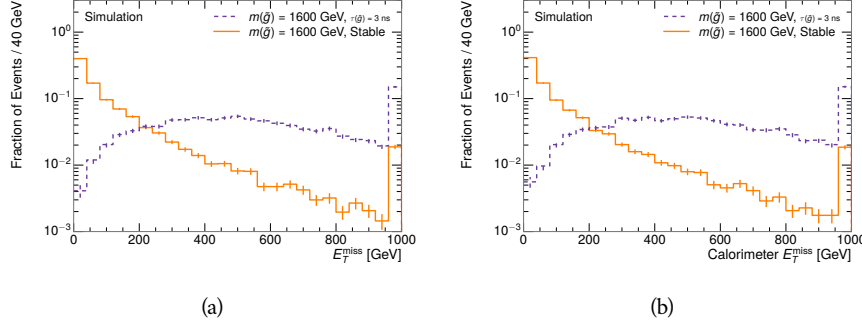


Figure 73: The distribution of (a)  $E_T^{\text{miss}}$  and (b) Calorimeter  $E_T^{\text{miss}}$  for simulated signal events before the trigger requirement. The final bin includes all events above the axis range.

3235 lifetime particles, roughly 40%, and efficiencies between 65% and 95% for shorter  
 3236 lifetimes depending on both the mass and the lifetime.

## 3237 10.2 KINEMATICS AND ISOLATION

3238 After the trigger requirement, each event is required to have a primary vertex  
 3239 reconstructed from at least two well-measured tracks in the inner detector, each  
 3240 with  $p_T > 400$  MeV. If more than one such vertex exists, the primary vertex is  
 3241 taken to be the one with the largest summed  $p_T^2$  for all tracks associated to that  
 3242 vertex. The offline reconstructed  $E_T^{\text{miss}}$  is required to be above 130 GeV to addi-  
 3243 tionally reject SM backgrounds. The transverse missing energy is calculated us-  
 3244 ing fully reconstructed and calibrated offline objects, as described in Section 6.5.  
 3245 In particular the  $E_T^{\text{miss}}$  definition in this selection uses jets reconstructed with the  
 3246 anti- $k_t$  algorithm with radius  $R = 0.4$  from clusters of energy in the calorimeter  
 3247 (Section 6.4) and with  $p_T > 20$  GeV, as well as reconstructed muons, electrons,  
 3248 and tracks not identified as another object type.

3249 The  $E_T^{\text{miss}}$  distributions are shown for data and a few simulated signals in Fig-  
 3250 ure 74, after the trigger requirement. The data contains some events with  $E_T^{\text{miss}}$   
 3251 below the nominal trigger threshold of 70 GeV, which can occur because  $E_T^{\text{miss}}$   
 3252 at trigger level uses only calorimeter information while the full offline  $E_T^{\text{miss}}$   
 3253 additionally includes tracks and muons which can balance the event. The cut  
 3254 placed at 130 GeV is 95% efficient for LL and 90% efficient for VLL particles, after  
 3255 the trigger requirement, because of the missing energy generating mechanisms  
 3256 discussed previously. The distribution of data in this figure and subsequent fig-  
 3257 ures in this section can be interpreted as the distribution of backgrounds, as any  
 3258 signal contamination would be negligible if present at these early stages of the  
 3259 selection (prior to the final requirement on ionization). The background falls  
 3260 rapidly with missing energy, motivating the direct requirement on  $E_T^{\text{miss}}$  for the  
 3261 signal region.

3262 It is typically the practice for searches for new physics on ATLAS to place an  
 3263 offline requirement on the triggering variable that is sufficiently tight to guar-

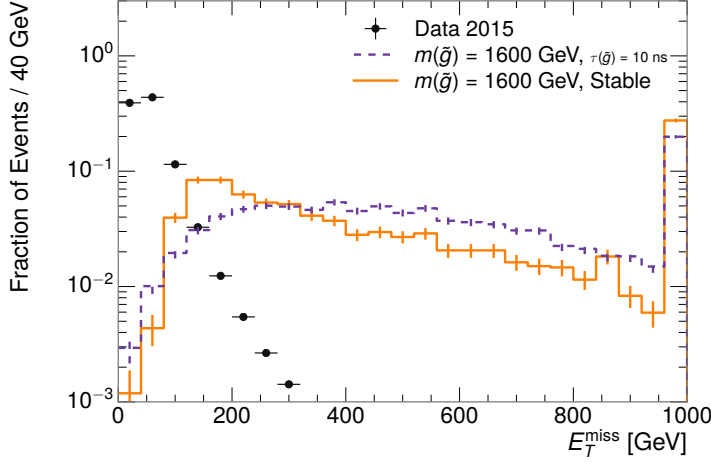


Figure 74: The distribution of  $E_T^{\text{miss}}$  for data and simulated signal events, after the trigger requirement. The final bin includes all events above the axis range.

3264 antee that the event would pass the trigger. Such a tight requirement makes the  
 3265 uncertainty on the trigger efficiency of the simulation negligible, as modeling the  
 3266 regime where the trigger is only partially efficient can be difficult. In this analy-  
 3267 sis, however, because of the atypical interactions of R-Hadrons with the tracker  
 3268 and the calorimeter, the offline requirement on  $E_T^{\text{miss}}$  is not sufficient to guar-  
 3269 antee a 100% trigger efficiency even at large values, as can be seen in Figure 75.  
 3270 This figure shows the efficiency for passing the HLT\_xe70 trigger as a function  
 3271 of the requirement on  $E_T^{\text{miss}}$ , which plateaus to roughly 85% even at large values.  
 3272 This plateau does not reach 100% because events which have large offline miss-  
 3273 ing energy from a neutral R-Hadron produced opposite of a charged R-Hadron  
 3274 can have low missing energy in the calorimeters. The Calorimeter  $E_T^{\text{miss}}$ , on the  
 3275 other hand, does not have this effect and reaches 100% efficiency at large values  
 3276 because it is the quantity that directly corresponds to the trigger threshold. In  
 3277 both cases the efficiency of triggering is greater for the short lifetime sample be-  
 3278 cause the late decays to hadrons and LSPs produce an imbalance in the calorime-  
 3279 ters even though they may not be reconstructed offline as tracks or jets. For this  
 3280 reason, the requirement on  $E_T^{\text{miss}}$  is determined by optimizing the background  
 3281 rejection even though it corresponds to a value of trigger efficiency significantly  
 3282 below 1.0.

3283 The events are then required to have at least one candidate LLP track. Al-  
 3284 though the LLPs are produced in pairs, many models do not consistently yield  
 3285 two charged particles, as discussed in Chapter 9. For example, in the R-Hadron  
 3286 model highlighted here, only 20% of events have two charged R-Hadrons while  
 3287 47% of events have just one. A signal region requiring two charged particle can-  
 3288 didates could be a powerful improvement in background rejection for a larger  
 3289 dataset, but it is not considered in this version of the analysis as it was found to  
 3290 be unnecessary to reject the majority of backgrounds.

3291 For a track to be selected as a candidate, it must have  $p_T > 50 \text{ GeV}$  and pass  
 3292 basic quality requirements. The track must be associated to the primary vertex.

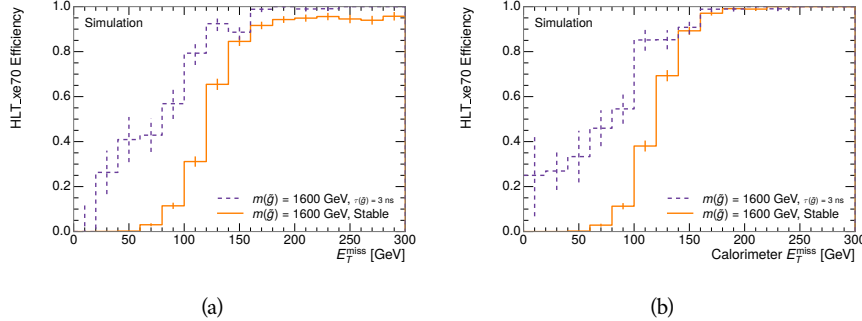


Figure 75: The trigger efficiency for the HLT\_xe70 trigger requirement as a function of (a)  $E_T^{\text{miss}}$  and (b) Calorimeter  $E_T^{\text{miss}}$  for simulated signal events.

It must also have at least seven clusters in the silicon layers in the inner detector to ensure an accurate measurement of momentum. Those clusters must include one in the innermost layer if the extrapolated track is expected to pass through that layer. And to ensure a reliable measurement of ionization, the track is required to have at least two clusters in the pixel detector that provide a measurement of  $dE/dx$ .

At this point in the selection, there is a significant high-ionization background from multiple tracks that significantly overlap in the Pixel detector. Previous versions of this analysis have rejected these overlaps by an explicit overlap rejection between pairs of fully reconstructed tracks, typically by requiring no additional tracks within a cone around the candidate. This technique, however, fails to remove the background from tracks that overlap so precisely that the tracks cannot be separately resolved, which can be produced in very collimated photon conversions.

Another observable, which more directly targets track overlaps, identifies cluster shapes that are likely formed by multiple particles based on a neural network classification algorithm, as discussed in Section 6.1.1. The number of clusters on a given track that are estimated to have contributions from more than one particle is called  $N_{\text{split}}$ . As the shape of clusters requires significantly less spatial separation to identify overlaps than it does to reconstruct two fully resolved tracks, this variable is more effective at rejecting backgrounds from overlaps. Figure 76 shows the dependence of ionization on  $N_{\text{split}}$ ; as  $N_{\text{split}}$  increases the most probable value of  $dE/dx$  grows significantly up to twice the expected value when  $N_{\text{split}} = 4$ .

A requirement of  $N_{\text{split}} = 0$  is very successful in reducing the long positive tail of the  $dE/dx$  distributions, as can be seen in Figure 77. Comparing the distribution for “baseline tracks”, tracks with only the above requirements on clusters applied and before the requirement on  $N_{\text{split}}$ , to the distribution with  $N_{\text{split}} = 0$ , it is clear that the fraction of tracks with large  $dE/dx$  is reduced by several orders of magnitude. The tracks without split hits are very close to the  $dE/dx$  distribution of identified muons, which are usually well isolated. Figure 77 also includes the distribution of  $dE/dx$  in an example signal simulation to demonstrate how effective  $dE/dx$  is as a discriminating variable with this isolation applied. The

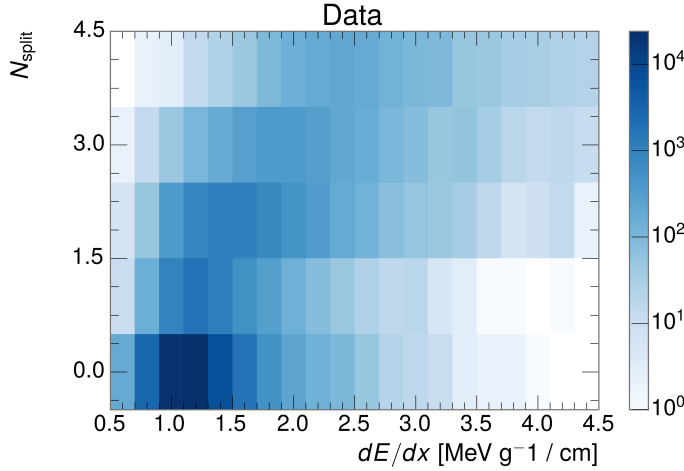


Figure 76: The dependence of  $dE/dx$  on  $N_{\text{split}}$  in data after basic track hit requirements have been applied.

background falls rapidly for  $dE/dx > 1.8 \text{ MeVg}^{-1}\text{cm}^2$  while the majority of the signal, approximately 90% depending on the mass, falls above that threshold. Over 90% of LLP tracks in simulated signal events pass the  $N_{\text{split}}$ -based isolation requirement.

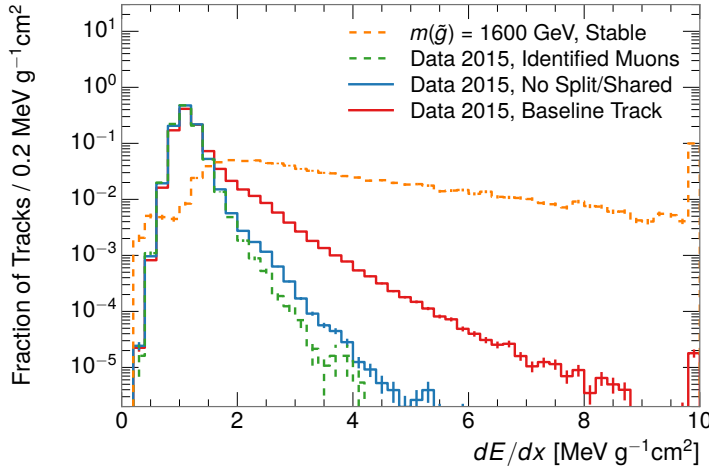


Figure 77: The distribution of  $dE/dx$  with various selections applied in data and simulated signal events. The final bin includes all tracks above the axis range.

A few additional kinematic requirements are imposed to help reduce SM backgrounds. The momentum of the candidate track must be at least 150 GeV, and the uncertainty on that measurement must be less than 50%. The distribution of momentum is shown in Figure 78 for tracks in data and simulated signal events after the previously discussed requirements on clusters, transverse momentum, and isolation have been imposed. The signal particles are much harder on av-

verage than their backgrounds as shown in Figure 67. The transverse mass,  $M_T$ , defined as

$$M_T = \sqrt{2p_T E_T^{\text{miss}}(1 - \cos(\Delta\phi(E_T^{\text{miss}}, \text{track})))} \quad (21)$$

estimates the mass of a decay of to a single charged particle and an undetected particle and is required to be greater than 130 GeV to reject contributions from the decay of W bosons. Figure 79 shows the distribution of  $M_T$  for data and simulated signal events. The signal is distributed over a wide range of  $M_T$ , with about 90% above the threshold value of 130 GeV. The data has a large number of contributions below 100 GeV from W boson decays and an additional peak from a kinematic shaping imposed by the requirements on  $E_T^{\text{miss}}$  and the track  $p_T$  in dijet events.

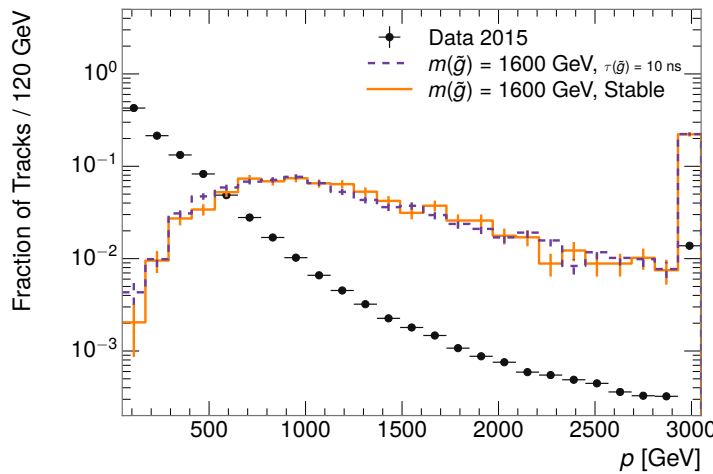


Figure 78: The distribution of track momentum for data and simulated signal events, after previous selection requirements have been applied. The final bin includes all tracks above the axis range.

### 10.3 PARTICLE SPECIES REJECTION

The amount of ionization deposited by particles with low mass and high momentum has a large positive tail [6], so backgrounds can be formed by a wide variety of SM processes when various charged particles have a few randomly large deposits of energy in the pixel detector. Those backgrounds can be additionally reduced by targeting other interactions with the detector where they are expected to have different behavior than R-Hadrons. The interactions with the detector depend on the types of particles produced rather than the processes which produce them, so this search forms a series of rejections to remove backgrounds from individual particle species. These rejections focus on using additional features of the event, other than the kinematics of the candidate track, as they can provide a powerful source of background rejection with very high signal efficiency. However, the lifetime of an R-Hadron can significantly change

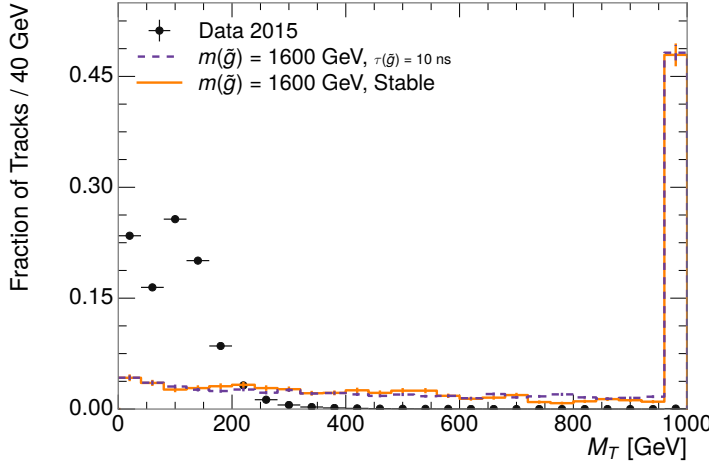


Figure 79: The distribution of  $M_T$  for data and simulated signal events, after previous selection requirements have been applied. The final bin includes all tracks above the axis range.

its detector characteristics, as discussed in Section 9.1.2. To accommodate these differences, the **SM** rejections defined in this section are split to form two signal regions, one for long-lifetimes particles, the **VLL** region ( $\tau[\text{ns}] \geq 50 \text{ ns}$ ), and one for intermediate lifetime particles, the **LL** region ( $0.4 < \tau[\text{ns}] < 50$ ).

Jets can contribute high momentum track backgrounds when an individual jet constituent carries large  $p_T$ . These tracks can be sufficiently well isolated from the other constituents that they are separately reconstructed and pass the  $N_{\text{split}}$  requirement. However, jets can be very effectively rejected by considering the larger-scale isolation of the candidate track. In this case the isolation focuses on the production of nearby particles as a jet-veto, rather than the isolation from overlapping tracks based on  $N_{\text{split}}$  that was used to reduce high-ionization backgrounds. As explained in Section 9.1, the fragmentation process which produces an R-Hadron is very hard and thus is not expected to produce additional particles with a summed momentum of more than 5 GeV. Nearby particles may be produced in the decay of the R-Hadron, but they will be significantly displaced, so the jet-veto only considers tracks associated to the primary vertex. The jet-veto uses the summed momentum of tracks with a cone of  $\Delta R < 0.25$ , referred to as  $p_T^{\text{Cone}}$ , which is shown in Figure 80 for data and simulated signal events. In the data this value has a peak at zero from isolated tracks such as leptons, and a long tail from jets which contains as much as 80% of the background above 20 GeV at this stage of the selection. In signal events  $p_T^{\text{Cone}}$  is strongly peaked at zero and significantly less than 1% of signal events have  $p_T^{\text{Cone}}$  above 20 GeV. This makes a requirement of  $p_T^{\text{Cone}} < 20 \text{ GeV}$  a very effective method to reject background without losing signal efficiency. For the **VLL** signal region, this cut is further tightened to  $p_T^{\text{Cone}} < 5 \text{ GeV}$  as it is the most effective variable remaining to extend the search reach for long lifetimes.

Even for fully isolated particles, there are additional methods to reject each type of particle using information in the muon system and calorimeters. Muons

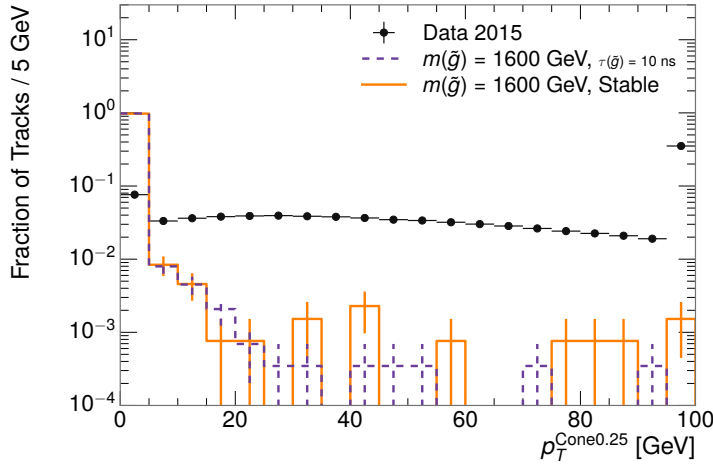


Figure 80: The distribution of summed tracked momentum within a cone of  $\Delta R < 0.25$  around the candidate track for data and simulated signal events, after previous selection requirements have been applied. The final bin includes all tracks above the axis range.

can be identified very reliably using the tracks in the muon system, as described in Section 6.3. For intermediate lifetimes ( $0.4 < \tau[\text{ns}] < 30$ ), the LLPs do not survive long enough to reach the muon system, and so muons are vetoed by rejecting tracks that associate to a muon with medium muon identification requirements (Section 6.3). For longer lifetimes ( $\tau > 30$  ns), this rejection is not applied because LLPs which reach the muon system can be identified as muons as often as 30% of the time in simulated samples.

Calorimeter-based particle rejection relies on the expected small deposits of energy from LLPs. When the lifetime is long enough to reach the calorimeter, a LLP deposits little of its energy as it traverses the material, as discussed in Section 9.1. Even when the particle does decay before the calorimeter, the majority of its energy is carried away by the LSP and not deposited in the calorimeter. In both cases the energy is expected to be distributed across the layers of the calorimeters and not peaked in just one layer. This can be quantified in terms of  $E/p$ , the ratio of calorimeter energy of a nearby jet to the track momentum, and  $f_{\text{EM}}$ , the fraction of energy in that jet within the electromagnetic calorimeter. When no jets fall within a cone of 0.05 of the particle,  $E/p$  and  $f_{\text{EM}}$  are both defined as zero.  $E/p$  is expected to be above 1.0 for electrons and hadrons because of the contributions from other nearby particles. At these momenta there is no significant fraction of tracks with no associated clusters due to interactions with the detector or insufficient energy deposits (see Section 7.2.2).  $f_{\text{EM}}$  is peaked close to 1.0 for electrons, and distributed between 10% and 90% for hadrons.

These trends can be seen in the two dimensional distribution for signal in Figure 81 for VLL and LL (10 ns) signal events. The majority of R-Hadrons in both samples fall into the bin for  $E/p = 0$  and  $f_{\text{EM}} = 0$  because the majority of the time there is no associated jet. In the VLL sample, when there is an associated jet,  $E/p$  is typically still below 0.1, and the  $f_{\text{EM}}$  is predominantly less than 0.8.

3414 In the LL sample, on the other hand,  $E/p$  is larger on average because of the jets  
 3415 produced in the R-Hadron decay. It is still typically below 0.1, however, because  
 3416 most of the energy of the R-Hadron is carried by the LSP and not the jet. The  
 3417  $f_{\text{EM}}$  is much lower on average in this case, below 0.1, because the 10 ns lifetime  
 3418 particles rarely decay before passing through the electromagnetic calorimeter.  
 3419 Figure 81 also includes simulated Z decays to electrons or tau leptons. From the  
 3420 decays to electrons it is clear that the majority of electrons have  $f_{\text{EM}}$  above 0.9.  
 3421 The  $\tau$  decays include a variety of products. Muons can be seen in the bin where  
 3422  $E/p = 0$  and  $f_{\text{EM}} = 0$  because they do not have an associated jet. Electrons fall  
 3423 into the range where  $E/p > 1$  and  $f_{\text{EM}} > 0.9$ . Hadronic tau decays are the most  
 3424 common, and fall in the range of  $0.1 < f_{\text{EM}} < 0.9$  and  $E/p > 1.0$ .

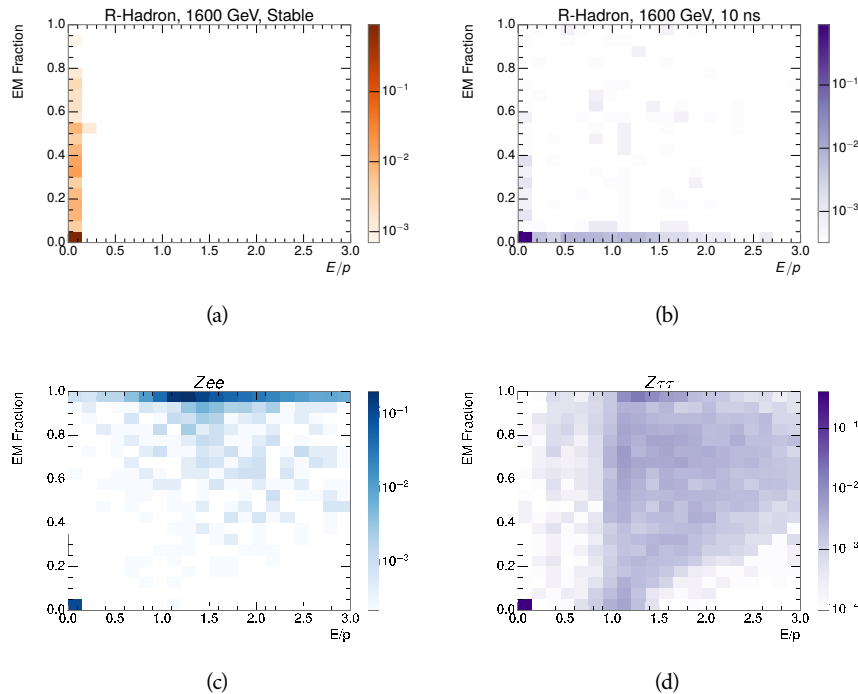


Figure 81: The normalized, two-dimensional distribution of  $E/p$  and  $f_{\text{EM}}$  for simulated  
 (a) 1200 GeV VLL R-Hadron, and (b) 1200 GeV, 10 ns R-Hadron, (c)  $Z \rightarrow ee$ ,  
 and (d)  $Z \rightarrow \tau\tau$  events.

3425 The differences motivate an electron rejection by requiring  $f_{\text{EM}} < 0.9$ . Simi-  
 3426 larly, isolated hadrons are rejected by requiring  $E/p < 1.0$ . These requirements  
 3427 combine to remove the majority of isolated electrons and hadrons but retain over  
 3428 95% of the simulated signal across a range of masses and lifetimes. The suite of  
 3429 particle species rejection techniques provide a significant analysis improvement  
 3430 over previous iterations of ionization-based searches on ATLAS by providing  
 3431 additional background rejection with minimal loss in signal efficiency.

3432 10.4 IONIZATION

3433 The final requirement on the candidate track is the primary discriminating vari-  
 3434 able, the ionization in the pixel detector. That ionization is measured in terms  
 3435 of  $dE/dx$ , which was shown for data and simulated signal events in Figure 77.  
 3436  $dE/dx$  is dramatically greater for the high mass signal particles than the back-  
 3437 grounds, which start to fall immediately after the minimally ionizing peak at 1.1  
 3438 MeV g $^{-1}$  cm $^2$ . The  $dE/dx$  for candidate tracks must be greater than a pseudorapidity-  
 3439 dependent threshold, specifically  $1.80 - 0.11|\eta| + 0.17\eta^2 - 0.05|\eta|^3$  MeV g $^{-1}$  cm $^{-2}$ ,  
 3440 in order to correct for an approximately 5% dependence of the MIP peak position  
 3441 on  $\eta$ . The requirement was chosen as part of the signal region optimization, and  
 3442 reduces the backgrounds by a factor of 100 while remaining 70-90% efficient for  
 3443 simulated signal events depending on the mass.

3444 10.4.1 MASS ESTIMATION

3445 The mean value of ionization in silicon is governed by the Bethe equation and  
 3446 the most probable value follows a Landau-Vavilov distribution [6]. Those forms  
 3447 inspire a parametric description of  $dE/dx$  in terms of  $\beta\gamma$ ,

$$(dE/dx)_{\text{MPV}}(\beta\gamma) = \frac{p_1}{\beta p_3} \ln(1 + [p_2\beta\gamma]^{p_5}) - p_4 \quad (22)$$

3448 which performs well in the range  $0.3 < \beta\gamma < 1.5$ . This range includes the  
 3449 expected range of  $\beta\gamma$  for the particles targeted for this search, with  $\beta\gamma \approx 2.0$   
 3450 for lower mass particles (O(100 GeV)) and  $\beta\gamma \approx 0.5$  for higher mass parti-  
 3451 cles (O(1000 GeV)). The parameters,  $p_i$ , are fit using a 2015 data sample of  
 3452 low-momentum pions, kaons, and protons as described in Ref. [98]. Figure 82  
 3453 shows the two-dimensional distribution of  $dE/dx$  and momentum along with  
 3454 the above fitted values for  $(dE/dx)_{\text{MPV}}$ .

3455 The above equation (22) is then numerically inverted to estimate  $\beta\gamma$  and the  
 3456 mass for each candidate track. In simulated signal events, the mean of this mass  
 3457 value reproduces the generated mass up to around 1800 GeV to within 3%. The  
 3458 mass distributions are shown for a few VLL mass points in Figure 83. The large  
 3459 widths of these distributions come from the high variability in energy deposits  
 3460 in the pixel detector as well as the uncertainty on momentum measurements at  
 3461 high momentum, but the means converge to the expected values. A constant  
 3462 shift of 3% is observed between the mean of the reconstructed mass distribution  
 3463 and the generated mass, which is then corrected by applying a 3% shift in the  
 3464 opposite direction.

3465 This analysis evaluates expected yields and the resulting cross sectional limits  
 3466 using windows in this mass variable. The windows are formed by fitting mass  
 3467 distributions in simulated signal events like those in Figure 83 to Gaussian distri-  
 3468 butions and taking all events that fall within  $\pm 1.4\sigma$  of the mean. As can be seen  
 3469 in Figure 83, typical values for this width are  $\sigma \approx 300 - 500$  GeV depending on  
 3470 the generated mass.

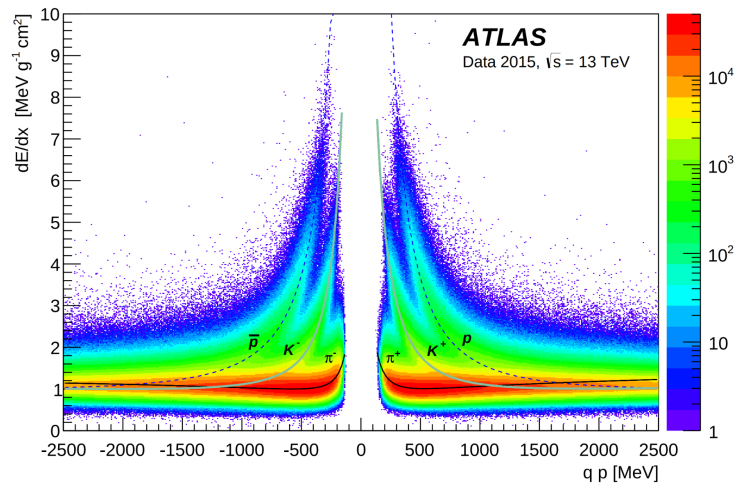


Figure 82: Two-dimensional distribution of  $dE/dx$  versus charge signed momentum ( $qp$ ) for minimum-bias tracks. The fitted distributions of the most probable values for pions, kaons and protons are superimposed.

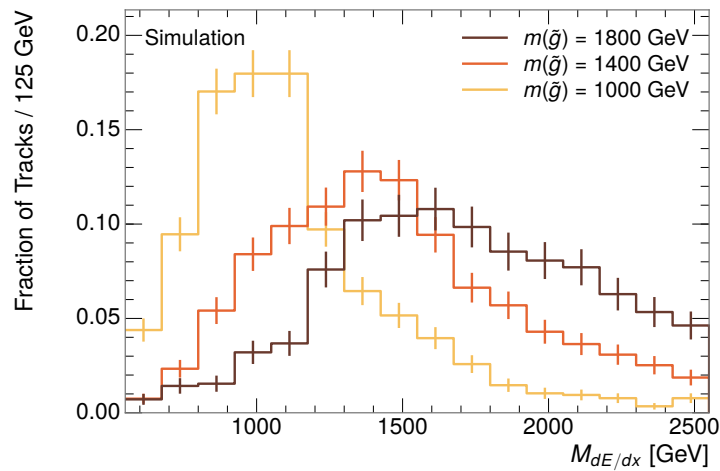


Figure 83: The distribution of mass estimated using  $dE/dx$  for simulated VLL R-Hadrons with masses between 1000 and 1600 GeV.

## 3471 10.5 EVENT SELECTION

3472 The numbers of events passing each requirement are shown in Table 10 for the  
 3473 full 2015 dataset and a simulated 1600 GeV, 10 ns lifetime R-Hadron sample.  
 3474 The table highlights the overall acceptance  $\times$  efficiency for signal events, which  
 3475 for this example is 19%. Between SM rejection and ionization, the selection re-  
 3476 quirements reduce the background of tracks which pass the kinematic require-  
 3477 ments down by an additional factor of almost 2000.

Selection	Signal Events (%)	Data Events	Rejection
Generated	$26.0 \pm 0.3$		
$E_T^{\text{miss}}$ Trigger	$24.8 \pm 0.3$ (95%)		
$E_T^{\text{miss}} > 130 \text{ GeV}$	$23.9 \pm 0.3$ (92%)		
Track Quality and $p_T$	$10.7 \pm 0.2$ (41%)	368324	1.0
Isolation Requirement	$9.0 \pm 0.2$ (35%)	108079	3.4
Track $p > 150 \text{ GeV}$	$6.6 \pm 0.2$ (25%)	47463	7.8
$M_T > 130 \text{ GeV}$	$5.8 \pm 0.2$ (22%)	18746	20
Electron/Hadron Veto	$5.5 \pm 0.2$ (21%)	3612	100
Muon Veto	$5.5 \pm 0.2$ (21%)	1668	220
Ionization Requirement	$5.0 \pm 0.1$ (19%)	11	33000

Table 10: The expected number of events at each level of the selection for LL 1600 GeV, 10 ns R-Hadrons, along with the number of events observed in data, for  $3.2 \text{ fb}^{-1}$ . The simulated yields are shown with statistical uncertainties only. The total efficiency  $\times$  acceptance is also shown for the signal and the rejection factor relative to initial track requirement is shown for data.

3478 There is a strong dependence of this efficiency on lifetime and mass, with effi-  
 3479 ciencies dropping to under 1% at low lifetimes. Figure 84 shows the dependence  
 3480 on both mass and lifetime for all signal samples considered in this search. The  
 3481 dependence on mass is relatively slight and comes predominantly from the in-  
 3482 creasing fraction of R-Hadrons which pass the ionization cut with increasing  
 3483 mass. The trigger and  $E_T^{\text{miss}}$  requirements are most efficient for particles that  
 3484 decay before reaching the calorimeters. However, the chance of a particle to be  
 3485 reconstructed as a high-quality track decreases significantly at low lifetimes as  
 3486 the particle does not propagate sufficiently through the inner detector. These  
 3487 effects lead to a maximum in the selection efficiency for lifetimes around 10-30  
 3488 ns. The lifetimes up to and including 30 ns are shown with the LL selection and  
 3489 the 50 ns and stable points are shown with the VLL selection.

3490 The inefficiency of this signal region at short lifetimes comes almost exclu-  
 3491 sively from an acceptance effect, in that the particles do not reach the necessary  
 3492 layers of the SCT. This can be seen more clearly by defining a fiducial region  
 3493 which includes events with at least one R-Hadron that is produced with non-  
 3494 zero charge,  $p_T > 50 \text{ GeV}$ ,  $p > 150 \text{ GeV}$ ,  $|\eta| < 2.5$ , and a decay distance greater  
 3495 than 30 cm in the transverse plane. At short (1 ns) lifetimes, the acceptance into

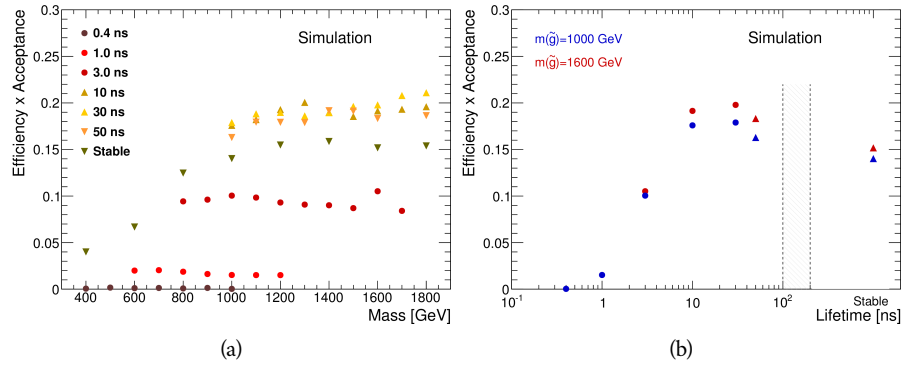


Figure 84: The acceptance  $\times$  efficiency as a function of R-Hadron (a) mass and (b) lifetime. (a) shows all of the combinations of mass and lifetime considered in this search, and (b) highlights the lifetime dependence for 1000 GeV and 1600 GeV R-Hadrons.

3496 this region is as low as 4%. Once this acceptance is accounted for, the selection  
 3497 efficiency ranges from 25% at lifetimes of 1 ns up to 45% at lifetimes of 10 ns.

3498

3499 BACKGROUND ESTIMATION

---

3500 The event selection discussed in the previous section focuses on detector sig-  
 3501 natures, emphasizing a single high-momentum, highly-ionizing track. That track  
 3502 is then required to be inconsistent with the expected properties of SM particles,  
 3503 with various requirements designed to reject jets, hadrons, electrons, and muons  
 3504 (Section 10.3). Therefore the background for this search comes entirely from  
 3505 backgrounds that are outliers of various distributions including  $dE/dx$ ,  $f_{EM}$ ,  
 3506 and  $p_T^{\text{Cone}}$ . The simulation can be tuned in various ways to do an excellent job of  
 3507 modeling the average properties of each particle type [99], but it is not necessarily  
 3508 expected to accurately reproduce outliers. For this reasons, the background  
 3509 estimation used for this search is estimated entirely using data.

## 3510 11.1 BACKGROUND SOURCES

3511 SM charged particles with lifetimes long enough to form tracks in the inner de-  
 3512 tector can be grouped into three major categories based on their detector in-  
 3513 teractions: hadrons, electrons, and muons. Every particle that contributes to the  
 3514 background for this search belongs to one of these types. Relatively pure samples  
 3515 of tracks from each of these types can be formed in data by inverting the various  
 3516 rejection techniques in Section 10.3. Specifically, muons are selected requiring  
 3517 medium muon identification, electrons requiring  $E/p > 1.0$  and  $f_{EM} > 0.95$ ,  
 3518 and hadrons requiring  $E/p > 1.0$  and  $f_{EM} < 0.95$ .

3519 Figure 85 shows the distributions of momentum and  $dE/dx$  for these cate-  
 3520 gories in data, after requiring the event level selection as well as the track re-  
 3521 quirements on  $p_T$ , hits, and  $N_{\text{split}}$ , as discussed in Section 10.2. Simulated signal  
 3522 events are included for reference. These distribution are only illustrative of the  
 3523 differences between types, as the rejection requirements could alter their shape.  
 3524 This is especially significant for momentum which enters directly into  $E/p$  and  
 3525 can indirectly affect muon identification. However it is clear that there are some  
 3526 differences between types in both distributions, even though the trends are sim-  
 3527 ilar. The distributions of momentum are not necessarily expected to match be-  
 3528 tween the various types because the production mechanisms for each type result  
 3529 in different kinematic distributions.  $dE/dx$  is also different between types be-  
 3530 cause of incomplete isolation; although the requirement on  $N_{\text{split}}$  helps to reduce  
 3531 the contribution of nearby particles it does not completely remove the effect  
 3532 of overlaps. Muons are better isolated because they do not have the additional  
 3533 particle from hadronization present for hadrons and they are significantly less  
 3534 likely do interact with the detector and produce secondary particles compared to  
 3535 hadrons and electrons. Thus muons have the smallest fraction of  $dE/dx$  above  
 3536 the threshold of  $1.8 \text{ MeVg}^{-1}\text{cm}^2$ ; hadrons and electrons have a larger fraction  
 3537 above this threshold.

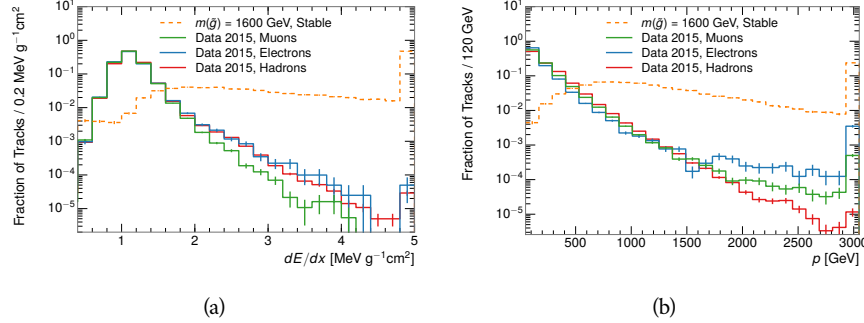


Figure 85: The distribution of (a)  $dE/dx$  and (b) momentum for tracks in data and simulated signal after requiring the event level selection and the track selection on  $p_T$ , hits, and  $N_{\text{split}}$ . Each sub-figure shows the normalized distributions for tracks classified as hadrons, electrons, and muons in data and R-Hadrons in the simulated signal.

It is difficult to determine what fraction of each particle type enters into the final signal region. The background method will not have significant dependence on the relative contributions of each species, but it is useful to understand the differences between each when considering the various tests of the method.

## 3542 11.2 PREDICTION METHOD

The data-driven background estimation relies on the independence between the ionization measurement and other kinematic variables in the event. For standard model particles with momenta above 50 GeV,  $dE/dx$  is not correlated with momentum; though there is a slight relativistic rise as momentum increases, the effect is small compared to the width of the distribution of ionization energy deposits.. So, the proposed method to estimate the mass distribution of the signal region is to use the momentum from a track with low  $dE/dx$  (below the threshold value) and to combine it with a random  $dE/dx$  value from a  $dE/dx$  template. The resulting track is just as likely as the original, so a large set of random generations provide the expected distributions of momentum and ionization. These are then combined using the parametrization described in Section 10.4.1 to estimate  $\beta\gamma$  and then form a distribution of mass for the signal region using Equation 20.

Algorithmically this method is implemented by forming two distinct Control Regions (**CRs**). The first **CR**, CR1, is formed by applying the entire event selection from Chapter 10 apart from the  $dE/dx$  and mass requirements. The  $dE/dx$  requirement is instead inverted for this region. Because of the independence of  $dE/dx$  and  $p$ , the tracks in this control region have the same kinematic distribution as the tracks in the signal region, and are used to measure a two-dimensional template of  $p$  and  $\eta$ . The second **CR**, CR2, is formed from the event selection through the  $dE/dx$  requirement, but with an inverted  $E_T^{\text{miss}}$  requirement. The tracks in this control region are expected to have similar  $dE/dx$  distributions as the signal region before the ionization requirement, and so this region is used to measure a two-dimensional template of  $dE/dx$  and  $\eta$ .

3566     The contribution of any signal to the control regions is minimized by the in-  
 3567     verted selection requirements. Only less than 10% of simulated signal events  
 3568     have either  $dE/dx$  or  $E_T^{\text{miss}}$  below the threshold values in the original signal re-  
 3569     gion, while the backgrounds are significantly enhanced by inverting those re-  
 3570     quirements. The signal contamination is less than 1% in both control regions  
 3571     for all of the simulated masses and lifetimes considered in this analysis.

3572     With those measured templates, the shape of the mass estimation is generated  
 3573     by first selecting a random ( $p$ ,  $\eta$ ) combination from CR1. This momentum  
 3574     value is combined with a  $dE/dx$  value taken from the appropriate distribution  
 3575     of  $dE/dx$  for the selected  $\eta$  from CR2. The use of  $\eta$  in both random samplings  
 3576     controls for any correlation between  $p$ ,  $dE/dx$ , and  $\eta$ . Those values are then  
 3577     used to calculate a mass in the same way that is done for regular tracks in data,  
 3578     see Section 10.4.1. As this procedure includes all  $dE/dx$  values, the cut at 1.8  
 3579     MeVg $^{-1}$ cm $^2$  is then enforced to fully model the signal region. The generated  
 3580     mass distribution is then normalized by scaling the background estimate to the  
 3581     data in the region  $M < 160$  GeV, where signals of this type have already been  
 3582     excluded [83]. This normalization uses the distributions of mass generated with-  
 3583     out the ionization requirement.

3584     The statistical uncertainties on these background distributions are calculated  
 3585     by independently fluctuating each bin of the input templates according to their  
 3586     Poisson uncertainties. These fluctuations are repeated a large number of times,  
 3587     and the uncertainty on the resulting distribution is taken as the root mean square  
 3588     (RMS) deviation of the fluctuations from the average. As the procedure uses one  
 3589     million random combinations to generate the distributions, The statistical un-  
 3590     certainty from the actual random generations is negligible compared to the un-  
 3591     certainty from measuring the templates.

## 3592     11.3 VALIDATION

3593     The validity of the background estimation technique can be evaluated in both  
 3594     data and simulation. The underlying assumption that random combinations of  
 3595      $dE/dx$  and momentum can predict a mass distribution in an orthogonal region  
 3596     can be tested using simulated samples where concerns like multiple particle types  
 3597     can be controlled. Using the same technique in another set of signal-depleted  
 3598     regions in data then extends this confidence to the more complicated case where  
 3599     several particle species are inherently included.

### 3600     11.3.1 CLOSURE IN SIMULATION

3601     The first test of the procedure is done using a simulated sample of  $W \rightarrow \mu\nu$   
 3602     decays. These types of events provide the ingredients required to test the back-  
 3603     ground estimate,  $E_T^{\text{miss}}$  and isolated tracks, with high statistics. In this example  
 3604     there is no signal, so simulated events in the orthogonal CRs are used to estimate  
 3605     the shape of the mass distribution of the simulated events in the signal region. To  
 3606     reflect the different topology for W boson decays, the CRs use slightly modified  
 3607     definitions. In all CRs, the requirement of  $p > 150$  GeV and the SM rejection

3608 requirements are removed. Additionally, for the signal region the requirement  
 3609 on  $E_T^{\text{miss}}$  is relaxed to 30 GeV and the corresponding inverted requirement on  
 3610 CR2 is also set at 30 GeV.

3611 With these modified selections, the simulated and randomly generated distri-  
 3612 butions of  $M_{dE/dx}$  are shown in Figure 86. This figure includes the mass distri-  
 3613 butions before and after the requirement on  $dE/dx$ , which significantly shapes  
 3614 the distributions. In both cases the background estimation technique repro-  
 3615 duces the shape of  $M_{dE/dx}$  in the signal region. There is a small difference in the pos-  
 3616 itive tail of the mass distribution prior to the ionization cut, where the random  
 3617 events underestimate the fraction of tracks with mass above 150 GeV by about  
 3618 20%. After the ionization requirement, however, this discrepancy is not present  
 3619 and the two distributions agree to within statistical uncertainties in the positive  
 3620 tail.

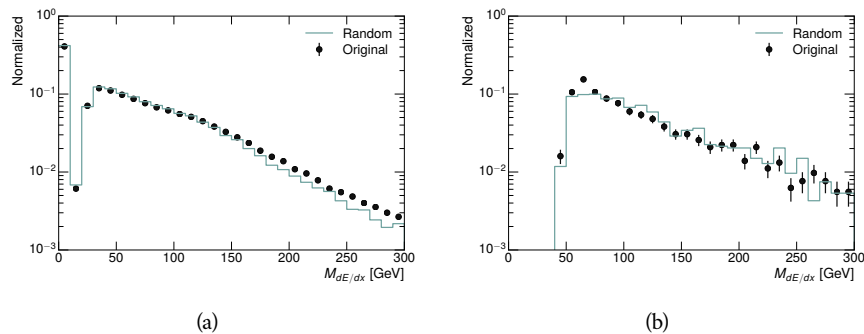


Figure 86: The distribution of  $M_{dE/dx}$  (a) before and (b) after the ionization requirement for tracks in simulated W boson decays and for the randomly generated background estimate.

3621 This ability to reproduce the shape of the mass distribution in simulated events  
 3622 shows that the technique works as expected. No significant biases are acquired  
 3623 in using low  $dE/dx$  events to select kinematic templates or in using low  $E_T^{\text{miss}}$   
 3624 events to select ionization templates, as either would result in a mismodeling of  
 3625 the shape of the mass distribution. The simulated events contain only one par-  
 3626 ticle type, however, so this test only establishes that the technique works well  
 3627 when the the CRs are populated by exactly the same species.

### 3628 11.3.2 VALIDATION REGION IN DATA

3629 The second test of the background estimate is performed using data in an or-  
 3630 thogonal validation region. The validation region, and the corresponding CRs,  
 3631 are formed using the same selection requirements as in the nominal method but  
 3632 with a modified requirement on momentum,  $50 < p[\text{GeV}] < 150$ . This allows  
 3633 the technique to be checked in a region with very similar properties but where  
 3634 the signal is depleted, as the majority of the signal has momentum above 150  
 3635 GeV while the backgrounds are enhanced below that threshold. Any biases on  
 3636 the particle composition of the CRs for the signal region will be reflected in the  
 3637 CRs used to estimate the mass distribution in the validation region.

3638     Figure 87 shows the measured and randomly generated mass distributions for  
 3639     data before and after the ionization requirement. The background estimate mod-  
 3640     els the actual background before the ionization requirement very well, with good  
 3641     agreement to within the statistical uncertainties out to the limit of the mass dis-  
 3642     tribution. There are very few events in the validation region after the ionization  
 3643     requirement, but the few observed events are consistent with the background  
 3644     prediction. The good agreement in this validation region provides a confirma-  
 3645     tion that the technique works even in the full-complexity case with multiple par-  
 3646     ticle types entering the distributions. Any bias from changes in particle compo-  
 3647     sition between regions is small compared to statistical uncertainties.

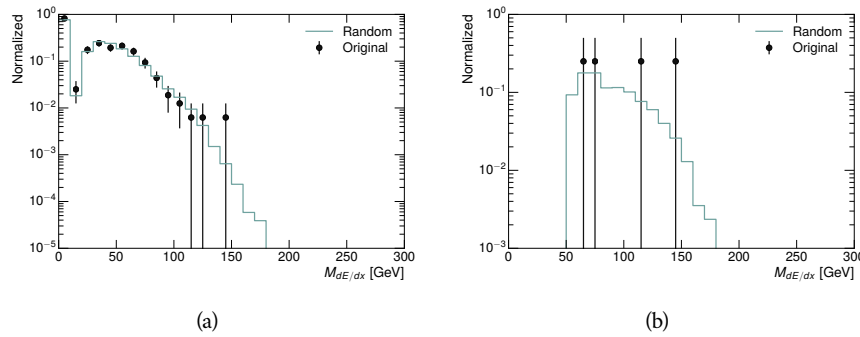


Figure 87: The distribution of  $M_{dE/dx}$  (a) before and (b) after the ionization require-  
 ment for tracks in the validation region and for the randomly generated back-  
 ground estimate.

## 3648     11.4 EXPECTED BACKGROUND

3649     Using the full technique in the primary regions described in Section 11.2 pro-  
 3650     vides a final background estimate for the signal region of this search. It predicts  
 3651     a total background of  $11.1 \pm 1.7$  events in the **LL** region and  $17.2 \pm 2.6$  events in  
 3652     the **VLL** region. Table 11 shows the number of events predicted in mass windows  
 3653     for the grid of mass points, for each of the **LL** and **VLL** signal regions. Only one  
 3654     to two events are expected in each mass window, as the background distribution  
 3655     falls with increasing mass.

Mass	Expected Background, <a href="#">LL</a>	Expected Background, <a href="#">VLL</a>
1000	$1.328 \pm 0.063$	$1.803 \pm 0.081$
1100	$1.255 \pm 0.060$	$1.409 \pm 0.069$
1200	$1.193 \pm 0.058$	$1.310 \pm 0.066$
1300	$0.997 \pm 0.051$	$1.431 \pm 0.069$
1400	$1.131 \pm 0.056$	$1.273 \pm 0.065$
1500	$1.111 \pm 0.055$	$1.115 \pm 0.059$
1600	$1.193 \pm 0.058$	$1.041 \pm 0.057$
1800	$1.138 \pm 0.056$	$0.918 \pm 0.053$

Table 11: The expected number of background events within each of the mass windows for the stable and metastable signal regions.

3656

3657 SYSTEMATIC UNCERTAINTIES

---

3658 A number of systematic uncertainties affect the interpretation of the results of  
 3659 the search. These uncertainties can be broken down into two major categories,  
 3660 those which affect the estimate of the background using data and those which  
 3661 affect the measurement of the signal yield estimated with simulated events. The  
 3662 total measured systematic uncertainties range between 6-7% for the background  
 3663 estimation and 29-33% for the signal yield depending on lifetime. These system-  
 3664 atic uncertainties are expected to be small compared to the statistical fluctuations  
 3665 of the measured yields so that measured cross-sectional limits will be dominated  
 3666 by statistical uncertainties. Only the systematic uncertainties on the background  
 3667 estimation are relevant for the search for LLPs, as the systematics on the signal  
 3668 yield enter only into the calculation of limits in the absence of a signal. The fol-  
 3669 lowing sections describe each source of systematic uncertainty for each of the  
 3670 two types.

## 3671 12.1 BACKGROUND ESTIMATE

3672 The systematic uncertainties on the background estimate come primarily from  
 3673 considering alternative methods for generating the background distributions.  
 3674 These uncertainties are small compared to the statistical uncertainties on the  
 3675 background estimate which come from the limited statistics in measuring the  
 3676 template distributions, as described in Section 11.2. They are summarized in  
 3677 Table 12.

Source of Uncertainty:	Value [%]
Analytic Description of $dE/dx$	4.0
Muon Fraction ( <a>VLL</a> Region only)	3.0
IBL Ionization Correction	3.8
Normalization	3.0
Total ( <a>LL</a> Region):	6.3
Total ( <a>VLL</a> Region):	7.0

Table 12: A summary of the sources of systematic uncertainty for the data-driven back-  
 ground in the signal region. If the uncertainty depends on the mass, the maxi-  
 mum values are reported.

3678 12.1.1 ANALYTIC DESCRIPTION OF  $dE/dX$ 

3679 The background estimate uses a binned template distribution to estimate the  
 3680  $dE/dx$  of tracks in the signal region, as described in Section 11.2. It is also possi-  
 3681 ble to fit that measured distribution to a functional form to help smooth the dis-  
 3682 tribution in the tails of  $dE/dx$  where the template is driven by a small number  
 3683 of tracks. Both Landau convolved with a Gaussian and Crystal Ball functions  
 3684 are considered as the functional form and used to re-estimate the background  
 3685 distribution. The deviations compared to the nominal method are found to be  
 3686 4%, and this is taken as a systematic uncertainty to cover the inability to care-  
 3687 fully predict the contribution from the long tail of  $dE/dx$  where there are few  
 3688 measurements available in data.

## 3689 12.1.2 MUON FRACTION

3690 The signal region for **VLL** R-Hadrons explicitly includes tracks identified as muons,  
 3691 which have a known difference in their  $dE/dx$  distributions compared to non-  
 3692 muon tracks (Section 11.1). To account for a difference in muon fraction be-  
 3693 tween the background region and the signal region for this selection, the  $dE/dx$   
 3694 templates for muons and non-muons are measured separately and then the rel-  
 3695 ative fraction of each is varied in the random generation. The muon fraction  
 3696 is varied by its statistical uncertainty and the resulting difference of 3% in back-  
 3697 ground yield is taken as the systematic uncertainty.

3698 12.1.3 **IBL** CORRECTIONS

3699 The **IBL**, described in Section 5.3.1, received a significant dose of radiation during  
 3700 the data collection in 2015. The irradiation can cause a drift in the **ToT** calibra-  
 3701 tion of the frontend electronics and thus alter the  $dE/dx$  measurement which  
 3702 includes the **ToT** output by the **IBL**. These effects are corrected for in the nomi-  
 3703 nal analysis by scaling the  $dE/dx$  measurements by a constant factor derived for  
 3704 each run to match the average  $dE/dx$  value to a reference run. However, this  
 3705 corrective factor does not account for inter-run variations. To account for the  
 3706 potential drift of  $dE/dx$  within a single run, the correction procedure is repeated  
 3707 by varying the corrections up and down by the maximal run-to-run variation  
 3708 from the full data-taking period, which results in an uncertainty of 3.8%.

## 3709 12.1.4 NORMALIZATION

3710 As described in Section 11.2, the generated distribution of masses is normalized  
 3711 in a shoulder region ( $M < 160$  GeV) where signals have been excluded by pre-  
 3712 vious analyses. That normalization factor is varied by its statistical uncertainty  
 3713 and the resulting fluctuation in the mass distribution of 3% is taken as a system-  
 3714 atic uncertainty on the background estimate.

## 3715 12.2 SIGNAL YIELD

3716 The systematic uncertainties on the signal yield can be divided into three cate-  
 3717 gories; those on the simulation process, those on the modeling of the detector  
 3718 efficiency or calibration, and those affecting the overall signal yield. They are  
 3719 summarized in Table 12. The largest uncertainty comes from the uncertainty on  
 3720 the production cross section for gluinos.

Source of Uncertainty	-[%]	+[%]
ISR Modeling ( <a href="#">LL</a> Region)	1.5	1.5
ISR Modeling ( <a href="#">VLL</a> Region)	14	14
Pile-up Reweighting	1.1	1.1
Trigger Efficiency Reweighting	0.9	0.9
$E_T^{\text{miss}}$ Scale	1.1	2.2
Ionization Parametrization	7.1	0
$\mu$ Identification	4.3	4.3
Luminosity	5	5
Signal size uncertainty	28	28
Total ( <a href="#">LL</a> Region)	30	29
Total ( <a href="#">VLL</a> Region)	33	32

Table 13: A summary of the sources of systematic uncertainty for the simulated signal yield. The uncertainty depends on the mass and lifetime, and the maximum negative and positive values are reported in the table.

3721 12.2.1 [ISR](#) MODELING

3722 As discussed in Section 9.2, MadGraph is expected to reproduce the distribution  
 3723 of [ISR](#) in signal events more accurately than the nominal Pythia samples [83].  
 3724 The analysis reweights the distribution of [ISR](#) in the simulated signal events to  
 3725 match the distribution found in generated MadGraph samples. This has an effect  
 3726 on the selection efficiency in the signal samples, where [ISR](#) contributes to the  
 3727 generation of  $E_T^{\text{miss}}$ . To account for the potential inaccuracy on the simulation  
 3728 of [ISR](#) at high energies, half of the difference between the signal efficiency with  
 3729 the reweighted distribution and the original distribution is taken as a systematic  
 3730 uncertainty.

## 3731 12.2.2 PILEUP REWEIGHTING

3732 The simulated events were generated prior to data collection with an estimate of  
 3733 the average number of interactions per bunch crossing. This estimate does not  
 3734 match the value of pileup during actual data collection, but a large fraction of the

3735 simulated events would be discarded in order to match the distribution in data.  
 3736 Therefore the simulated signal events are not reweighted for pileup by default  
 3737 in the analysis. The effect of the pileup on signal efficiency is not expected to  
 3738 depend on the mass or lifetime of the generated signal events, which allows all  
 3739 of the generated signal events to be used together to assess the pileup dependence.  
 3740 To account for the potential effect of the difference in the number of interactions  
 3741 per bunch crossing between data and simulation, the difference in yield between  
 3742 the nominal signal events and the reweighted events averaged over all masses  
 3743 and lifetimes is taken as a systematic uncertainty on the yield for each mass and  
 3744 lifetime (1.1%).

### 3745 12.2.3 TRIGGER EFFICIENCY REWEIGHTING

3746 As described in Section 10.2, the selection for this analysis does not require a suf-  
 3747 ficiently large value of  $E_T^{\text{miss}}$  to be above the plateau of trigger efficiency. There-  
 3748 fore, some signal events which would otherwise pass the event selection can be  
 3749 excluded because of the trigger requirement. These effects can be difficult to es-  
 3750 timate in simulation, and thus are constrained by comparing data and simulated  
 3751 events in an alternative W boson region which uses decays to muons to find a rel-  
 3752 atively pure sample of events with missing energy. The trigger efficiencies for  
 3753 data and simulated W events are shown in Figure 88. The comparison between  
 3754 data and MC in this region constrains the simulation of the trigger efficiency.  
 3755 The simulated signal events are reweighted by the ratio of data to simulation in  
 3756 the W boson decays, while the difference between the data and simulation in  
 3757 those decays is taken as a systematic uncertainty. This results in an uncertainty  
 3758 of only 0.9% as the majority of events are well above the plateau and the dis-  
 3759 agreement between data and simulation is small even below that plateau.

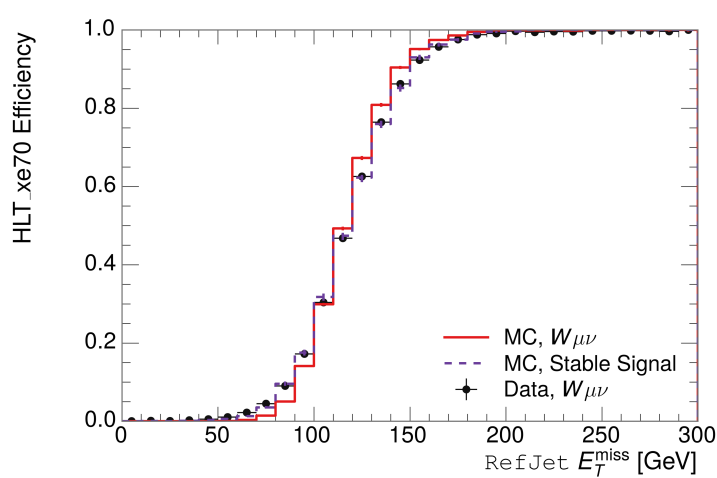


Figure 88: The trigger efficiency for the HLT\_xe70 trigger requirement as a function of Calorimeter  $E_T^{\text{miss}}$  for simulated data events with a W boson selection. Simulated signal events and simulated W boson events are also included.

Systematic Variation	-[%]	+[%]
JET_GroupedNP_1	-0.7	1.3
JET_GroupedNP_2	-0.7	1.2
JET_GroupedNP_3	-0.5	1.3

Table 14: Example of the contributing systematic variations to the total systematic for the  $E_T^{\text{miss}}$  Scale, as measured in a 1200 GeV, VLL R-Hadron signal sample.

#### 3760 12.2.4 MISSING TRANSVERSE MOMENTUM SCALE

3761 Variations on the JES enter into this analysis only in the requirement on  $E_T^{\text{miss}}$ ,  
 3762 as variations on individual jets can alter the reconstructed  $E_T^{\text{miss}}$  in signal events.  
 3763 The effect of the measured  $E_T^{\text{miss}}$  is evaluated by varying the  $E_T^{\text{miss}}$  scale accord-  
 3764 ing to the one sigma variations on objects affecting event kinematics in simu-  
 3765 lated signal events. Missing energy is reconstructed from fully reconstructed  
 3766 objects so any systematic uncertainties affecting jets, muons, electrons, or the  
 3767  $E_T^{\text{miss}}$  soft terms are included. The variations on these objects are taken from  
 3768 measurements in data using balance techniques as discussed in Section 6.4.3.  
 3769 The resulting difference in selection efficiency is expected to be small, because  
 3770 the jet variations only alter energies by a few percent. The only non-negligible  
 3771 contributions found using this method are itemized in Table 14 for an example  
 3772 signal sample (1200 GeV, VLL R-Hadron), where the systematic is measured as  
 3773 the relative difference in the final signal efficiency after applying the associated  
 3774 variation through the CP tools. The only variations that are significant are the  
 3775 grouped jet systematic variations, which combine recommended jet systematic  
 3776 uncertainties into linearly independent variations.

3777 As the peak of the reconstructed  $E_T^{\text{miss}}$  distribution in the signal is significantly  
 3778 above the current threshold for events which pass the trigger requirement, the  
 3779 effect of scale variation is expected to be small, which is consistent with the mea-  
 3780 sured systematic error of approximately 2%. Events which do not pass the trigger  
 3781 requirement usually fail because there are no ISR jets in the event to balance the  
 3782  $R$ -hadrons' transverse momentum, so the reconstructed  $E_T^{\text{miss}}$  is low and there-  
 3783 fore also expected to be not very sensitive to scale changes.

#### 3784 12.2.5 MOMENTUM PARAMETRIZATION

3785 The uncertainty on the signal efficiency from track momentum is calculated us-  
 3786 ing the sagitta bias for  $q/P_{\text{trk}}$ , the only systematic variation of tracking that effects  
 3787 track momentum. The systematic is only important for tracks that are near the  
 3788 150 GeV momentum threshold, as the variation may push these tracks above  
 3789 or below the selection requirement. Because the majority of R-Hadron tracks  
 3790 are well above this value (Figure 78), the resulting uncertainty is expected to be  
 3791 small. This uncertainty is propagated to the final selection efficiency by varying

3792 the track momentum by the measured one sigma variations from tracking mea-  
 3793 surements [100], and the associated uncertainty is found to be negligible (0.3%).

3794 12.2.6 IONIZATION REQUIREMENT

3795 The  $dE/dx$  distributions in data and simulated events have different most prob-  
 3796 able values, which is due in part to radiation effects in the detector that are not  
 3797 fully accounted for in the simulation. The difference does not affect the mass  
 3798 measurement used in this analysis, as independent calibrations are done in sim-  
 3799 ulation and in data. However, it does affect the efficiency of the high  $dE/dx$   
 3800 selection requirement. To calculate the size of the effect on the signal efficiency,  
 3801 the  $dE/dx$  distribution in signal simulation is scaled by a factor obtained from  
 3802 comparing the  $dE/dx$  distribution of inclusive tracks in data and in simulation.  
 3803 The difference in efficiency for this sample with a scaled  $dE/dx$  distribution, rel-  
 3804 ative to the nominal case, is taken as a systematic uncertainty on signal efficiency.  
 3805 The uncertainty is as large as 7% for low masses and falls to a negligible effect for  
 3806 large masses.

3807 12.2.7 ELECTRON AND JET REJECTION

3808 The systematic uncertainty on the electron rejection is measured by varying the  
 3809 EM fraction requirement significantly, from 0.95 to 0.9. This is found to have  
 3810 a less than 0.04% effect on signal acceptance, on average, and so is completely  
 3811 negligible. Similarly, the uncertainty on jet rejection is measured by tightening  
 3812 the  $E/p$  requirement from 0.5 to 0.4. This is found to have no effect on signal  
 3813 acceptance, so again the systematic is again negligible.

3814 12.2.8 MUON VETO

3815 The signal region for [LL](#) particles has a requirement that the candidate tracks are  
 3816 not identified as medium muons because the majority of R-Hadrons in the life-  
 3817 time range included in that region do not reach the muon spectrometers before  
 3818 they decay. However, the exponential tail of the R-Hadron lifetime distribution  
 3819 results in some R-Hadrons traversing the muon spectrometer. Even these R-  
 3820 Hadrons can still fail the muon medium identification some of the time, because  
 3821 they may arrive late to the muon spectrometer as discussed in Section 9.1.1. The  
 3822 hits generated by a R-Hadron will not be readout if it arrives 25 ns after the  
 3823 bunch crossing, causing it to fail the loose muon selection (Section 6.3.1). This  
 3824 can be seen in Figure 89, which shows the efficiency of the muon veto as a func-  
 3825 tion of  $1/\beta$ , for two simulated [VLL](#) R-Hadron samples.

3826 Thus, the efficiency of the muon veto depends on the timing resolution of  
 3827 the spectrometer, so an uncertainty is applied to the signal efficiency to cover  
 3828 differences in timing resolution between data and simulation. First, a sample of  
 3829  $Z \rightarrow \mu\mu$  events is selected in data in which one of the muons has a late arrival  
 3830 time measured in the [MDT](#). Then the reconstructed  $\beta$  distribution is compared  
 3831 to the distribution in simulated  $Z \rightarrow \mu\mu$  events; the difference between these

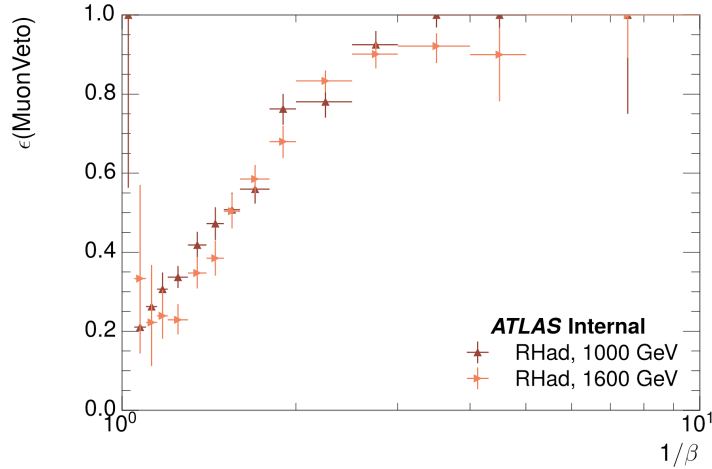


Figure 89: The efficiency of the muon veto for  $R$ -hadrons of two different masses, as a function of  $\frac{1}{\beta}$  for simulated R-Hadron tracks.

two distributions reflects the difference in timing resolution between data and simulation. To emulate this difference in simulated signal events, the magnitude of the difference is used to scale and shift the true  $\beta$  distribution of R-Hadrons in simulation. Signal events are then reweighted based on this varied  $\beta$  distribution, and the difference in the efficiency of the muon veto selection is compared with the nominal and reweighted true  $\beta$  distributions. The difference in muon veto efficiency is taken as a systematic uncertainty of the muon veto.

The comparison of reconstructed  $\beta$  between data and simulation is performed separately in the barrel, transition, and endcap regions of the spectrometer, and the reweighting of the true  $\beta$  distribution in signal is done per region. The comparison of average reconstructed MDT  $\beta$  between data and simulation for the barrel region is shown in Figure 90 for  $Z \rightarrow \mu\mu$  events. As expected, The uncertainty is found to be negligible for  $R$ -hadrons with short lifetimes, and is only significant for lifetimes above 30 ns.

### 12.2.9 LUMINOSITY

The luminosity uncertainty is provided by a luminosity measurement on ATLAS and was measured to be 5% at the time of the publication of this analysis. The uncertainty is estimated by comparing luminosity measurements using several independent luminometers [101].

### 12.2.10 SIGNAL CROSS SECTION

As discussed in Section 9.2, the signal cross sections are calculated at NLO in the strong coupling constant with a resummation of soft-gluon emission at NLL. The nominal predictions and the uncertainties for each mass point are taken from an envelope of cross-section predictions using different PDF sets and factorization

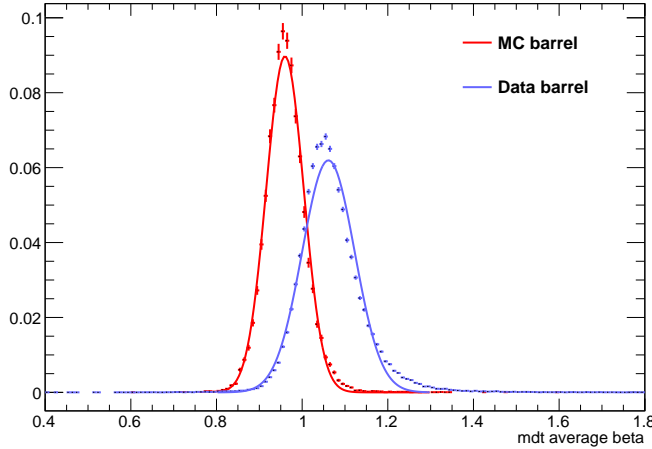


Figure 90: The average reconstructed MDT  $\beta$  distribution for  $Z \rightarrow \mu\mu$  events in which one of the muons has a late arrival time in the MDT, for both data and simulation. A gaussian fit is superimposed.

3856 and renormalization scales [94], as discussed in Section 9.2. The uncertainties  
 3857 on those cross sections range between 14% and 28% for R-Hadrons in the range  
 3858 of 400 to 1800 GeV [95, 96]. The uncertainty increases with the mass.

3859

3860 RESULTS

---

3861 Sixteen events were observed in the **VLL** signal region and eleven events were  
 3862 observed in the **LL** signal region, prior to requirements on the candidate track  
 3863 mass. The background estimate predicts  $17 \pm 2.6(\text{stat}) \pm 1.2(\text{syst})$  events for  
 3864 the **VLL** region and  $11.1 \pm 1.7(\text{stat}) \pm 0.7(\text{syst})$  events for the **LL** region. These  
 3865 counts are summarized in Table 15.

3866 The mass estimated using  $dE/dx$  (Section 10.4.1) provides the final discrimi-  
 3867 nating variable, where the signal would be expected as an excess in the falling ex-  
 3868 ponential tail of the expected background. The observed distribution of masses  
 3869 is shown in Figure 91, along with the predicted distribution from the background  
 3870 estimate for each signal region. Both include a few example simulated signal dis-  
 3871 tributions, which show the scale of an excess were the R-Hadron signals present.  
 3872 Their is no statistically significant evidence of an excess in the data over the back-  
 3873 ground estimation. From this distribution it is clearly possible to rule out signals  
 3874 with lower masses, around 1200 GeV, which have larger cross sections.

## 3875 13.1 CROSS SECTION LIMITS

3876 Because there is no significant excess of events observed in the signal region, this  
 3877 analysis sets upper limits on the allowed cross section for R-Hadron production.  
 3878 These limits are set for each mass point by counting the observed events in data,  
 3879 along with the expected background and simulated signal events, in windows of  
 3880 mass. The mass windows are formed by fitting the distribution of signal events to  
 3881 a Gaussian distribution, and the window is then  $\pm 1.4\sigma$  around the center of that  
 3882 Gaussian. Two examples of the windows formed by this procedure are shown in  
 3883 Tables 16-17, for the **VLL** and 10 ns working points. The corresponding counts of  
 3884 observed data, expected background, and simulated signal for those same work-  
 3885 ing points are shown in Tables 18-19. Appendix A includes the mass windows  
 3886 and counts for all of the considered signal points.

3887 The 95% confidence level upper limits on the cross sections for a large grid  
 3888 of masses (between 800 and 1800 GeV) and lifetimes (between 0.4 and **VLL**) are

Selection Region	Expected Background	Data
<b>VLL</b>	$17.2 \pm 2.6 \pm 1.2$	16
<b>LL</b>	$11.1 \pm 1.7 \pm 0.7$	11

Table 15: The estimated number of background events and the number of observed events in data for the specified selection regions prior to the requirement on mass. The background estimates show statistical and systematic uncertainties.

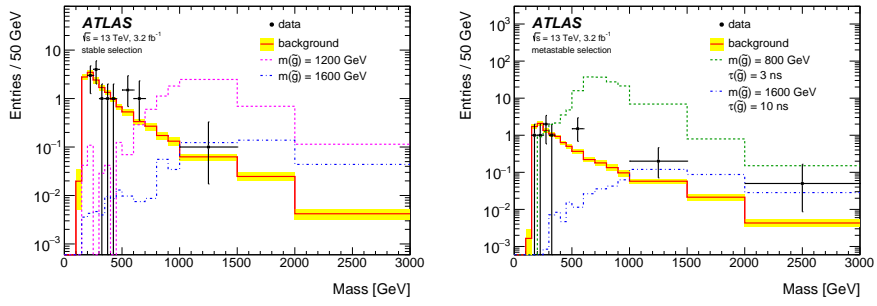


Figure 91: The observed mass distribution of events in data and the generated background distribution in (a) the [VLL](#) and (b) the [LL](#) signal region. A few example simulated signal distributions are superimposed.

$m(\tilde{g})$ [GeV]	Left Extremum [GeV]	Right Extremum [GeV]
1000	655	1349
1100	734	1455
1200	712	1631
1300	792	1737
1400	717	1926
1500	815	2117
1600	824	2122
1700	900	2274
1800	919	2344

Table 16: The left and right extremum of the mass window for each generated mass point with a 10 ns lifetime.

$m(\tilde{g})$ [GeV]	Left Extremum [GeV]	Right Extremum [GeV]
800	627	1053
1000	726	1277
1200	857	1584
1400	924	1937
1600	993	2308
1800	1004	2554

Table 17: The left and right extremum of the mass window used for each generated [VLL](#) mass point.

$m(\tilde{g})$ [GeV]	Expected Signal	Expected Background	Observed Data
800	$462.83 \pm 14.86$	$1.764 \pm 0.080$	2
1000	$108.73 \pm 3.38$	$1.458 \pm 0.070$	1
1200	$31.74 \pm 0.95$	$1.137 \pm 0.060$	1
1400	$10.22 \pm 0.29$	$1.058 \pm 0.058$	1
1600	$3.07 \pm 0.09$	$0.947 \pm 0.054$	1
1800	$1.08 \pm 0.05$	$0.940 \pm 0.054$	1

Table 18: The expected number of signal events, the expected number of background events, and the observed number of events in data with their respective statistical errors within the respective mass window for each generated `VLL` mass point

$m(\tilde{g})$ [GeV]	Expected Signal	Expected Background	Observed Data
1000	$144.48 \pm 5.14$	$1.499 \pm 0.069$	2
1100	$73.19 \pm 2.61$	$1.260 \pm 0.060$	2
1200	$41.54 \pm 1.41$	$1.456 \pm 0.067$	2
1300	$22.58 \pm 0.77$	$1.201 \pm 0.058$	2
1400	$12.70 \pm 0.42$	$1.558 \pm 0.071$	2
1500	$6.73 \pm 0.24$	$1.237 \pm 0.060$	2
1600	$3.90 \pm 0.13$	$1.201 \pm 0.058$	2
1700	$2.27 \pm 0.07$	$1.027 \pm 0.052$	2
1800	$1.34 \pm 0.04$	$1.019 \pm 0.052$	2

Table 19: The expected number of signal events, the expected number of background events, and the observed number of events in data with their respective statistical errors within the respective mass window for each generated mass point with a lifetime of 10 ns.

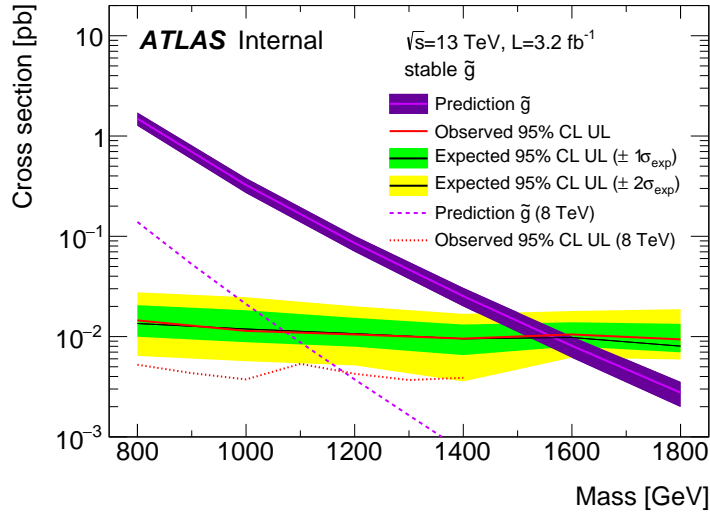


Figure 92: The observed and expected cross section limits as a function of mass for the [VLL](#) simulated signal. The predicted cross section values for the corresponding signals are also shown.

3889 extracted from these counts with the  $CL_S$  method using the profile likelihood  
 3890 ratio as a test statistic [102]. For this procedure, the systematic uncertainties esti-  
 3891 mated for the signal and background yields are treated as Gaussian-distributed  
 3892 nuisance parameters. The uncertainty on the normalization of the expected  
 3893 background distribution is included in the expected background events. At this  
 3894 point the expected cross section limit is calculated for both the [LL](#) and [VLL](#) signal  
 3895 region for each lifetime point, and the region with the best expected limit is se-  
 3896 lected for each lifetime. Using that procedure, the [LL](#) region is used for lifetimes  
 3897 up to and including 30 ns, and the [VLL](#) region for lifetimes above it.

3898 The resulting upper limits on the cross sections are shown as a function of  
 3899 mass in Figure 92 and Figure 93 for each lifetime considered. The limits are  
 3900 interpolated linearly between each mass point, and the dependence of the limit  
 3901 on the mass is small as the efficiency is relatively constant for large R-Hadron  
 3902 masses. There is however a strong dependence on lifetime, as discussed in Sec-  
 3903 tion 10.5, where the probability to form a fully reconstructed track and the kine-  
 3904 matic freedom to produce  $E_T^{\text{miss}}$  result in a local maximum in the limit at 10-30  
 3905 ns. The figures also include the expected cross section for pair-produced gluino  
 3906 R-Hadrons for reference. For the 10 ns and [VLL](#) cross section limits, both the  
 3907 observed limit and expected cross section for the Run 1, 8 TeV version of this  
 3908 analysis are also shown. There the cross section limits are lower because of the  
 3909 larger available luminosity. The signal cross sections are also much lower be-  
 3910 cause of the lower collision energy.

## 3911 13.2 MASS LIMITS

3912 The cross section limits can then be used to derive a lower mass limit for gluino  
 3913 R-Hadrons by comparing them to the theoretically predicted production cross

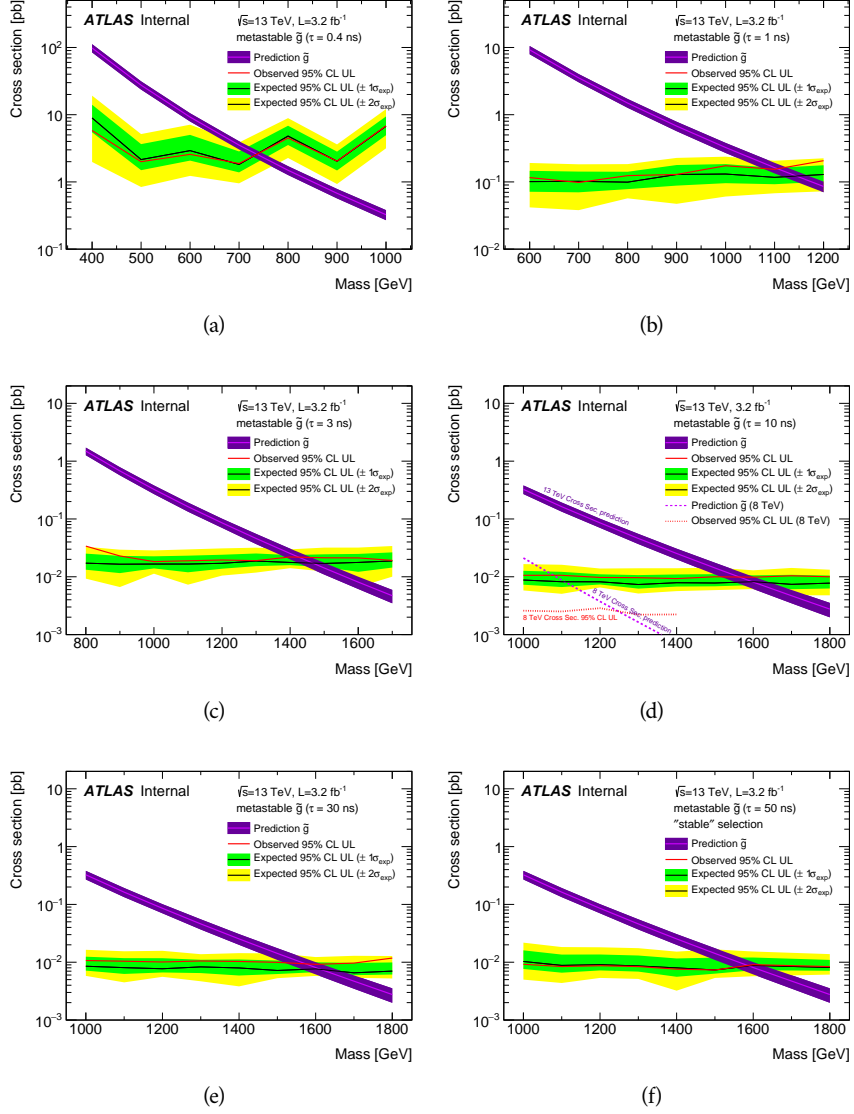


Figure 93: The observed and expected cross section limits as a function of mass for each generated lifetime. The predicted cross section values for the corresponding signals are also shown. An example of Run 1 cross section limits and predicted cross sections are shown in (d) for comparison.

sections. These mass limits range from only 740 GeV at the lowest lifetimes considered, where the selection efficiency is very low, to up to 1580 GeV at 30 ns where the selection efficiency is maximized. The observed and expected mass limits for each lifetime point are detailed in Table 20, which also lists which selection region was used for each lifetime. These excluded range of masses as a function of lifetime is also shown in Figure 94. The Run 1 limits are included for comparison; the limits have increased by about 200 GeV on average. The search has also improved since the previous incarnation from Run 1 in optimizing the region between 30 GeV and detector-stable lifetimes by introducing the second signal region. The definition of the VLL region prevents the significant drop in mass limit that occurred above 30 GeV in the Run 1 analysis.

Selection	$\tau$ [ns]	$M_{\text{obs}} > [\text{GeV}]$	$M_{\text{exp}} > [\text{GeV}]$
LL	0.4	740	730
"	1.0	1110	1150
"	3.0	1430	1470
"	10	1570	1600
"	30	1580	1620
VLL	50	1590	1590
"	VLL	1570	1580

Table 20: The observed and expected 95% CL lower limit on mass for gluino R-Hadrons for each considered lifetime.

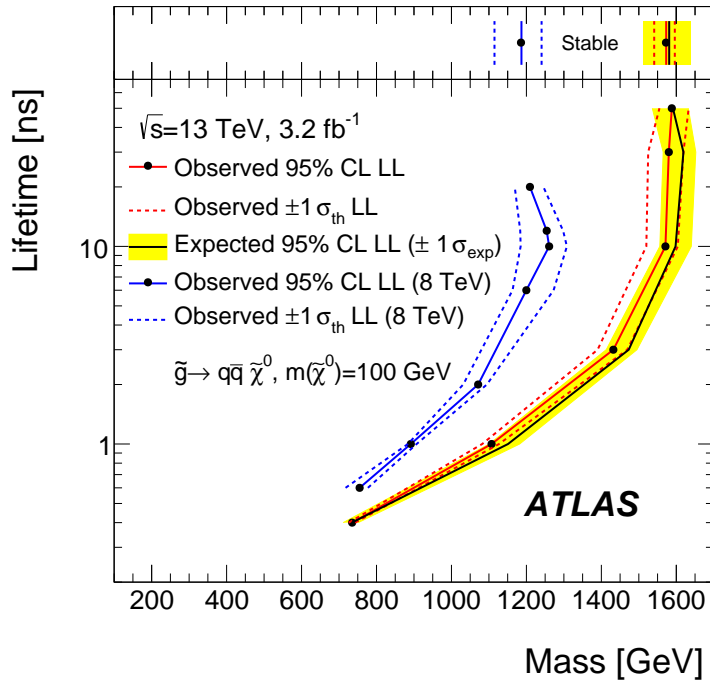


Figure 94: The excluded range of masses as a function of gluino lifetime. The expected lower limit (LL), with its experimental  $\pm 1\sigma$  band, is given with respect to the nominal theoretical cross section. The observed 95% LL obtained at  $\sqrt{s} = 8 \text{ TeV}$  [83] is also shown for comparison.

3925

3926 SUMMARY AND OUTLOOK

---

3927 The search described herein targetted the unique signature of TeV-scale, charged  
3928 **LLPs**, which are predicted in a variety of extensions to the **SM** including some  
3929 versions of **SUSY**. The dataset of 13 TeV proton-proton collisions was collected  
3930 during 2015 by the ATLAS detector at the **LHC**, with an integrated luminosity  
3931 of  $3.2 \text{ fb}^{-1}$ . The specific search strategy focused on identifying massive, charged  
3932 particles which propagate through the Pixel detector in ATLAS by their characteristically large ionization.  
3933 Recent updates to the strategy also include a number of rejection techniques that significantly reduce **SM** backgrounds compared  
3934 to previous iterations. The analysis also provided a data-driven background estimation method that was shown to be effective with validation tests in both  
3935 simulation and actual data.

3936 No significant excesses above the background prediction were found in the  
3937 data, and so limits were placed on the production of massive, charged, **LLPs**. Using  
3938 a benchmark model of simulated R-Hadrons, cross sections above 10-100  
3939  $\text{fb}$  were excluded at 95% confidence level, depending on the lifetime of the R-  
3940 Hadron. Together with the predicted gluino pair-production cross sections, these  
3941 lead to mass limits on R-Hadrons up to 1600 GeV where the search is most sensitive.  
3942 Though these specific values assume an R-Hadron **LLP**, the search strategy accomodates a number of other species and the limits can be interpreted for  
3943 other models.

3944 This search plays an important role in the current, combined ATLAS search  
3945 for long lived particles. The mass limits provided by various ATLAS searches for  
3946 long-lived gluino R-Hadrons can be seen in Figure 95. This search provides the  
3947 most competitive limit for lifetimes between 3 ns up through very long lifetimes,  
3948 where it is still competitive with dedicated searches for **VLL** particles. The limits  
3949 placed on gluino production are very similar to the limits on promptly decaying  
3950 models.

3951 These results are expected to be significantly improved in the following years,  
3952 primarily because of continuing data collection at 13 TeV at the **LHC**. During  
3953 2016, but after the release of this analysis, ATLAS recorded an additional 35.5  
3954  $\text{fb}^{-1}$  of collisions, and analysis of this data would significantly extend the limits  
3955 presented here. The next iteration of the analysis can also provide additional  
3956 interpretations of the search, by explicitly including other models like stop R-  
3957 Hadrons and charginos in the limit calculations, as has been done in previous  
3958 searches [83]. This strategy will continue to provide a competitive approach to  
3959 discovering new **LLPs** throughout the lifetime of the **LHC**.

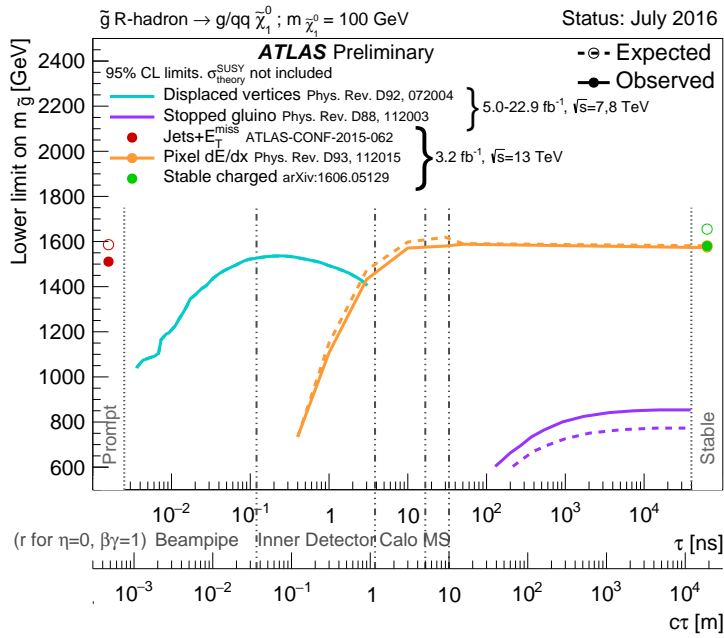


Figure 95: The constraints on the gluino mass as a function of lifetime for a split-supersymmetry model with the gluino R-Hadrons decaying into a gluon or light quarks and a neutralino with mass of 100 GeV. The solid lines indicate the observed limits, while the dashed lines indicate the expected limits. The area below the curves is excluded. The dots represent results for which the particle is assumed to be prompt or VLL. This curve representing this analysis is shown in orange.

3963

## PART V

3964

## APPENDIX

3965

$m(\tilde{g})$ [GeV]	Left Extremum [GeV]	Right Extremum [GeV]
1000	682	1387
1100	763	1478
1200	801	1606
1300	809	1841
1400	861	2011
1500	920	2032
1600	952	2173
1800	1017	2422

Table 21: The left and right extremum of the mass window for each generated mass point with a 50 ns lifetime.

$m(\tilde{g})$ [GeV]	Left Extremum [GeV]	Right Extremum [GeV]
1000	689	1321
1100	746	1513
1200	788	1670
1300	860	1734
1400	833	1925
1500	852	2048
1600	833	2283
1700	946	2379
1800	869	2505

Table 22: The left and right extremum of the mass window for each generated mass point with a 30 ns lifetime.

$m(\tilde{g})$ [GeV]	Left Extremum [GeV]	Right Extremum [GeV]
1000	655	1349
1100	734	1455
1200	712	1631
1300	792	1737
1400	717	1926
1500	815	2117
1600	824	2122
1700	900	2274
1800	919	2344

Table 23: The left and right extremum of the mass window for each generated mass point with a 10 ns lifetime.

$m(\tilde{g})$ [GeV]	Left Extremum [GeV]	Right Extremum [GeV]
800	531	1065
900	576	1165
1000	610	1345
1100	635	1432
1200	663	1563
1300	620	1667
1400	742	1727
1500	761	1937
1600	573	2000
1700	621	2182

Table 24: The left and right extremum of the mass window used for each generated mass point with a lifetime of 3 ns.

$m(\tilde{g})$ [GeV]	Left Extremum [GeV]	Right Extremum [GeV]
600	411	758
700	385	876
800	486	970
900	406	987
1000	408	1136
1100	555	1196
1200	516	1378

Table 25: The left and right extremum of the mass window used for each mass point with a lifetime of 1 ns.

$m(\tilde{g})$ [GeV]	Left Extremum [GeV]	Right Extremum [GeV]
400	204	510
500	295	639
600	288	702
700	323	701
800	190	771
900	277	677
1000	249	688

Table 26: The left and right extremum of the mass window for each generated mass point with a lifetime of 0.4 ns.

$m(\tilde{g})$ [GeV]	Left Extremum [GeV]	Right Extremum [GeV]
800	627	1053
1000	726	1277
1200	857	1584
1400	924	1937
1600	993	2308
1800	1004	2554

Table 27: The left and right extremum of the mass window used for each generated stable mass point.

$m(\tilde{g})$ [GeV]	Expected Signal	Expected Background	Observed Data
1000	$131.18 \pm 6.35$	$1.803 \pm 0.081$	$1.0 \pm 1.0$
1100	$71.11 \pm 3.35$	$1.409 \pm 0.069$	$1.0 \pm 1.0$
1200	$37.18 \pm 1.75$	$1.310 \pm 0.066$	$1.0 \pm 1.0$
1300	$20.76 \pm 0.95$	$1.431 \pm 0.069$	$1.0 \pm 1.0$
1400	$12.63 \pm 0.57$	$1.273 \pm 0.065$	$1.0 \pm 1.0$
1500	$6.57 \pm 0.29$	$1.115 \pm 0.059$	$1.0 \pm 1.0$
1600	$3.56 \pm 0.16$	$1.041 \pm 0.057$	$1.0 \pm 1.0$
1800	$1.27 \pm 0.05$	$0.918 \pm 0.053$	$1.0 \pm 1.0$

Table 28: The expected number of signal events, the expected number of background events, and the observed number of events in data with their respective statistical errors within the respective mass window for each generated mass point with a lifetime of 50 ns.

$m(\tilde{g})$ [GeV]	Expected Signal	Expected Background	Observed Data
1000	$144.65 \pm 6.34$	$1.328 \pm 0.063$	$2.0 \pm 1.4$
1100	$75.28 \pm 3.27$	$1.255 \pm 0.060$	$2.0 \pm 1.4$
1200	$40.51 \pm 1.75$	$1.193 \pm 0.058$	$2.0 \pm 1.4$
1300	$20.91 \pm 0.93$	$0.997 \pm 0.051$	$2.0 \pm 1.4$
1400	$11.97 \pm 0.51$	$1.131 \pm 0.056$	$2.0 \pm 1.4$
1500	$6.81 \pm 0.28$	$1.111 \pm 0.055$	$2.0 \pm 1.4$
1600	$4.19 \pm 0.16$	$1.193 \pm 0.058$	$2.0 \pm 1.4$
1700	$2.42 \pm 0.09$	$0.963 \pm 0.050$	$2.0 \pm 1.4$
1800	$1.46 \pm 0.05$	$1.138 \pm 0.056$	$3.0 \pm 1.7$

Table 29: The expected number of signal events, the expected number of background events, and the observed number of events in data with their respective statistical errors within the respective mass window for each generated mass point with a lifetime of 30 ns.

$m(\tilde{g})$ [GeV]	Expected Signal	Expected Background	Observed Data
1000	$144.48 \pm 5.14$	$1.499 \pm 0.069$	$2.0 \pm 1.4$
1100	$73.19 \pm 2.61$	$1.260 \pm 0.060$	$2.0 \pm 1.4$
1200	$41.54 \pm 1.41$	$1.456 \pm 0.067$	$2.0 \pm 1.4$
1300	$22.58 \pm 0.77$	$1.201 \pm 0.058$	$2.0 \pm 1.4$
1400	$12.70 \pm 0.42$	$1.558 \pm 0.071$	$2.0 \pm 1.4$
1500	$6.73 \pm 0.24$	$1.237 \pm 0.060$	$2.0 \pm 1.4$
1600	$3.90 \pm 0.13$	$1.201 \pm 0.058$	$2.0 \pm 1.4$
1700	$2.27 \pm 0.07$	$1.027 \pm 0.052$	$2.0 \pm 1.4$
1800	$1.34 \pm 0.04$	$1.019 \pm 0.052$	$2.0 \pm 1.4$

Table 30: The expected number of signal events, the expected number of background events, and the observed number of events in data with their respective statistical errors within the respective mass window for each generated mass point with a lifetime of 10 ns.

$m(\tilde{g})$ [GeV]	Expected Signal	Expected Background	Observed Data
800	$362.97 \pm 14.68$	$1.841 \pm 0.080$	$5.0 \pm 2.2$
900	$169.20 \pm 6.69$	$1.710 \pm 0.076$	$3.0 \pm 1.7$
1000	$84.78 \pm 3.23$	$1.727 \pm 0.076$	$2.0 \pm 1.4$
1100	$40.06 \pm 1.60$	$1.679 \pm 0.075$	$2.0 \pm 1.4$
1200	$20.06 \pm 0.81$	$1.598 \pm 0.072$	$2.0 \pm 1.4$
1300	$10.76 \pm 0.43$	$1.851 \pm 0.080$	$2.0 \pm 1.4$
1400	$5.52 \pm 0.22$	$1.374 \pm 0.064$	$2.0 \pm 1.4$
1500	$3.16 \pm 0.13$	$1.355 \pm 0.064$	$2.0 \pm 1.4$
1600	$2.13 \pm 0.11$	$2.235 \pm 0.093$	$3.0 \pm 1.7$
1700	$1.10 \pm 0.06$	$1.995 \pm 0.085$	$2.0 \pm 1.4$

Table 31: The expected number of signal events, the expected number of background events, and the observed number of events in data with their respective statistical errors within the respective mass window for each generated mass point with a lifetime of 3 ns.

$m(\tilde{g})$ [GeV]	Expected Signal	Expected Background	Observed Data
600	$431.80 \pm 36.60$	$2.418 \pm 0.099$	$3.0 \pm 1.7$
700	$192.77 \pm 15.28$	$3.267 \pm 0.126$	$3.0 \pm 1.7$
800	$69.63 \pm 5.90$	$2.125 \pm 0.089$	$3.0 \pm 1.7$
900	$28.91 \pm 2.59$	$3.114 \pm 0.121$	$3.0 \pm 1.7$
1000	$13.64 \pm 1.22$	$3.359 \pm 0.129$	$5.0 \pm 2.2$
1100	$6.13 \pm 0.57$	$1.879 \pm 0.081$	$3.0 \pm 1.7$
1200	$3.24 \pm 0.30$	$2.387 \pm 0.098$	$5.0 \pm 2.2$

Table 32: The expected number of signal events, the expected number of background events, and the observed number of events in data with their respective statistical errors within the respective mass window for each generated mass point with a lifetime of 1 ns.

$m(\tilde{g})$ [GeV]	Expected Signal	Expected Background	Observed Data
400	$181.71 \pm 75.59$	$6.780 \pm 0.238$	$4.0 \pm 2.0$
500	$103.88 \pm 30.05$	$4.310 \pm 0.160$	$4.0 \pm 2.0$
600	$28.34 \pm 9.34$	$4.868 \pm 0.177$	$4.0 \pm 2.0$
700	$13.62 \pm 4.00$	$3.908 \pm 0.147$	$4.0 \pm 2.0$
800	$2.75 \pm 1.15$	$9.001 \pm 0.308$	$8.0 \pm 2.8$
900	$2.25 \pm 0.71$	$5.045 \pm 0.183$	$5.0 \pm 2.2$
1000	$0.34 \pm 0.19$	$6.026 \pm 0.214$	$6.0 \pm 2.4$

Table 33: The expected number of signal events, the expected number of background events, and the observed number of events in data with their respective statistical errors within the respective mass window for each generated mass point with a lifetime of p4 ns.

$m(\tilde{g})$ [GeV]	Expected Signal	Expected Background	Observed Data
800	$462.83 \pm 14.86$	$1.764 \pm 0.080$	$2.0 \pm 1.4$
1000	$108.73 \pm 3.38$	$1.458 \pm 0.070$	$1.0 \pm 1.0$
1200	$31.74 \pm 0.95$	$1.137 \pm 0.060$	$1.0 \pm 1.0$
1400	$10.22 \pm 0.29$	$1.058 \pm 0.058$	$1.0 \pm 1.0$
1600	$3.07 \pm 0.09$	$0.947 \pm 0.054$	$1.0 \pm 1.0$
1800	$1.08 \pm 0.05$	$0.940 \pm 0.054$	$1.0 \pm 1.0$

Table 34: The expected number of signal events, the expected number of background events, and the observed number of events in data with their respective statistical errors within the respective mass window for each generated stable mass point

- 
- 3969 [1] A. D. Martin, W. J. Stirling, R. S. Thorne, and G. Watt. “Parton distributions for the LHC”. In: *Eur. Phys. J.* C63 (2009), pp. 189–285. doi: [10.1140/epjc/s10052-009-1072-5](https://doi.org/10.1140/epjc/s10052-009-1072-5). arXiv: [0901.0002](https://arxiv.org/abs/0901.0002) [hep-ph].
- 3970 [2] Nobelprize.org. “The 2004 Nobel Prize in Physics - Popular Information”. 2014. URL: <https://cds.cern.ch/record/1165534>.
- 3971 [3] Prajwal Raj Kafle, Sanjib Sharma, Geraint F. Lewis, and Joss Bland-Hawthorn. “On the Shoulders of Giants: Properties of the Stellar Halo and the Milky Way Mass Distribution”. In: *Astrophys. J.* 794.1 (2014), p. 59. doi: [10.1088/0004-637X/794/1/59](https://doi.org/10.1088/0004-637X/794/1/59). arXiv: [1408.1787](https://arxiv.org/abs/1408.1787) [astro-ph.GA].
- 3972 [4] Savas Dimopoulos and Howard Georgi. “Softly broken supersymmetry and SU(5)”. In: *Nuclear Physics B* 193.1 (1981), pp. 150 – 162. ISSN: 0550-3213. doi: [http://dx.doi.org/10.1016/0550-3213\(81\)90522-8](https://dx.doi.org/10.1016/0550-3213(81)90522-8).
- 3973 [5] A. Djouadi et al. “The Minimal supersymmetric standard model: Group summary report”. In: *GDR (Groupement De Recherche) - Supersymetrie Montpellier, France, April 15-17, 1998*. 1998. arXiv: [hep-ph/9901246](https://arxiv.org/abs/hep-ph/9901246) [hep-ph]. URL: [https://inspirehep.net/record/481987/files/arXiv-hep-ph\\_9901246.pdf](https://inspirehep.net/record/481987/files/arXiv-hep-ph_9901246.pdf).
- 3974 [6] K. A. Olive et al. “Review of Particle Physics”. In: *Chin. Phys.* C38 (2014), p. 090001. doi: [10.1088/1674-1137/38/9/090001](https://doi.org/10.1088/1674-1137/38/9/090001).
- 3975 [7] Lawrence J. Hall, Yasunori Nomura, and Satoshi Shirai. “Spread Supersymmetry with Wino LSP: Gluino and Dark Matter Signals”. In: *JHEP* 01 (2013), p. 036. doi: [10.1007/JHEP01\(2013\)036](https://doi.org/10.1007/JHEP01(2013)036). arXiv: [1210.2395](https://arxiv.org/abs/1210.2395) [hep-ph].
- 3976 [8] G. F. Giudice and A. Romanino. “Split supersymmetry”. In: *Nucl. Phys. B* 699 (2004), p. 65. doi: [10.1016/j.nuclphysb.2004.11.048](https://doi.org/10.1016/j.nuclphysb.2004.11.048). arXiv: [hep-ph/0406088](https://arxiv.org/abs/hep-ph/0406088).
- 3977 [9] N. Arkani-Hamed, S. Dimopoulos, G. F. Giudice, and A. Romanino. “Aspects of split supersymmetry”. In: *Nucl. Phys. B* 709 (2005), p. 3. doi: [10.1016/j.nuclphysb.2004.12.026](https://doi.org/10.1016/j.nuclphysb.2004.12.026). arXiv: [hep-ph/0409232](https://arxiv.org/abs/hep-ph/0409232).
- 3978 [10] Lyndon Evans and Philip Bryant. “LHC Machine”. In: *JINST* 3 (2008), S08001. doi: [10.1088/1748-0221/3/08/S08001](https://doi.org/10.1088/1748-0221/3/08/S08001).
- 3979 [11] C Lefevre. “LHC: the guide (English version). Guide du LHC (version anglaise)”. 2009. URL: <https://cds.cern.ch/record/1165534>.
- 3980 [12] “LEP Design Report Vol.1”. In: (1983).
- 3981 [13] ATLAS Collaboration. “The ATLAS Experiment at the CERN Large Hadron Collider”. In: *JINST* 3 (2008), S08003. doi: [10.1088/1748-0221/3/08/S08003](https://doi.org/10.1088/1748-0221/3/08/S08003).

- 4007 [14] S. Chatrchyan et al. “The CMS experiment at the CERN LHC”. In: *JINST*  
 4008 3 (2008), S08004. doi: [10.1088/1748-0221/3/08/S08004](https://doi.org/10.1088/1748-0221/3/08/S08004).
- 4009 [15] A. Augusto Alves Jr. et al. “The LHCb Detector at the LHC”. In: *JINST* 3  
 4010 (2008), S08005. doi: [10.1088/1748-0221/3/08/S08005](https://doi.org/10.1088/1748-0221/3/08/S08005).
- 4011 [16] K. Aamodt et al. “The ALICE experiment at the CERN LHC”. In: *JINST*  
 4012 3 (2008), S08002. doi: [10.1088/1748-0221/3/08/S08002](https://doi.org/10.1088/1748-0221/3/08/S08002).
- 4013 [17] Daniel Froidevaux and Paris Sphicas. “General-Purpose Detectors for  
 4014 the Large Hadron Collider”. In: *Annual Review of Nuclear and Particle Sci-  
 4015 ence* 56.1 (2006), pp. 375–440. doi: [10.1146/annurev.nucl.54.  
 4016 070103.181209](https://doi.org/10.1146/annurev.nucl.54.070103.181209). url: <http://dx.doi.org/10.1146/annurev.nucl.54.070103.181209>.
- 4017 [18] M Capeans, G Darbo, K Einsweiller, M Elsing, T Flick, M Garcia-Sciveres,  
 4018 C Gemme, H Pernegger, O Rohne, and R Vuillermet. *ATLAS Insertable B-  
 4019 Layer Technical Design Report*. Tech. rep. CERN-LHCC-2010-013. ATLAS-  
 4020 TDR-19. 2010. url: <https://cds.cern.ch/record/1291633>.
- 4021 [19] T. Cornelissen, M. Elsing, S. Fleischmann, W. Liebig, and E. Moyse. “Con-  
 4022 cepts, Design and Implementation of the ATLAS New Tracking (NEWT)”.  
 4023 In: (2007). Ed. by A. Salzburger.
- 4024 [20] “Performance of the ATLAS Inner Detector Track and Vertex Recon-  
 4025 struction in the High Pile-Up LHC Environment”. In: (2012).
- 4026 [21] A. Salzburger. “The ATLAS Track Extrapolation Package”. In: (2007).
- 4027 [22] ATLAS Collaboration. “A neural network clustering algorithm for the  
 4028 ATLAS silicon pixel detector”. In: *JINST* 9 (2014), P09009. doi: [10.1088/1748-0221/9/09/P09009](https://doi.org/10.1088/1748-0221/9/09/P09009). arXiv: [1406.7690 \[hep-ex\]](https://arxiv.org/abs/1406.7690).
- 4029 [23] ATLAS Collaboration. *Performance of primary vertex reconstruction in proton-  
 4030 proton collisions at  $\sqrt{s} = 7$  TeV in the ATLAS experiment*. ATLAS-CONF-  
 4031 2010-069. 2010. url: <https://cds.cern.ch/record/1281344>.
- 4032 [24] ATLAS Collaboration. “Electron reconstruction and identification effi-  
 4033 ciency measurements with the ATLAS detector using the 2011 LHC proton-  
 4034 proton collision data”. In: *Eur. Phys. J. C* 74 (2014), p. 2941. doi: [10.1140/epjc/s10052-014-2941-0](https://doi.org/10.1140/epjc/s10052-014-2941-0). arXiv: [1404.2240 \[hep-ex\]](https://arxiv.org/abs/1404.2240).  
 4035 PERF-2013-03.
- 4036 [25] ATLAS Collaboration. *Electron efficiency measurements with the ATLAS  
 4037 detector using the 2012 LHC proton–proton collision data*. ATLAS-CONF-  
 4038 2014-032. 2014. url: <https://cds.cern.ch/record/1706245>.
- 4039 [26] ATLAS Collaboration. *Measurements of the photon identification efficiency  
 4040 with the ATLAS detector using  $4.9 \text{ fb}^{-1}$  of  $pp$  collision data collected in 2011*.  
 4041 ATLAS-CONF-2012-123. 2012. url: <https://cds.cern.ch/record/1473426>.
- 4042 [27] ATLAS Collaboration. “Muon reconstruction performance of the AT-  
 4043 LAS detector in proton–proton collision data at  $\sqrt{s} = 13$  TeV”. In: (2016).  
 4044 arXiv: [1603.05598 \[hep-ex\]](https://arxiv.org/abs/1603.05598). PERF-2015-10.
- 4045
- 4046
- 4047
- 4048

- 4049 [28] ATLAS Collaboration. “Topological cell clustering in the ATLAS calorimeters and its performance in LHC Run 1”. In: (2016). arXiv: [1603.02934](https://arxiv.org/abs/1603.02934) [hep-ex]. PERF-2014-07.
- 4050  
4051  
4052  
4053  
4054  
4055 [29] ATLAS Collaboration. *Properties of jets and inputs to jet reconstruction and calibration with the ATLAS detector using proton–proton collisions at  $\sqrt{s} = 13$  TeV*. ATL-PHYS-PUB-2015-036. 2015. URL: <https://cds.cern.ch/record/2044564>.
- 4056  
4057  
4058 [30] Matteo Cacciari, Gavin P. Salam, and Gregory Soyez. “The anti- $k_t$  jet clustering algorithm”. In: *JHEP* 04 (2008), p. 063. doi: [10.1088/1126-6708/2008/04/063](https://doi.org/10.1088/1126-6708/2008/04/063). arXiv: [0802.1189](https://arxiv.org/abs/0802.1189) [hep-ph].
- 4059  
4060  
4061 [31] ATLAS Collaboration. *Jet global sequential corrections with the ATLAS detector in proton–proton collisions at  $\sqrt{s} = 8$  TeV*. ATLAS-CONF-2015-002. 2015. URL: <https://cds.cern.ch/record/2001682>.
- 4062  
4063  
4064 [32] S. Agostinelli et al. “GEANT4: A simulation toolkit”. In: *Nucl. Instrum. Meth. A* 506 (2003), pp. 250–303. doi: [10.1016/S0168-9002\(03\)01368-8](https://doi.org/10.1016/S0168-9002(03)01368-8).
- 4065  
4066  
4067  
4068 [33] ATLAS Collaboration. “A study of the material in the ATLAS inner detector using secondary hadronic interactions”. In: *JINST* 7 (2012), P01013. doi: [10.1088/1748-0221/7/01/P01013](https://doi.org/10.1088/1748-0221/7/01/P01013). arXiv: [1110.6191](https://arxiv.org/abs/1110.6191) [hep-ex]. PERF-2011-08.
- 4069  
4070  
4071  
4072 [34] ATLAS Collaboration. “Electron and photon energy calibration with the ATLAS detector using LHC Run 1 data”. In: *Eur. Phys. J. C* 74 (2014), p. 3071. doi: [10.1140/epjc/s10052-014-3071-4](https://doi.org/10.1140/epjc/s10052-014-3071-4). arXiv: [1407.5063](https://arxiv.org/abs/1407.5063) [hep-ex]. PERF-2013-05.
- 4073  
4074  
4075  
4076 [35] ATLAS Collaboration. “A measurement of the calorimeter response to single hadrons and determination of the jet energy scale uncertainty using LHC Run-1  $pp$ -collision data with the ATLAS detector”. In: (2016). arXiv: [1607.08842](https://arxiv.org/abs/1607.08842) [hep-ex]. PERF-2015-05.
- 4077  
4078  
4079  
4080 [36] ATLAS Collaboration. “Single hadron response measurement and calorimeter jet energy scale uncertainty with the ATLAS detector at the LHC”. In: *Eur. Phys. J. C* 73 (2013), p. 2305. doi: [10.1140/epjc/s10052-013-2305-1](https://doi.org/10.1140/epjc/s10052-013-2305-1). arXiv: [1203.1302](https://arxiv.org/abs/1203.1302) [hep-ex]. PERF-2011-05.
- 4081  
4082  
4083 [37] ATLAS Collaboration. “The ATLAS Simulation Infrastructure”. In: *Eur. Phys. J. C* 70 (2010), p. 823. doi: [10.1140/epjc/s10052-010-1429-9](https://doi.org/10.1140/epjc/s10052-010-1429-9). arXiv: [1005.4568](https://arxiv.org/abs/1005.4568) [hep-ex]. SOFT-2010-01.
- 4084  
4085  
4086 [38] T. Sjöstrand, S. Mrenna, and P. Skands. “A Brief Introduction to PYTHIA 8.1”. In: *Comput. Phys. Commun.* 178 (2008), pp. 852–867. doi: [10.1016/j.cpc.2008.01.036](https://doi.org/10.1016/j.cpc.2008.01.036). arXiv: [0710.3820](https://arxiv.org/abs/0710.3820).
- 4087  
4088 [39] ATLAS Collaboration. *Summary of ATLAS Pythia 8 tunes*. ATL-PHYS-PUB-2012-003. 2012. URL: [http://cds.cern.ch/record/1474107](https://cds.cern.ch/record/1474107).

- 4089 [40] A.D. Martin, W.J. Stirling, R.S. Thorne, and G. Watt. “Parton distributions for the LHC”. In: *Eur. Phys. J. C* 63 (2009). Figures from the [MSTW Website](#), pp. 189–285. doi: [10.1140/epjc/s10052-009-1072-5](https://doi.org/10.1140/epjc/s10052-009-1072-5). arXiv: [0901.0002](https://arxiv.org/abs/0901.0002).
- 4090  
4091  
4092
- 4093 [41] A. Sherstnev and R.S. Thorne. “Parton Distributions for LO Generators”. In: *Eur. Phys. J. C* 55 (2008), pp. 553–575. doi: [10.1140/epjc/s10052-008-0610-x](https://doi.org/10.1140/epjc/s10052-008-0610-x). arXiv: [0711.2473](https://arxiv.org/abs/0711.2473).
- 4094  
4095
- 4096 [42] A. Ribon et al. *Status of Geant4 hadronic physics for the simulation of LHC experiments at the start of LHC physics program*. CERN-LCGAPP-2010-02. 2010. URL: <http://lcgapp.cern.ch/project/docs/noteStatusHadronic2010.pdf>.
- 4097  
4098  
4099
- 4100 [43] M. P. Guthrie, R. G. Alsmiller, and H. W. Bertini. “Calculation of the capture of negative pions in light elements and comparison with experiments pertaining to cancer radiotherapy”. In: *Nucl. Instrum. Meth.* 66 (1968), pp. 29–36. doi: [10.1016/0029-554X\(68\)90054-2](https://doi.org/10.1016/0029-554X(68)90054-2).
- 4101  
4102  
4103
- 4104 [44] H. W. Bertini and P. Guthrie. “News item results from medium-energy intranuclear-cascade calculation”. In: *Nucl. Instr. and Meth. A* 169 (1971), p. 670. doi: [10.1016/0375-9474\(71\)90710-X](https://doi.org/10.1016/0375-9474(71)90710-X).
- 4105  
4106
- 4107 [45] V.A. Karmanov. “Light Front Wave Function of Relativistic Composite System in Explicitly Solvable Model”. In: *Nucl. Phys. B* 166 (1980), p. 378. doi: [10.1016/0550-3213\(80\)90204-7](https://doi.org/10.1016/0550-3213(80)90204-7).
- 4108  
4109
- 4110 [46] H. S. Fesefeldt. *GHEISHA program*. Pitha-85-02, Aachen. 1985.
- 4111  
4112
- 4113 [47] G. Folger and J.P. Wellisch. “String parton models in Geant4”. In: (2003). arXiv: [nucl-th/0306007](https://arxiv.org/abs/nucl-th/0306007).
- 4114  
4115
- 4116 [48] N. S. Amelin et al. “Transverse flow and collectivity in ultrarelativistic heavy-ion collisions”. In: *Phys. Rev. Lett.* 67 (1991), p. 1523. doi: [10.1103/PhysRevLett.67.1523](https://doi.org/10.1103/PhysRevLett.67.1523).
- 4117  
4118
- 4119 [49] N. S. Amelin et al. “Collectivity in ultrarelativistic heavy ion collisions”. In: *Nucl. Phys. A* 544 (1992), p. 463. doi: [10.1016/0375-9474\(92\)90598-E](https://doi.org/10.1016/0375-9474(92)90598-E).
- 4120  
4121
- 4122 [50] L. V. Bravina et al. “Fluid dynamics and Quark Gluon string model - What we can expect for Au+Au collisions at 11.6 AGeV/c”. In: *Nucl. Phys. A* 566 (1994), p. 461. doi: [10.1016/0375-9474\(94\)90669-6](https://doi.org/10.1016/0375-9474(94)90669-6).
- 4123  
4124
- 4125 [51] L. V. Bravin et al. “Scaling violation of transverse flow in heavy ion collisions at AGS energies”. In: *Phys. Lett. B* 344 (1995), p. 49. doi: [10.1016/0370-2693\(94\)01560-Y](https://doi.org/10.1016/0370-2693(94)01560-Y).
- 4126  
4127
- 4128 [52] B. Andersson et al. “A model for low-pT hadronic reactions with generalizations to hadron-nucleus and nucleus-nucleus collisions”. In: *Nucl. Phys. B* 281 (1987), p. 289. doi: [10.1016/0550-3213\(87\)90257-4](https://doi.org/10.1016/0550-3213(87)90257-4).
- 4129  
4130
- 4128 [53] B. Andersson, A. Tai, and B.-H. Sa. “Final state interactions in the (nuclear) FRITIOF string interaction scenario”. In: *Z. Phys. C* 70 (1996), pp. 499–506. doi: [10.1007/s002880050127](https://doi.org/10.1007/s002880050127).

- 4131 [54] B. Nilsson-Almqvist and E. Stenlund. “Interactions Between Hadrons  
 4132 and Nuclei: The Lund Monte Carlo, Fritiof Version 1.6”. In: *Comput. Phys.*  
 4133 *Commun.* 43 (1987), p. 387. doi: [10.1016/0010-4655\(87\)90056-7](https://doi.org/10.1016/0010-4655(87)90056-7).
- 4134 [55] B. Ganhuyag and V. Uzhinsky. “Modified FRITIOF code: Negative charged  
 4135 particle production in high energy nucleus nucleus interactions”. In: *Czech.*  
 4136 *J. Phys.* 47 (1997), pp. 913–918. doi: [10.1023/A:1021296114786](https://doi.org/10.1023/A:1021296114786).
- 4137 [56] ATLAS Collaboration. “Topological cell clustering in the ATLAS calorime-  
 4138 ters and its performance in LHC Run 1”. In: (2016). arXiv: [1603.02934](https://arxiv.org/abs/1603.02934)  
 4139 [[hep-ex](#)].
- 4140 [57] Peter Speckmayer. “Energy Measurement of Hadrons with the CERN  
 4141 ATLAS Calorimeter”. Presented on 18 Jun 2008. PhD thesis. Vienna: Vi-  
 4142 enna, Tech. U., 2008. URL: <http://cds.cern.ch/record/1112036>.
- 4143 [58] CMS Collaboration. “The CMS barrel calorimeter response to particle  
 4144 beams from 2 to 350 GeV/c”. In: *Eur. Phys. J. C* 60.3 (2009). doi: [10.1140/epjc/s10052-009-0959-5](https://doi.org/10.1140/epjc/s10052-009-0959-5).
- 4146 [59] J. Beringer et al. (Particle Data Group). “Review of Particle Physics”. In:  
 4147 *Chin. Phys. C* 38 (2014), p. 090001. URL: <http://pdg.lbl.gov>.
- 4148 [60] P. Adragna et al. “Measurement of Pion and Proton Response and Lon-  
 4149 gitudinal Shower Profiles up to 20 Nuclear Interaction Lengths with the  
 4150 ATLAS Tile Calorimeter”. In: *Nucl. Instrum. Meth. A* 615 (2010), pp. 158–  
 4151 181. doi: [10.1016/j.nima.2010.01.037](https://doi.org/10.1016/j.nima.2010.01.037).
- 4152 [61] ATLAS Collaboration. “Jet energy measurement and its systematic un-  
 4153 certainty in proton–proton collisions at  $\sqrt{s} = 7$  TeV with the ATLAS de-  
 4154 tector”. In: *Eur. Phys. J. C* 75 (2015), p. 17. doi: [10.1140/epjc/s10052-014-3190-y](https://doi.org/10.1140/epjc/s10052-014-3190-y). arXiv: [1406.0076](https://arxiv.org/abs/1406.0076) [[hep-ex](#)]. PERF-2012-01.
- 4156 [62] Hung-Liang Lai, Marco Guzzi, Joey Huston, Zhao Li, Pavel M. Nadolsky,  
 4157 et al. “New parton distributions for collider physics”. In: *Phys. Rev. D* 82  
 4158 (2010), p. 074024. doi: [10.1103/PhysRevD.82.074024](https://doi.org/10.1103/PhysRevD.82.074024). arXiv: [1007.2241](https://arxiv.org/abs/1007.2241) [[hep-ph](#)].
- 4160 [63] E. Abat et al. “Study of energy response and resolution of the ATLAS  
 4161 barrel calorimeter to hadrons of energies from 20 to 350 GeV”. In: *Nucl.*  
 4162 *Instrum. Meth. A* 621.1-3 (2010), pp. 134 –150. doi: <http://dx.doi.org/10.1016/j.nima.2010.04.054>.
- 4164 [64] ATLAS Collaboration. “Jet energy measurement with the ATLAS detec-  
 4165 tor in proton–proton collisions at  $\sqrt{s} = 7$  TeV”. In: *Eur. Phys. J. C* 73  
 4166 (2013), p. 2304. doi: [10.1140/epjc/s10052-013-2304-2](https://doi.org/10.1140/epjc/s10052-013-2304-2). arXiv:  
 4167 [1112.6426](https://arxiv.org/abs/1112.6426) [[hep-ex](#)]. PERF-2011-03.
- 4168 [65] Nausheen R. Shah and Carlos E. M. Wagner. “Gravitons and dark mat-  
 4169 ter in universal extra dimensions”. In: *Phys. Rev. D* 74 (2006), p. 104008.  
 4170 doi: [10.1103/PhysRevD.74.104008](https://doi.org/10.1103/PhysRevD.74.104008). arXiv: [hep-ph/0608140](https://arxiv.org/abs/hep-ph/0608140)  
 4171 [[hep-ph](#)].

- 4172 [66] Jonathan L. Feng, Arvind Rajaraman, and Fumihiro Takayama. “Graviton cosmology in universal extra dimensions”. In: *Phys. Rev.* D68 (2003),  
 4173 p. 085018. doi: [10.1103/PhysRevD.68.085018](https://doi.org/10.1103/PhysRevD.68.085018). arXiv: [hep-ph/0307375](https://arxiv.org/abs/hep-ph/0307375) [hep-ph].
- 4176 [67] Paul H. Frampton and Pham Quang Hung. “Long-lived quarks?” In: *Phys.  
 4177 Rev. D* 58 (5 1998), p. 057704. doi: [10.1103/PhysRevD.58.057704](https://doi.org/10.1103/PhysRevD.58.057704).  
 4178 URL: <http://link.aps.org/doi/10.1103/PhysRevD.58.057704>.
- 4180 [68] C. Friberg, E. Norrbin, and T. Sjostrand. “QCD aspects of leptoquark  
 4181 production at HERA”. In: *Phys. Lett.* B403 (1997), pp. 329–334. doi: [10.1016/S0370-2693\(97\)00543-1](https://doi.org/10.1016/S0370-2693(97)00543-1). arXiv: [hep-ph/9704214](https://arxiv.org/abs/hep-ph/9704214) [hep-ph].
- 4183 [69] Herbert K. Dreiner. “An introduction to explicit R-parity violation”. In:  
 4184 (1997). arXiv: [hep-ph/9707435](https://arxiv.org/abs/hep-ph/9707435).
- 4185 [70] Edmond L. Berger and Zack Sullivan. “Lower limits on R-parity-violating  
 4186 couplings in supersymmetry”. In: *Phys. Rev. Lett.* 92 (2004), p. 201801. doi:  
 4187 [10.1103/PhysRevLett.92.201801](https://doi.org/10.1103/PhysRevLett.92.201801). arXiv: [hep-ph/0310001](https://arxiv.org/abs/hep-ph/0310001).
- 4188 [71] R. Barbieri, C. Berat, M. Besancon, M. Chemtob, A. Deandrea, et al. “R-  
 4189 parity violating supersymmetry”. In: *Phys. Rept.* 420 (2005), p. 1. doi: [10.1016/j.physrep.2005.08.006](https://doi.org/10.1016/j.physrep.2005.08.006). arXiv: [hep-ph/0406039](https://arxiv.org/abs/hep-ph/0406039).
- 4191 [72] M. Fairbairn et al. “Stable massive particles at colliders”. In: *Phys. Rept.*  
 4192 438 (2007), p. 1. doi: [10.1016/j.physrep.2006.10.002](https://doi.org/10.1016/j.physrep.2006.10.002). arXiv:  
 4193 [hep-ph/0611040](https://arxiv.org/abs/hep-ph/0611040).
- 4194 [73] Christopher F. Kolda. “Gauge-mediated supersymmetry breaking: Intro-  
 4195 duction, review and update”. In: *Nucl. Phys. Proc. Suppl.* 62 (1998), p. 266.  
 4196 doi: [10.1016/S0920-5632\(97\)00667-1](https://doi.org/10.1016/S0920-5632(97)00667-1). arXiv: [hep-ph/9707450](https://arxiv.org/abs/hep-ph/9707450).
- 4197 [74] Howard Baer, Kingman Cheung, and John F. Gunion. “A Heavy gluino as  
 4198 the lightest supersymmetric particle”. In: *Phys. Rev. D* 59 (1999), p. 075002.  
 4199 doi: [10.1103/PhysRevD.59.075002](https://doi.org/10.1103/PhysRevD.59.075002). arXiv: [hep-ph/9806361](https://arxiv.org/abs/hep-ph/9806361).
- 4200 [75] S. James Gates Jr. and Oleg Lebedev. “Searching for supersymmetry in  
 4201 hadrons”. In: *Phys. Lett. B* 477 (2000), p. 216. doi: [10.1016/S0370-2693\(00\)00172-6](https://doi.org/10.1016/S0370-2693(00)00172-6). arXiv: [hep-ph/9912362](https://arxiv.org/abs/hep-ph/9912362).
- 4203 [76] Glennys R. Farrar and Pierre Fayet. “Phenomenology of the Production,  
 4204 Decay, and Detection of New Hadronic States Associated with Super-  
 4205 symmetry”. In: *Phys. Lett.* B76 (1978), pp. 575–579. doi: [10.1016/0370-2693\(78\)90858-4](https://doi.org/10.1016/0370-2693(78)90858-4).
- 4207 [77] A.C. Kraan, J.B. Hansen, and P. Nevski. “Discovery potential of R-hadrons  
 4208 with the ATLAS detector”. In: *Eur. Phys. J.* C49 (2007), pp. 623–640. doi:  
 4209 [10.1140/epjc/s10052-006-0162-x](https://doi.org/10.1140/epjc/s10052-006-0162-x). arXiv: [hep-ex/0511014](https://arxiv.org/abs/hep-ex/0511014)  
 4210 [hep-ex].
- 4211 [78] Rasmus Mackeprang and David Milstead. “An Updated Description of  
 4212 Heavy-Hadron Interactions in GEANT-4”. In: *Eur. Phys. J.* C66 (2010),  
 4213 pp. 493–501. doi: [10.1140/epjc/s10052-010-1262-1](https://doi.org/10.1140/epjc/s10052-010-1262-1). arXiv:  
 4214 [0908.1868](https://arxiv.org/abs/0908.1868) [hep-ph].

- 4215 [79] ATLAS Collaboration. “Search for massive, long-lived particles using mul-  
 4216 titrack displaced vertices or displaced lepton pairs in  $pp$  collisions at  
 4217  $\sqrt{s} = 8$  TeV with the ATLAS detector”. In: *Phys. Rev. D* 92 (2015), p. 072004.  
 4218 doi: [10.1103/PhysRevD.92.072004](https://doi.org/10.1103/PhysRevD.92.072004). arXiv: [1504.05162 \[hep-ex\]](https://arxiv.org/abs/1504.05162).  
 4219 SUSY-2014-02.
- 4220 [80] ATLAS Collaboration. “Search for charginos nearly mass degenerate with  
 4221 the lightest neutralino based on a disappearing-track signature in  $pp$   
 4222 collisions at  $\sqrt{s} = 8$  TeV with the ATLAS detector”. In: *Phys. Rev. D*  
 4223 88 (2013), p. 112006. doi: [10.1103/PhysRevD.88.112006](https://doi.org/10.1103/PhysRevD.88.112006). arXiv:  
 4224 [1310.3675 \[hep-ex\]](https://arxiv.org/abs/1310.3675). SUSY-2013-01.
- 4225 [81] ATLAS Collaboration. “Searches for heavy long-lived sleptons and R-  
 4226 Hadrons with the ATLAS detector in  $pp$  collisions at  $\sqrt{s} = 7$  TeV”. In:  
 4227 *Phys. Lett. B* 720 (2013), p. 277. doi: [10.1016/j.physletb.2013.02.015](https://doi.org/10.1016/j.physletb.2013.02.015). arXiv: [1211.1597 \[hep-ex\]](https://arxiv.org/abs/1211.1597). SUSY-2012-01.
- 4229 [82] ATLAS Collaboration. “Searches for heavy long-lived charged particles  
 4230 with the ATLAS detector in proton–proton collisions at  $\sqrt{s} = 8$  TeV”. In:  
 4231 *JHEP* 01 (2015), p. 068. doi: [10.1007/JHEP01\(2015\)068](https://doi.org/10.1007/JHEP01(2015)068). arXiv:  
 4232 [1411.6795 \[hep-ex\]](https://arxiv.org/abs/1411.6795). SUSY-2013-22.
- 4233 [83] ATLAS Collaboration. “Search for metastable heavy charged particles  
 4234 with large ionisation energy loss in  $pp$  collisions at  $\sqrt{s} = 8$  TeV using the  
 4235 ATLAS experiment”. In: *Eur. Phys. J. C* 75 (2015), p. 407. doi: [10.1140/epjc/s10052-015-3609-0](https://doi.org/10.1140/epjc/s10052-015-3609-0). arXiv: [1506.05332 \[hep-ex\]](https://arxiv.org/abs/1506.05332). SUSY-  
 4236 2014-09.
- 4238 [84] ATLAS Collaboration. “Search for heavy long-lived charged  $R$ -hadrons  
 4239 with the ATLAS detector in  $3.2 \text{ fb}^{-1}$  of proton–proton collision data at  
 4240  $\sqrt{s} = 13$  TeV”. In: *Phys. Lett. B* 760 (2016), pp. 647–665. doi: [10.1016/j.physletb.2016.07.042](https://doi.org/10.1016/j.physletb.2016.07.042). arXiv: [1606.05129 \[hep-ex\]](https://arxiv.org/abs/1606.05129).
- 4242 [85] Torbjorn Sjöstrand, Stephen Mrenna, and Peter Skands. “PYTHIA 6.4  
 4243 Physics and Manual”. In: *JHEP* 0605 (2006), p. 026. doi: [10.1088/1126-6708/2006/05/026](https://doi.org/10.1088/1126-6708/2006/05/026). arXiv: [hep-ph/0603175](https://arxiv.org/abs/hep-ph/0603175).
- 4245 [86] ATLAS Collaboration. *Further ATLAS tunes of PYTHIA 6 and Pythia 8*. ATL-  
 4246 PHYS-PUB-2011-014. 2011. url: <https://cds.cern.ch/record/1400677>.
- 4248 [87] Aafke Christine Kraan. “Interactions of heavy stable hadronizing parti-  
 4249 cles”. In: *Eur. Phys. J. C* 37 (2004), pp. 91–104. doi: [10.1140/epjc/s2004-01946-6](https://doi.org/10.1140/epjc/s2004-01946-6). arXiv: [hep-ex/0404001 \[hep-ex\]](https://arxiv.org/abs/hep-ex/0404001).
- 4251 [88] M. Fairbairn et al. “Stable massive particles at colliders”. In: *Phys. Rept.*  
 4252 438 (2007), p. 1. doi: [10.1016/j.physrep.2006.10.002](https://doi.org/10.1016/j.physrep.2006.10.002). arXiv:  
 4253 [hep-ph/0611040](https://arxiv.org/abs/hep-ph/0611040).
- 4255 [89] W. Beenakker, R. Hopker, M. Spira, and P. M. Zerwas. “Squark and gluino  
 4256 production at hadron colliders”. In: *Nucl. Phys. B* 492 (1997), p. 51. doi:  
 4258 [10.1016/S0550-3213\(97\)00084-9](https://doi.org/10.1016/S0550-3213(97)00084-9). arXiv: [hep-ph/9610490](https://arxiv.org/abs/hep-ph/9610490).

- 4257 [90] A. Kulesza and L. Motyka. “Threshold resummation for squark-antisquark  
 4258 and gluino-pair production at the LHC”. In: *Phys. Rev. Lett.* 102 (2009),  
 4259 p. 111802. doi: [10.1103/PhysRevLett.102.111802](https://doi.org/10.1103/PhysRevLett.102.111802). arXiv: [0807.2405 \[hep-ph\]](https://arxiv.org/abs/0807.2405).
- 4261 [91] A. Kulesza and L. Motyka. “Soft gluon resummation for the production  
 4262 of gluino-gluino and squark-antisquark pairs at the LHC”. In: *Phys. Rev.*  
 4263 *D* 80 (2009), p. 095004. doi: [10.1103/PhysRevD.80.095004](https://doi.org/10.1103/PhysRevD.80.095004). arXiv:  
 4264 [0905.4749 \[hep-ph\]](https://arxiv.org/abs/0905.4749).
- 4265 [92] Wim Beenakker, Silja Brensing, Michael Kramer, Anna Kulesza, Eric Lae-  
 4266 nen, et al. “Soft-gluon resummation for squark and gluino hadroproduc-  
 4267 tion”. In: *JHEP* 0912 (2009), p. 041. doi: [10.1088/1126-6708/2009/12/041](https://doi.org/10.1088/1126-6708/2009/12/041). arXiv: [0909.4418 \[hep-ph\]](https://arxiv.org/abs/0909.4418).
- 4269 [93] W. Beenakker, S. Brensing, M.n Kramer, A. Kulesza, E. Laenen, et al. “Squark  
 4270 and Gluino Hadroproduction”. In: *Int. J. Mod. Phys. A* 26 (2011), p. 2637.  
 4271 doi: [10.1142/S0217751X11053560](https://doi.org/10.1142/S0217751X11053560). arXiv: [1105.1110 \[hep-ph\]](https://arxiv.org/abs/1105.1110).
- 4272 [94] Michael Krämer et al. *Supersymmetry production cross sections in pp colli-*  
 4273 *sions at  $\sqrt{s} = 7 \text{ TeV}$* . 2012. arXiv: [1206.2892 \[hep-ph\]](https://arxiv.org/abs/1206.2892).
- 4274 [95] Rasmus Mackeprang and Andrea Rizzi. “Interactions of Coloured Heavy  
 4275 Stable Particles in Matter”. In: *Eur. Phys. J. C*50 (2007), pp. 353–362. doi:  
 4276 [10.1140/epjc/s10052-007-0252-4](https://doi.org/10.1140/epjc/s10052-007-0252-4). arXiv: [hep-ph/0612161 \[hep-ph\]](https://arxiv.org/abs/hep-ph/0612161).
- 4278 [96] Rasmus Mackeprang and David Milstead. “An Updated Description of  
 4279 Heavy-Hadron Interactions in GEANT-4”. In: *Eur. Phys. J. C*66 (2010),  
 4280 pp. 493–501. doi: [10.1140/epjc/s10052-010-1262-1](https://doi.org/10.1140/epjc/s10052-010-1262-1). arXiv:  
 4281 [0908.1868 \[hep-ph\]](https://arxiv.org/abs/0908.1868).
- 4282 [97] J. Alwall, R. Frederix, S. Frixione, V. Hirschi, F. Maltoni, O. Mattelaer, H.  
 4283 S. Shao, T. Stelzer, P. Torrielli, and M. Zaro. “The automated computation  
 4284 of tree-level and next-to-leading order differential cross sections, and  
 4285 their matching to parton shower simulations”. In: *JHEP* 07 (2014), p. 079.  
 4286 doi: [10.1007/JHEP07\(2014\)079](https://doi.org/10.1007/JHEP07(2014)079). arXiv: [1405.0301 \[hep-ph\]](https://arxiv.org/abs/1405.0301).
- 4287 [98] “dE/dx measurement in the ATLAS Pixel Detector and its use for particle  
 4288 identification”. In: (2011).
- 4289 [99] ATLAS Collaboration. “The ATLAS Simulation Infrastructure”. In: *Eur.*  
 4290 *Phys. J. C*70 (2010), pp. 823–874. doi: [10.1140/epjc/s10052-010-1429-9](https://doi.org/10.1140/epjc/s10052-010-1429-9). arXiv: [1005.4568 \[physics.ins-det\]](https://arxiv.org/abs/1005.4568).
- 4292 [100] ATLAS Collaboration. *Early Inner Detector Tracking Performance in the*  
 4293 *2015 Data at  $\sqrt{s} = 13 \text{ TeV}$* . ATL-PHYS-PUB-2015-051. 2015. URL: <https://cds.cern.ch/record/2110140>.
- 4295 [101] ATLAS Collaboration. “Luminosity determination in pp collisions at  $\sqrt{s}$   
 4296 = 8 TeV using the ATLAS detector at the LHC”. In: (2016). arXiv: [1608.03953 \[hep-ex\]](https://arxiv.org/abs/1608.03953).

- 4298 [102] Alexander L. Read. “Presentation of search results: The CL(s) technique”.  
4299 In: *J. Phys. G* 28 (2002). [,11(2002)], pp. 2693–2704. doi: [10.1088/0954-3899/28/10/313](https://doi.org/10.1088/0954-3899/28/10/313).  
4300